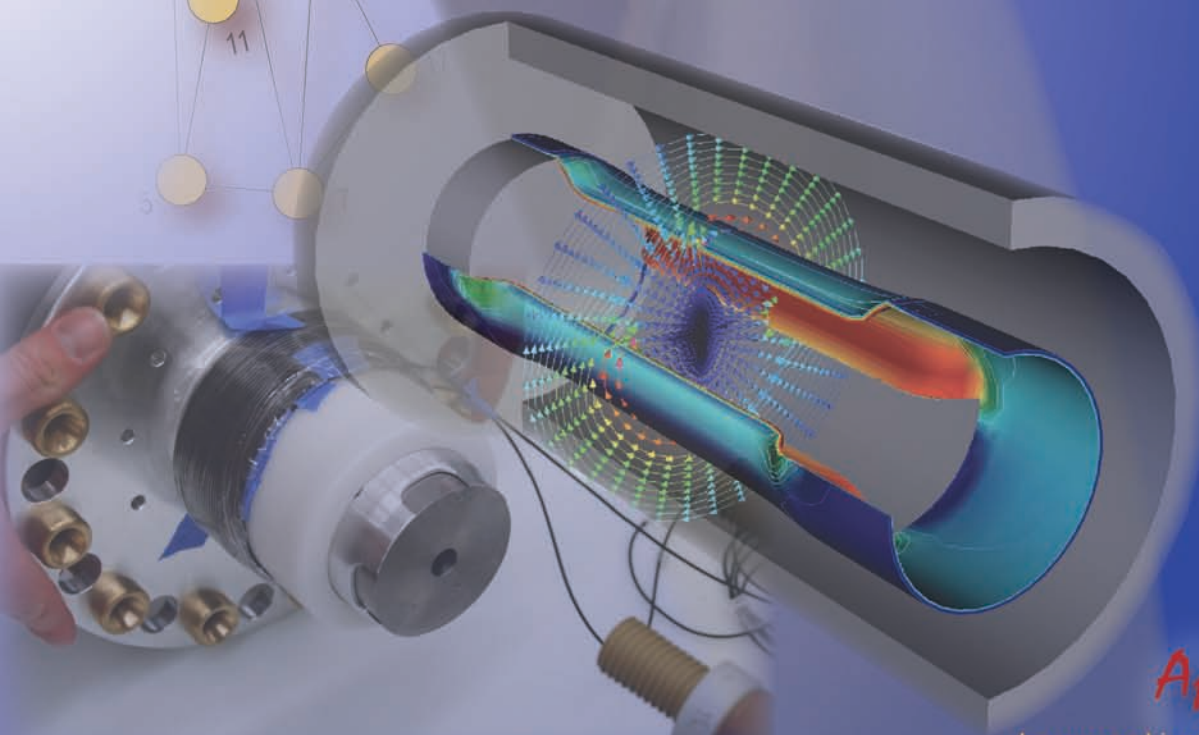
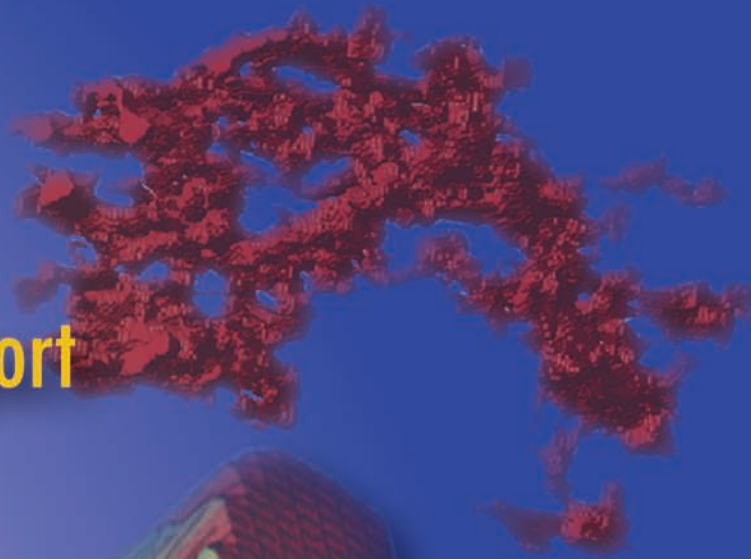
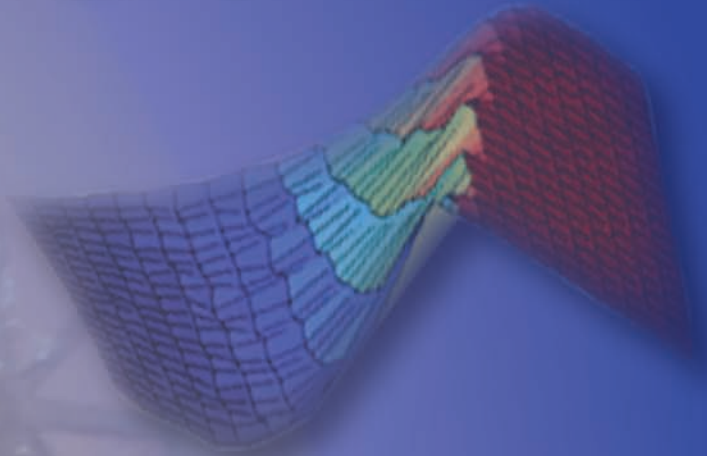
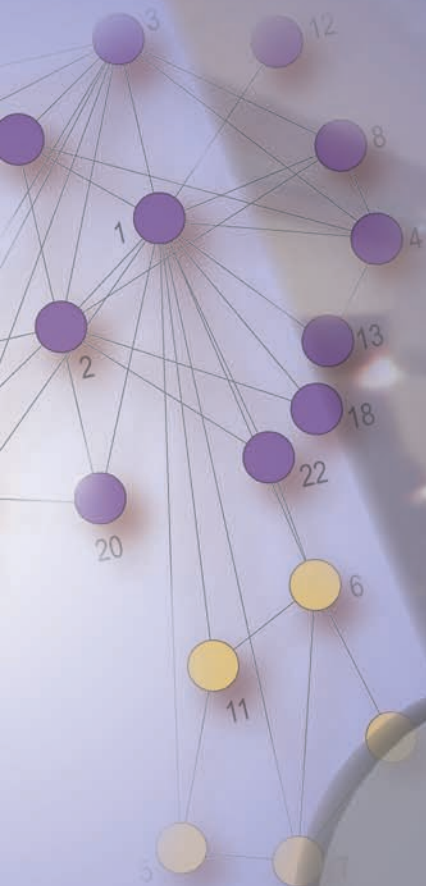


# FY07

## Engineering Research and Technology Report



*April 2008*

Lawrence Livermore National Laboratory  
LLNL-TR-401927

## *Acknowledgments*

### **Scientific Editor**

Camille Minichino

### **Graphic Designer**

Irene J. Chan

### **Project Manager**

Debbie A. Ortega

### **Production Staff**

Jeffrey B. Bonivert

Lucy C. Dobson

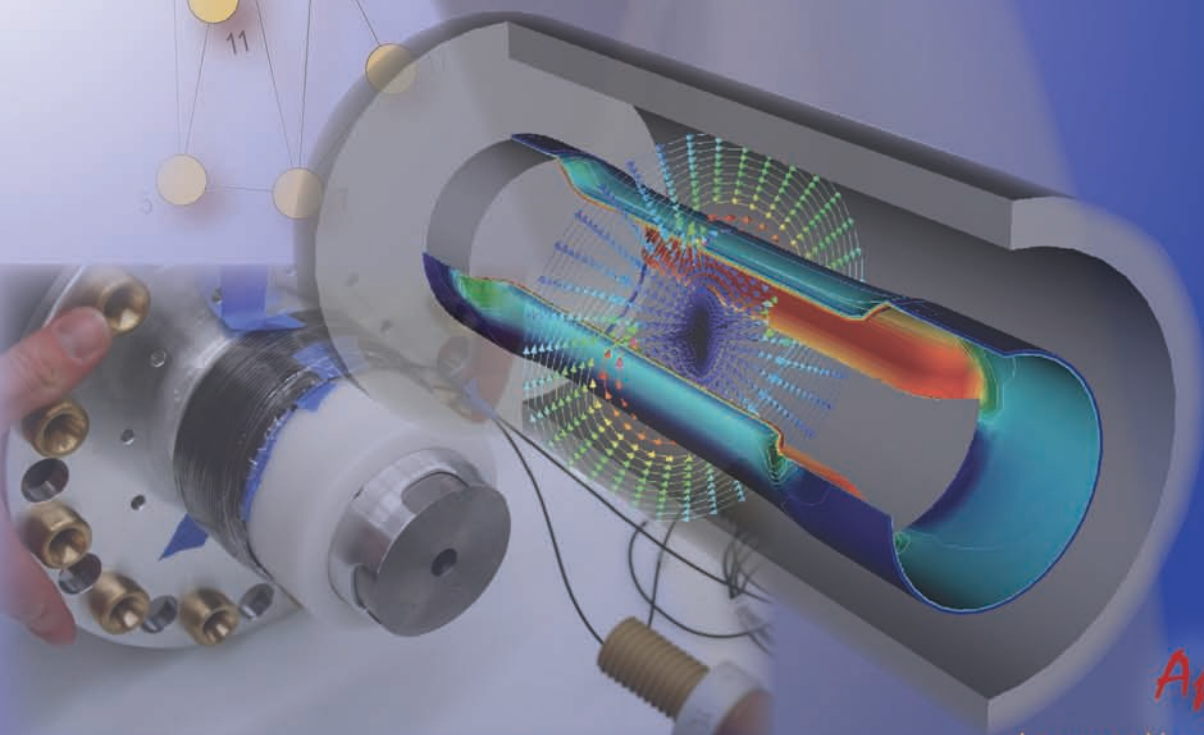
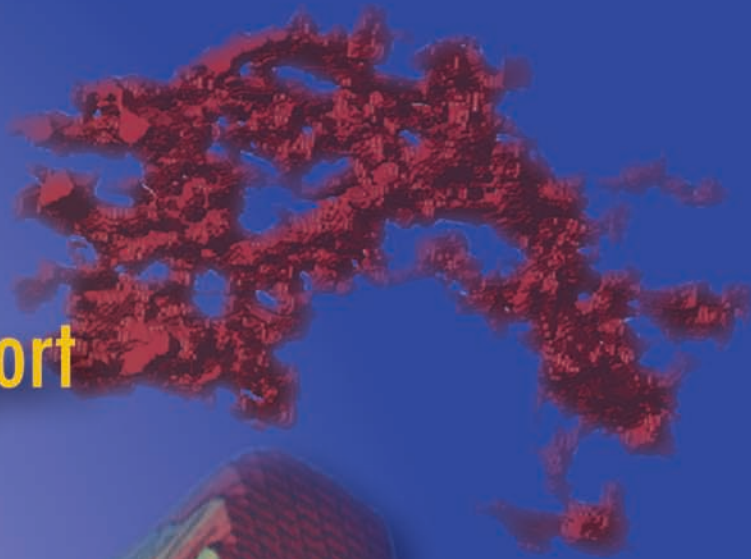
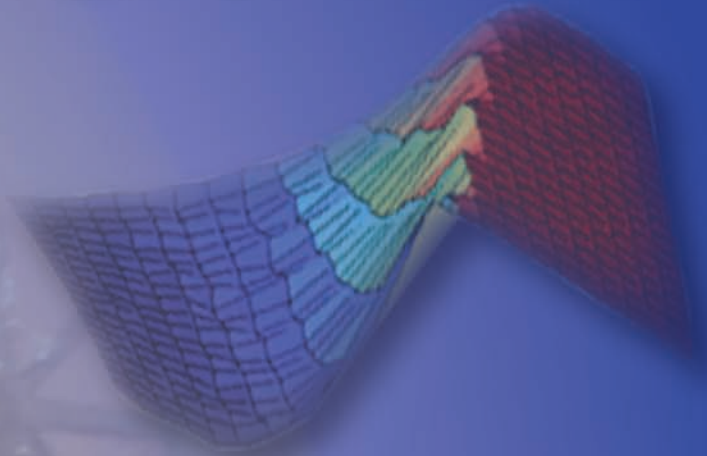
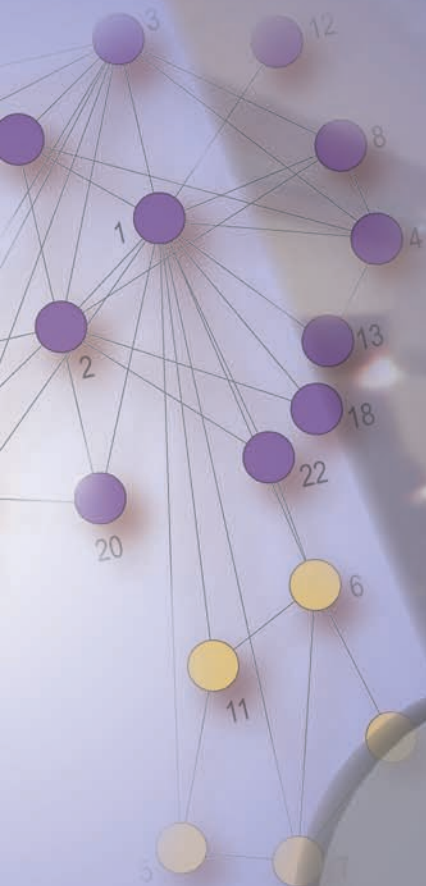
Kathy J. McCullough

### *Cover:*

Graphics representing projects from  
Engineering's technology areas.

# FY07

## Engineering Research and Technology Report



*April 2008*

Lawrence Livermore National Laboratory  
LLNL-TR-401927

# A Message from

**Steven R. Patterson**

**Associate Director for Engineering**



**T**his report summarizes the core research, development, and technology accomplishments in Lawrence Livermore National Laboratory's Engineering Directorate for FY2007. These efforts exemplify Engineering's more than 50-year history of developing and applying the technologies needed to support the Laboratory's national security missions. A partner in every major program and project at the Laboratory throughout its existence, Engineering has prepared for this role with a skilled workforce and technical resources developed through both internal and external venues. These accomplishments embody Engineering's mission: "Enable program success today and ensure the Laboratory's vitality tomorrow."

Engineering's mission is carried out through research and technology. Research is the vehicle for creating competencies that are cutting-edge, or require discovery-class groundwork to be fully understood. Our technology efforts are discipline-oriented, preparing research breakthroughs for broader application to a variety of Laboratory needs. The term commonly used for technology-based projects is "reduction to practice."

This report combines our work in research and technology into one volume, organized into thematic technical areas: Engineering Modeling and Simulation; Measurement Technologies; Micro/ Nano-Devices and Structures; Engineering Systems for Knowledge and Inference; and Energy Manipulation.

**Engineering Modeling and Simulation** efforts focus on the research, development, and deployment of computational technologies that provide the foundational capabilities to address most facets of Engineering's mission. Current activities range from fundamental advances to enable accurate modeling of full-scale DOE

and DoD systems performing at their limits, to advances for treating photonic and microfluidic systems.

FY2007 research projects encompassed coupling standard finite element analysis methods with "meshless" methods to address systems performing at and beyond failure; and multi-physics coupling of electromagnetics with structural mechanics to simulate systems such as electromagnetic railguns. Technology projects included enhancements, verification, and validation of engineering simulation tools and capabilities; progress in visualization and data management tools; and extensions of our competence in structural damage analysis.

**Measurement Technologies** comprise activities in nondestructive characterization, metrology, sensor systems, and ultrafast technologies for advanced diagnostics. The advances in this area are essential for the future experimental needs in Inertial Confinement Fusion, High-Energy-Density Physics, Weapons, and Department of Homeland Security programs.

FY2007 research featured probes for micrometer-scale metrology; investigations into terahertz systems for explosives and detection; illicit radionuclide detection; and investigation of the structure and properties of nanoporous materials. Technology projects included new error budgeting tools for nondestructive evaluation systems; x-ray system modeling; laser-based ultrasound applications; and tools to aid in the identification of defects in large CT data sets.

**Micro/Nano-Devices and Structures** encompass technology efforts that fuel the commercial growth of microelectronics and sensors, while simultaneously customizing these technologies for unique, noncommercial applications that are mission-specific to the Laboratory and DOE. The Laboratory's R&D talent

and unique fabrication facilities have enabled highly innovative and custom solutions to technology needs in Stockpile Monitoring and Stewardship, Homeland Security, and Intelligence.

FY2007 research projects included systems for defense against biothreats and for the manipulation of biomolecules and viruses; studies of transport behavior and crystal-driven neutron sources. Technology projects included laser pantography; pyrosequencing and validation of acoustic modeling for microfluidic systems; construction of diagnostics for optical gating; applications of lasers and optical sensors; and new capabilities for micro- and nano-fabrication.

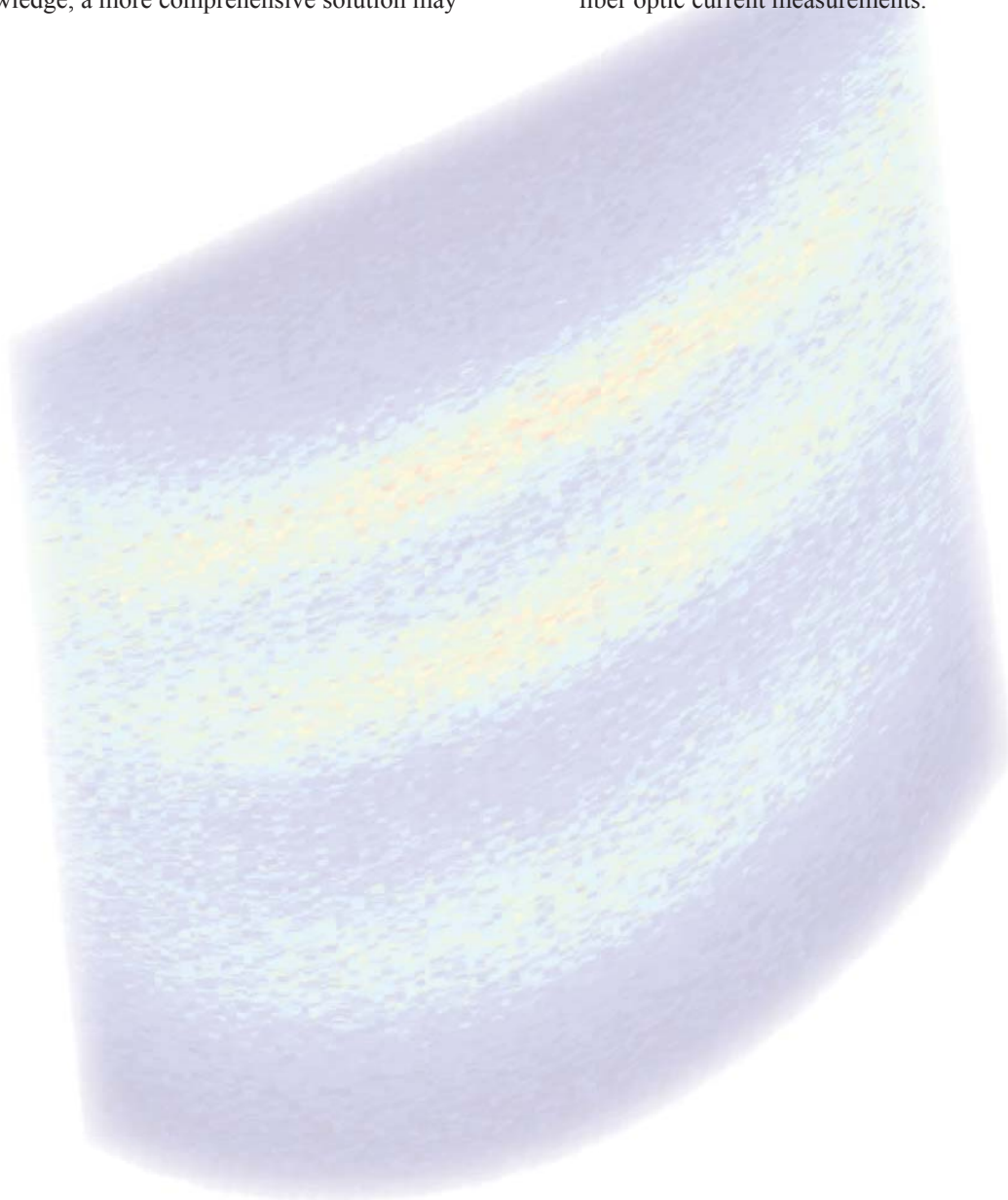
**Engineering Systems for Knowledge and Inference**, an emerging focus area for Engineering as well as for the country at large, encompasses a wide variety of technologies. The goal is to generate new understanding or knowledge of situations, thereby allowing anticipation or prediction of possible outcomes. With this knowledge, a more comprehensive solution may

be possible for problems as complex as the prediction of disease outbreaks or advance warning of terrorist threats.

FY2007 research efforts were centered on the decomposition of large-scale semantic graphs. Technology efforts included a testbed to evaluate hierarchical clustering; and work on a statistical approach to the design of complex systems in the presence of uncertainty.

**Energy Manipulation**, a long time focus that is receiving increased emphasis due to newly emerging applications, encompasses the fundamental understanding and technology deployment for many modern pulsed-power applications. This area has broad applications for magnetic flux compression generators and components for modern accelerators.

FY2007 research focused on an ultra-high velocity railgun. Technology efforts focused on railgun pulse power systems and diagnostics; UV-induced flashover; diagnostics for electrical breakdown in vacuum; and fiber optic current measurements.



# Contents

## Introduction

A Message from Steven R. Patterson.....	ii
---	----

## Engineering Modeling and Simulation

<b>Deformation of Low Symmetry and Multiphase Materials</b> Nathan R. Barton .....	2
<b>Plasticity at High Pressures and Strain Rates Using Oblique-Impact Isentropic-Compression Experiments</b> Jeffrey N. Florando .....	4
<b>“Natural Neighbor” Meshless Method for Modeling Extreme Deformations and Failure</b> Michael A. Puso .....	6
<b>Laser Glass Damage: Computational Analysis of Mitigation Process</b> James S. Stölken .....	8
<b>Electro-Thermal-Mechanical Simulation Capability</b> Daniel White .....	10
<b>Petascale Simulation Initiative</b> John M. May .....	12
<b>Electromagnetics Code Management</b> Daniel White .....	14
<b>Finite Element Analysis Visualization and Data Management</b> Bob Corey .....	16
<b>Rotational Kinematics Output and Other Improvements in DYNA3D</b> Jerry I. Lin .....	18
<b>NIDE3D Code Maintenance and Enhancement</b> Michael A. Puso .....	20
<b>Validation of Reinforced Concrete Modeling Capabilities for Seismic Response</b> Steven W. Alves .....	22
<b>Thermal-Structural Analysis of the MacArthur Maze Collapse</b> Charles R. Noble .....	24
<b>Enhanced Composite Modeling Tools</b> Andrew Anderson .....	26
<b>EMP Simulation and Measurement Data Analysis in Support of the Titan Experiments</b> Charles G. Brown, Jr. ....	28
<b>Full-Process Computer Model of Magnetron Sputter: Testing Existing State-of-the-Art Components</b> Christopher Walton .....	30

<b>Direct Simulation Monte Carlo Benchmarking and Code Comparison</b> Aaron P. Wemhoff .....	32
<b>Photonic Doppler Velocimetry</b> Adam White .....	34
 <i>Measurement Technologies</i>	
<b>Standing Wave Probes for Micrometer-Scale Metrology</b> Richard M. Seugling .....	38
<b>Error Budgeting and Certification of Dimensional Metrology Tools</b> Jeremy J. Kroll .....	40
<b>Uncertainty Analysis with Inspection Shop Measurements</b> Walter W. Nederbragt .....	42
<b>X-Ray System Modeling</b> William D. Brown .....	44
<b>Detection, Classification, and Estimation of Radioactive Contraband from Uncertain, Low-Count Measurements</b> James V. Candy .....	46
<b>Terahertz Spectroscopic Imaging for Standoff Detection of High Explosives</b> Michael W. Burke .....	48
<b>Application of Laser-Based Ultrasound to Glovebox Enclosed Materials</b> Robert Huber .....	50
<b>Defect Detection in Large CT Image Sets</b> Douglas N. Poland .....	52
<b>The Structure and Properties of Nanoporous Materials</b> Anthony Van Buuren .....	54
<b>Construction of a Frequency Resolved Optical Gating (FROG) Diagnostic</b> Corey V. Bennett .....	56
<b>Picosecond Response, Recirculating Optical Probe for Encoding Radiation (ROPER)</b> Stephen P. Vernon .....	58
<b>Serrated Light Illumination for Deflection Encoded Recording (SLIDER)</b> John E. Heebner .....	60
 <i>Micro/Nano-Devices and Structures</i>	
<b>Biological Sample Preparation Infrastructure</b> N. Reginald Beer .....	64
<b>Rapid Defense Against the Next-Generation Biothreat</b> Raymond P. Mariella, Jr. ....	66

<b>Validation of 3-D Acoustic Modeling of Commercial Codes for Microfluidic Systems</b> Raymond P. Mariella, Jr. ....	68
<b>Thermal-Fluidic System for Manipulation of Biomolecules and Viruses</b> Kevin D. Ness .....	70
<b>Flow-Through Pyrosequencing in a Microfluidic Device</b> Klint A. Rose.....	72
<b>Investigation of Hybridization Times for DNA Microarrays</b> Robin Miles .....	74
<b>Microfabricated Silicon Nib for Low-Cost, Multiplexed Micro-Coating</b> Erik V. Mukerjee .....	76
<b>Advanced Polymerase Chain Reaction Module</b> Satinderpall Pannu .....	78
<b>Tunable Optical Cavities for Gas Sensor</b> Tiziana Bond .....	80
<b>Extending Lasers to Universal Gates for Photonic FPGAs</b> Tiziana Bond .....	82
<b>Compact Tunable Optical Sensors</b> Jack Kotovsky .....	84
<b>Transport Behavior and Conversion Efficiency in Pillar Structured Neutron Detectors</b> Rebecca J. Nikolić .....	86
<b>Compact High-Intensity Crystal-Driven Neutron Source</b> Jeffrey D. Morse .....	88
<b>Pillar Neutron Detector Fabrication</b> Rebecca J. Nikolić .....	90
<b>Flow Programmed Mesoscale Assembly of Nanoengineered Materials and Net Shape Components</b> Klint A. Rose .....	92
<b>Laser Pantography</b> Christopher M. Spadaccini .....	94
<b>Bridging the Length and Time Scales from Atomistics to the Microscale</b> Todd Weisgraber .....	96
<b>“HE-Less” Detonator Modeling</b> James F. McCarrick .....	98
<b>Chip Slapper Detonator Processing for Rapid Prototyping and Hydrodynamic Properties</b> Mark A. Schmidt .....	100

*Engineering Systems for Knowledge and Inference*

**Semantic Graph Hierarchical Clustering and Analysis Testbed**

Tracy D. Lemmond ..... 104

**Decomposition of Large-Scale Semantic Graphs via an Efficient Communities Algorithm**

Yiming Yao ..... 106

**Statistical Approach to Complex Systems in the Presence of Uncertainty**

Lee G. Glascoe ..... 108

*Energy Manipulation*

**Ultrahigh-Velocity Railgun**

Jerome M. Solberg ..... 112

**Pulse Power Systems and Diagnostics for the Fixed Hybrid Armature Railgun**

Todd J. Clancy ..... 114

**Fast Diagnostic for Electrical Breakdowns in Vacuum**

Timothy L. Houck ..... 116

**UV-Induced Insulator Flashover**

Jay Javedani ..... 118

**Evaluation of Light Activated Thyristors for Pulsed Power Applications**

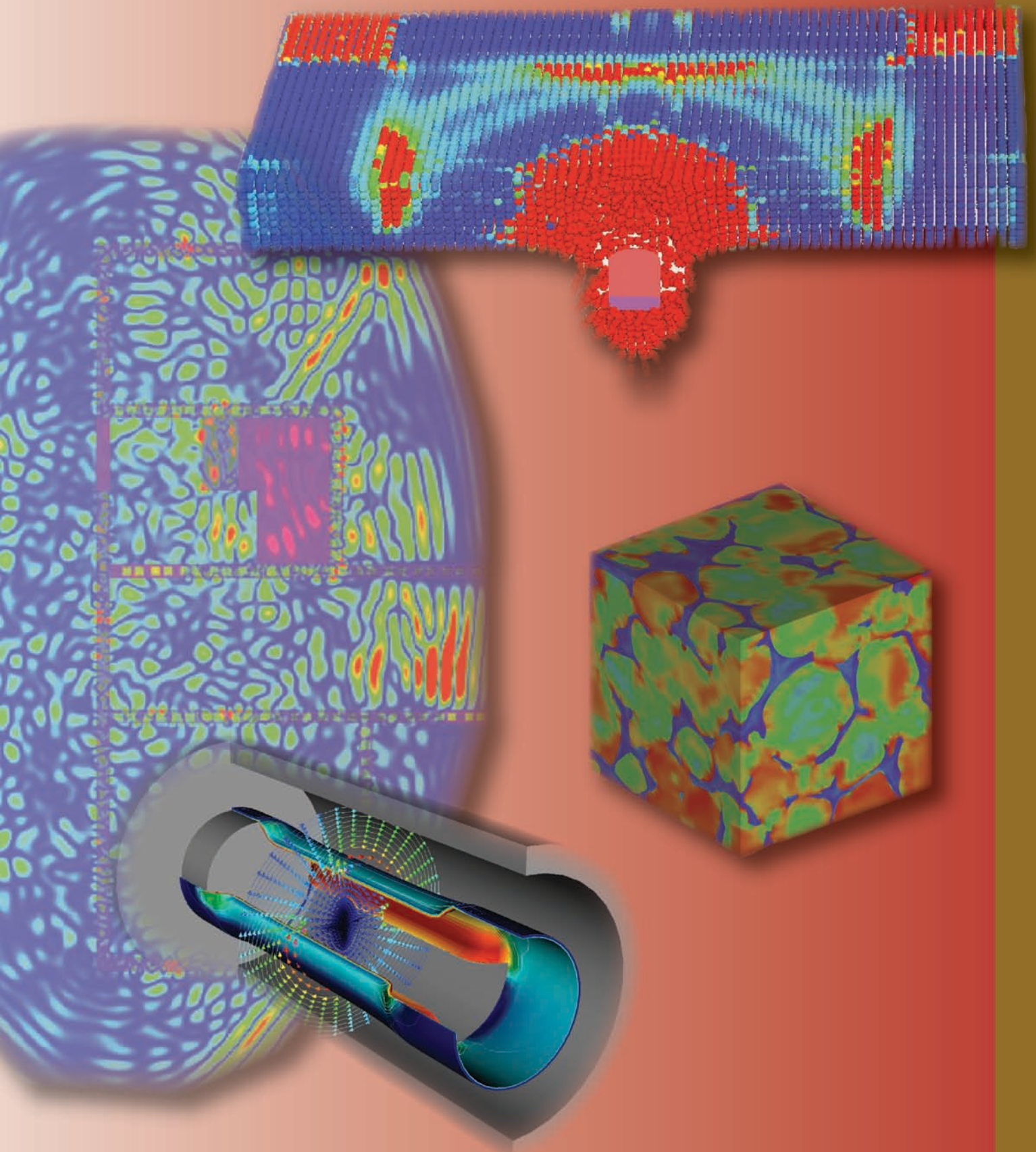
Laura Tully ..... 120

**Fiber Optic Current Measurements Using Faraday Rotation Diagnostics**

Brent McHale ..... 122

*Author Index*..... 125





Engineering Modeling and Simulation



# Deformation of Low Symmetry and Multiphase Materials

**M**aterials composed of low symmetry crystals or of multiple solid phases exhibit heterogeneous deformation at the microstructural scale, presenting significant challenges to efforts to construct macroscale constitutive models. This deformation heterogeneity at the microstructural scale also produces stress concentration, which can lead to fracture or influence the onset and progress of phase transformations. We are developing an approach that explicitly incorporates effects of microstructure and deformation heterogeneity in a framework suited to analysis of engineering scale components.

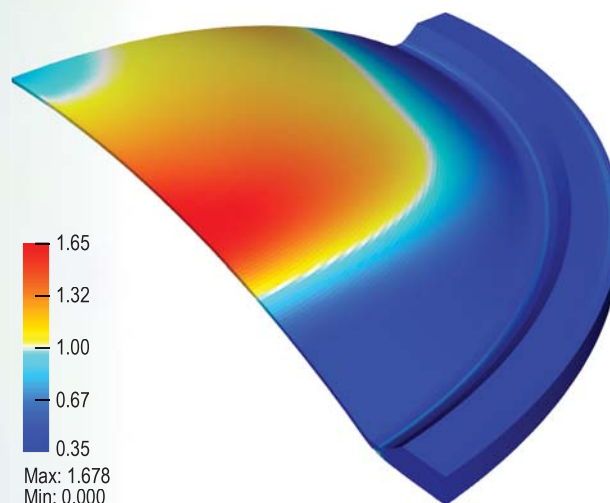
Applications involving fully developed plastic flow are targeted. We explicitly represent the microstructure, directly treating deformation heterogeneities, and we build on emerging technologies for effectively combining microscale plasticity simulations with macroscale models. New capabilities will capture the impact of microstructure, and thus material processing, on performance of engineering scale components.

For example, phenomena such as shear localization arise naturally from application of the method at the appropriate scale.

## Project Goals

The overarching goal of this project is to produce effective macroscale models through novel homogenization methods for materials where conventional methods fail. The immediate application space includes a broad class of engineering simulations, ranging from forming operations to dynamic loading scenarios. Figure 1 shows an example application, with computation performed using similar techniques appropriate to single-phase cubic symmetry polycrystalline materials. Software is developed in a component-oriented fashion, making use of tools that enhance parallel load-balancing through task parallelism, as shown in Fig. 2. Initial development is focused on the Ti-6%Al-4%V (Ti-6Al-4V) alloy, given its widespread use and the availability of relevant experimental data.

**Figure 1.** A biaxial bulge test workpiece, deformed by application of pressure to the lower surface. The false color depicts the relative effective plastic strain rate. Due to its lattice orientation distribution function, the sheet material has orthotropic symmetry and exhibits macroscopic strain localization, as indicated by the red region along the nearer symmetry plane.



*Nathan R. Barton*  
(925) 422-9426  
barton22@llnl.gov

## Relevance to LLNL Mission

In multiphase materials of interest to LLNL, such as Ti-6Al-4V, microstructure influences yield and flow stresses, ductility, high- and low-cycle fatigue, creep, fracture toughness, and large crack growth properties. Microstructure has also been shown to influence response under dynamic loading conditions. The presence of low symmetry phases can contribute to severe anisotropy and a tendency for strain localization. Explicit inclusion of the microstructure allows for the effective treatment of deformation heterogeneities at the microstructural scale. In addition to multiphase titanium alloys, the approach is applicable to low symmetry crystalline metals such as uranium (orthorhombic), beryllium (hexagonal), and  $\alpha$ -plutonium (monoclinic).

## FY2007 Accomplishments and Results

Our first completed milestone is associated with the assessment of important features for microstructures of interest in Ti-6Al-4V. We are able to use experimental data to inform numerical multiphase microstructure realizations (Fig. 3). New techniques have been developed to capture the morphology of the experimentally observed microstructures.

Another milestone is associated with new capabilities for fine-scale calculations in the ALE3D finite element program. We have determined a fine-scale implementation strategy and have tested ALE3D in the role of the fine-scale model. New capabilities have been developed for obtaining steady plastic flow solutions in ALE3D, with a specialized elasto-viscoplastic fine-scale material model. Figure 4 depicts results from an example calculation performed using ALE3D.

Implementation is under way for new physics and software requirements for the appropriate coarse/fine coupling strategy. This includes homogenization to obtain anisotropic coarse-scale elastic response from fine-scale data, new coupling software for fine-scale models that do not provide derivative information, and velocity-gradient-driven parameterized plastic flow.

**Related References**

1. Arsenlis, A., N. R. Barton, R. Becker, and R. E. Rudd, "Generalized *In Situ* Adaptive Tabulation for Constitutive Model Evaluation in Plasticity," *Compt. Methods Appl. Mech. & Eng.*, **196**, pp. 1-13, 2006.

2. Barton, N. R., J. Knap, A. Arsenlis, R. Becker, R. D. Horning, and D. R. Jefferson, "Embedded Polycrystal Plasticity and Adaptive Sampling," *Int. J. Plasticity*, **24**, pp. 242-266, 2008.

3. Barton N. R., and H.-R. Wenk, "Dauphiné Twinning in Polycrystalline Quartz," *Modeling Simul. Mater. Sci. Eng.*, **15**, pp. 369-394, 2007.

4. Brechet, Y. J. M., P. Dawson, J. D. Embury, C. G'sell, S. Suresh, and H.-R. Wenk, "Recommendations on Modeling Polyphase Plasticity: Conclusions of Panel Discussions," *Mater. Sci. Eng.*, **A175**, pp. 1-5, 1994.

5. Pope, S. B., "Computationally Efficient Implementation of Combustion Chemistry Using *In Situ* Adaptive Tabulation," *Combust. Theory Modeling*, **1**, pp. 41-63, 1997.

*FY2008 Prepared Work*

In the coming fiscal year, software components that have been developed for various aspects of the multiscale problem will be combined into a working whole. After testing, algorithm refinement, performance tuning, and model calibration, the overall capability will be validated by comparison with available experimental data at the appropriate length scale. We also plan to demonstrate extension of the method to another low symmetry or multiphase material such as beryllium or uranium.

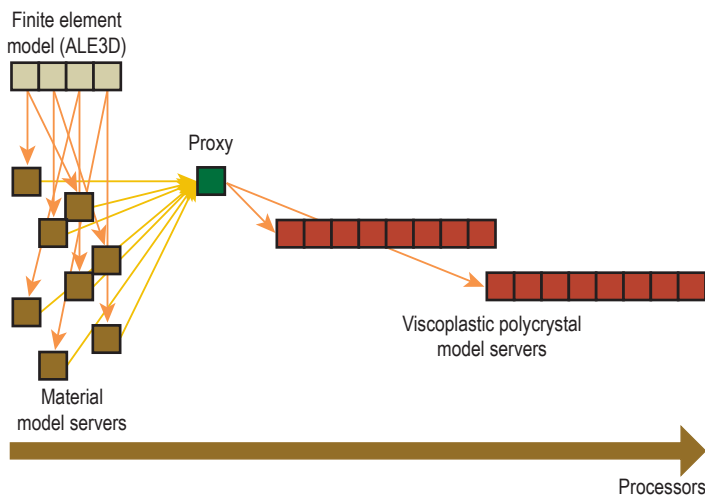


Figure 2. Schematic of Multiple-Program, Multiple-Data (MPMD) parallelism showing the Remote Method Invocation (RMI) pattern during the material model evaluation. Each box indicates a separate instance of a given executable program, with box subdivisions indicating parallelism within an executable.

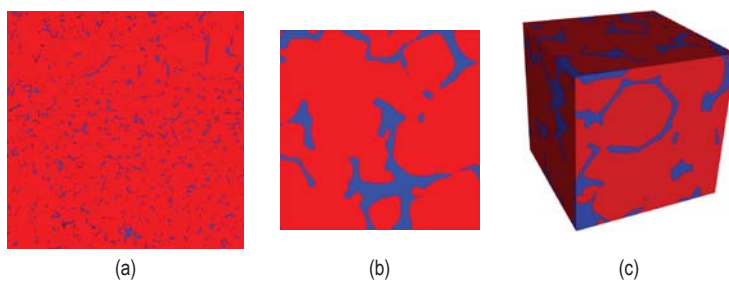


Figure 3. (a) Measured, (b) and (c) numerically generated (at different magnifications) microstructures for Ti-6Al-4V. Red indicates  $\alpha$  phase; blue indicates  $\beta$  phase. Microstructures are obtained experimentally using electron backscatter diffraction. Numerical microstructures are generated by sampling the appropriate distribution functions and using particle-packing techniques. Numerical microstructures reproduce experimentally observed morphologies, with tunable parameters to control features such as phase volume fraction.

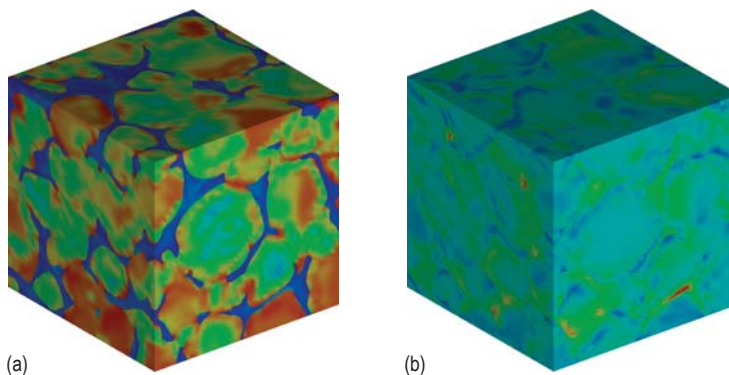


Figure 4. Heterogeneity of (a) stress magnitude and (b) plastic strain rate in a two-phase Ti-6Al-4V microstructure simulated in ALE3D, with relative plastic strain rates reaching ten times the nominal applied value. The highest relative plastic strain rates are observed in the  $\beta$  phase, which has a more isotropic flow behavior, while the highest stress magnitudes are observed in the more anisotropic  $\alpha$  phase.

# Plasticity at High Pressures and Strain Rates Using Oblique-Impact Isentropic-Compression Experiments



Jeffrey N. Florando  
(925) 422-0698  
florando1@llnl.gov

Various aspects of the Laboratory's national security mission depend on accurate computer code simulations of high-strain-rate plastic flow (*i.e.*, nonreversible deformation) under conditions of high hydrostatic pressures. While progress has been made in recent years, especially at the extreme cases of pressure and strain rate, there is still an uncertainty in understanding the strength of materials under conditions of combined high strain rate ( $10^4$  to  $10^6$  s<sup>-1</sup>) and high pressure (1 to 100 GPa).

Current strength models used in simulations include some physically based models such as the Mechanical Threshold Stress formulation, which has over 20 parameters. The uncertainty in the values for these parameters as well as values for the parameters in other physically based models is under question due to the inherent difficulties in conducting and extracting high-quality experimental data in the high-pressure and high-strain-rate regimes. The experimental studies of material strength at these pressure and strain rate regimes will further the understanding of the underlying physical strength mechanisms needed for accurate material strength models.

## Project Goals

The goals of this project are to develop an oblique-impact isentropic-compression experiment (Fig. 1) to measure the strength of materials under a condition of combined high strain rate ( $10^4$  to  $10^6$  s<sup>-1</sup>) and high pressure (1 to 100 GPa). The isentropic compression allows for high pressures to be achieved over relatively long time frames (micro-seconds), and the oblique impact allows for a measurement of the strength properties under pressure. The strength data will then be used to refine and enhance the current strength models. When completed, this work will increase the Laboratory's ability to develop predictive strength models for use in computer code simulations.

## Relevance to LLNL Mission

Understanding and simulating the strength of materials under dynamic loading conditions is a major component of the Laboratory's Stockpile Stewardship Program and is applicable to future National Ignition Facility (NIF) experiments. These computer code simulations, however, require additional experimental data in order to develop new models and validate the existing codes.

## FY2007 Accomplishments and Results

The oblique-impact isentropic-compression experiment requires a keyed barrel. The experiments are developed at LLNL and tests are performed at Brown University. A formal collaboration has been established with a three-year contract that is now in place. The first year

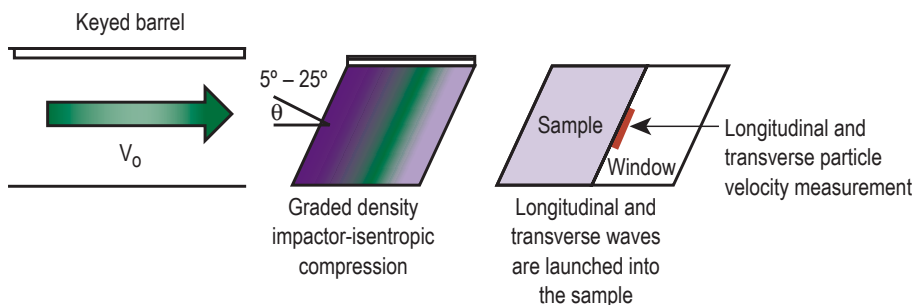
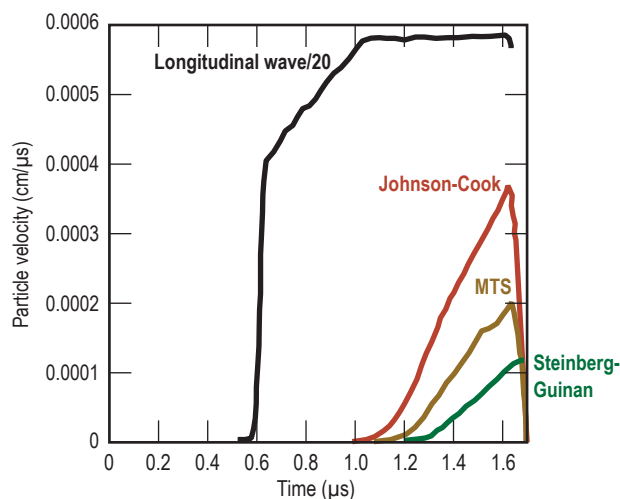
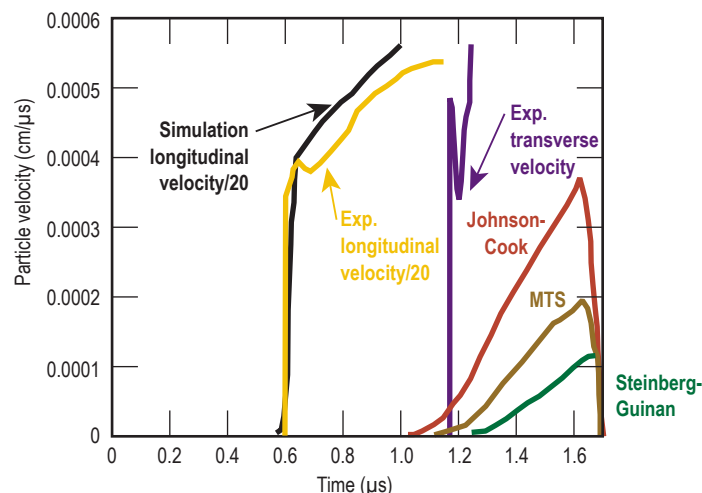


Figure 1. Oblique-impact isentropic-compression experiment.



**Figure 2.** 3-D hydrodynamics simulation showing the longitudinal wave and the sensitivity of the transverse waves to the different strength models.



**Figure 3.** Experimental data showing the measured longitudinal and transverse waves. While there is good agreement between the simulation and experiment in the longitudinal wave, the experimental transverse wave is much larger, signifying a material that has higher strength than predicted.

has focused on fielding the experiment at low pressures, which includes sample preparation and characterization, simulations of the proposed experiment, and results from the initial experiments.

**Sample Preparation and Characterization.** The initial sample configuration is a Cu sample with a sapphire window, which was chosen due to its close impedance match. A fine diffraction grating of 1200 lines/mm, which is used to measure the normal and transverse waves, is etched into the sapphire windows, and a thin layer (~130 nm) of Cu is deposited on top of the grating. The Cu sample is then attached to the deposited Cu using epoxy on the circumference. In order to achieve a near isentropic compression, a graded density impactor is used. Diffusion bonded impactors have been characterized to understand the strength and waves imparted into the sample.

**Simulations.** We have performed a series of simulations (Fig. 2), which shows the validity of the proposed experiments. The simulation results show that the transverse wave, which is related to the strength of the material under pressure, is very sensitive to the strength model used. The

simulations are also used to help guide the experiments, such as determining the optimal sample and sapphire thickness.

**Experimental Results.** Experiments have been performed at Brown University on Cu/sapphire samples. The longitudinal and transverse wave results are shown in Fig. 3. A couple of key features are that the graded density impactor causes a ramp in the pressure (isentropic compression) which controls the strain rate to  $\sim 10^5$ , and that the transverse wave arrives near peak pressure. Also, the transverse signal measured is much higher than expected, signifying that the Cu is stronger than the models predict.

### Related References

1. Remington, *et al.*, *Mat. Sci. and Tech.*, **22**, p. 474, 2006.
2. Follansbee, P. S., and U. F. Kocks, *Acta Metall.*, **36**, p. 81, 1988.
3. Nguyen, J. H., D. Orlikowski, F. H. Streit, N. C. Holmes, and J. A. Moriarty, *AIP Proceedings*, **706**, p.1225, 2004.
4. Clifton, R. J., and R. W. Klopp, *ASM Handbook 9th ed.*, **8**, p. 230, 1985.

### FY2008 Proposed Work

In FY2008, additional low-pressure experiments and intermediate pressure experiments (150 to 300 kbar) on Cu, Ta, and V are planned at Brown University. The results from the tests will give us the necessary data to begin the development and refinement of strength models. Based on the results, the designs for a 2-in. graded density impactor and a soft recovery experiment will be explored. Simulations will continue to be conducted to aid in the design of the experiments.

# “Natural Neighbor” Meshless Method for Modeling Extreme Deformations and Failure



Michael A. Puso  
(925) 422-8198  
puso1@llnl.gov

The objective of this work is to develop a fully Lagrangian analysis approach based on “natural neighbor” discretization techniques to model extreme deformation and failure for analyses such as earth penetration and dam failure. The standard finite element approaches often do not work in these applications because of “mesh tangling” (Fig. 1). Lagrangian methods allow the tracking of particles and free surfaces, which makes handling of sophisticated material models and effects due to debris and fragmentation much more straightforward and natural as compared to Eulerian and arbitrary-Lagrangian-

Eulerian (ALE)-type methods. On the other hand, the standard meshless particle methods have other pathologies such as instabilities and insufficient treatment of boundaries and inefficiencies. The application of novel shape functions based on natural neighbors has been successfully used in this work to overcome many of these pathologies.

## Project Goals

The goal of this work is to fix many of the inherent problems associated with meshless methods. This involves the development of several neighbor-based approximation methods, stable

time-step calculations, and techniques for improving efficiency. A number of refereed journal articles resulted from this work and the methods are currently implemented and available in Laboratory codes. Verification and validation and material modeling have also been a key component of our effort.

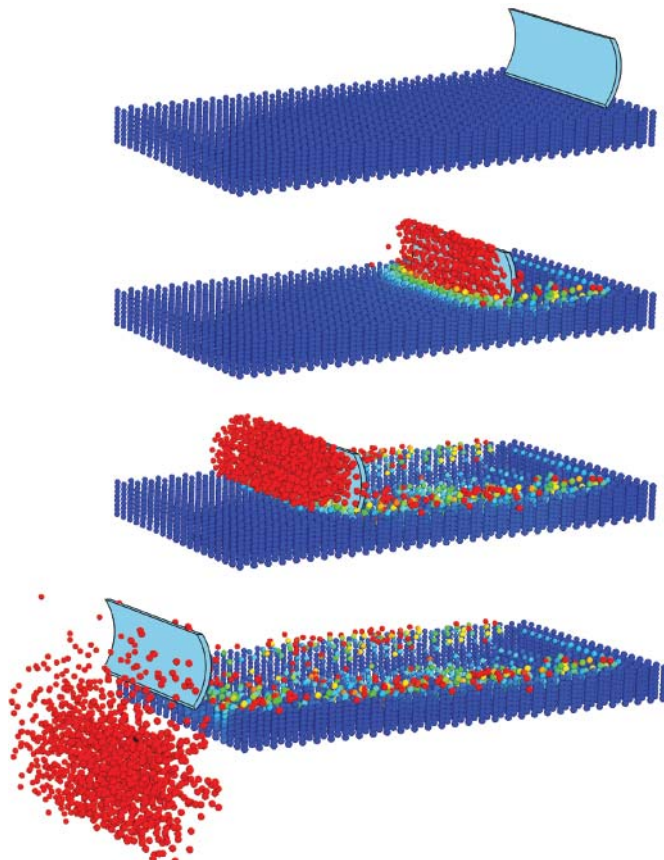


Figure 1. DYN3D particle simulation of earth moving problem. This type of analysis would not be feasible with finite elements due to mesh tangling.

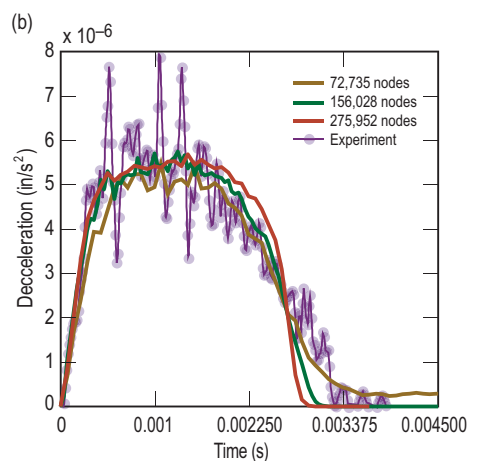
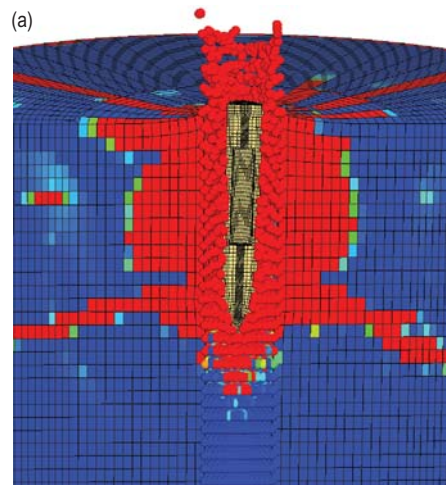
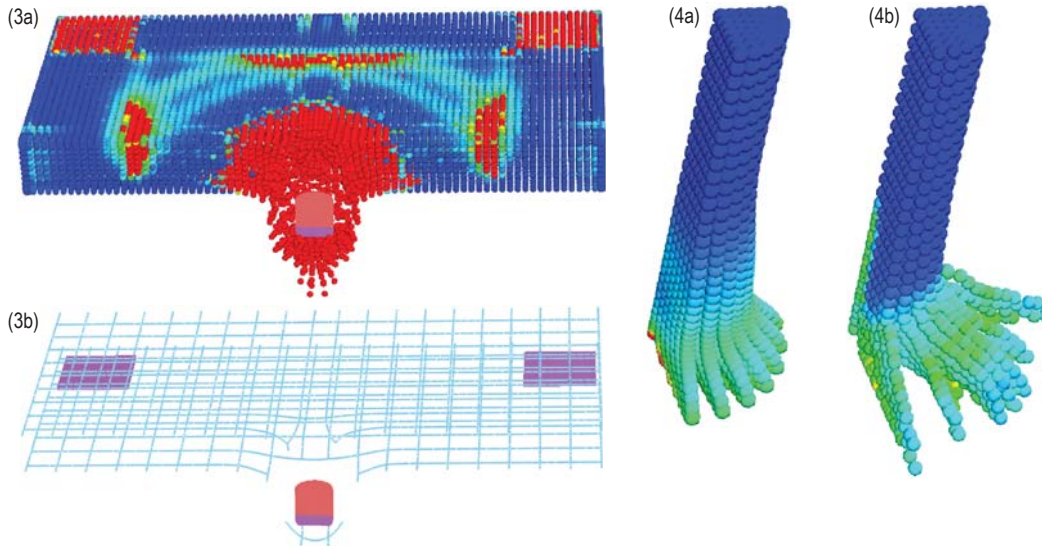


Figure 2. (a) DYN3D simulation of concrete penetration (tensile damage shown in red); (b) comparison of simulation results to experimental results from Sandia National Laboratories. Three different nodal discretizations were used in the simulation and all compare well to the Sandia test results.



**Figure 3.** (a) DYN3D simulation of penetration of reinforced concrete (tensile damage shown in red); (b) rebar (shown alone) attached to particles in the simulation (eventually fails upon exit). Simulations compare well to data in the literature.

**Figure 4.** (a) View of Taylor bar from new particle method simulation. An evolving elliptical kernel was used to maintain proper particle connectivity. (b) Results from classical particle methods (e.g. Smoothed Particle Hydrodynamics) where "toeing" results. This effect is often attributed to a tensile instability.

### Relevance to LLNL Mission

A number of high profile analysis areas will benefit from this work. High rate penetration dynamics is identified as a challenge area in engineering and validation work in this area (Fig. 2) has already been done using the new approaches with the LLNL code DYN3D. Homeland Security applications are important to the LLNL mission and validation has begun looking at the effects of penetrators on reinforced concrete walls (Fig. 3).

### FY2007 Accomplishments and Results

Our FY2005 implementation used a natural neighbor scheme that required the computation of a Voronoi diagram at each step of an analysis. In FY2006, we proposed a simplified scheme where natural neighbors were used to form elliptical kernel functions in a moving least squares (MLS) approach for computing shape functions.

In FY2007 this method was extended to the treatment of large deformation problems by applying the appropriate evolution scheme for the elliptical kernels (Fig. 4). In addition, a maximum entropy (MAXENT) method was applied as an alternative to the MLS approach to better treat essential boundary conditions. Given an elliptical kernel function  $\omega_i$  at node  $i$ , MAXENT shape functions  $\phi_i$  are chosen by minimizing the informational entropy function  $f$  in (1), subject to the partition of unity and linear exactness constraints in (2).

$$f(x; \phi) = - \sum_{i=1}^n \phi_i(x) \ln \left( \frac{\phi_i(x)}{\omega_i(x)} \right) \quad (1)$$

$$\begin{aligned} \sum_{i=1}^n \phi_i(x) &= 1, \\ \sum_{i=1}^n \phi_i(x)(x^i - x) &= 0, \end{aligned} \quad (2)$$

Finally, a new method for handling principal stress damage with plasticity was implemented in the concrete model used in the penetrator analysis shown in Figs. 2 and 3. The remainder of our work was in the area of verification and validation as demonstrated in Figs. 2 through 4.

### Related References

1. Puso, M. A., "An Improved Linear Tetrahedral Element for Plasticity," *Joint ASME/ASCE/SES Conference on Mechanics and Materials, Proceedings of McMat*, Baton Rouge, Louisiana, June 1 – 3, 2005.
2. Puso, M. A., and J. Solberg, "A Formulation and Analysis of a Stabilized Nodally Integrated Tetrahedral," *International Journal for Numerical Methods in Engineering*, **67**, pp. 841-867, 2006.
3. Puso, M. A., J. S. Chen, and E. Zywickz, "A New Stabilized Nodal Integration Approach," *Third International Workshop on Meshfree Methods, Proceedings of Third International Workshop on Meshfree Methods, Meshfree Methods for Partial Differential Equations III*, volume 57 of *Lecture Notes in Computational Science and Engineering*, Bonn, Germany, September 12 – 15, 2005.

*Lecture Notes in Computational Science and Engineering*, Bonn, Germany, September 12 – 15, 2005.

4. Chen, J. S., W. Hu, and M. A. Puso, "Strain Smoothing for Stabilization and Regularization of Galerkin Meshfree Methods," *Third International Workshop on Meshfree Methods, Proceedings of Third International Workshop on Meshfree Methods, Meshfree Methods for Partial Differential Equations III*, volume 57 of *Lecture Notes in Computational Science and Engineering*, Bonn, Germany, September 12 – 15, 2005.
5. Chen, J. S., W. Hu, and M. A. Puso, "Orbital HP-Clouds and Higher Order SCNI for Solving Schrodinger Equation in Quantum Mechanics," *International Journal for Numerical Methods in Engineering*, **67**, pp. 847-867, 2007.

### FY2008 Proposed Work

Our goal of developing an accurate and efficient particle method has been met. Nonetheless, a number of research areas still exist. For example, initial particle placement has a large influence on the accuracy of the results. Continued work in the area of large deformation material modeling is also needed.

# Laser Glass Damage: Computational Analysis of Mitigation Process



James S. Stölken  
(925) 423-2234  
stolken1@lnl.gov

Understanding and controlling the physical processes that cause laser-induced damage to optical components is crucial to the success of many high-energy-density experimental facilities including NIF. Experimental and theoretical investigations of laser damage in silica glass are legion and are actively being pursued within the NIF Program. The insight garnered from experimental data is limited by the extremely short time-scale ( $\sim 1$  ns) of the damage events and the complex interplay between energy deposition and hydrodynamic response. A further complication is the stochastic nature of damage initiation, necessitating a *post priori* approach where the damage process must be deduced via forensic reconstruction.

Understanding laser-damage initiation and growth is just half of the problem. Creating an effective strategy to detect and mitigate laser damage is the essential second part. One promising approach is to use infrared wavelength ( $\text{CO}_2$ ) laser energy to excise/anneal the damage site. Key parameters to be optimized include the laser wavelength, intensity, pulse duration, and scan pattern in relation to the size and type of damage site. Both damage initiation/growth studies and mitigation process development could benefit from a high-fidelity

predictive simulation capability that incorporates the essential ingredients of the laser-material interaction and the resulting coupled material response in experimentally relevant configurations.

We are addressing the technical challenges associated with energy deposition, dynamic material response, and the nature of the coupling between these two processes. Our approach is to adapt the current simulations capability within the EMSolve code to simulate the time, space, and material state dependence of the laser energy deposition process. The material's dynamic response is then simulated using advanced multi-phase equations of state (EOS) and failure models within the ALE3D multi-physics code. This also provides some capability to model damage initiation in silica, which would provide a self-consistent facility to establish initial conditions for mitigation studies.

## Project Goals

The primary goal is to implement a capability to perform coupled EM simulations of laser energy deposition and subsequent material hydrodynamic response that includes the dependence of the energy deposition processes on local variations in state-dependent material properties.

A key objective is to couple the Hydro and EM simulations to facilitate exploring how strongly this interaction must be implemented. The degree of coupling required to adequately simulate a given phenomenon is problem-dependent and greatly affects the computational costs and efficacy of the overall simulation methodology.

Our technical approach has been as follows.

1. Implement spatial and material state-dependent EM properties, such as the complex dielectric constant. Using a Lorenz-Lorentz formulism, we explicitly modeled the dependence of the material conductivity and permittivity upon density (Fig. 1). This same approach explicitly accounts for the laser energy frequency dependence, thereby facilitating the investigation of this important parameter in candidate mitigation processes. To improve the quality of the boundary conditions of the EM simulations and enhance their dynamic range, we adopted a scattered electric-field methodology (Fig. 2).
2. Adapt existing models of material deformation, phase transformations, and damage to simulate such processes under conditions relevant to laser damage in silica glass. We adopted a unified-creep model for the deformation of silica at high temperatures using material parameters consistent with a linear viscous solid and a temperature-dependent shear modulus. The two-phase EOS is based on combining two analytic forms for the low and high-pressure phases with an irreversible kinetic relation (Fig. 3).
3. As a first step, consider only a single material state variable: the material density. The material density plays a central role in both the hydrodynamic response and the energy deposition.

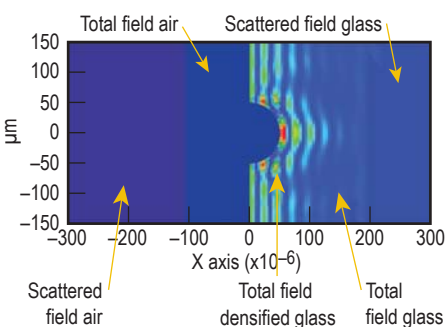


Figure 1. Simulated Joule heating in glass around an artificial defect with 20% greater permittivity and conductivity than the bulk glass.

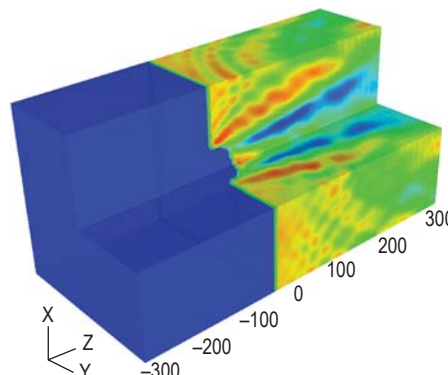


Figure 2. 3-D rendering of laser heat deposition similar to that shown in Fig. 1. Energy deposition varies by a factor of one hundred from blue to red.

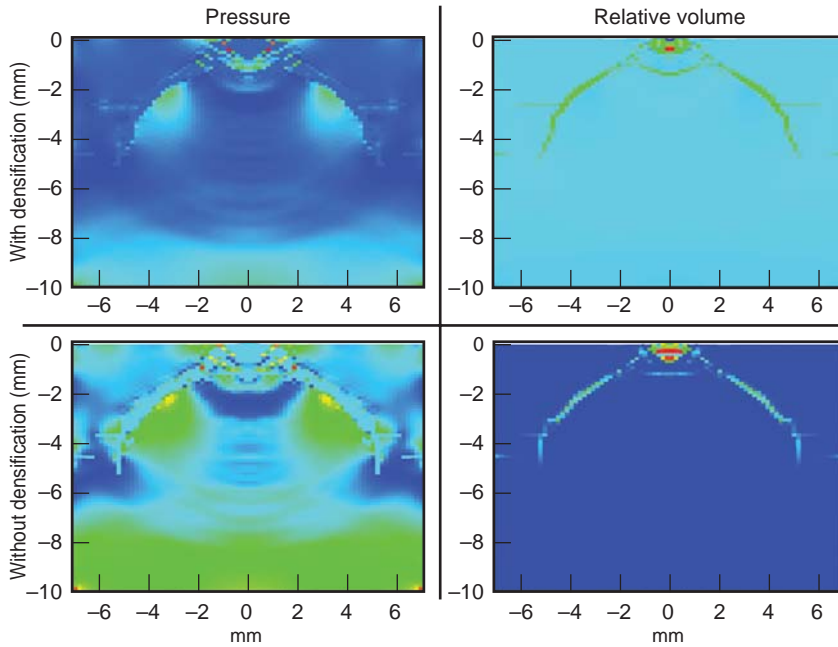


Figure 3. Residual pressure and relative volume following indentation of glass with a smooth circular punch.

Furthermore, under high-pressure loading, such as laser-induced shocks, the reference density of silica is modified, providing material “memory” of previous history such as glass damage.

A loosely coupled scheme was used to connect the hydrodynamics simulations (ALE3D) to the laser energy deposition simulations (EMSolve) via a file passing mechanism (Fig. 4). This approach leverages existing capabilities within ALE3D to specify spatially and temporally varying heat sources using an external file.

**Relevance to LLNL Mission**

This high fidelity predictive simulation capability, incorporating laser-material interactions and coupled material response, will provide a valuable capability to help advance our understanding of the physical processes involved in optical material damage and mitigation.

**FY2007 Accomplishments and Results**

A two-phase equation-of-state (EOS) model has been adapted to account for the permanent densification of silica glass that occurs under high-pressure loading. Model parameters have been fit

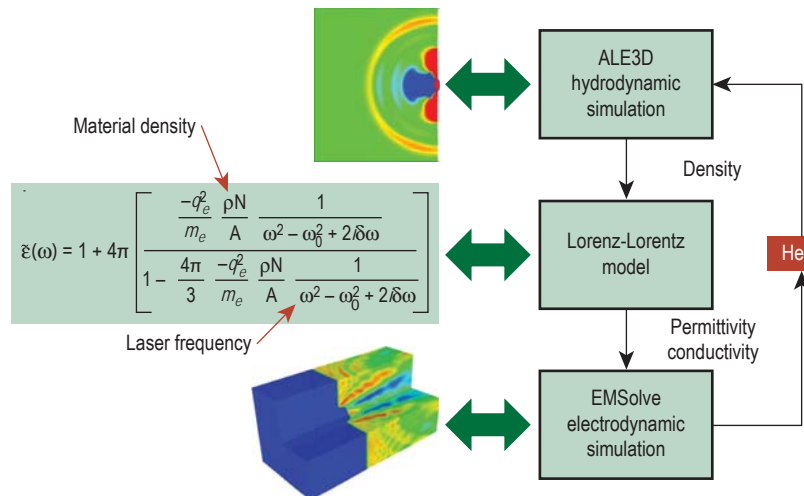


Figure 4. Loosely coupled scheme that includes the effects of laser frequency and material density.

to the reference density, bulk modulus, and thermal expansion coefficients associated with both the high- and low-pressure phases. A simple model of brittle damage has been adapted to account for cracking under tensile loading and successfully tested in conjunction with the above densification EOS model. A scattered electric field formulation has been implemented to improve the efficiency of the E&M simulations.

The capability to account for spatially varying permittivity and conductivity has been implemented. The dependence of the real and imaginary parts of the refractive index on material density and radiation wavelength has been addressed in the framework of a Lorenz-Lorentz model and implemented in the EMSolve code. The Hydro and E&M simulations were coupled via a file-sharing scheme by extending existing capabilities within the ALE3D software and adapting the EMSolve software to import and export the requisite files. An example of a coupled code simulation is shown in Fig. 5.

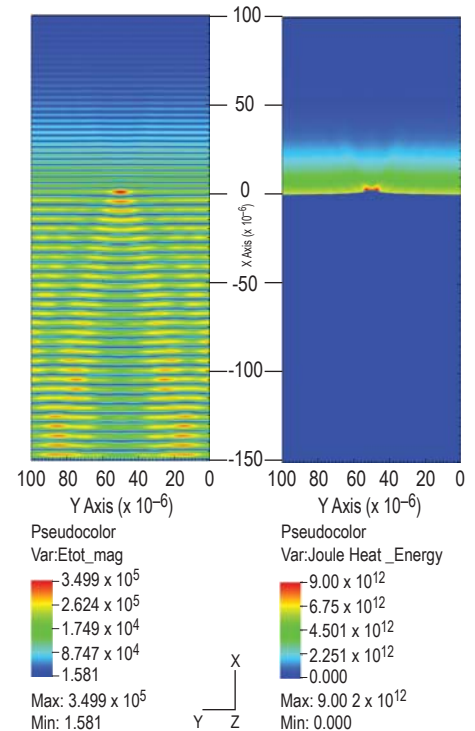


Figure 5. Coupled EMSolve/ALE3D simulation of a laser illuminated damage site similar to that shown in Fig. 3. The total electric field (left) and Joule heating (right) are modulated by local variations in density captured by hydrocode simulation of the indentation process.

# Electro-Thermal-Mechanical Simulation Capability

The purpose of this project is to research and develop numerical algorithms for 3-D electro-thermal-mechanical (ETM) simulations. LLNL has long been a world leader in the area of computational solid mechanics, and recently several solid mechanics codes have become “multi-physics” codes with the addition of fluid dynamics, heat transfer, and chemistry. However, these multi-physics codes do not incorporate the electromagnetics that is required for a coupled ETM simulation. There are numerous applications for an ETM simulation capability, such as explosively driven magnetic flux compressors, electromagnetic launchers, inductive heating and mixing of metals, and micro-electromechanical systems (MEMS).

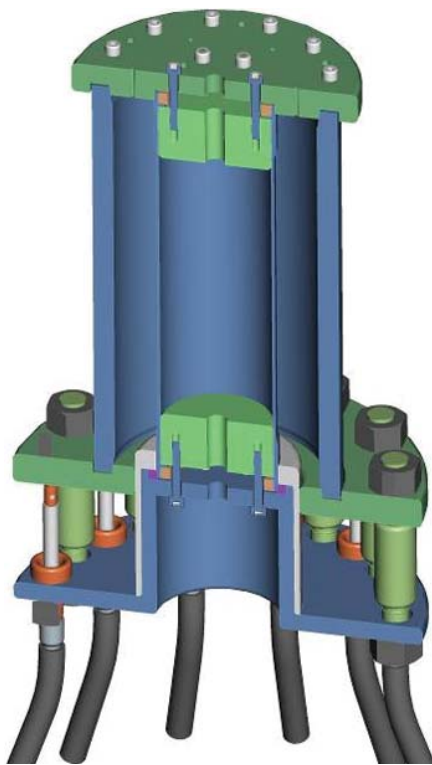


Figure 1. CAD image of the coaxial load experiment. The image shows the steel outer tube, the aluminum inner tube, the torlon bolts, and the coaxial cables.

## Project Goals

A coupled ETM simulation is a simulation that solves, in a self-consistent manner, the equations of electromagnetics (primarily statics and diffusion), heat transfer (primarily conduction), and nonlinear mechanics (elastic-plastic deformation, and contact with friction). Our goal is to add electromagnetics to two existing mechanics codes, ALE3D and Diablo. ALE3D is a heavily used Arbitrary-Lagrangian-Eulerian hydrodynamics code; Diablo is an implicit Lagrangian thermal-mechanics code currently under development.

Our objective is to develop a novel simulation capability that is not available commercially or from the other national laboratories. With this capability, LLNL will have an unprecedented ability to simulate, design, and optimize ETM systems.

## Relevance to LLNL Mission

This project is aligned with LLNL’s core competency in simulation science and engineering. It contributes to the



Daniel White  
(925) 422-9870  
white37@llnl.gov

mission to enhance/extend the simulation capabilities and specifically addresses the need for simulation capability in the area of energy manipulation. A robust ETM simulation capability will enable LLNL physicists and engineers to better support current DOE programs, and will prepare LLNL for some very exciting long-term DoD opportunities.

## FY2007 Accomplishments and Results

FY2007 was our final six-month effort with emphasis on code enhancements, verification, validation, publications, and initiation of follow-on activities. The two primary code enhancements were the development of an RLC circuit model and the incorporation of a multigrid solver.

The RLC circuit model is used to model capacitor banks and associated cables and pulse-shaping hardware. With this circuit model it is not necessary to know the applied voltage *a-priori*; instead the applied voltage is computed by solving the ETM PDE’s and the RLC circuit model self-consistently.



Figure 2. Photograph of the coaxial load experiment test fixture.

We incorporated a multigrid solver for the curl-curl equations. The solver has numerous parameters and requires auxiliary mesh information such as element connectivity and nodal coordinates. The end result is that the solver is approximately 10x faster for typical problems of interest, and has better scalability.

The primary code validation task was designing and executing a coaxial load experiment and comparing experimental data to computational simulations. A CAD image of the test fixture is shown in Fig. 1 and a photograph is shown in Fig. 2. A sequence of tests were executed, with the initial tests at low current such that the deformation of the inner tube was small and the material response was linear. Subsequent

tests used larger current with significant plastic deformation of the inner tube. An example result is shown in Fig. 3. Overall, the simulation agreed quite well with the experimental data for early times ( $t < 100 \mu\text{s}$ ), showing that there are no major errors in the numerical algorithms or the software implementation.

The final experiment was with a 0.030-in. inner tube with slots. The purpose of the slots is twofold: they make the problem become a fully 3-D problem, and the deformation of the metal should be significant. In fact, we expect a complete destruction of the tube. The simulation result is shown in Fig. 4; the experimental data is still being examined.

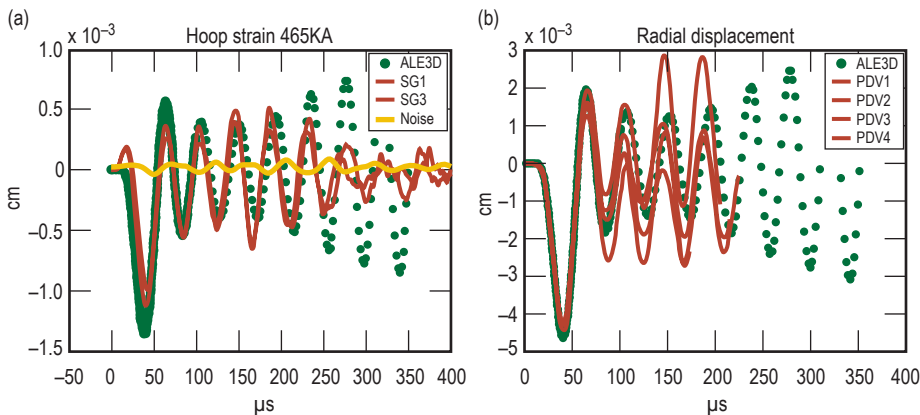


**Figure 3.** Comparison of experimental data with computed results for the 465-kA, 0.060-in. tube shot. (a) Hoop strain measure by the two strain gauges; (b) radial displacement measure by the four PDV gauges. Note that the current peaks at 30  $\mu\text{s}$  and returns to zero at 100  $\mu\text{s}$ , so it is the early time data that tests the coupling of electromagnetics and hydrodynamics. The late time data is determined solely by momentum and material models.

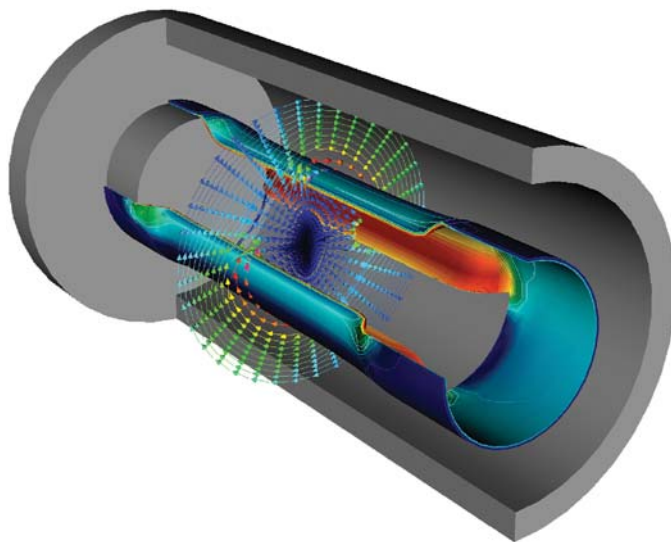


**Figure 4.** Simulation of a coaxial load test shot. This image shows both the magnetic flux density (vectors) and the current density (pseudo color). This particular shot had slots cut in the inner tube so that it was a fully 3-D problem; axial symmetry did not apply.

## Related References

- White, D. A., B. J. Fasenfest, R. N. Rieben, and M. L. Stowell, "A QR Accelerated Volume-To-Surface Boundary Condition for the Finite Element Solution of Eddy Current Problems," *IEEE Trans. Magnetics*, **43**, 5, pp. 1920-1934, 2007.
- Rieben, R., and D. White, "Verification of High-Order Mixed Finite Element Solution of Transient Magnetic Diffusion Problems," *IEEE Trans. Magnetics*, **42**, 1, pp. 25-39, 2006.
- White, D., and B. Fasenfest, "Performance of Low-Rank QR Approximation of the Finite Element Biot-Savart Law," *IEEE Trans. Magnetics*, **43**, 4, pp. 1485-1488, April 2007.
- White, D., R. Rieben, and B. Wallin, "Coupling Magnetic Fields and ALE Hydrodynamics for 3D Simulations of MFCG's," *IEEE International Conference on Megagauss Magnetic Field Generation*, Santa Fe, New Mexico, November 5-10, 2006.
- Solberg, J. M., D. A. White, and R. N. Rieben, "A Mortar-Based Method for Zero-Conductivity Regions in a Coupled Electro-Thermal-Mechanical Simulation Code," *7th World Congress on Computational Mechanics*, Los Angeles, California, 2006.

## FY2008 Proposed Work

We have proposed future experiments using the same coaxial test fixture to validate kink instabilities, bucking instabilities, and electrical contacts.

Based on our success with this project we were asked to participate in the Bore Life Consortium of the Office of Naval Research (ONR) Railgun S&T Program. The consortium is tasked with gaining an understanding of phenomena that affect railgun bore life, such as thermal ablation, gouging, and arcing. We will continue to develop the ETM simulation capability, to use the ETM simulation capability to model the notional ONR railgun, and to investigate novel materials and diagnostics.

# Petascale Simulation Initiative



John M. May  
(925) 423-8102  
may10@llnl.gov

Future supercomputers will gain performance mainly from increased parallelism, rather than faster processors. To use these machines effectively, application developers must find new ways to exploit massive parallelism. At present, most parallel applications use a single program, multiple data (SPMD) model, in which each processor simultaneously applies the same algorithm to a different portion of the workload. This approach is conceptually simple, but balancing the workload to maximize efficiency can be tricky, especially if the workload distribution changes as the computation proceeds. Moreover, load balancing becomes harder with increasing parallelism.

The Petascale Simulation Initiative has developed a new programming model called Cooperative Parallelism that lets applications manage and distribute work more flexibly. It is a multiple program, multiple data (MPMD) model, so different parts of a parallel application can work concurrently on different tasks running different executables. Cooperative Parallelism is designed to complement the SPMD model, so existing parallel applications can be

combined or augmented to form larger federations.

A Cooperative Parallel federation (Fig. 1) begins with the execution of a single software component, which is a sequential or SPMD parallel program. Any process within this component may launch additional components running different executables, and those may launch others, and so on. Components communicate through remote method invocation (RMI), in which a thread of control within one component may invoke a method (*i.e.*, call a function) in another component. Cooperative Parallelism is a loosely-coupled model of computing that permits components to be designed independently of each other while making the interfaces through which they interact more explicit.

We have also investigated a technique called Adaptive Sampling that can greatly improve performance in a broad class of multiscale and multi-physics simulations. This technique supports simulations in which coarse-scale computations are augmented with data from costly fine-scale computations. The application can assign the two kinds of work to separate pools of processors

Figure 1. Cooperative Parallel application, consisting of multiple components that can be launched and terminated as needed. Each component is an executing sequential or parallel program. Components communicate through RMI.

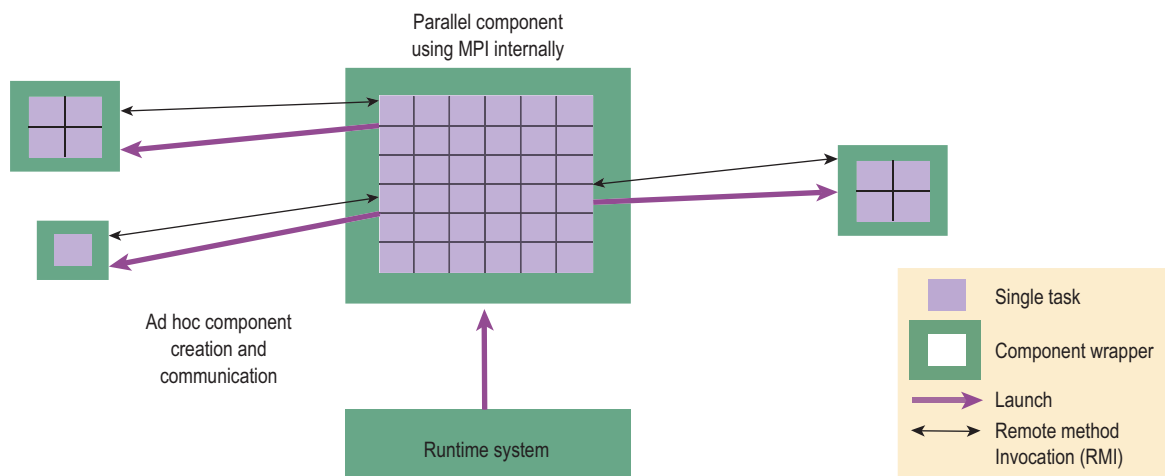


(Fig. 2). That step by itself can improve load balance, since a pool of fine scale “servers” can provide data to any processor in the coarse-scale computation that needs it. However, even more substantial performance gains arise when the simulation caches fine-scale data and uses it to satisfy future requests from the coarse-scale model instead of recalculating it.

### Project Goals

We aim to create a programming model that large scientific applications

can adopt incrementally to create more sophisticated simulations and better utilize massively parallel computers. The project also seeks to demonstrate that Cooperative Parallelism can benefit a range of applications of interest to LLNL by allowing them to adopt a federated model to complement standard SPMD parallelism.

### Relevance to LLNL Mission

Cooperative Parallelism should benefit large-scale codes as developers seek efficient ways to use massive parallelism.

Its task-parallel model lets applications exploit multiple dimensions of parallelism at once. It also offers a natural route to designing simulations that combine multiple interacting models. Moreover, because cooperative parallelism can coexist with current SPMD parallelism, applications can adopt it incrementally. Cooperative Parallelism will also benefit users of smaller-scale simulations that are executed repeatedly for parameter studies or optimization studies. Our model greatly simplifies the process of orchestrating multiple instances of a simulation running concurrently.

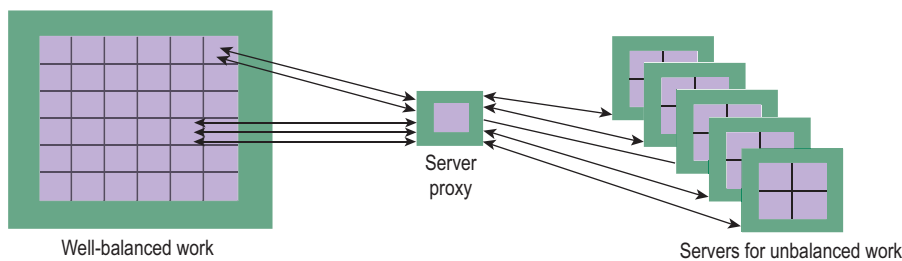


**Figure 2.** Adaptive sampling. Applications can be factored into well-balanced and imbalanced portions, with each portion assigned to a different pool of nodes. When processes in the well-balanced portion need additional data, they can send a request using RMI through a server proxy, which assigns the work to an available server component.

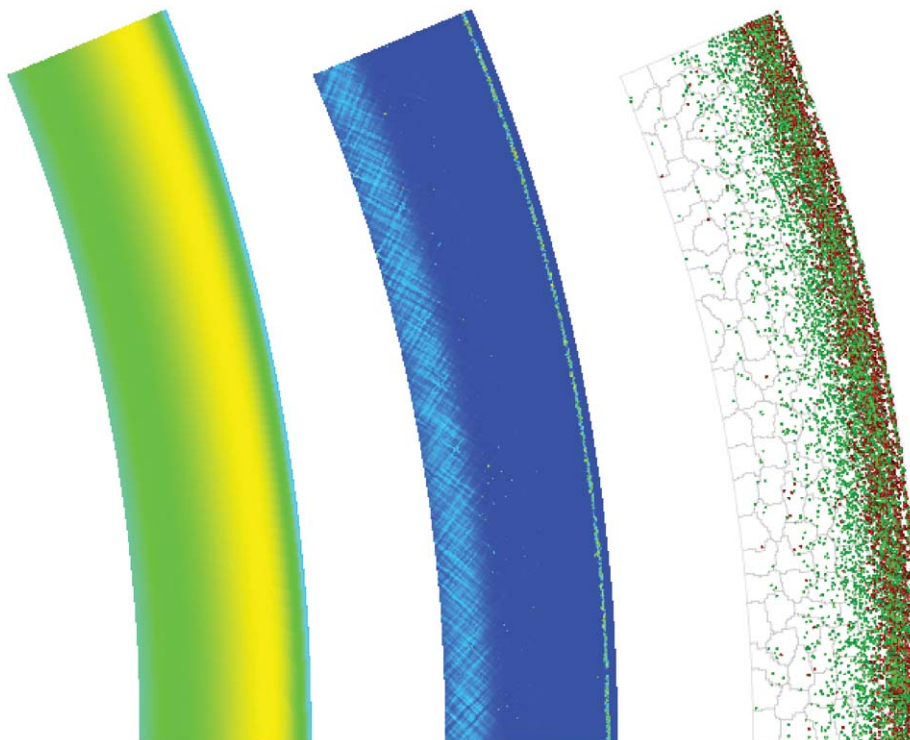


**Figure 3.** A multiscale material model of a part of an expanding cylinder, showing pressure on the left, plastic strain rate in the middle, and the number of fine-scale evaluations required on the right. Green indicates one evaluation; red indicates two or more evaluations. The locations requiring these extra calculations track loading changes induced by passage of waves through the material. Data are shown for a time increment over which a relatively large number of evaluations are performed. Parallel domain decomposition is also indicated by light gray boundaries in the plot on the left.

### FY2007 Accomplishments and Results

The Petascale Simulation Initiative concluded its three-year term in April 2007. We designed the Cooperative Parallel model, implemented an application-independent approach to adaptive sampling, developed a working prototype of the Cooperative Parallelism runtime system and demonstrated a multiscale materials modeling simulation (Fig. 3) using adaptive sampling on more than 1,000 processors. The project also demonstrated its utility as a means for simplifying parameter studies through collaboration with LLNL’s PSUADE project.

### Related References

1. Ashby, S., and J. May, “Multiphysics Simulations and Petascale Computing,” *Petascale Computing: Algorithms and Applications*, D. Bader, Ed., Chapman & Hall/CRC Press, 2007.
2. Barton, N., J. Knap, A. Arsenlis, R. Becker, R. Hornung, and D. Jefferson, “Embedded Polycrystal Plasticity and *In Situ* Adaptive Tabulation,” *Int. J. Plasticity*, in press, 2007.
3. Kumfert, G., J. Leek, and T. Epperly, “Babel Remote Method Invocation,” *IEEE Int. Parallel and Distributed Processing Symp.*, March 2007.

### FY2008 Proposed Work

Further work, including closer collaborations with major LLNL simulation codes, is anticipated in FY2008.

# Electromagnetics Code Management



*Daniel White*  
(925) 422-9870  
white37@llnl.gov

**L**LNL's EMSolve code is a 3-D, parallel, finite element code for solving Maxwell's equations. EMSolve, which has been used in support of many LLNL programs, has modules for electrostatics, magnetostatics, eigenvalues, eddy currents, and wave propagation. The purpose of this project is to verify, document, and maintain the EMSolve suite of computational electromagnetics codes.

## Project Goals

The goals for FY2007 are:

1. install EMSolve on the new Peleton machines: Yana, Zeus, Hopi, and Rhea;
2. incorporate a new linear equation solver into EMSolve;
3. set up efficiency enhancements for an important class of applications described by a tensor product mesh; and
4. collaborate with Ohio State University (OSU) on local higher-order absorbing boundary conditions (ABCs).

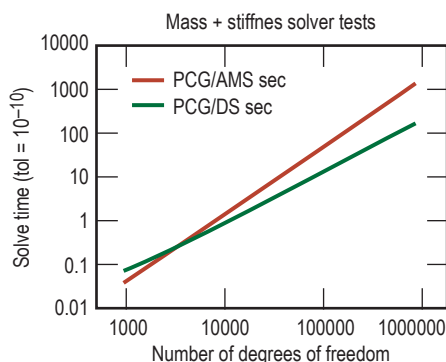


**Figure 1.** Improved run time of AMS solver vs. diagonally scaled preconditioned conjugate gradient (PCG). For a 1-million-unknowns problem, the AMS solver is approximately 10 times faster than the existing solver.

## Relevance to LLNL Mission

EMSolve can perform electromagnetic analyses that cannot be performed by commercial codes. Having this unique computational EM capability allows LLNL to have a competitive edge. Increasing the accuracy and efficiency of our CEM codes will benefit all customers.

## FY2007 Accomplishments and Results

**AMS.** In 2006 the HYPRE iterative solver library introduced an experimental multigrid solver called the Auxiliary Space Maxwell Solver (AMS) for linear systems involving edge elements and the corresponding CurlCurl operator. The goal of this project was to evaluate this solver's effectiveness on our class of problems and, should it prove effective, to incorporate it into the EMSolve suite.

We produced an iterative solver that is tuned specifically for edge-element discretization of curl-curl equations. The AMS is applicable to magnetostatic problems, eddy current problems, and implicit full-wave problems. The solver is based on multigrid concepts and is almost scalable, meaning that the computation time increases linearly with the problem size.

Incorporation of AMS into EMSolve was not a trivial procedure because AMS requires additional information beyond the system matrix. It also requires information about the edge-to-node connectivity of the mesh and coordinates of the individual nodes. This necessitated augmenting the generic solver interface and modifying a large number of modules that make use of this interface.

The end result is that the EMSolve suite of codes now has a new and effective multigrid solver for electromagnetic

problems as well as a more useful and robust interface for all of our linear solvers (Fig. 1).

**Efficiency Enhancements.** We implemented a specialized simulation code that can model electromagnetic wave propagation using the scattered field formulation of Maxwell's coupled first-order field equations. This code is tuned to model blocks of materials arranged in Manhattan geometries with varying permittivity, permeability, and electrical conductivity.

This code was used to model several problems for the DARPA VisiBuilding project which endeavors to determine the location and makeup of interior walls of buildings using radar techniques. EMSolve was used to evaluate the importance of correctly modeling cinderblock voids and metal reinforcing rods within walls. Using these full-wave techniques, we were able to show that solid walls and floors produce strong wave guiding effects that are virtually destroyed by the presence of voids or rebar within those structures.

Using this new code we performed extraordinary computations (Fig. 2) on the Zeus machine. The computations consisted of a series of four simulations of a two-story building with and without cinderblock voids and metal reinforcing rods resolved to 1 cm. Each of these simulations required over 10 billion mesh elements (60 billion field unknowns) and 2.1 TB of memory.

Figure 3 shows a cut-away view of a radar pulse propagating in the two-story building. Figure 4 is a close-up of the geometry of the building.

**Local ABCs.** Electromagnetic radiation and scattering problems require that an ABC be applied to the boundary of the mesh. The ABC is often the

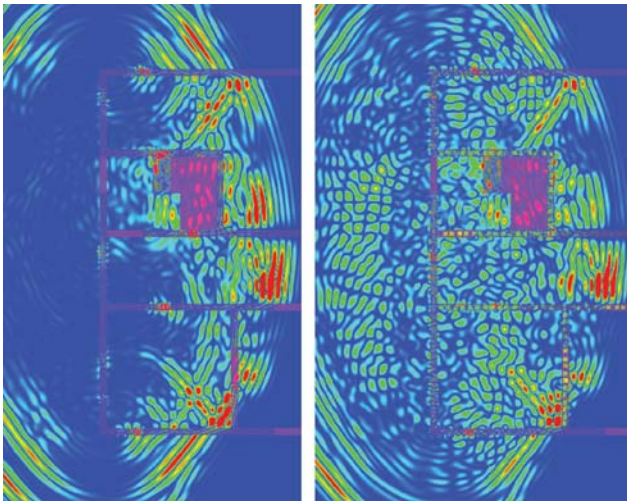


Figure 2. Comparison of radar scattering in a solid cement wall building (left) vs. a rebar reinforced cinder block building (right). Note that this is a slice through a full 3-D simulation. The color represents the magnitude of the electric field: red is maximum and blue is minimum.

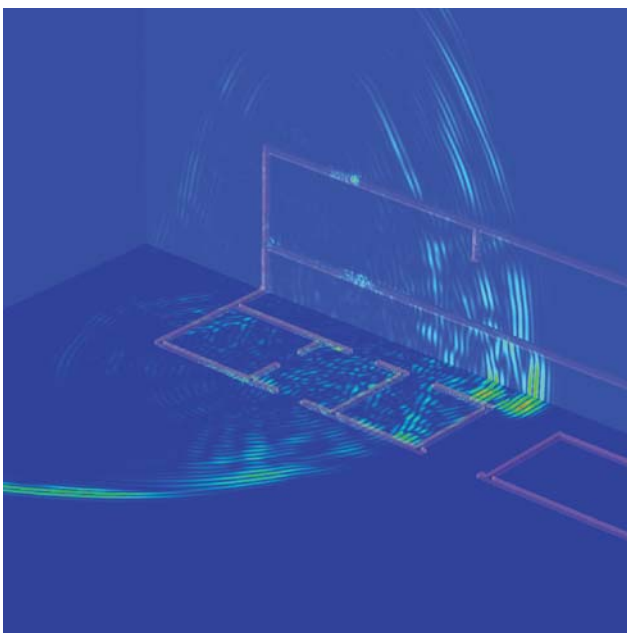


Figure 3. Cutaway snapshot of a radar pulse propagating through the building. Note how the walls themselves act as waveguides. The field propagates within the wall at a slower velocity compared to free-space.

limiting factor in achieving an accurate simulation. This task was to incorporate recent work on higher-order local ABCs into EMSolve. The term “higher-order” refers to the performance of the ABC for off-normal incidence. The term “local” means that the ABC requires only local field information, in contrast to “global”

boundary conditions, which require an integral over the entire bounding surface. Figure 5 shows verification of the implementation of the second-order local ABC in EMSolve. The addition of this new capability will result in more accurate simulations with little increase in computational cost.

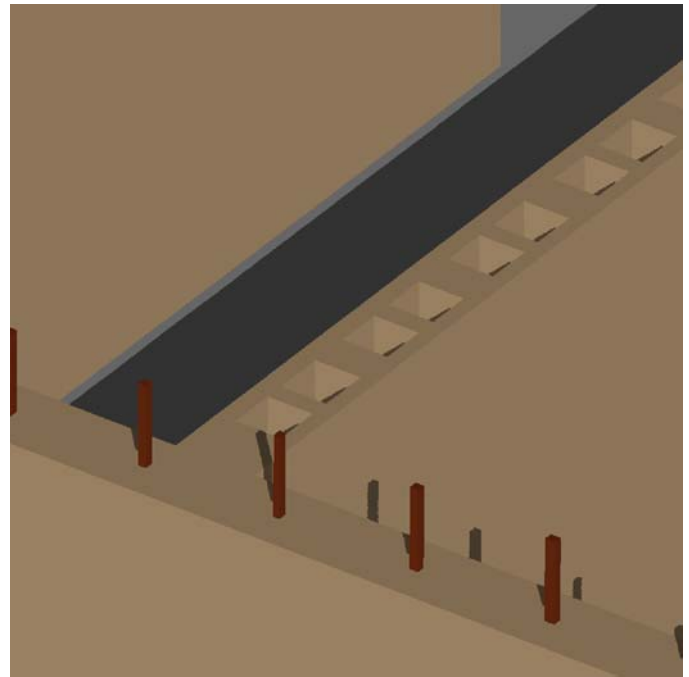


Figure 4. Close-up view of the modeling detail. Custom software was used to generate the mesh for the 10-billion-element simulations.

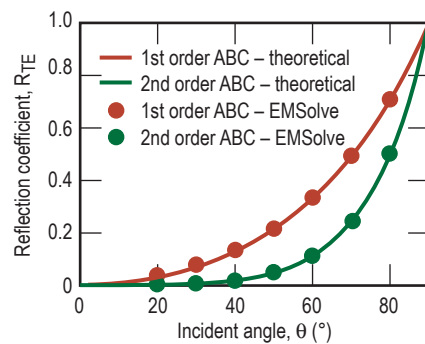


Figure 5. Verification of the second-order local ABC. The solid lines are the theoretical results; the circles represent the computed results. Note how the second-order ABC is significantly better than the first-order ABC for off-normal incidence, providing more attenuation (y-axis) over a greater range of incidence angles (x-axis).

### FY2008 Proposed Work

There are three tasks for FY2008. We will collaborate with OSU on 1) higher-order local ABCs, with the goal of constructing a time-domain version of the algorithm; and 2) an algebraic domain decomposition preconditioner for Helmholtz equations. We will also construct software infrastructure to support *hp*-refinement. The challenge is to implement the algorithm in an existing code, rather than starting from scratch. This effort will result in a simulation capability that is much more robust and easier for end-users.

# Finite Element Analysis Visualization and Data Management



**Bob Corey**  
(925) 423-3271  
ircorey@llnl.gov

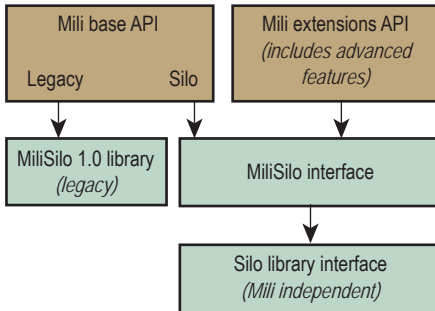
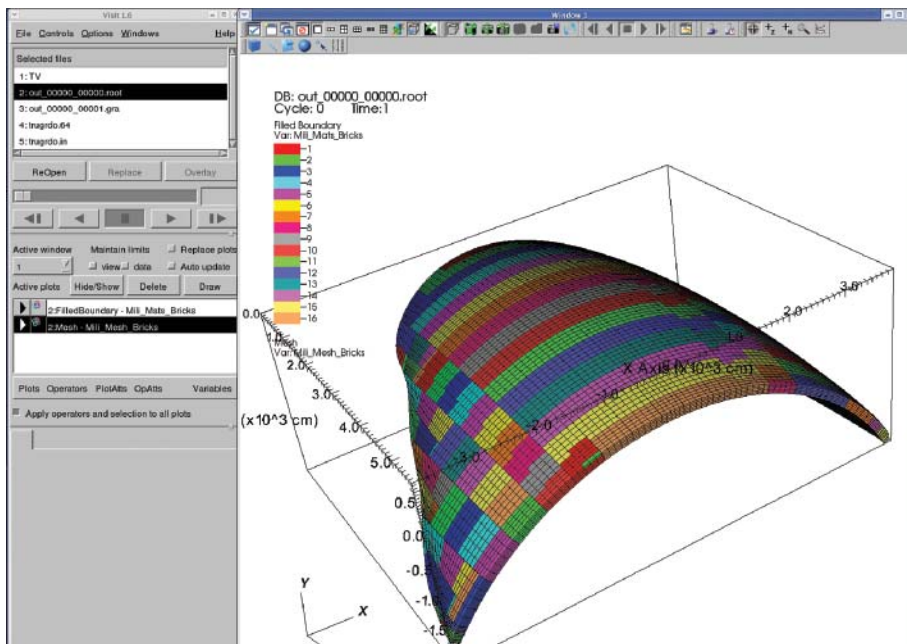


Figure 1. Mili 1.0 and 2.0 API hierarchy.

A key component of our project is its support for post-processing and visualization tools, including the Griz finite element visualization post-processor, the Mili data management library, and a data utility tool called Xmilics. These tools are used by analysts and engineers across LLNL to interpret data from a variety of simulation codes such as DYNA3D, ParaDyn, NIKE3D, TOPAZ3D and Diablo.

Griz is our primary tool for visualizing finite element analysis results on 2- and 3-D unstructured grids. Griz provides advanced 3-D visualization techniques such as isocontours and isosurfaces, cutting planes, vector field display, particle traces, and free-particles or free-node approaches. Mili is a high-level mesh I/O library intended to support computational analysis and post-processing on unstructured meshes. It provides the primary data path between analysis codes and Griz. Mili databases are also viewable with the LLNL VisIt post-processor.

Figure 2. Engineering model as viewed in VisIt and generated from new Mili/Silo Library.



Xmilics is a utility used to combine results that are generated by our large parallel computing platforms.

## Project Goals

The project provides ongoing support for visualization and post-processing tools and adds new capabilities to these tools to support evolving, multi-programmatic requirements.

## Relevance to LLNL Mission

These post-processing tools provide important user interfaces for our simulation capabilities and are critical elements in our tool suite. Analysts would otherwise be severely limited in their ability to interpret the vast amounts of data generated by simulations, and to synthesize key results.

## FY2007 Accomplishments and Results

User support continues to be a high-priority goal. The group is currently supporting approximately 30 to 40 active users on a variety of platforms across LLNL and some off-site users, including LANL. This year we saw a high level of usage and special requests from users and a higher number of analysts using Griz and VisIt concurrently to meet their needs.

We made significant progress in migrating Mili to a modern file structure. We defined and documented the requirements. We then created a useful model, choosing the LLNL-supported Silo format, because of its application programming interface (API) and its compatibility with the VisIt visualization tool. The architecture is hierarchical with a separation between the Silo and Mili layers (Fig. 1). Both new and legacy interfaces are maintained in one library to provide backward compatibility and reduce the migration impacts to our simulation codes. Figure 2 shows an example of a model written using

the new Mili/Silo format and rendered directly with VisIt without a conversion utility. This is one example of our ongoing effort to integrate Mili database support directly with VisIt.

We added a variety of new visualization features to Griz, with the most significant being: 1) a capability to render models in wireframe mode and a combination of wireframe and solid (Fig. 3); 2) a capability to render materials with undefined results in grayscale (Fig. 4); 3) the capability to generate JPEG and PNG graphic files on nearly all Griz-supported platforms; and 4) the ability to use Griz on the new Windows platforms.

Collaboration continued with exploring “meshless” techniques having an unstructured cloud of particles with no continuum elements. The results are treated in Griz in much the same way as the “free-node” capability delivered in FY2006 to support the Department of Homeland Security. This year we added capabilities to plot any typically nodal or hex result, such as displacements, onto their associated particles (Fig. 5), and to select individual particles and view a result. Software quality engineering efforts expanded to include the use of a commercial tool to create a baseline assessment of potential defects.

**FY2008 Proposed Work**  
 We will continue to provide support for our user base. Efforts targeted for next year include: 1) releasing the Mili/Silo Library for general usage with streamlined connections to VisIt; 2) adding support for higher-order elements to Mili and Griz; 3) completing the static analysis of Griz for potential defects and performing the same analysis for Mili; and 4) implementing automated regression testing for Mili.

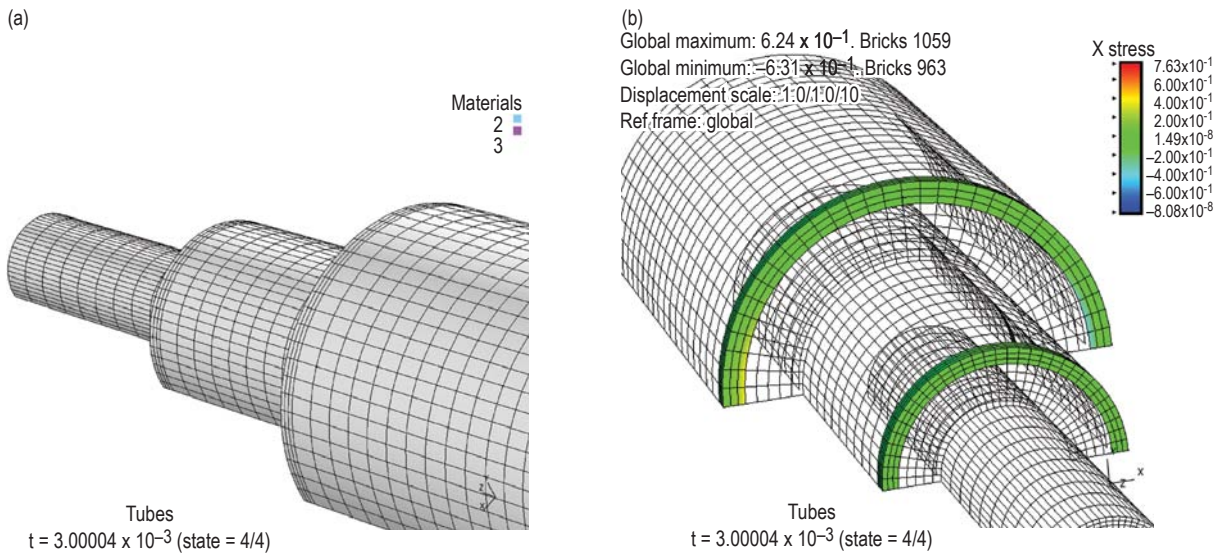


Figure 3. (a) Rendering of model in wireframe mode. (b) Example of wireframe and solid rendering mode.

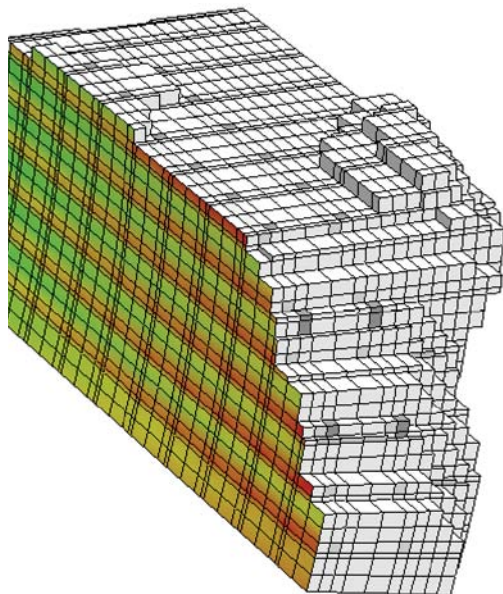


Figure 4. Rendering of results with inactive materials as grayscale.

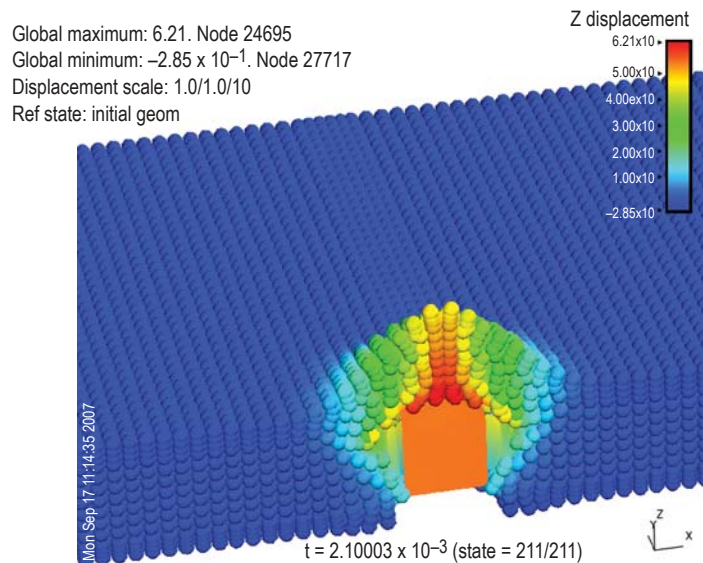


Figure 5. Example of plotting nodal displacement result onto particles.

# Rotational Kinematics Output and Other Improvements in DYNA3D



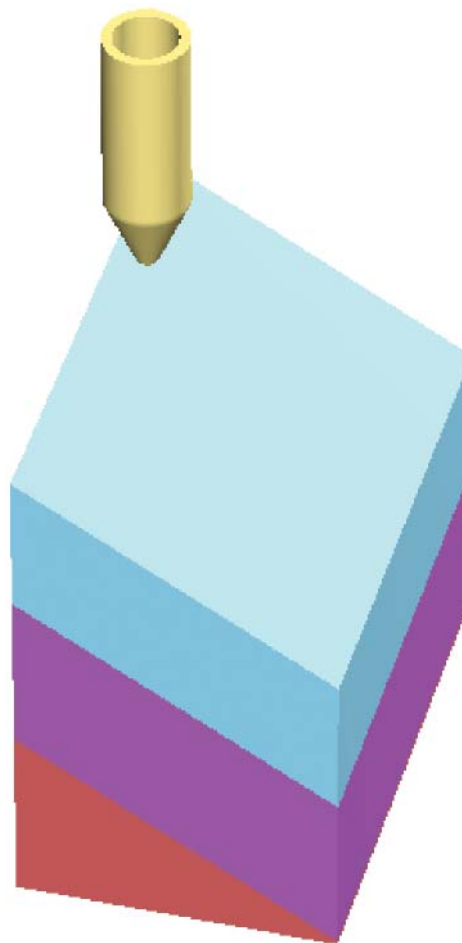
*Jerry I. Lin*  
(925) 423-0907  
lin5@llnl.gov

**D**YNA3D is a main engineering tool for the simulation of transient response of solids and structures to fast, impulsive loadings. This explicit finite element code was originally created to support weapons activities, but over the years has found broader use in other applications, such as infrastructure vulnerability and protection. The code also provides the mechanics functionalities of the highly parallel ParaDyn simulation tool. This project funds the ongoing implementation of user-requested features, general technical support,

documentation updates, and Software Quality Assurance (SQA) compliance for DYNA3D.

This project also supports the broader interagency DYNA3D activities through LLNL's Collaborator Program. The Collaborator Program grants access to selected licensed users to LLNL's computational mechanics/thermal codes in exchange for their information, results, and acknowledgement. These collaborative members include our sister laboratories, U.S. government agencies, and other institutions.

Figure 1. Spinning hollow projectile striking a layered target.



## Project Goals

The planned tasks include the implementation of functionalities for various programs needs, enhancement of existing features, the addition of new result display capabilities, and continued compliance work on SQA and the Fortran 95 standard.

## Relevance to LLNL Mission

Many Laboratory programs require new functionalities and technical support to complete their missions. Some of these programs and projects involve the Laboratory's collaboration with other institutions and federal agencies, such as the Los Alamos National Laboratory, Department of Homeland Security, Bureau of Reclamation, U. S. Army Corps of Engineers, the Naval Surface Warfare Center, and selected universities.

## FY2007 Accomplishments and Results

Based upon multiple requests, rotational velocity and acceleration histories for an entire model, or parts of the model, were added. These quantities can be output to the full-state visualization database, or designated as

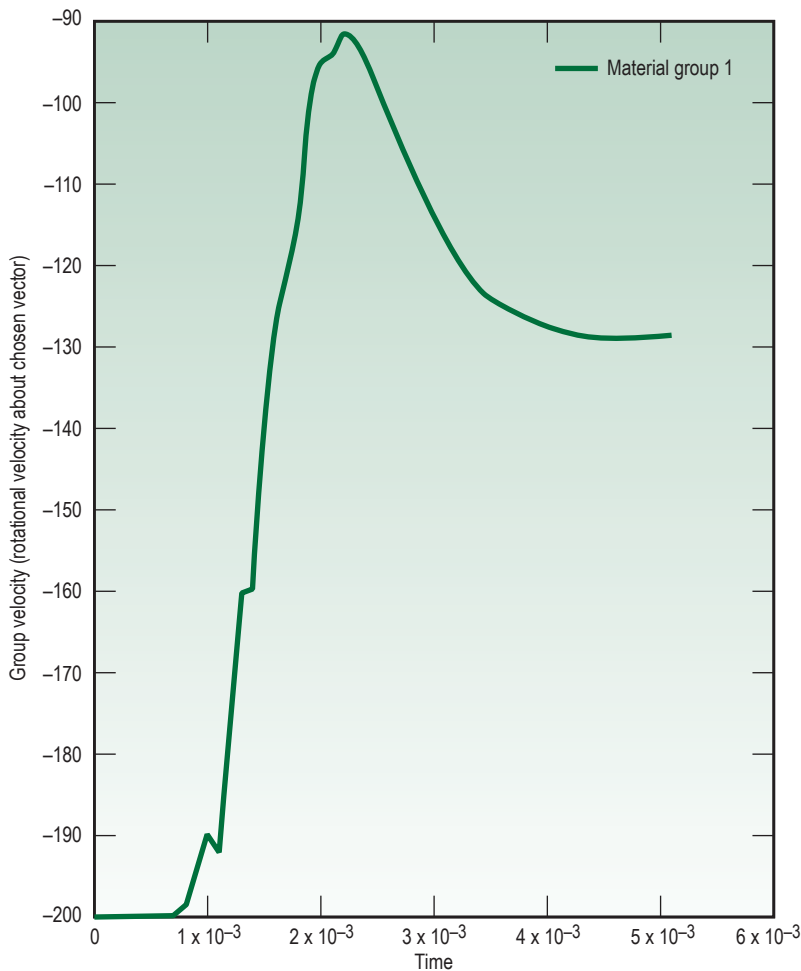


Figure 2. Time history of the projectile rotational velocity about its principal axis. Note that the projectile slows down and partially recovers its spin as it interacts with the target.

one of the limited number of quantities sent more frequently to a dedicated time history database.

These results are made available in terms of components in the global coordinate system or about a user-defined orientation. The user-defined axis may move arbitrarily in space over the simulation time. These quantities supplement their existing translational counterparts in providing the users more detailed understanding of the structure's overall motion or relative motion between parts.

A generic hollow projectile with a blunt nose impacting an inclined flat target surface, shown in Fig. 1, is used as an example. The projectile, modeled by finite elements with isotropic elastic properties, is traveling with an initial translational velocity along with a rotational velocity about its principal axis. The target, modeled by the penetration load-predicting

code PENCURV3D, contains layers of materials of different stiffness. Figure 2 shows the projectile's change of spin velocity about its principal axis as it interacts with the target.

The Rayleigh damping features in DYNA3D have been effective tools for achieving quasistatic response, stress initialization, shock noise reduction, and other applications. We made the mass-proportional part of the damping more versatile by excluding selected rigid bodies at the user's choice. This capability, combined with the existing rigid-deformable material switching feature, provides a valuable means to avoid undesirable damping-induced motion slowdown. For the stiffness-proportional part of this feature, a more user-friendly input allows direct specification of fraction of critical damping, and damping frequency is added.

### FY2008 Proposed Work

Targeted efforts include general technical support for DYNA3D users, the addition of user-requested capabilities, and the ongoing modernization toward Fortran 95-compatible and SQA-compliance work.

A modified Mili surface capability with more essential attributes is near its completion. This will be integrated into DYNA3D and enable many additional state variables and parameters to be included in the output databases for visualization by analysts.

We will evaluate the possibility of identifying element facets that belong to a model's exterior surfaces. These facets may be assigned special attributes or properties for strengthened numerical stability. Targeted applications include augmented hourglass control and contact surface smoothing.

# NIKE3D Code Maintenance and Enhancement



Michael A. Puso  
(925) 422-8198  
puso1@llnl.gov

The objective of this work is to enhance, maintain, and support the implicit structural mechanics finite element code NIKE3D. This tool is LLNL's primary capability for simulating the slowly evolving or steady-state response of nonlinear solids and structures. New features are continually added to accommodate engineering analysis needs. Maintenance includes bug fixes and code porting to new or updated platforms. User support includes assisting analysts in model debugging and general analysis recommendations.

## Project Goals

Code enhancement requires continuous interactions with users as well as new features to meet our evolving needs. Each year some activities are pre-planned, *e.g.*, completing production versions of higher-order elements and nodally integrated tetrahedrals. Other efforts arise in response to real-time needs.

Such "just in time" enhancements included new material model capabilities for weapons analysts and new contact analysis features.

## Relevance to LLNL Mission

Structural analysis is one of the most important functions of Engineering and motivates in-house maintenance for LLNL's suite of codes. NIKE3D, in particular, is a premier code for handling difficult nonlinear static structural analysis problems. It has the most diverse and robust contact algorithms at the Laboratory to handle the complex interactions of unbonded material interfaces.

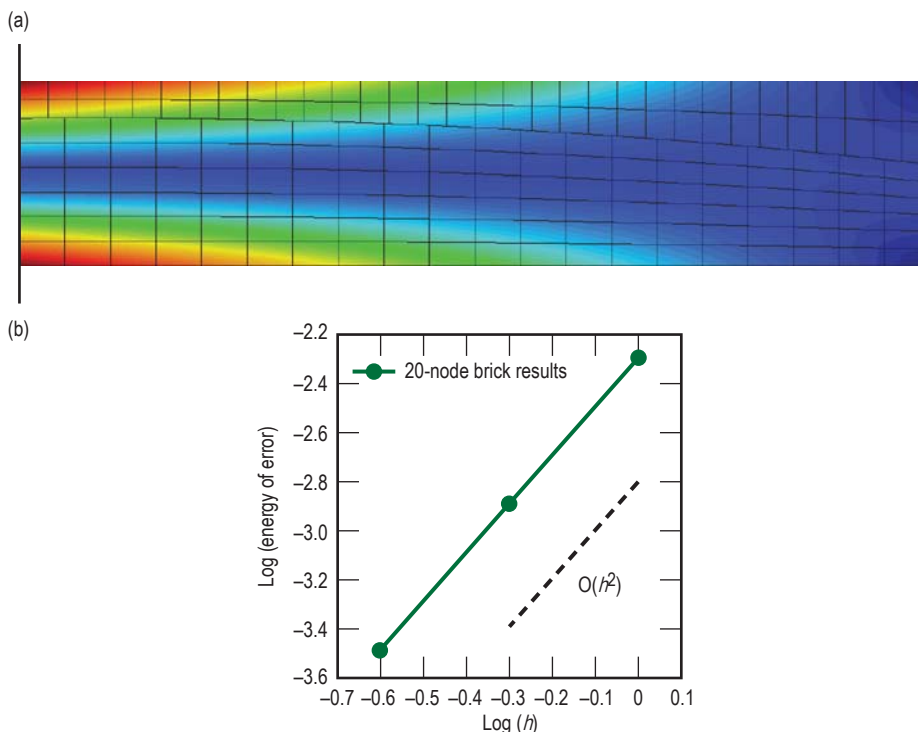
## FY2007 Accomplishments and Results

A number of new element technologies and discretization technologies have been developed at LLNL, most notable being higher-order elements (10-node tetrahedrals, 20- and 27-node hexahedrals), nodally integrated tetrahedrals, and meshless methods. Efforts are required to make them fully integrated functionalities available for production use by analysts. For example, these implementations exploited more modern, hierarchical data structures available in Fortran 95.

NIKE3D's existing technique of writing a monolithic restart database did not work with these new features. Instead, the data needed to be written and read recursively to perform this task for each data structure. The process of writing these dedicated recursive algorithms was automated using a PERL script adapted from one first created by the Diablo project and then adapted for new data structures in DYNA3D.

To finalize the production capability of higher-order elements, modifications were made for using GRIZ to visualize higher-order element results. Previously,

Figure 1. (a) Bending stress shown on 20-node model of loaded cantilever beam with (curved) contact surface separating top and bottom. (b) Convergence plot demonstrating optimal quadratic convergence of the energy norm of the discretization error.



higher-order elements results could be visualized only by GID. Now TrueGrid and Cubit can be used to build quadratic element meshes, and our quadratic mortar contact algorithms can be used without loss of quadratic convergence rate (Fig. 1) for nonlinear analysis using higher-order elements (Fig. 2) in NIKE3D.

New material model features were added in support of weapons analysis. One example is a new thermal-plastic model that captures thermal material response over an arbitrary range of temperatures (Fig. 3). Finally, a number of contact features were added. Most notably, new work has begun on the improvement of the quasi-Newton contact solver. The quasi-Newton method is used for

solving the nonlinear system of equations in NIKE3D and is a keystone to its success. Nonetheless, there is much room for improvement. As part of this effort, a new Armijo-type line search algorithm was added along with several small modifications to improve solution robustness.

**Related References**

1. Puso, M. A., and T. A. Laursen, "A Segment-To-Segment Mortar Contact Method for Quadratic Elements and Large Deformations," *Computer Methods in Applied Mechanics and Engineering*, in press.
2. Christensen, P. W., et al., "Formulation and Comparison of Algorithms for Frictional Contact Problems," *International Journal for Numerical Methods in Engineering*, **42**, pp. 145-173, 1998.

*FY2008 Proposed Work*  
 Our existing mortar contact implementation currently uses an  $N^2$  search algorithm. In FY2008, we will implement better and faster search algorithms such as the bucket sort.  
 We will implement an improved quasi-Newton method. A number of new methods have been created in the area of optimization that could be converted to treat computational contact mechanics.

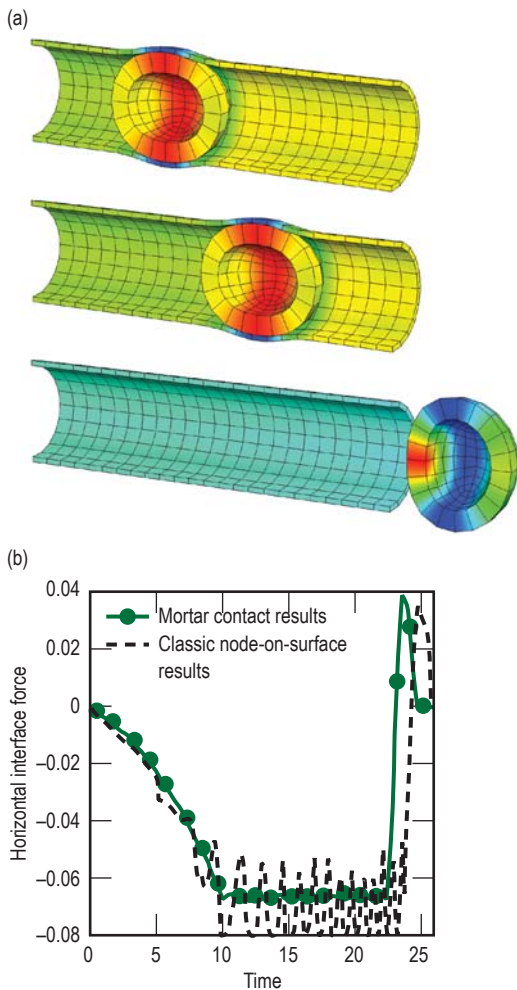


**Figure 2.** (a) Simulation of elastic sphere being forced out of pressurized elastic tube. Twenty-node brick elements are used. (b) Horizontal force on tube versus time. This force is mainly due to frictional resistance. Force is very smooth for mortar contact results, whereas node-on-surface force is not.

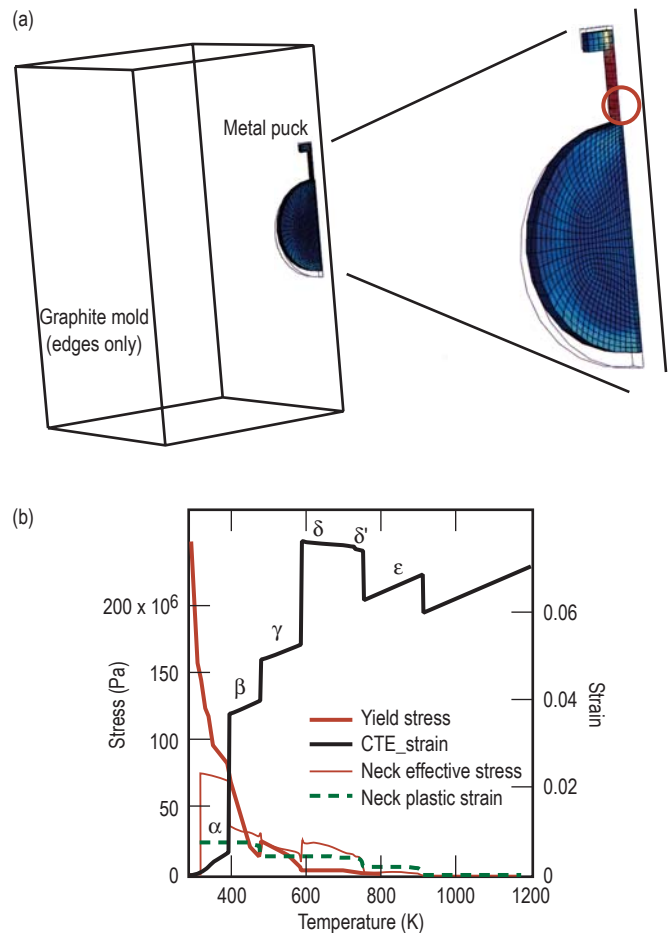


**Figure 3.** (a) Metal "puck" cast inside graphite mold (3-D solid mesh not shown). (b) Evolution of stress and strain at critical location (red circle in (a)) in casting as metal is cooled. The thermal phase changes indicated in yield stress and CTE strain are provided in the arbitrary format of the new material model feature.

# Validation of Reinforced Concrete Modeling Capabilities for Seismic Response

This project assesses the ability of our explicit solid mechanics codes DYNA3D/ParaDyn to simulate the seismic response of reinforced concrete structures. These codes were originally created to simulate rapid, large-deformation response. For example, the concrete model was created to assess shock loadings on reinforced concrete structures. In contrast to shock loading, structures subjected to seismic loading will likely go through multiple load reversals over a longer response period.

Recent shake table tests at the University of California, San Diego (UCSD), provide a significant assessment case. A full-scale seven-story slice of a reinforced concrete building was constructed on the Large High-Performance Outdoor Shake Table (LHPOST) at UCSD (Fig. 1). This facility is part of the Network for Earthquake



Figure 1. Seven-story structure on shake table.

Engineering Simulation. The structure was subjected to four earthquake ground motions of successively increasing amplitude.

## Project Goals

Previous work has shown that there are difficulties in modeling seismic response of a reinforced concrete structure using the homogenized concrete/rebar model implemented in DYNA3D/ParaDyn. An instability in the model implementation leads to non-physical stress states and subsequent inversion of elements that terminates the simulation. This misbehavior appears to be more likely with the long duration and load reversals necessary for a seismic simulation.

The goals of this project were to improve the material model and then continue the assessment of the model by

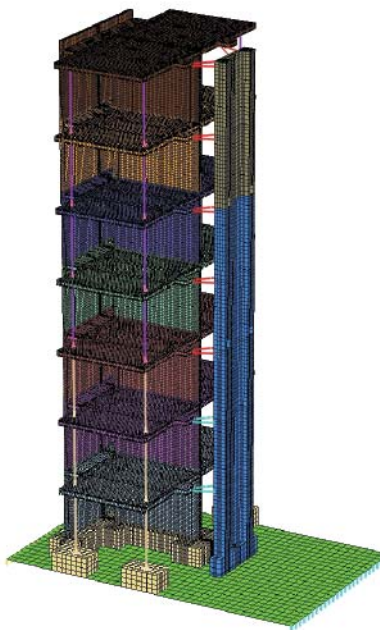


Figure 2. Finite element model of the structure and shake table.



Steven W. Alves  
(925) 423-2391  
alves6@llnl.gov

comparison with the shake table experiments. The latter included refinement of the boundary conditions and material properties in the finite element model to obtain a better representation of the structure.

## Relevance to LLNL Mission

Simulation of the seismic response of reinforced concrete structures is of importance to LLNL's Nuclear Fuel Cycle & Reactor Program, the Global Nuclear Energy Partnership (GNEP), and the National Ignition Facility (NIF). In general, validating this capability would allow LLNL to attract new projects in the area of seismic analysis. This project also promotes collaboration with UCSD.

## FY2007 Accomplishments and Results

The numerical robustness of the concrete model in DYNA3D was investigated. The code failure was determined to occur during calculation of a quantity related to the effective plastic strain increment. This error condition can be eliminated by scaling the stress in an element to zero. This improvement was implemented, but it should be noted that large effective plastic strain increments can still be calculated for an element causing large deformations. While this does not prevent simulations from running, the user must assess whether the computed response is significantly affected before using the results. Other corrections to the material model, which were identified during the investigation of the instability, were also implemented.

A finite element model of the structure was generated with separate concrete properties for each level of the building. The properties were based on concrete test data provided by UCSD. Also, rotational stiffness of the shake table platen was included in the model.

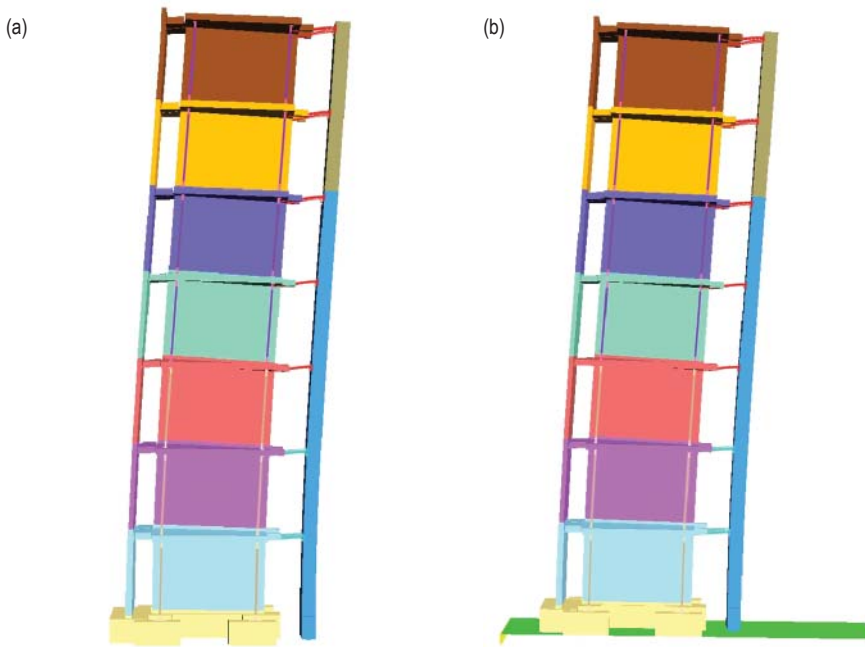


Figure 3. Longitudinal mode at 2.51 Hz with no table (a) and at 1.97 Hz with table rotational stiffness (b).

Both of these features are believed to be important factors in modeling the seismic response of the structure on the shake table.

A linear version of the finite element model was created for running static analyses and then determining the natural frequencies and mode shapes using NIKE3D (Fig. 2). These analyses illustrate the importance of including the rotational stiffness of the table platen in

the model. The first longitudinal mode of the structure ranges from 2.51 Hz with no table rotation to 1.97 Hz with a relatively low rotational stiffness of the table (Fig. 3).

Dynamic simulations were performed using ParaDyn for a finite element model with concrete and rebar, using the nonlinear material models. The stiffness of the structure is not captured during the first earthquake

motion (Fig. 4) unless the rotational stiffness of the table platen is reduced to a level that is a lower bound for the rotational stiffnesses estimated by UCSD from recorded motions. While the agreement of the modeled response with the experiment is good for the first earthquake, the simulation deviates for the subsequent earthquakes by under-predicting the response (Fig. 4). A possible explanation for this is that as the structure is progressively damaged and the stiffness decreases, the prescribed damping becomes too high in the model.

It is believed that these results partially validate the use of the homogenized concrete/rebar model in DYNA3D/ParaDyn for seismic simulations of reinforced concrete structures. While the numerical instability causing code termination has been corrected, there is still concern about the large deformations caused by the remaining numerical anomaly. The approach is believed to be viable for simulations to determine moderate levels of deformation and damage, but performing simulations for long durations after sustaining significant deformation and damage levels is of questionable value. Obviously, attention must be paid to accurately defining boundary conditions, material properties and damping. Perhaps damping should be modified as the structure is progressively damaged.

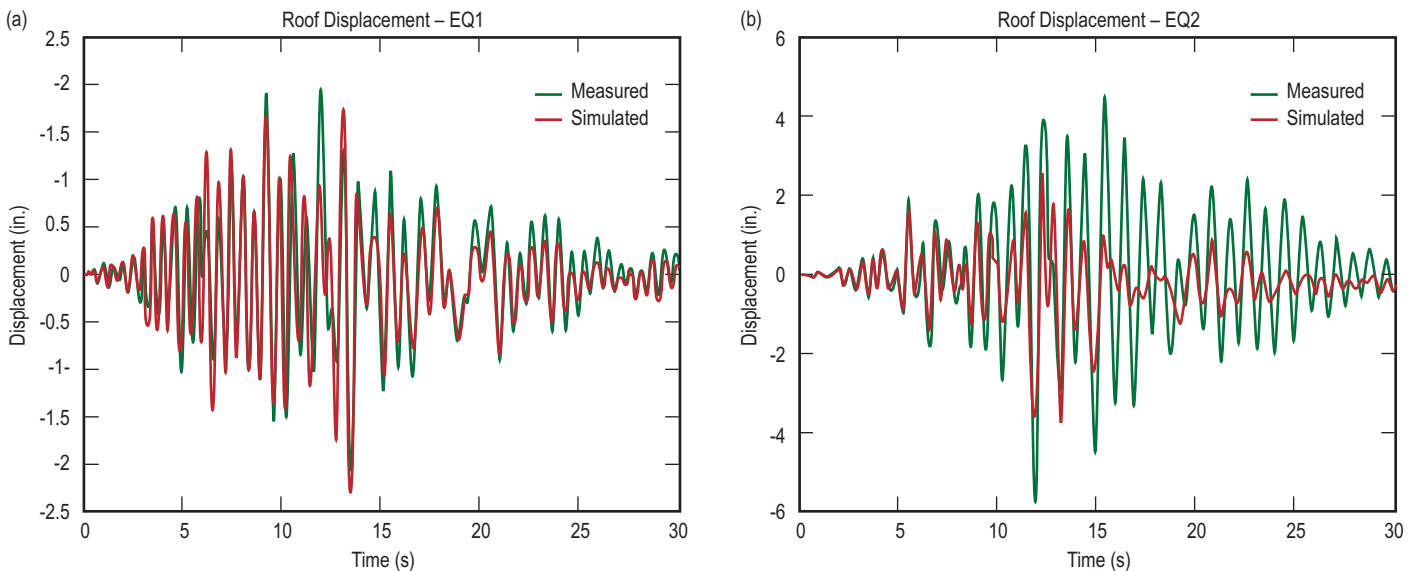


Figure 4. Comparison of simulated roof displacement to measured roof displacement for the first (a) and second (b) earthquakes. (Note difference in vertical scales.)

# Thermal-Structural Analysis of the MacArthur Maze Collapse



Charles R. Noble  
(925) 422-3057  
noble9@llnl.gov

At approximately 3:45 AM on the morning of April 29, 2007, a tractor-trailer rig carrying 8,600 gallons of fuel overturned on the connector from Interstate 80 to Interstate 880 in Oakland, California. The accident resulted in an intense fuel fire that weakened the steel superstructure above it and initiated connection failures between the bridge deck and main girder, causing an approximately 50-yard long section of the connecting ramp to collapse onto the lower connector. It was determined that studying the structural collapse of the MacArthur Maze would provide the opportunity to:

1. study the methods needed to properly stimulate the thermal loading on a structure from this type of event;
2. determine the predictive capability of LLNL's finite element software for progressive collapse analysis; and
3. validate this type of thermal/structural failure analysis, which would then assist in determining the threat to other critical infrastructure in the United States.

## Project Goals

The end goal of this project was to simulate progressive collapse of the

MacArthur Maze connector using LLNL thermal and structural finite element simulation codes TOPAZ3D, Diablo, NIKE3D, and ParaDyn. Other goals included:

1. validating that TOPAZ3D and Diablo obtain similar results for a thermal analysis;
2. validating that NIKE3D, Diablo, and ParaDyn obtain similar results for a structural analysis; and
3. performing a fully-coupled thermal-structural analysis using Diablo in a parallel computing environment.

## Relevance to LLNL Mission

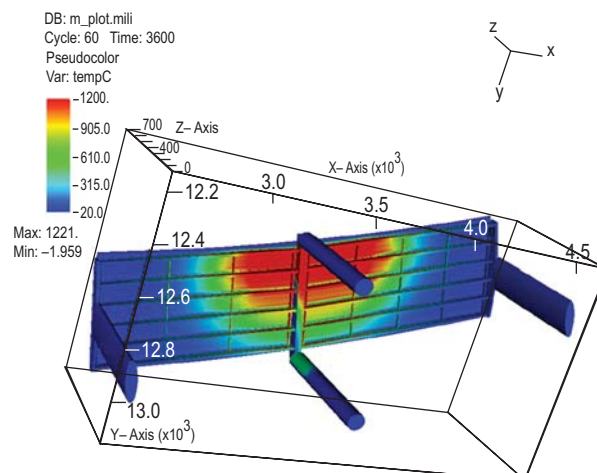
Validation of computational software for predicting progressive collapse of large structural systems is extremely difficult. The ability to perform progressive collapse simulations of critical infrastructure is important for Homeland Security applications, and therefore relevant to the mission of LLNL.

## FY2007 Accomplishments and Results

A thermal model was successfully developed for TOPAZ3D and Diablo that showed equivalent calculated temperature values within 2% at key locations in the model. Figure 1 shows the temperature distribution at one hour for a flame temperature of 1200 °C using TOPAZ3D.

The thermal model approximated the fire as a box-shaped region for determination of heat transfer to the structure. This "flame box" extended from the underside of the concrete roadway down to sixteen feet elevation below the center of the main box girder. The lateral position, orientation, and shape of the flame box were adjusted as a function of time corresponding to video footage from the East Bay Municipal Utility District. The amount of radiative and convective transport from the flame box to a given surface facet at a given time

Figure 1. Simulated temperature distribution from a stationary fire at one hour using the code TOPAZ3D.



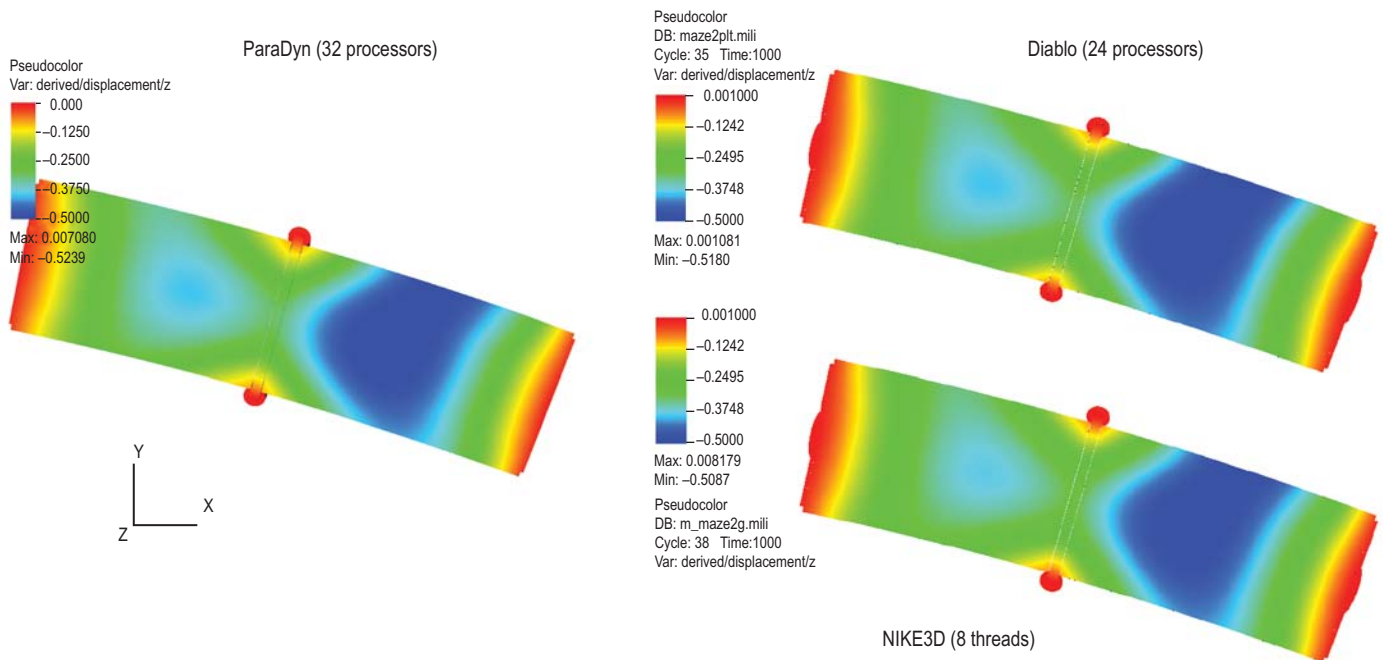


**Figure 2.** Overhead view of MacArthur Maze connector under pure gravity load. The three plots show all three LLNL structural codes providing the same resulting displacement. The red is 0.0 in.; the blue represents a vertical displacement of  $-0.5$  in. For comparison, the peak CalTrans calculated displacement was  $-0.5$  in. for the right span.

was determined based on the facet and flame box location and orientation, where radiative view factors and an applied thermal decay length for the convective gas temperature were used.

Structural models for the MacArthur Maze were developed for NIKE3D, Diablo, and ParaDyn. Both NIKE3D and ParaDyn have the ability to incorporate the thermal loads calculated within TOPAZ3D for use in the structural analysis. However, this methodology does not account for transient structural deformation effects on the calculated thermal profiles.

Diablo, on the other hand, has the ability to perform the thermal and

structural analysis in a fully-coupled manner. Gravity loading was applied to the structure prior to performing the thermal-structural analysis. Figure 2 shows a displacement comparison of the model under gravity load for the LLNL structural finite element codes. Not only do all three finite element codes give similar results, but the codes predict similar vertical displacements to the calculated displacements of the California Department of Transportation (CalTrans). Figure 3 shows the simulated collapse of the MacArthur Maze connector using TOPAZ3D for the thermal loading and ParaDyn for the structural loading, assuming a flame temperature of  $1200^{\circ}\text{C}$ .

### Related References

1. Buyukozturk, O., and F. J. Ulm, *Materials and Structures*, pp. 83-105, MIT Press, 2002.
2. Chen, J., and B. Young, "Experimental Investigation of Cold-Formed Steel Material at Elevated Temperatures," *Thin-Walled Structures*, **45**, pp. 96-110, 2007.
3. Outinen, J., and P. Makelainen, "Mechanical Properties of Structural Steel at Elevated Temperatures and After Cooling Down," *Fire Mater.*, **28**, pp. 237-251, 2004.
4. Takagi, J., and G. Deierlein, "Strength Design Criteria for Steel Members at Elevated Temperatures," *Journal of Constructional Steel Research*, **63**, pp. 1036-1050, 2007.



**Figure 3.** Simulated collapse of the MacArthur Maze connector using TOPAZ3D for the thermal loading and ParaDyn for the structural loading. (Photo courtesy of San Francisco Chronicle.)

# Enhanced Composite Modeling Tools



Andrew Anderson  
(925) 423-9634  
anderson1@llnl.gov

Composite materials are used in many advanced weapons systems and structures at LLNL. We have previously enhanced our ability to simulate structural response and progressive failure of composite systems in ALE3D (an arbitrary Lagrange/Eulerian multi-physics code developed at LLNL) by porting an existing composite constitutive model (Model 22, the Fiber Composite with Damage Model) from DYNA3D (a nonlinear, explicit, 3-D FEM code for solid and structural mechanics). This year, a more advanced model (DYNA3D Model 62, the Uni-Directional Elasto-Plastic Composite Model) has been implemented. Experiments were conducted to validate the elastic response of the model and to give insights and data needed for the addition of a failure algorithm into the model.

## Project Goals

We implemented the Uni-Directional Elasto-Plastic Composite Model into ALE3D. This included implementing the ability to input orthotropic orientation data into prescribed local volume elements. Another modeling goal was to enhance the model by incorporating a failure algorithm that includes matrix delamination, fiber tensile, and fiber



Figure 1. Fiber composite compression cylinder with 1.0-in.-diameter pin.

compressive failure. Several experiments were conducted to provide data for the verification and validation of the model's implementation in ALE3D.

## Relevance to LLNL Mission

The improved fiber composite material models can be used in simulations (to failure) in the many LLNL programs, such as those for composite munitions, armor penetration, pressure vessels, and rocket motors. This project has been beneficial in supporting the composite modeling efforts within the DoD Joint Munition Program and the Focused Lethality Munition Program. This study supports LLNL's engineering core competency in high-rate mechanical deformation simulations of large complex structures by providing an enhanced capability to model composite structures with ALE3D.

## FY2007 Accomplishments and Results

The implementation of the Fiber Composite with Damage model into ALE3D, which was completed in the first year of this project, was verified with several code-to-code comparisons. The hoop stresses in pressurized cylinders from simulations run with DYNA3D, with the new Fiber Composite model in ALE3D, and with an existing anisotropic ALE3D model, all agreed within 1%. This included both explicit and implicit ALE3D runs.

The Uni-Directional Elasto-Plastic Composite model was implemented into ALE3D. An important part of this task was creating an algorithm to initialize and update material directions at the ply and element levels. The model was validated using the same pressurized-cylinder simulations described above, and the results were found to closely match the DYNA3D predictions.

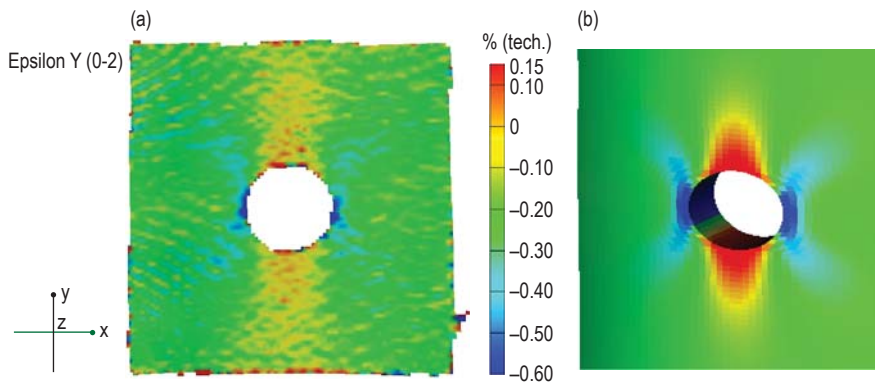


Figure 2. (a) Aramis axial strain results for fiber composite compression cylinder with no pin at 300,000 lbs of load. (b) The ALE3D simulation.

Composite failure mechanisms can be divided into two types: intra-ply failure mechanisms, such as fiber breakage, matrix failure (cracking/crushing), and fiber buckling; and inter-ply failure mechanisms involving ply delamination.

Intra-ply failure can be applied at the ply level and so fits in well with this model's "unit cell" approach. Inter-ply failure that includes crack opening between plies and plies sliding relative to each other affects all layers simultaneously, and so is more difficult to implement. All the relevant mathematical expressions necessary for these functionalities have been derived, and the corresponding changes to the existing code have outlined. Implementation will be undertaken next year.

A series of compression tests to failure were conducted on eight different composite cylinder specimens with different fiber, fiber orientations,

and resins. The data collected on the stiffness, Poisson's ratio, and ultimate strength of each specimen provide model validation data for the newly implemented models 22 and 62. The data also provide an expanded source of failure data for upcoming failure model validation in ALE3D.

Strain concentration factors in fiber composite cylinders with holes and bonded pins were measured using the Aramis video strain measurement system. The basic fiber composite cylinder with pin configuration is shown in Fig. 1. Figure 2 shows a comparison for the case of no pin (open hole) between the measured experimental data and the simulated response from ALE3D. The results appear to be very similar.

Strain concentration factors due to focused shear in composites were measured using the specimen shown in Fig. 3. This sample was loaded in compression to produce a concentrated shear band in the composite sample. The Aramis load strain curve is shown in Fig. 4.

### Related References

1. Christensen, R., and E. Zywicki, "A Three Dimensional Constitutive Theory for Fiber Composite Laminants," *Journal of Applied Mechanics*, **57**, pp. 948-955, December 1990.
2. Chang, F. K., and K. Y. Chang, "A Progressive Damage Model for Laminated Composites Containing Stress Concentration," *Journal of Composite Materials*, **21**, pp. 834-855, 1987.

### FY2008 Proposed Work

In a proposed follow-on project, we will continue to improve fiber composite modeling in ALE3D, with an emphasis on local bending response and progressive damage. We plan to implement ply-level capabilities and damage algorithms taken from a specialized LLNL ply-level composite code known as ORTHO3D, and verify their implementation experimentally.



Figure 3. Composite shear specimen from section of a Mk82.

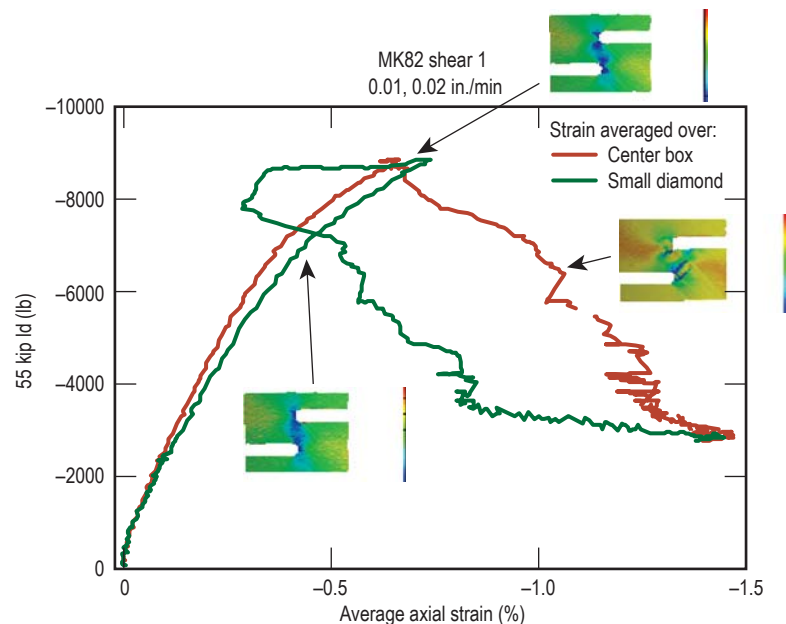


Figure 4. Shear strain concentration in composite Mk82 shear specimen.

# EMP Simulation and Measurement Data Analysis in Support of the Titan Experiments



*Charles G.  
Brown Jr.*  
(925) 423-4435  
brown207@llnl.gov

**E**lectromagnetic pulse (EMP) is a known issue for a variety of situations including short-pulse laser facilities such as LLNL's Titan and Omega, and experts believe EMP will also be an issue with NIF. During FY2007, this project focused on improving simulation capabilities of EM fields due to electrons from laser/target interactions, and providing post-processing algorithms and software.

## Project Goals

The overarching goal of this project is to simulate EMP in situations like the Titan short-pulse laser due to electrons from laser/target interactions and to compare measurement results with the simulations. To accomplish the simulation task, we used EMSolve 3, an LLNL EM solver. Unlike most available codes, EMSolve's architecture allows seamless integration of user-created sources and boundary conditions, and EMSolve has been augmented with electron beam sources.

## Relevance to LLNL Mission

An understanding of the EMP in Titan, through the simulation

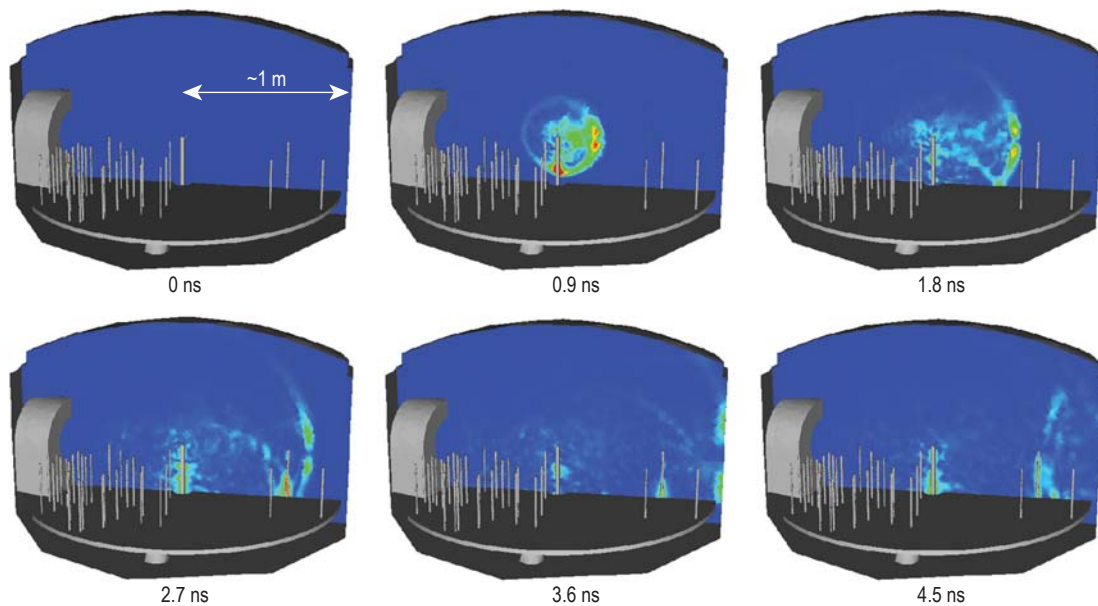
and analysis in this project, will be extrapolated to NIF and other short-pulse lasers around the world to better mitigate EMP effects.

## FY2007 Accomplishments and Results

During FY2007, we gained further experience in performing simulations using the EMSolve processing chain, which consists of Cubit, EMSolve, and VisIt. Cubit is a meshing tool from Sandia National Laboratories that is used to construct models for EMSolve. VisIt is an LLNL code for visualizing simulation data.

We created more realistic CAD models of the Titan chamber, including finer details such as optics stands modeled as rods. Further, we augmented EMSolve so that both the magnetic and electric fields of electron beam sources can be simulated accurately. We also advanced our ability to post-process data measured by B- and D-dot probes, in particular deconvolution of the probe response.

The deconvolution method we used is an optimal method based on the Wiener filter, which is implemented in processing software. We have extended the software tool and created a user



Time sequence of simulation of magnetic field due to propagating electron bunch.

interface called Time-Series Analysis Tool (TSAT) that allows quick and easy manipulation of time-series data and includes data input, signal processing, and display capabilities. The simulation and post-processing capabilities originating from this project have allowed us recently to publish a comparison of a simulation of an electron beam in Titan and actual, measured data.

The figure depicts frames of a time sequence of the magnetic fields due to  $10^{12}$  electrons in a Gaussian bunch with a full-width at half maximum of 100 ps.

### Related References

1. Mead, M. J., *et al.* "Electromagnetic Pulse Generation within a Petawatt Laser Target Chamber," *Review of Scientific Instruments*, **75**, 10, pp. 4225-4227, October 2004.
2. "VisIt Visualization Tool," <http://www.llnl.gov/VisIt/home.html>.
3. Candy, J. V., *Model-Based Signal Processing*, Wiley-IEEE Press, 2006.
4. Brown, C. G., Jr., *et al.*, "Electromagnetic Pulses at Short-Pulse Laser Facilities," *Proceedings of the 5th International Conference on Inertial Fusion Sciences and Applications*, Kobe, Japan, September 9-14, 2007.

### FY2008 Proposed Work

Our FY2008 work will include improving our CAD models to perform more realistic simulations; continuing to perform EMSolve simulations; assisting the experimental team in the measurement process to better understand the measurement system; and working with signal processing experts to calibrate and analyze the data, particularly the data obtained from the September 2007 dedicated shots in Titan.

# Full-Process Computer Model of Magnetron Sputter: Testing Existing State-of-the-Art Components

This work is the first part of a larger project to create a modeling capability for magnetron sputter deposition. The process is divided into four steps: plasma transport, target sputter, neutral gas and sputtered atom transport, and film growth, shown schematically in Fig. 1. Each of these is simulated separately in this part of the project.

The plasma modeling was performed using the Object-Oriented Particle-In-Cell code (OOPIC) from the University of California, Berkeley. Figure 2 shows the electron density in the simulated region, using magnetic field strength input from experiments where a scale of 1% was used. Figures 3 and 4 depict the magnetic field components that were generated using 2-D linear interpolation of the experimental data.

## Project Goals

The goal of the overall modeling tool is to understand, and later predict, relationships among parameters of film deposition we can change (such as gas pressure, gun voltage, and target-substrate distance) and key properties of

the results (such as film stress, density, and stoichiometry.) The simulation must use existing codes, either open-source or low in cost. In FY2007 we identified and tested the best available code for each process step, then determined if it could cover the size and time scales we need for reasonable computation times. We also had to determine if the process steps are sufficiently decoupled that they can be treated separately, and identify any issues preventing practical use of these codes. The second part of the project will consider whether the codes can be (or need to be) made to talk to each other and integrated into a whole.

## Relevance to LLNL Mission

LLNL has multiple projects that depend on precision film deposition for critical goals. A prime example is control of film microstructure and stress in 180-mm-thick sputtered Be metal shells for NIF targets. Others include stress control in large-area sputtered nanolaminate adaptive optics, and film stoichiometry in high-power capacitors.



Christopher Walton  
(925) 423-2834  
walton9@llnl.gov

## FY2007 Accomplishments and Results

In the plasma simulations, we demonstrated an approach to a realistic plasma model, eliminated computational heating, and discovered the computational limitations of the plasma code. Figure 1 shows the largest obtainable domain size, 1% of real dimensions, which features a grid of cells, 340 x 638. We discovered that a 5% scale simulation using a grid of cells 1702 x 3192 crashes the code on a Windows platform, which calls for future work in implementing the code on high performance machines and creating a parallel electrostatic solver.

In the larger project we partly validated models of the pressure and temperature distribution in the gas in front of the sputter gun. This model enabled us to calculate arrival angles and energies for sputtered Be atoms passing through the gas. These were then used as inputs for simulations of the growth of the Be films. These simulations show columnar microstructure approaching a limiting grain size, with dome-shaped grains and a gap developing at the grain boundaries, all consistent with experiment and of key importance in understanding film density. An example of this qualitative agreement is shown in Fig. 5.

In the larger goal of testing all the separate codes for suitability, this project succeeded in identifying the plasma simulation as the most difficult of the four steps, showing us we must focus resources on it for the second year. We are negotiating a consulting contract with one of the authors of the plasma code, which will include parallel-processing capability since a single CPU seems to be insufficient for the system size we must simulate.

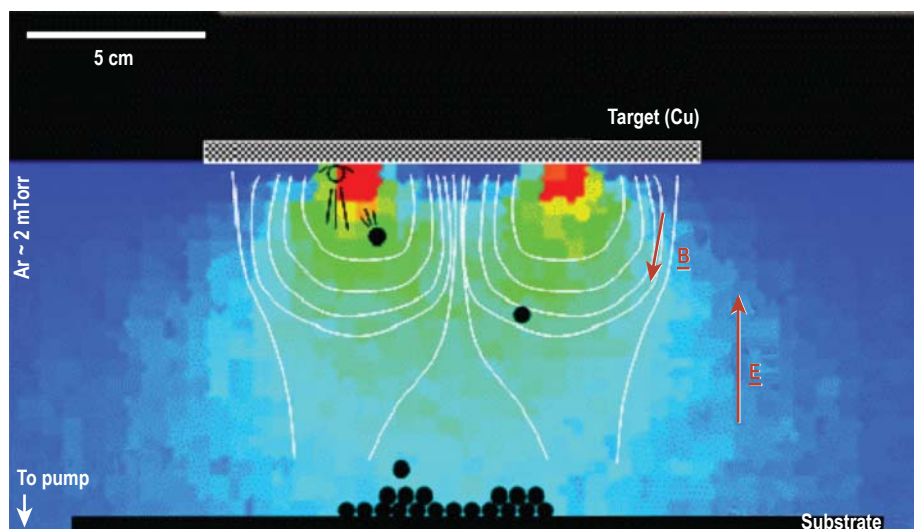


Figure 1. Schematic of magnetron deposition system to be simulated in overall project. The engineering part consists of simulating charge species and interaction with E and B fields.

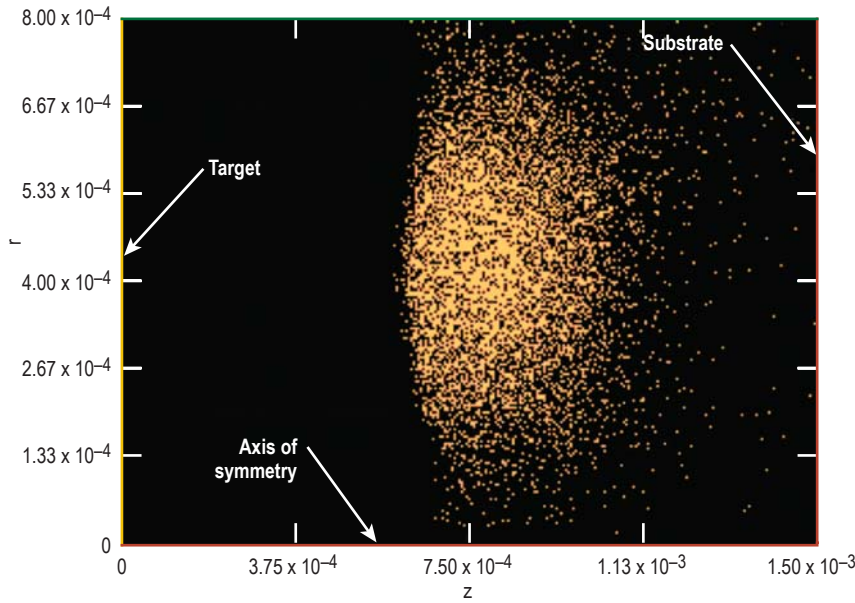


Figure 2. Test domain for plasma simulation, scaled 1%. Red points represent simulated clusters of electrons (argon ions and neutral gas not shown).

**Related References**

1. Verboncoeur, J. P., A. B. Langdon, and N. T. Gladd, "An Object-Oriented Electro-magnetic PIC Code," *Comp. Phys. Comm.*, **87**, pp. 199-211, 1995.
2. Bohlmark, J., U. Helmersson, M. Van-Zeeland, I. Axnas, J. Alami, and N. Brenning, "Measurement of the Magnetic Field Discharge in a Pulsed High Current Magnetron Discharge," *Plasma Sources Sci. Technol.*, **13**, pp. 654-661, 2004.

*FY2008 Proposed Work*  
All parts of this project are continuing in FY2008.

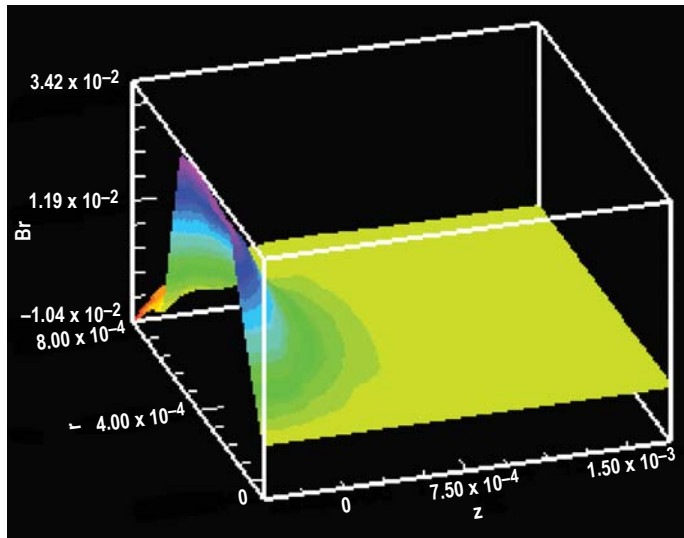


Figure 3. Radial magnetic field component used in plasma simulation.

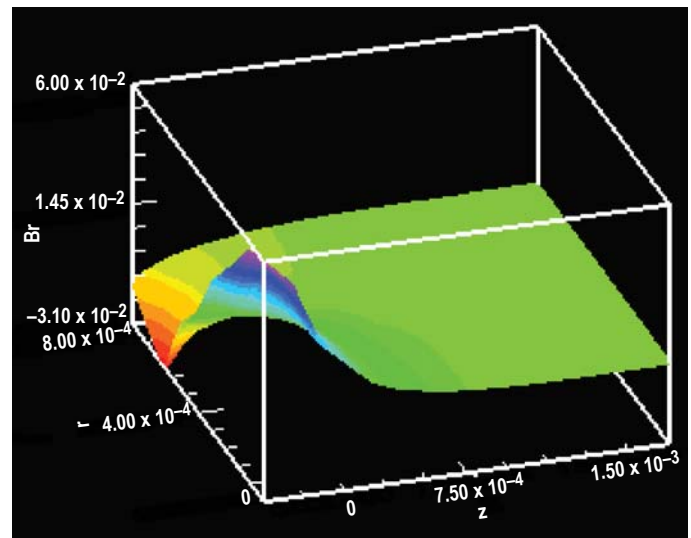


Figure 4. Axial magnetic field component used in plasma simulation.

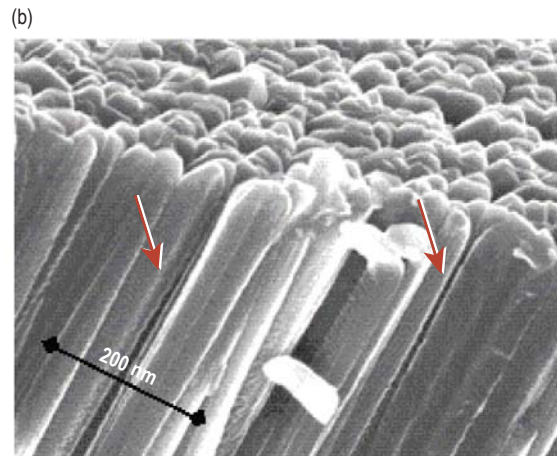
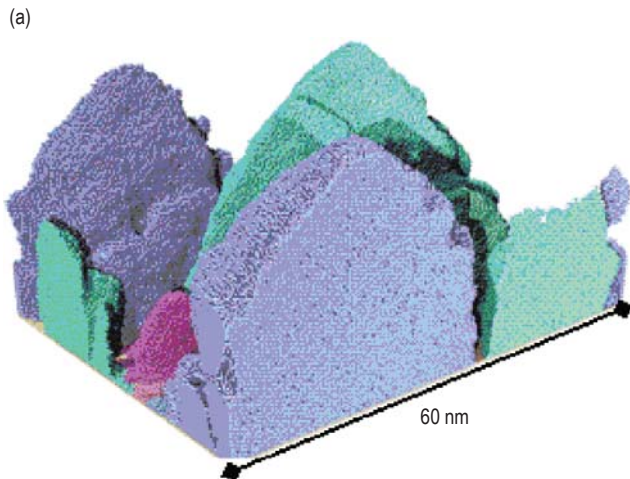


Figure 5. (a) Simulated and (b) experimental microstructure of sputtered Be films. Agreement of the columnar grains, reaching a steady-state width with dome-shaped tops and apparent gaps at the grain boundaries is our key qualitative result. Quantitative agreement remains as a future goal.

# Direct Simulation Monte Carlo Benchmarking and Code Comparison



Aaron P. Wemhoff  
(925) 423-9839  
wemhoff2@llnl.gov

A wide variety of applications require a core capability to model fluid flow on the subcontinuum scale. Direct Simulation Monte Carlo (DSMC) is the standard methodology used to model these types of flows.

The purpose of our project is to apply a series of available DSMC codes to two classes of problems. The first set comprises simple benchmark problems that contain either known or analytical solutions, which provides us confidence in our ability to use the codes effectively. The second set contains problems that are pertinent to LLNL applications, which allows us to determine which code contains the best capabilities to handle a given type of problem. Three suites of freely obtained codes were used: DS2V/DS3V; the DSMC Analysis Code (DAC); and MONACO2d/3d.

To supplement our study, we created fluid mesh generation tools to allow for efficient implementation of the codes. In addition, we performed traditional continuum CFD analysis of several of the benchmark problems at noncontinuum flow conditions. The results of this analysis demonstrated the loss of convergence ability in the CFD solver as the flow conditions deviate from the continuum limit.

Finally, we interviewed known leaders in the DSMC field to obtain

their opinions regarding the usage of the aforementioned codes for certain types of problems.

## Project Goals

The major goal of our study is to implement the codes on both classes of problems mentioned above in order to assess the accuracy of various code features. Systems ranged from internal flow problems such as a simple comparison of a temperature gradient in a microchannel using DSMC to an analytical temperature slip model (Fig. 1), or a model of an experimental chemical vapor deposition apparatus compared to experimental results (Fig. 2).

We also modeled chemically reacting external re-entry flows (Mach number  $> 18$ ) for a cylinder (Fig. 3) and a sphere (Fig. 4).

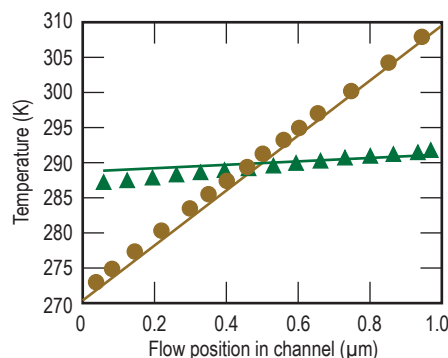
## Relevance to LLNL Mission

Systems containing subcontinuum fluids are seen in a wide variety of applications around the Laboratory, which generally feature very small length scales or low density (rarefied) gas conditions. Examples of the former group of systems include flow near sensors or inside microchannels, while the latter group includes microfabrication processes and vehicle re-entry scenarios. One of the LLNL-specific benchmarks we applied the codes to is a magnetron sputtering chamber used for growing films on large scale adaptive optics, which also has relevance to the microfabrication cluster tool and NIF target capsule manufacturing.

## FY2007 Accomplishments and Results

We successfully modeled six general problems and three LLNL-related problems using the codes DAC and DS2V. We also examined the use of

Figure 1. DSMC (lines) and analytical (markers) solutions to the steady-state temperature field of Ar in a 1- $\mu\text{m}$  channel for a Knudsen number of 0.01 (brown) and 10 (green), where the wall temperatures are 270 K and 310 K.



DS3V in the magnetron sputtering chamber analysis, and we applied the MONACO2d code for use in a re-entry chemistry sensitivity study. We obtained good agreement with analytical solutions for the classic Fourier problem (Fig. 1) and flow in a microchannel. Good agreement was also achieved when compared to experimental and

modified continuum simulations of the CVD chamber shown in Fig. 2. We also showed good code agreement between DAC and DS2V in a variety of external flow problems. All of our findings are available in a report that provides guidance on the advantages and disadvantages of using each DSMC code, when a continuum code is proper for a given

type of problem, and which DSMC code options are the most appropriate for a given system.

**Related References**

1. Davis, D. H., “Monte Carlo Calculation of Molecular Flow Rates Through a Cylindrical Elbow and Pipes of Other Shapes,” *J. Appl. Phys.*, **31**, 7, pp. 1169-1176, 1960.
2. LeBeau, G. J., and F. E. Lumpkin, “Application Highlights of the DSMC Analysis Code (DAC) Software for Simulating Rarefied Flows,” *Comp. Meth. Appl. Mech. Eng.*, **191**, 6-7, pp. 595-609, 2001.
3. Dietrich, S., and I. D. Boyd, “Scalar and Parallel Optimized Implementation of the Direct Simulation Monte Carlo Method,” *J. Comp. Phys.*, **126**, pp. 328-342, 1996.
4. Singh, V., B. Berney, and A. Krishnan, “Designing Low Pressure Systems With Continuum Models,” *J. Vac. Sci. Technol. A*, **14**, 3, pp. 1252-1257, 1996.
5. McNenly, M. J., A. P. Wemhoff, and H. Hsieh, “Sensitivity of a DSMC Solution to the Thermochemistry Model for Non-Equilibrium Reentry Flows,” *DSMC Theory, Methods, and Applications Conference*, Santa Fe, New Mexico, Sept. 30 – Oct. 3, 2007.

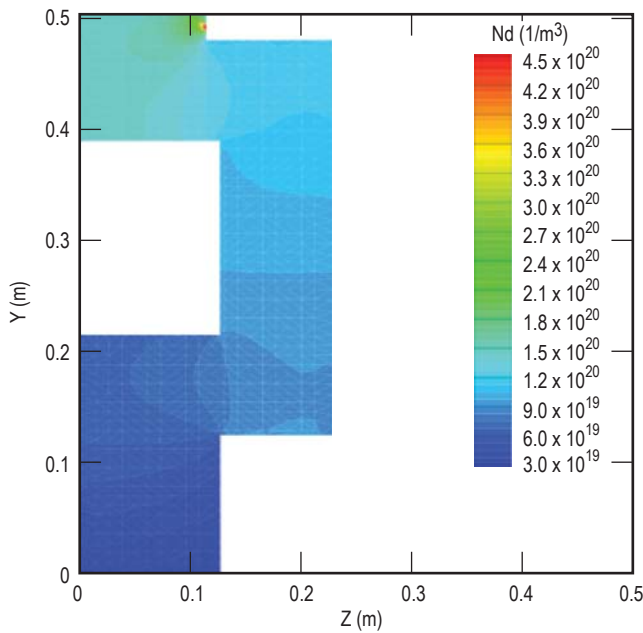


Figure 2. Simulation of Ar number density in a chemical vapor deposition chamber following the study of Singh *et al.*

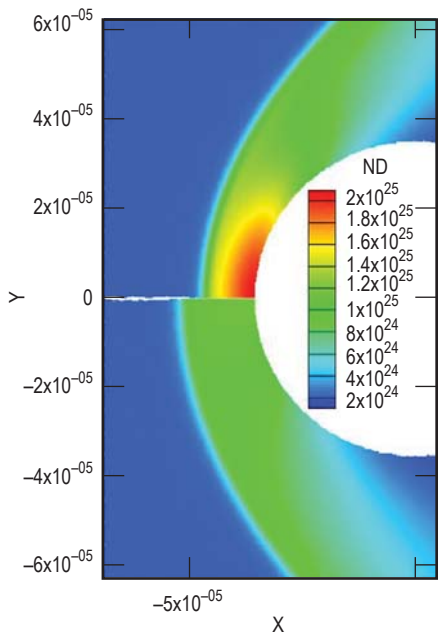


Figure 3. Number density for air impinging upon a cylinder at Mach 18. The upper and lower plots show results for reacting and nonreacting flow, respectively.

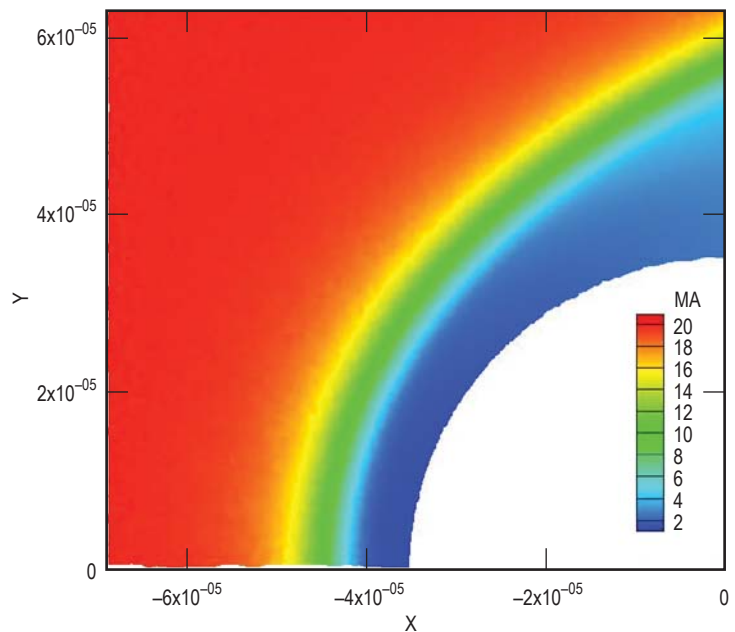


Figure 4. The simulated local Mach number for reacting airflow at 5901.38 m/s, 216.7 K, and  $1.8487 \times 10^{24} \text{ m}^{-3}$  around a 0.07-mm-diameter sphere.

# Photonic Doppler Velocimetry



Adam White  
(925) 424-5935  
white210@llnl.gov

Optical velocimeters are noncontact diagnostics widely used to measure the velocities of explosively driven metal surfaces in single-shot shock physics experiments. Photonic Doppler Velocimetry (PDV) is a novel optical velocimetric technique, developed at LLNL, that uses optical heterodyning to measure the beat frequency between light incident on and light reflected by a moving metal surface. In this project, we have used PDV in an atypical role on the coaxial load experiment with ALE3D.

## Project Goals

Our goal was to use PDV on the ALE3D coaxial load experiment to provide velocity and displacement versus time data for four locations on the sidewall of an aluminum tube during the

electromagnetically induced collapse of the tube. The measured PDV data would be used to validate and critique modeled results from ALE3D, an LLNL multi-physics hydrocode.

## Relevance to LLNL Mission

Velocimetry is one of the primary shock physics diagnostics. PDV is a particularly attractive diagnostic for experiments involving significant quantities of radiated electromagnetic energy or high-explosives because 1) the PDV probes and fibers that are exposed in the experimental environment are immune to electromagnetic interference; 2) PDV requires no direct mechanical contact with the measurement surface; and 3) PDV does not require any electrical connections to be made on or near the measured surface. Specific programs requiring this expertise include explosive pulsed power for high-energy-density physics research, high-velocity impact experiments for materials, EM launcher/shaker experiments for military applications, and subcritical component testing.

## FY2007 Accomplishments and Results

Four PDV probes were installed on the ALE3D coaxial load testbed to monitor the motion of the tube at four azimuthal positions separated by 90° at the mid-plane of the tube (Fig. 1). The interface between the PDV probes and coaxial load test stand were machined adapters that were locally designed and fabricated.

The PDV laser transmitted 1550-nm light over optical fiber to each PDV probe. A fraction of light incident on the fiber endface inside the probe

**Figure 1.** Block diagram of PDV system and probe layout. An optical circulator and power splitter within the PDV detector chassis routed optical power from the laser, to the probes, and into the detectors.

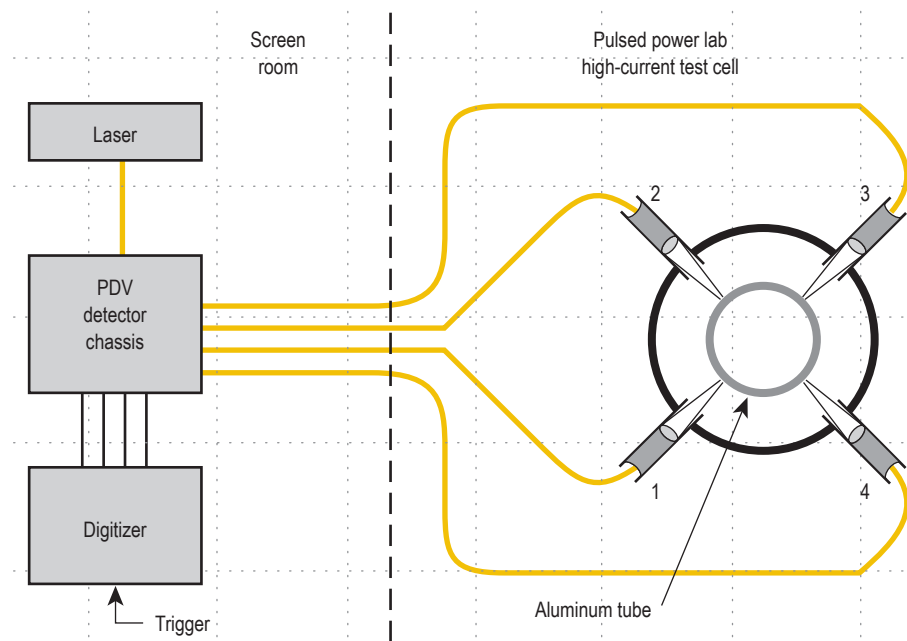
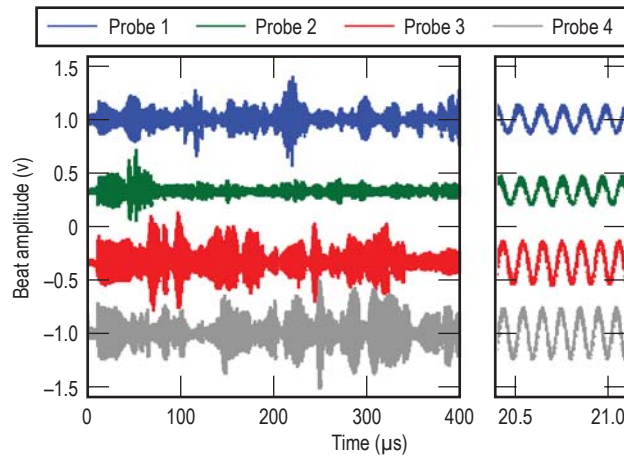


**Figure 2.** Raw PDV data. The beat frequency is clearly visible in the plot on the right, which depicts only a small sample in time (between 20.0 and 20.5  $\mu\text{s}$ ) of the total waveform on the left. The waveforms are offset vertically to improve visibility.



was reflected back along the fiber; a comparable amount was launched by the probe onto the moving tube surface, reflected and Doppler-shifted, and collected by the probe to also return along the fiber.

Both the endface reflected (unshifted) and reflected Doppler-shifted signals were coupled via an optical circulator onto the detectors. The beat signal (a signal that is amplitude modulated at a frequency equal to the difference in frequency between the two reflected signals) was recorded and digitized. With unshifted light at 1550 nm, this beat frequency corresponds to 1.29 MHz per

1 m/s surface velocity. The maximum velocity detectable by the PDV system we used was around 5 km/s, limited by the bandwidth of the detectors and digitizers, and well beyond our expected needs.

PDV data were taken on five shots of the ALE3D coaxial load experiment. Figure 2 shows raw data from one shot. The raw data, representing the beat waveform, is processed using a sliding Fast Fourier Transform (FFT) to determine beat frequency as a function of time. The transformed data are scaled by 1 m/s per 1.29 MHz to provide velocity versus time data, and integrated with

respect to time to provide displacement versus time data. The processed velocity and displacement data are shown in Fig. 3.

Our application of PDV was slightly unusual due to the low surface velocities measured—tens of meters per second rather than kilometers per second. We experienced no difficulty measuring these relatively low velocities.

In addition, our experiment confronted one of the disadvantages of PDV, that the magnitude of the Doppler shift can be detected, but not the direction of surface movement. Although this problem was prevalent in our data due to the oscillatory response of the tube walls, the issue was minimized by assuming that after the initial compression, each velocity zero corresponded to a reversal in direction of motion. These assumptions were supported by data from auxiliary diagnostics.

### Related Reference

Strand, O. T, D. R Goosman, C. Martinez, T. L. Whitworth, and W. W. Kuhlow, "A Novel System for High-Speed Velocimetry Using Heterodyne Techniques," *Rev. Sci. Instrum.*, **77**, 083108, 2006.

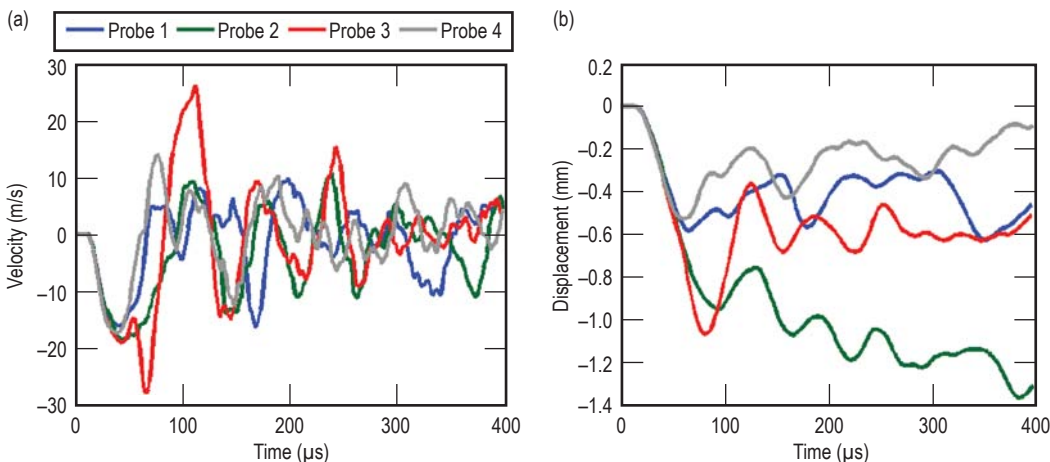


**Figure 3.** (a) Velocity and (b) displacement of the monitored surfaces as a function of time. Velocity is calculated by applying a sliding FFT to the raw data in Fig. 2, then scaling the transformed results. Displacement is calculated by integrating the velocity data with respect to time.





Measurement Technologies



# Standing Wave Probes for Micrometer-Scale Metrology



Richard M. Seugling  
(925) 423-8525  
seugling2@llnl.gov

In this project we are developing a low force, high-aspect-ratio, mechanical probe for the nondestructive characterization of manufactured components and assemblies. The key concept for the probe is the correlation between the dynamic response of an oscillating cantilever rod (probe) and the interaction of its tip with a surface (Fig. 1). The applications for this probe begin with surface location, but may encompass the characterization of the material properties of the surface, and perhaps branch into the modification of the surface. This project is a collaborative effort between LLNL, the University of North Carolina at Charlotte, the National Institute of Standards and Technology (NIST), and an industrial partner, InsituTec.

## Project Goals

We will provide the scientific understanding of a low force, contact probe capable of being used on a number of machine tools and metrology platforms with a characterized uncertainty based on the fundamental understanding of the probing process. The exit strategy includes continued collaboration with the UNC-Charlotte team, rigorous calibration efforts with NIST, engaging a commercial source of probing instruments, and the probe's practical application at LLNL and its vendors for Inertial Confinement Fusion (ICF) and High Energy Density Physics (HEDP) target fabrication. A prototype instrument developed during this project will provide an excellent platform for continual reduction-to-practice efforts.

The final goal of this work is to enhance LLNL's precision metrology capabilities, which encompass key core technologies supporting NIF, Weapons Complex Integration, and nanofabrication.

## Relevance to LLNL Mission

Currently, LLNL's ICF and HEDP targets comprise components with dimensions in the millimeter range, with micrometer-scale, high-aspect-ratio functional features, including fill-tube holes and counterbores, hohlraum starburst patterns, and step-joint geometry on hemispherical targets. In addition to the small-scale, complex geometry, these structures are often thin walled and manufactured out of delicate materials such as aerogels and/or metallic foams, which are susceptible to deformation and fracture during contact.

The near-term impact of this project is the expansion of LLNL's ability to accurately perform dimensional measurements of micrometer-scale features using a low force, high-aspect-ratio probe system.

## FY2007 Accomplishments and Results

A prototype probe system has been built and is operational at LLNL including advanced electronics for increased sensitivity and upgraded mechanics for integration to any number of arbitrary motion control platforms, as shown in Fig. 2. The probe has been integrated into a profiling station with nanometer-

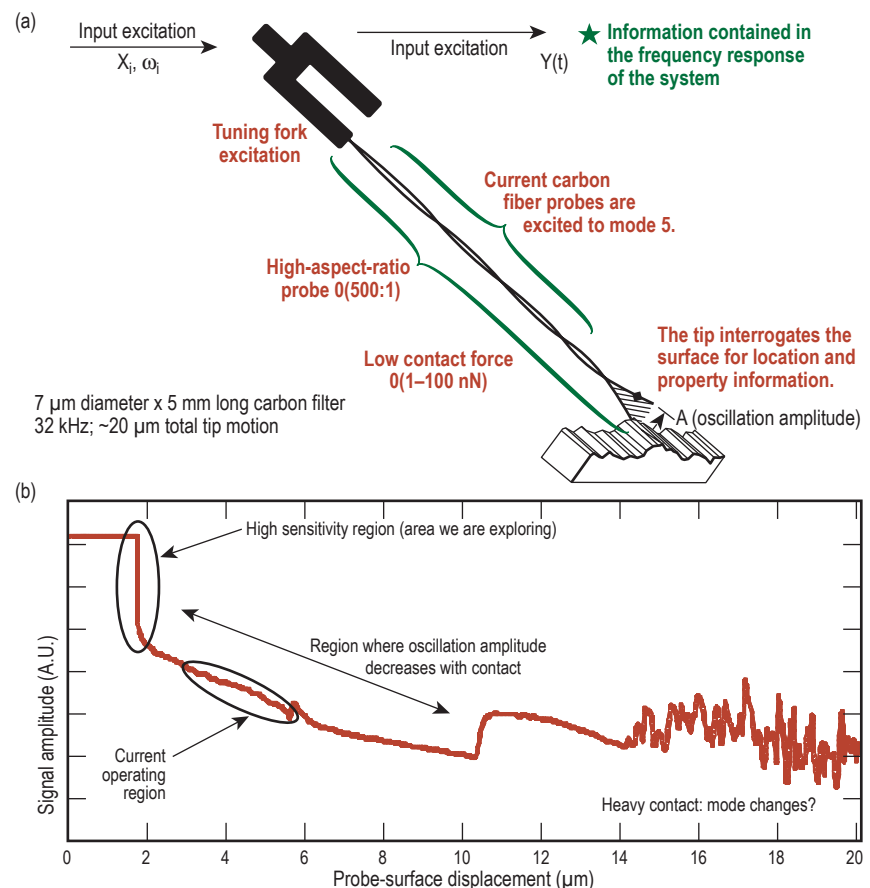


**Figure 1.** (a) Schematic description of probe system including tuning fork excitation and high-aspect-ratio rod. An input amplitude ( $X_i$ ) at a frequency ( $\omega_i$ ) is applied to the tuning fork while the output amplitude ( $Y$ ) is monitored as the probe comes into contact with the surface. (b) Output response of probe as it comes into contact with a surface.

level positioning capability and data acquisition. Experimental evaluation of probe performance is being quantified on this system. Probe sensitivity has been measured on three different materials including a metallic glass (Vitreyloy 105), gold, and a hardened steel gage block.

A typical sensitivity experiment of the probe contacting a steel gage block is shown in Fig. 3. Results of these experiments indicate that probe sensitivity varies based on materials with similar surface finishes, as illustrated in Fig. 4.

A model of the probe dynamics including contact has been derived as

a stand-alone model in Fortran. This model consists of an Euler-Bernoulli beam driven at one boundary by a tuning fork drive system; at the other end of the beam, we apply nonlinear contact conditions. Theoretical approximations of near surface (van der Waals, and electrostatic) and contact (impact, adhesion, and meniscus) forces have been developed and are applied to the numerical model.

Year one of the proposed effort comprises both the simulation of the probe's response when characterizing well-defined surfaces, and the acquisition of data using an experimental apparatus.

### Related References

1. Bauza, M. B., R. J. Hocken, S. T. Smith, and S. C. Woody, "Development of a Virtual Probe Tip with an Application to High Aspect Ratio Microscale Features," *Rev. Sci. Instrum.*, **76**, pp. 095112, 2005.
2. Burnham, N. A., O. P. Behrend, F. Oulevey, G. Gremaud, P.-J. Gallo, D. Gourdon, E. Dupas, A. J. Kulik, H. M. Pollock, and G. A. D. Briggs, "How Does a Tip Tap?" *Nanotechnology*, **8**, pp. 67-75, 1997.
3. Weckenmann, A., T. Estler, G. Peggs, and D. McMurtry, "Probing Systems in Dimensional Metrology," *CIRP Annals – Manufacturing Technology*, **53**, 2, pp. 657-684, 2004.
4. Griffith, J. E., and D. A. Grigg, "Dimensional Metrology with Scanning Probe Microscopes," *J. Appl. Phys.*, **74**, 9, pp. R83-R109, 1993.

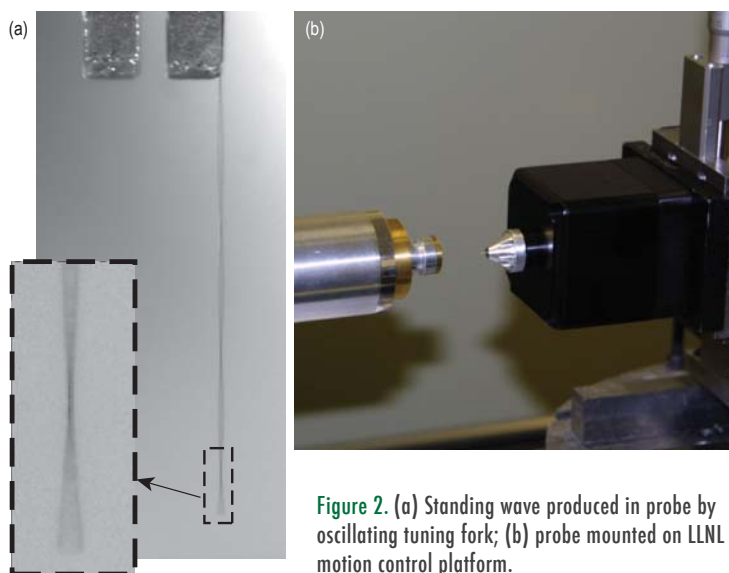


**Figure 2.** (a) Standing wave produced in probe by oscillating tuning fork; (b) probe mounted on LLNL motion control platform.

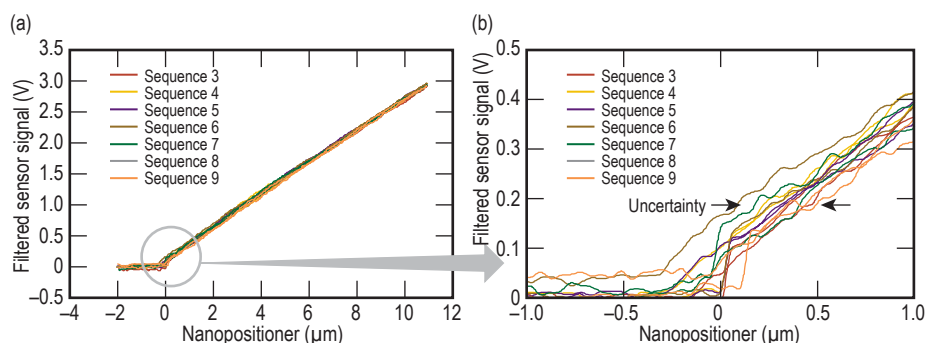


**Figure 3.** (a) Probe output contacting a steel gage block; (b) measurement uncertainty related to the variation in location of surface illustrated by the deviation between contact measurements. This deviation is a result of surface force interactions combined with environmental effects, such as thermal instability of the system and electronics.

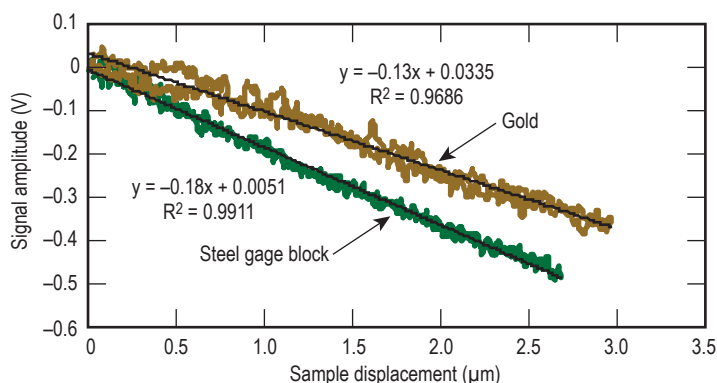


**Figure 4.** Sensitivity response as the probe comes into contact with a steel gage block and a gold sample of nominally the same surface finish.

### FY2008 Proposed Work

We plan on leveraging our understanding of the current probe system to develop a scaled version capable of operating on micrometer features with sub-micrometer-level sensitivity. We are also continuing analytical assessment of the probe system to incorporate actuation and sensitivity in multiple dimensions, and the feasibility of using the probe geometry for determination of material properties and/or surface modification.

# Error Budgeting and Certification of Dimensional Metrology tools



Jeremy J. Kroll  
(925) 422-6437  
kroll4@llnl.gov

**R**adiography and ultrasonic inspection have tremendous value in identifying features and defects in physical and biological samples and engineering structures. The historical focus of these inspection methods has been quantitative but without a clear understanding of uncertainty in the measurements. For many applications at LLNL, it would be of significant value to use these inspection techniques as quantitative metrology tools with well understood uncertainties. These could be used to obtain dimensional information on the internal structure of engineered components and assemblies, to be compared to specified tolerances. An example of the latter requirement would be in validating the precision of centering an inner component within an outer shell, which precludes access with a coordinate measuring machine (CMM) or visible light inspection.

In FY2006, we initiated a project to formulate error budgets for key LLNL radiographic and ultrasonic tools that would provide rigorously defined uncertainties in associating dimensional information with their acquired data. Specifically, for the Xradia Micro-XCT

(x-ray computed tomography) and the Laser UT (ultrasonic testing) systems, we prepared a framework for error budgets comprising the source, object, and detector.

In Fig. 1 we show how information flows in these systems and where errors can be accumulated.

In this project, we will form predictions of the uncertainty of dimensional measurements for NDE instruments, based on analyzing the physics of the information flow in the instruments and sources of uncertainty. We will also fabricate calibration artifacts that can be measured on other independent instruments, such as CMMs, which have existing uncertainty values for dimensional measurements. In comparing our predicted uncertainty with measurements on pre-characterized artifacts, we will validate our ability to associate uncertainties with dimensional measurements on these instruments.

## Project Goals

The goal is to produce validated quantitative error budgets for the Xradia Micro-XCT and the Laser UT systems, which will enable a structured approach for improving the capabilities of these machines, as well as provide insight into the effect of individual error sources.

## Relevance to LLNL Mission

The result of this project will be a broader view of dimensional metrology that extends beyond the traditional tools used in LLNL's precision engineering. Weapons Complex Integration (WCI) and NIF obtain improved quantification of the uncertainties in the fabrication of targets or other components. Both HEDP and ICF target fabrication will benefit from an improved understanding of the measurement uncertainties involved with these metrology tools.

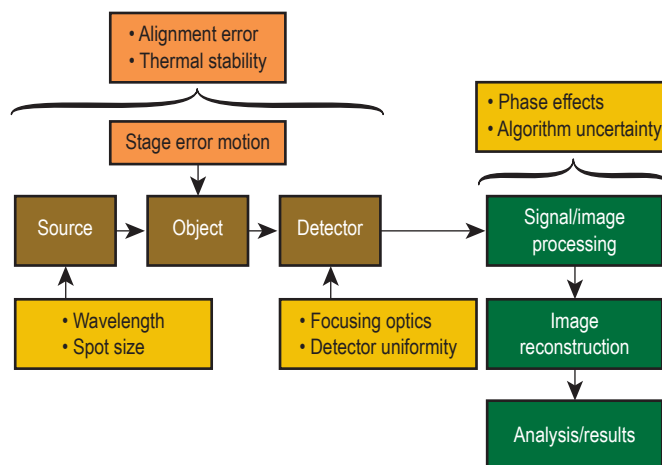


Figure 1. Error diagram showing possible sources of system uncertainty.

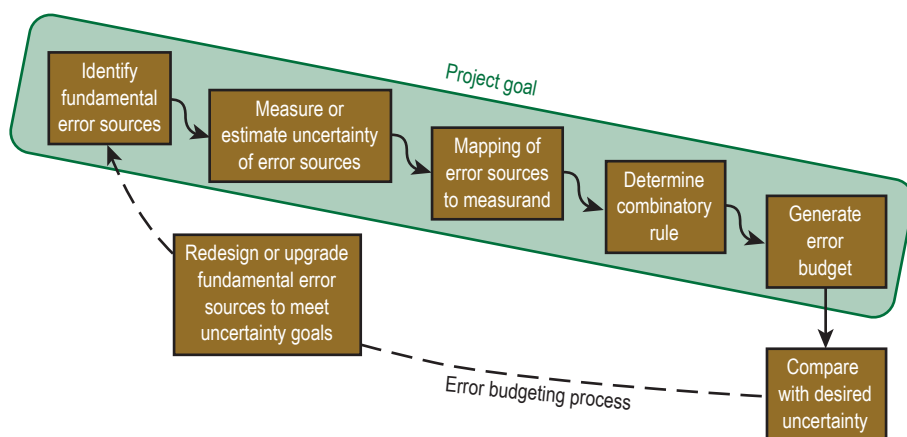


Figure 2. The error budgeting process.

### FY2007 Accomplishments and Results

Error budgets for the Xradia Micro-XCT and the Laser UT systems have been produced. Figure 2 shows the project goal of creating validated error budgets for the NDE machines. The feedback portion of Fig. 2 indicates the value in having an error budget to identify key areas of a metrology instrument to gain the most return on investment for upgrades or redesigns.

The Xradia Micro-XCT system consists of multiple sets of stacked axes between the source, object, and detector. Even though the source and detector axes are typically stationary during a CT scan, the thermal, vibrational, and

control stability of these axes are directly coupled to the uncertainty in the final CT data. Measurements of positional stability have been made between the source and object as well as between the object and detector.

Typically, the Xradia Micro-XCT system uses only the rotary axis to rotate the object with respect to a fixed source, and the detector to generate 2-D projections (radiographs) for computed tomographic image reconstruction of the object.

The first set of tests performed showed the angular positioning accuracy of the axis. Subsequent tests are being performed to measure the radial, axial,

and tilt motion of the rotary axis. Figure 3 shows that an object would move  $2.7 \mu\text{m}$  due to the rotary axis tilt error at a typical fixturing location above the axis. Data from the testing will be used to complete the population of the error budget, which will allow the propagation of these errors through object retrieval algorithms to determine system sensitivity.

### Related References

1. Donaldson, R. R., "Error Budgets in Technology of Machine Tools," *Technology of Machine Tools – Machine Tool Accuracy*, pp. 9.14-1-9.14-14, 1980.
2. BIPM, IEC, IFCC, ISO, IUPAC, IUPAP, and OIML, *Guide to the Expression of Uncertainty in Measurement*, Geneva, Switzerland: International Organization for Standardization, 1995.
3. Huber, R. H., D. J. Chinn, O. O. Balogun, and T. W. Murray, "High Frequency Laser-Based Ultrasound," *Review of Progress in Quantitative Nondestructive Evaluation*, August 2005.
4. Martz, H. E., Jr., and G. F. Albrecht, "Non-destructive Characterization Technologies for Metrology of Micro/Mesoscale Assemblies," *Proceedings of Machines and Processes for Microscale and Mesoscale Fabrication, Metrology, and Assembly*, ASPE Winter Topical Meeting, Gainesville, Florida, pp. 131-141, January 22-23, 2003.

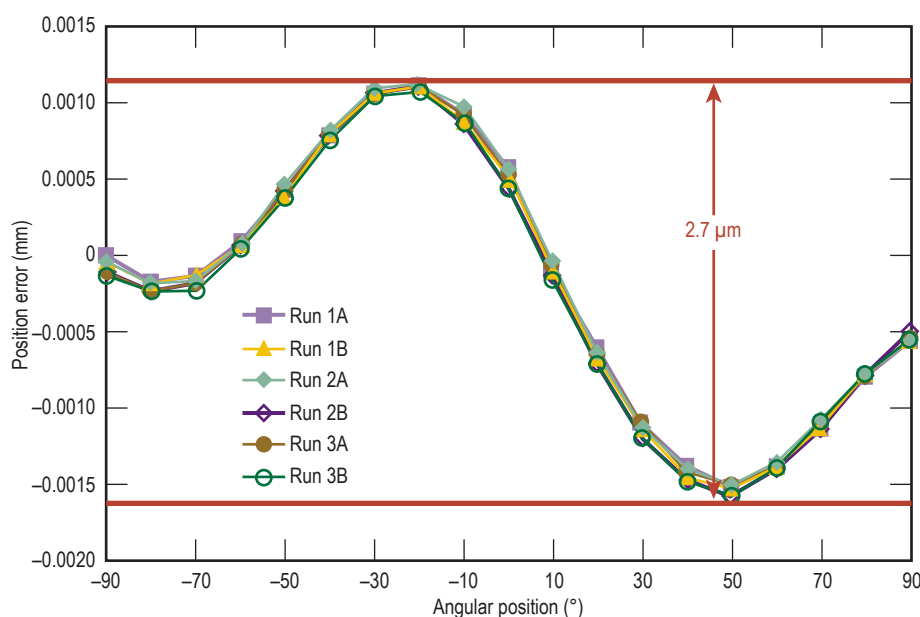


Figure 3. Position error of a part 25 mm above the rotary axis, due to tilt motion of the axis, for the Xradia Micro-XCT.

### FY2008 Proposed Work

For FY2008, we will use the sensitivity information from the error budgets to choose characteristic artifacts to validate the error budget predictions. These artifacts will be measured on both CMM and NDE tools to create validated error budgets for the Xradia Micro-XCT and Laser UT. These quantitative error budgets will be used to state uncertainties in dimensional measurements and will lead to improved uncertainties in future generations of these instruments.

# Uncertainty Analysis with Inspection Shop Measurements



Walter W.  
Nederbragt

(925) 424-2807  
nederbragt1@llnl.gov

The LLNL inspection shop is chartered to make dimensional measurements of components for critical programmatic experiments. These measurements ensure that components are within tolerance, and provide geometric details that can be used to further refine simulations. For these measurements to be useful, they must be significantly more accurate than the tolerances that are being checked. For example, if a part has a specified dimension of 100 mm and a tolerance of 1 mm, then the precision and/or accuracy of the measurement should be less than 1 mm. Using the “10-to-1 gagemaker’s rule of thumb,” the desired precision of the measurement should be less than 100  $\mu\text{m}$ . Currently, the process for associating measurement uncertainty with data is not standardized, nor is the uncertainty based on a thorough analysis.

The National Institute of Standards and Technology (NIST) has developed methods for analyzing measurement uncertainty. Figure 1 shows the key factors



Figure 2. The Z-Mike measurement instrument, which uses a laser to measure diameters and lengths.

that influence measurement uncertainty. This project aims to augment the efforts within the LLNL inspection shop with a standardized and commensurately rigorous approach to determining and reporting uncertainty.

During FY2006, a fundamental understanding of inspection shop operations and equipment was gained so that measurement uncertainty analysis could proceed in FY2007.

## Project Goals

The goal of this project is to begin providing measurement uncertainty statements with critical measurements performed in the inspection shop. To accomplish this task, comprehensive knowledge about the underlying sources of uncertainty for measurement instruments need to be understood and quantified. Moreover, measurements of elemental uncertainties for each physical source need to be combined in a meaningful way to obtain an overall measurement uncertainty.

## Relevance to LLNL Mission

The measurements being made by the inspection shop are used to make decisions about accepting or rejecting critical parts. The inspection shop is widely used and the measurements are typically accepted as being “sufficiently” accurate. This assumption should be verified by a measurement uncertainty analysis, which is the accepted practice at all of the other NNSA sites. There is a significant risk to Laboratory programs if measurement data is in error, which could lead to the use of components in experiments that are outside of specifications.

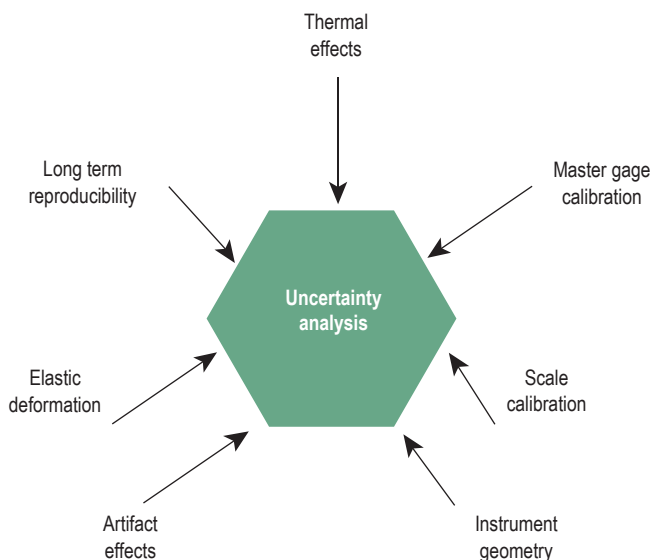


Figure 1. Schematic of the many factors that influence the uncertainty of a measurement.

### FY2007 Accomplishments and Results

During FY2007, four milestones were met: the reports written in FY2006 were finalized; a tutorial on uncertainty analysis was given to the inspectors in the inspection shop; an uncertainty analysis was performed on the inspection shop's Z-Mike measurement instrument; and an uncertainty analysis was performed on the inspection shop's four Coordinate Measurement Machines (CMMs).

The Z-Mike measurement instrument (Fig. 2) is a new instrument in the inspection shop for measuring diameters and lengths using a laser. Reproducibility data was collected on the Z-Mike instrument; this data was analyzed and an uncertainty analysis was completed using the methods described in the references.

Applying this same analysis method to the four CMMs in the inspection shop would be extremely cumbersome; hence, a different method was used. A commercial vendor has created a CMM program that uses algorithms developed at NIST to analyze the measurement uncertainties associated with the measurement of specific part features/geometries. Using this program, a generic part with common geometric features was input into the program along with the inspection shop's CMM calibration data, probe data, and temperature data. Using the data, the program created uncertainty reports for each part feature (Fig. 3). The analysis shows that the performance of the four CMMs in the inspection shop varies considerably (Fig. 4). This result is not a surprise, but it does show the importance of choosing the correct metrology tool when making a critical measurement.

### Related References

1. Doiron, T., and J. Stoup, "Uncertainty and Dimensional Calibrations," *Journal of Research of the National Institute of Standards and Technology*, **120**, 6, pp. 647-676, 1997.
2. Taylor, B. N., and C. E. Kuyatt, "Guidelines for Evaluating and Expressing the Uncertainty of NIST Measurement Results," *National Institute of Standards and Technology, Technical Note 1297*, 1994.

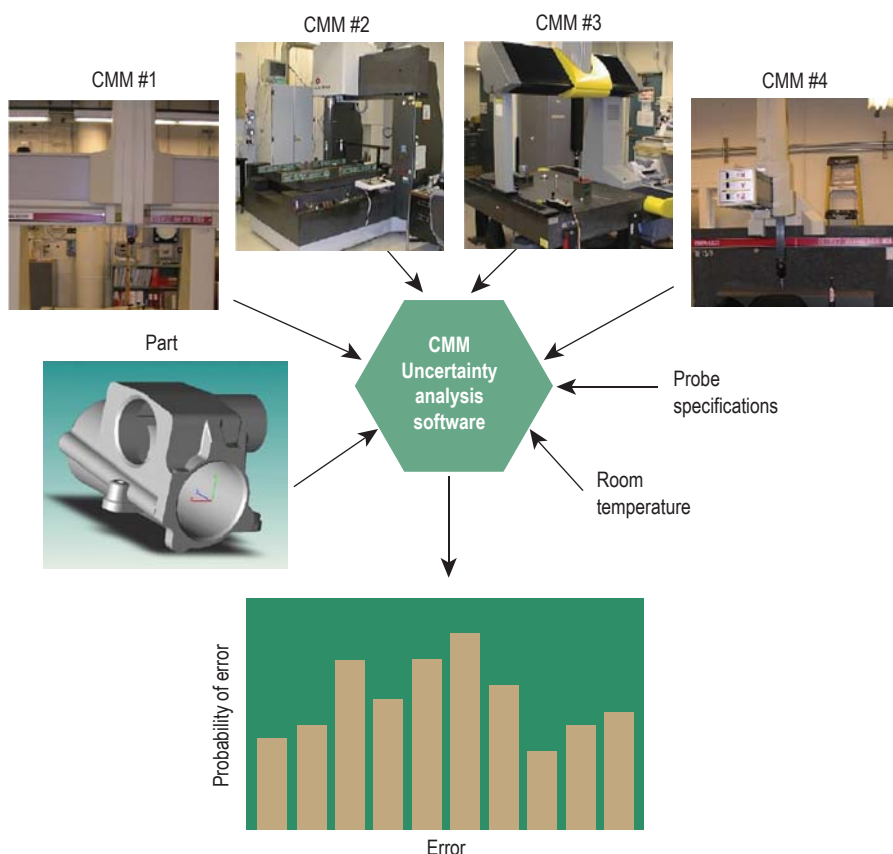


Figure 3. Performance analysis of CMMs. The software creates a report detailing the uncertainty of each feature measurement on each part for each CMM.

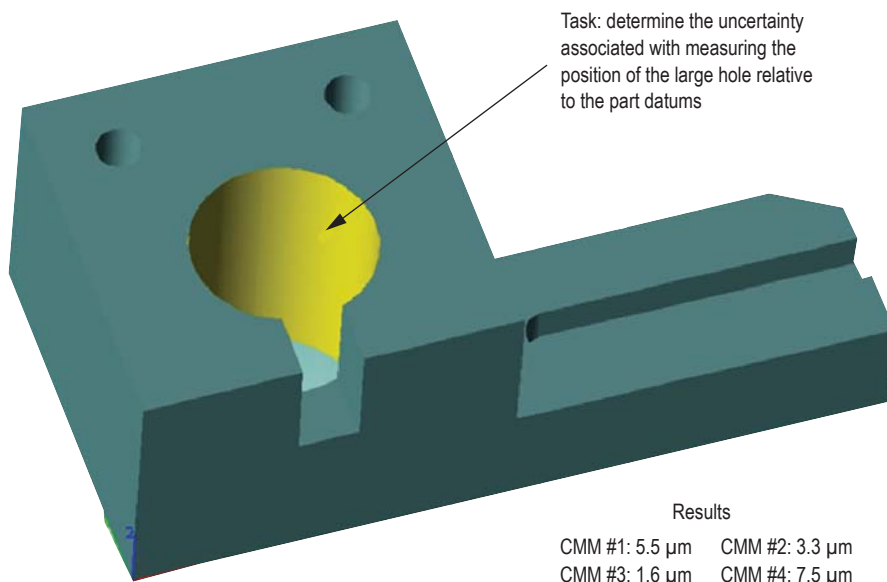


Figure 4. Uncertainty results for the four inspection shop CMMs when measuring the position of a hole using the uncertainty analysis software.

# X-Ray System Modeling



*William D.  
Brown*  
(925) 422-7933  
brown197@llnl.gov

**W**e are implementing a forward model for x-ray system response that will enable us to predict the capability of our systems and allow us to choose optimal system parameters. The system model will include the major components of a system: x-ray producing source, photon transport, and detector. The modeled components will be used in conjunction with an LLNL software program, HADES, to model the complete system.

## Project Goals

The overall project goal is to model the x-ray source, detector and x-ray transport of the Micro-XCT Xradia system and compare it to a known sample. The modeling techniques can later be expanded to other x-ray systems with different x-ray sources, detectors, and transport characteristics. The Xradia system uses a 150-kV Hamamatsu Brehmstrahlung source and a CsI scintillator mechanically coupled to a microscope objective. The microscope objective is

optically coupled to a scientific grade cooled CCD camera. We will compare the modeled x-ray spectrum, detector, and x-ray transport to a previously imaged double-shell Omega target that is used for high-energy-density physics (HEDP) experiments.

## Relevance to LLNL Mission

A forward model for system response will enable us to better perform experiments for WCI, NIF and Global Security (GS).

## FY2007 Accomplishments and Results

The first task was to create a model for the Brehmstrahlung source. We used Monte Carlo N-Particle (MCNP) to model the x-ray source. The Hamamatsu source is a conventional tungsten anode micro-focus system with a Brehmstrahlung continuous spectrum and characteristic K- and L-lines. The modeling parameters for the source were chosen from the parameters used to image the double-shell Omega targets. These parameters include

a 100-kV potential and a tube current of 40  $\mu$ A. The focal spot of the source at the 100-kV potential is 7  $\mu$ m<sup>2</sup> nominal. To validate the source model, measured data were obtained from an identical source using a high-purity germanium detector.

Figure 1 compares the model spectra and the measured data. The figure indicates the measured spectra  $E < 20$  keV has less flux than the model. This could indicate possible inherent filtering in the x-ray source that was not attributed to the model. The three K-lines (58, 59 and 67 keV) correspond correctly in the model and measured data. However, the intensity of the modeled lines is greater. The 9-keV L-line is barely evident in the measured data. This may be due to inherent source filtration.

To model the x-ray energy deposited in the Xradia CsI scintillator we used MCNP. The MCNP calculations were used to compute the scintillator blur function and the DQE. To validate the detector model, Modulation Transfer Functions (MTF) for the model and measured data were to be compared, but we were unable to obtain the modeled MTF in time. Future efforts would include modeling the MTF and comparing with measured results.

The sample modeled was the HEDP Omega double-shell (DS) target, consisting of two concentric shells. The outer shell is a CH (Br-doped) ablator consisting of upper and lower hemishell components that are joined together with an S-shaped step joint. Because of the complexity of the step joint, the model assumes a uniform ablator without the joint. The inner shell is made of glass, and is held in place within the outer shell with 50-mg/cm<sup>3</sup> SiO<sub>2</sub> aerogel. The HADES software, incorporates the source and detector models with its ray tracing techniques to output a radiographic model of the sample.

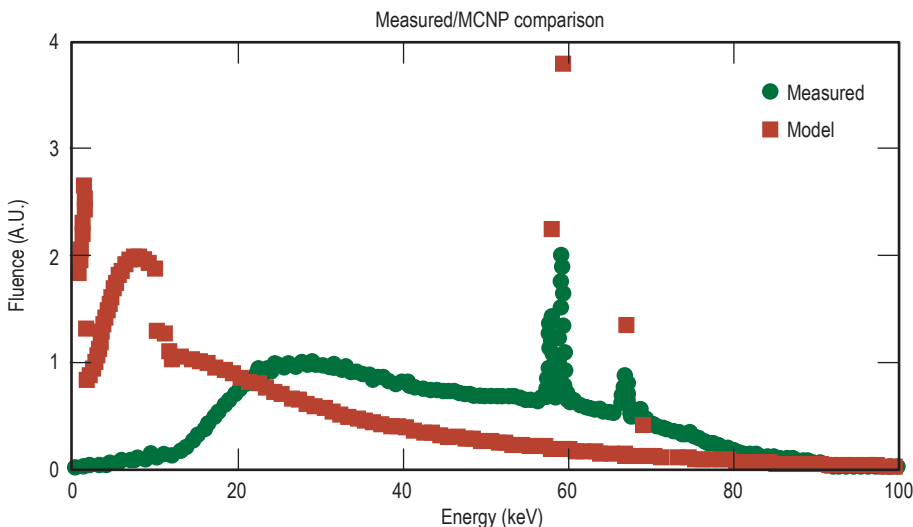


Figure 1. Comparison of x-ray source model and measured spectra.

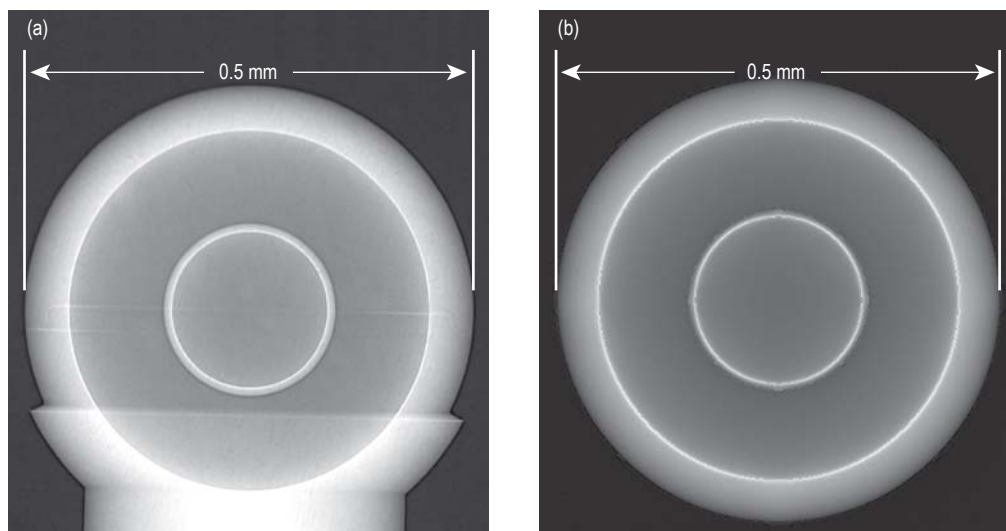


Figure 2. (a) Double-shell digital radiograph; (b) model. (The pedestal in (a) was not modeled in (b)).

Source blurring and detector resolution are computed for each energy bin of the spectra. The total intensity is computed from the sum of the doses at each DQE-weighted energy bin.

Figure 2 shows a Micro-XCT digital radiograph using 0.6- $\mu\text{m}$  pixel pitch of the double-shell target and a HADES simulated radiographic model. A qualitative comparison of the images shows a close comparison in resolution and contrast. Figure 3 shows a lineout through the ablator, aerogel, and inner glass sphere of the radiograph measurement and model. The lineouts of the model were obtained with and without adding the characteristic

lines. The model, both with and without lines, shows a stronger phase effect at material transition than is measured. Overall, a comparison of the model and measured data present a close agreement.

### Related References

1. Aufderheide, M. B., *et al.*, "Analysis and Modeling of Phase Contrast Radiography of Gradient Density Laser Targets," Symposium on Radiation Measurements and Applications, Ann Arbor, Michigan, May 23-25, 2006.
2. Brown, W. D., and H. E. Martz, Jr., "X-ray Digital Radiography and Computed Tomography of ICF and HEDP Materials, Subassemblies and Targets," Digital Imaging IX,

An ASNT Topical Conference, Mashantucket, Connecticut, July 24-26, 2006.

3. Hibbard, R. L., *et al.*, "Precision Manufacturing of Inertial Confinement Fusion Double Shell Laser Targets for OMEGA," *Fusion Science and Technology*, **45**, 2, pp. 117-123, 2004.
4. Martz, Jr., H. E., and G. F. Albrecht, "Non-destructive Characterization Technologies for Metrology of Micro/Mesoscale Assemblies," *Proceedings of: Machines and Processes for Micro-scale and Mesoscale Fabrication, Metrology, and Assembly*, American Society for Precision Engineering, Raleigh, North Carolina, pp. 131-141, 2003.
5. Xradia website: <http://www.xradia.com>.

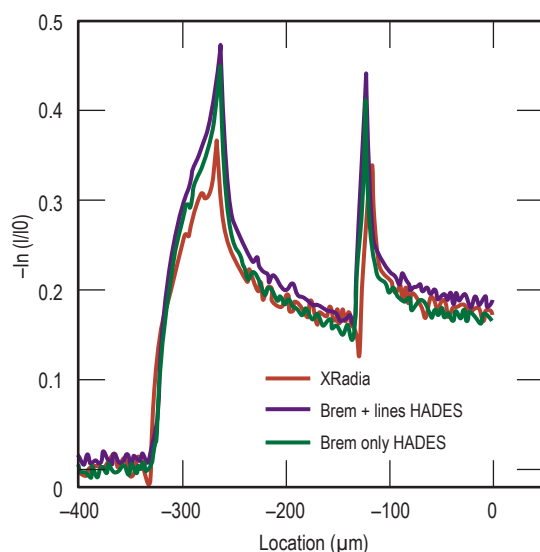


Figure 3. Lineouts as shown in Fig. 2 across ablator, aerogel, and inner shell.

### FY2008 Proposed Work

Additional work is needed to compare the MTF of the model with the empirical MTF from the Xradia system. The MTF comparison will allow us to quantitatively compare the contrast and spatial resolution of the model and empirical data. In addition, we need to expand the modeling to other x-ray sources up to 450 kV, additional detectors and finally full systems.

# Detection, Classification, and Estimation of Radioactive Contraband from Uncertain, Low-Count Measurements



James V. Candy  
 (925) 422-8675  
 candy1@llnl.gov

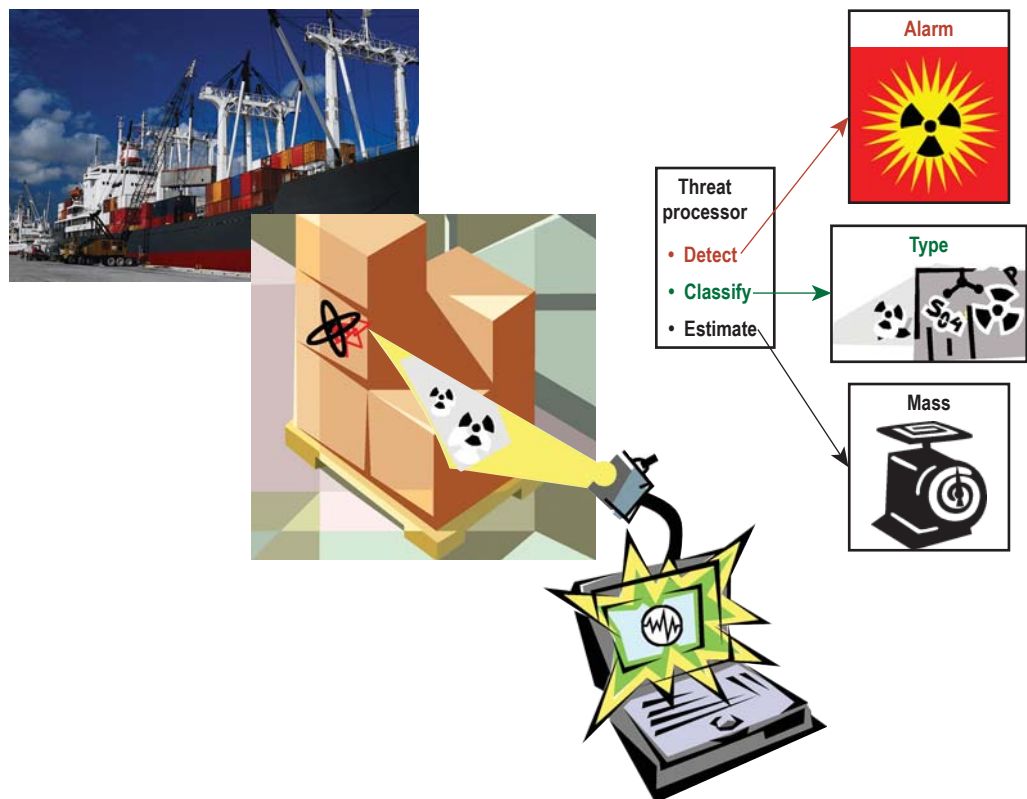
The detection of radioactive contraband smuggled into our nation is a serious national security issue. The objective of this project is to investigate fast, reliable radiation detection methods capable of making a more rapid decision with higher confidence along with the ability to quantify performance. Today's high-speed, high-throughput computers enable physics-based statistical models that capture essential signatures of radionuclides and incorporate them into a Bayesian sequential scheme capable of online, near real-time operation. This project is focused on the detection, classification, and estimation of illicit radioactive contraband from highly uncertain, low-count radionuclide measurements using a statistical approach based on

Bayesian inference and physics-based signal processing, as illustrated in Fig. 1 for a cargo scanning application.

## Project Goals

We expect to develop solutions for the detection, classification, and estimation of a moving radionuclide source and/or detector. Our goal is to reliably detect kilograms of shielded Pu with a 95% detection probability at a 5% false alarm rate in less than a minute. The Bayesian approach enables the development of a sequential framework establishing the foundation for future problems that are both time- and space-varying or equivalently statistically nonstationary.

Figure 1. A scenario of high importance in National Security: the processing of gamma-ray measurements for cargo containers using detection instrumentation along with sophisticated Bayesian processing techniques to detect, classify and estimate illicit radionuclides.



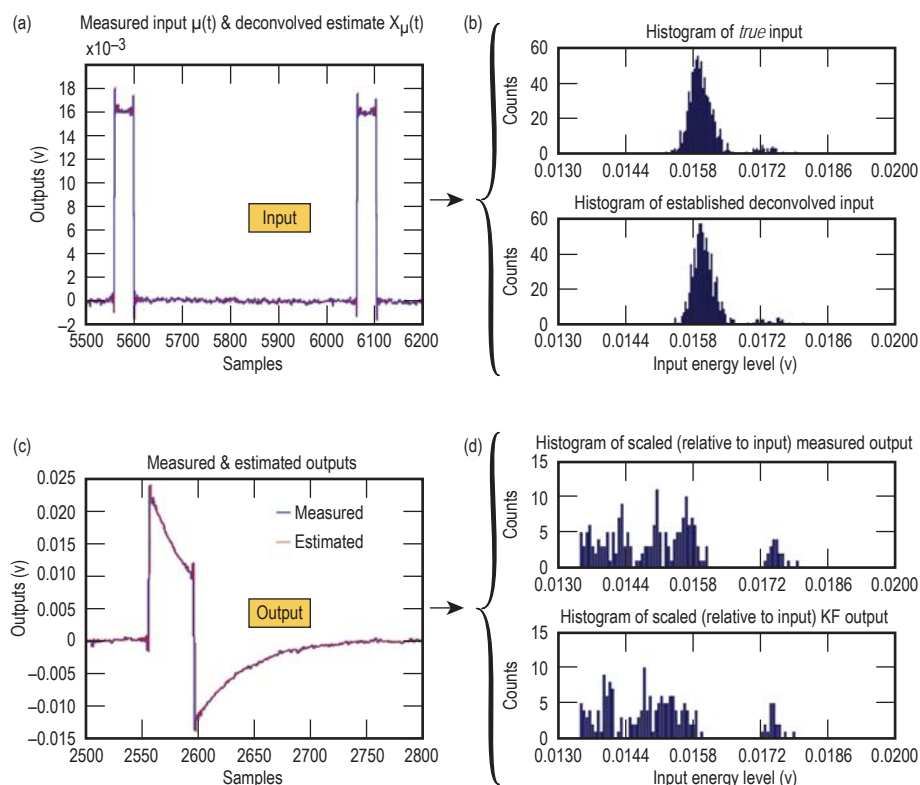


**Figure 2.** Bayesian deconvolution processor outputs from experimental data: (a) actual test input excitation pulse sequence and estimated (deconvolved) input (overlaid) to the preamplifier; (b) true and estimated (deconvolved) input excitation histograms; (c) measured and estimated preamplifier outputs; (d) measured and estimated output histograms.

### Relevance to LLNL Mission

The detection of illicit radionuclides is a top priority in furthering the national security mission of the Laboratory. Radionuclide detection, classification, and estimation are critical for detecting the transportation of radiological materials by terrorists, an important goal in both national and international security. This technology also supports the life extension program because of its potential application in defect detection.

### FY2007 Accomplishments and Results

Our FY2007 accomplishments included:

1. development of a radionuclide signal processing model (mathematically) by decomposition into monoenergetic sources;
2. incorporation of these embedded physics-based models into a sequential Bayesian processor;

3. validation through simulation/experiments;
  4. application to known controlled experimental data; publication of the results demonstrating the capability of the Bayesian processor to extract the unknown input (deconvolution) from measured radiation data (Fig. 2); and
  5. publication of a record of invention describing the initial detection/classification system design.
- Having just started this effort at mid-year we have performed the initial planned tasks of:

1. sophisticated modeling using COG, a Monte Carlo code developed at LLNL, for a variety of well-known radionuclides;
2. controlled experiments;
3. development of the required signal processing models such as instrumentation and detectors; and

4. development of sequential Bayesian processors for a high-purity germanium (HPG) detector.

We expect to finish similar runs for sodium-iodide detectors as well.

These results are quite promising and demonstrate the potential capability of the Bayesian model-based approach to solving a variety of radiation detection problems.

### Related References

1. Candy, J. V., "Nonlinear Statistical Signal Processing: A Particle Filtering Approach," *Imaging for Detection and Identification*, J. Byrnes (Ed.), Springer, pp. 129-150, 2007.
2. Candy, J. V., "Bootstrap Particle Filtering," *IEEE Signal Process. Magaz.*, **24**, 4, pp. 73-85, 2007.
3. Candy, J. V., K. Sale, B. Guidry, D. Manatt, and A. Meyer, "Bayesian Processing for the Detection of Radioactive Contraband from Uncertain Measurements," *IEEE Computational Advances in Multi-Channel Sensor Array Processing Proc.*, pp. 49-52, 2007.
4. Sale, K., J. V. Candy, B. Guidry, D. Manatt, and A. Meyer, "A Bayesian Signal Processor Approach to Spectroscopic Portal System Measurements," *Proc. S.P.I.E.*, pp. 670701-670723, 2007.

### FY2008 Proposed Work

Our proposed work for FY2008 consists of completing the sodium-iodide experiments and initiating a set of validated (based on our experiments) COG simulations to design the Bayesian processor incorporating more and more of the physics. Here we plan to incorporate more of the transport physics into the processor and begin to validate and refine our initial design concepts.

# Terahertz Spectroscopic Imaging for Standoff Detection of High Explosives



Michael W. Burke  
(925) 422-0192  
burke22@llnl.gov

**R**<sup>DX</sup> (1,3,5-trinitro-1,3,5-triazacyclohexane), a component in plastic explosives, including C-4 and Semtex-H, is extremely difficult to detect using air sampling due to its low vapor pressure (10 ppt). This project is examining the feasibility of using terahertz (THz) radiation in the standoff detection and identification of this high explosive (HE) compound. Our approach uses emerging spectroscopic and imaging technologies in the THz frequency regime. We propose to first develop a system-level analysis, a system simulation, and an experimental program.

The THz portion of the electromagnetic (EM) spectrum is rich with spectroscopic information about small- and medium-size molecules. RDX-based HE exhibit a distinctive sub-THz signature near 800 GHz that distinguishes them

from common background materials (Fig. 1). Since THz radiation can penetrate common dielectric concealants (e.g., fabrics and leather), and provides reasonable spatial resolution for imaging applications, spectral imaging near 800 GHz may provide a solution to the RDX detection problem.

Our primary goal is to assess the utility of THz spectral imaging for the detection of concealed, RDX-based explosives, for reliable RDX screening of people at safe (30- to 50-m) standoff distances. Our approach is to develop a systems concept and multispectral detection algorithms, and simulate the behavior of such a system in the presence of atmospheric absorption, obscurant losses, and system noise. Our final goal is to demonstrate detection of RDX-based explosives at 30 to 50 m through a concealing material, using multispectral imaging.

The algorithm is a two-channel approach that compares the return signal from two points on a target to remove the effects of the intervening atmosphere (Fig. 2), and then compares the return signals to a database of spectral signatures. Our strategy is to collect THz spectral data for materials of interest from both experiments and the literature, and combine it with systems analysis and simulation to assess the viability of the remote sensing capability.

## Relevance to LLNL Mission

Explosives detection that enables the interdiction of terrorists is an important capability for LLNL's missions in both national security and homeland security.

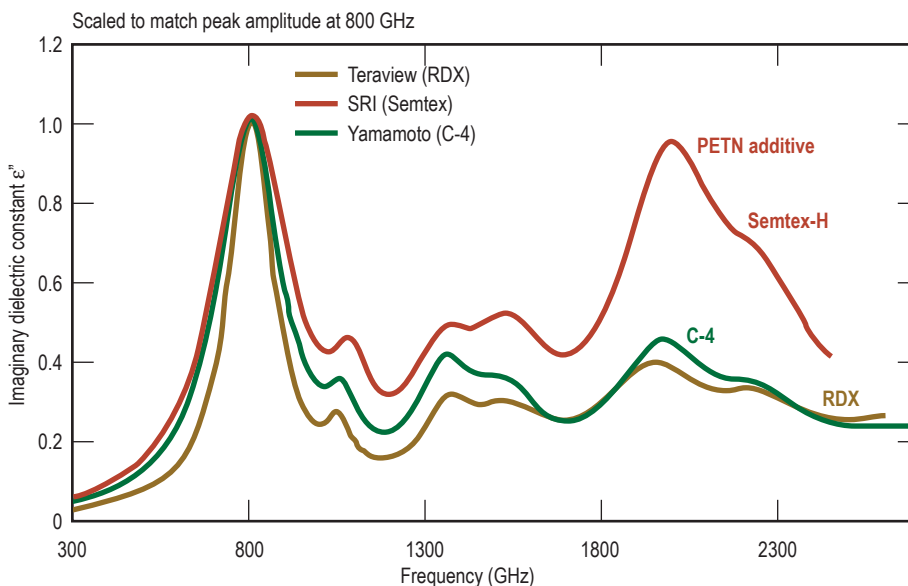
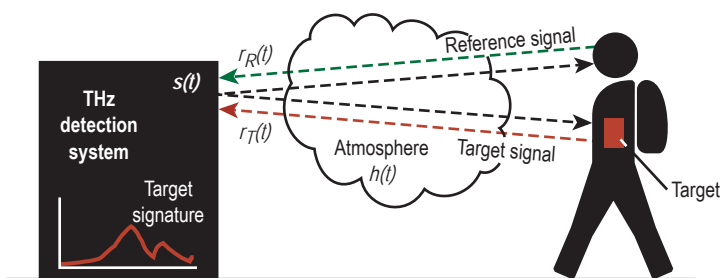


Figure 1. RDX-based HE signature. A distinctive sub-THz signature near 800 GHz distinguishes them from common background materials.



**Figure 2.** Two-channel approach. The return signals from two points on a target are compared to remove the effects of the intervening atmosphere. The return signals are then compared to a database of spectral signatures.

### FY2007 Accomplishments and Results

In FY2007, we developed a systems concept (link budget) and supporting algorithms for standoff THz spectral imaging. In particular, we: 1) completed collection of THz data on common HE materials; 2) developed a systems concept and link budget for a THz spectral imager; 3) developed supporting algorithms for THz spectral imaging; and 4) executed several Monte Carlo simulations of system performance.

The algorithms developed were for deconvolving the spectral modifications induced by atmospheric propagation. We simulated the performance of this

system using atmospheric absorption data from HITRAN (a standard database of atmospheric absorption properties), and material parameters we obtained.

Results of these simulations show the proposed system can achieve detection of bulk HE at safe standoff distances (~30 to 50 m), even when the explosive is concealed by a few layers of fabric. Simulated receiver operation characteristic curves, which show the probabilities of detection and false alarm, show excellent discrimination of C-4 against innocuous materials such as skin and lactose (Fig. 3).

### Related References

1. National Academy of Sciences, Existing and Potential Standoff Explosives Detection Techniques, National Academies Press, 2004.
2. Woolard, D. L., E. R. Brown, M. Pepper, and M. Kemp, "Terahertz Frequency Sensing and Imaging: A Time of Reckoning Future Applications?" *Proc. IEEE*, **93**, pp. 1722-1743, 2005.
3. Yamamoto, K., *et al.*, "Noninvasive Inspection of C-4 Explosive in Mails by Terahertz Time-Domain Spectroscopy," *Jap. J. Appl. Phys.*, **43**, L414, 2004.
4. Bjarnason, J. E., *et al.*, "Millimeter-Wave, Terahertz, and Mid-Infrared Transmission Through Common Clothing," *Appl. Phys. Lett.*, **85**, p. 519, 2004.

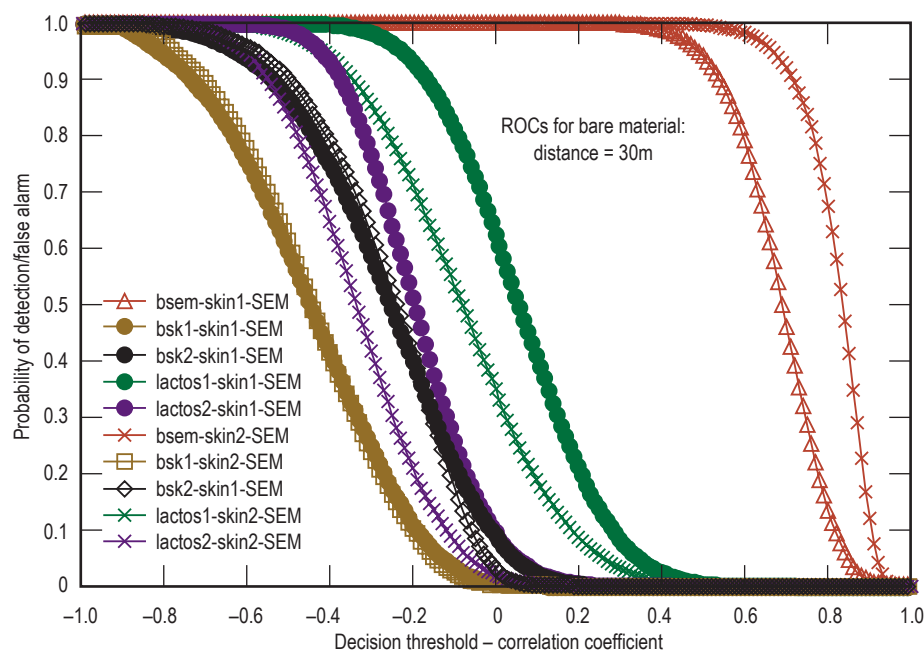


**Figure 3.** ROC-type curves for different targets (HE, skin, and lactose interferents), no covering material, at 30 m standoff. Skin 1 and 2 and lactose 1 and 2 are four different targets differing in their spectral reflectance.

### FY2008 Proposed Work

In FY2008 we will seek outside funding to verify experimentally our algorithms for spectral detection of RDX in the presence of atmospheric losses and concealants. We will first explore near-THz (800 to 900 GHz) imaging at the necessary standoff distances; then, if results are favorable, extend measurements to two lower frequency bands to obtain the required multispectral coverage.

# Application of Laser-Based Ultrasound to Glovebox Enclosed Materials



*Robert Huber*  
(925) 424-2002  
huber5@llnl.gov

**W**e have investigated laser-based ultrasound applied to materials enclosed in gloveboxes or other types of enclosures. Applications include materials at elevated temperatures in furnaces, radioactive materials in gloveboxes and materials being joined in welding enclosures. Laser-based ultrasound is ideal for these remote applications because the technique does not require contact with the surface, and the laser beams can be transmitted through windows.

## Project Goals

The main goal for this project is to perform initial studies to determine if laser-based ultrasound could be applied to materials important to LLNL, inside an enclosed laser welding station. Two main questions are to be answered by this project: 1) how well does ultrasound propagate in materials that are currently being welded by a laser welding process; and 2) will glovebox windows significantly affect the signal-to-noise

ratio of the ultrasound generated and detected using laser-based systems?

## Relevance to LLNL Mission

Joining technologies such as welding remain critical to manufacturing critical components at LLNL, which has state-of-the-art laser welding facilities. Nondestructive evaluation of the welds using a technique such as laser-based ultrasound can ensure that the welds meet the requirements. Provided that laser-based ultrasound can be used through the windows of a laser welding station, the potential exists for process control whereby the ultrasonic signal can determine when the appropriate welding depth has been reached.

## FY2007 Accomplishments and Results

Contact ultrasonic tests (UT) were performed on vanadium (Va) and titanium (Ti) plates. These plates were the same alloys and the same thicknesses currently being welded in the LLNL

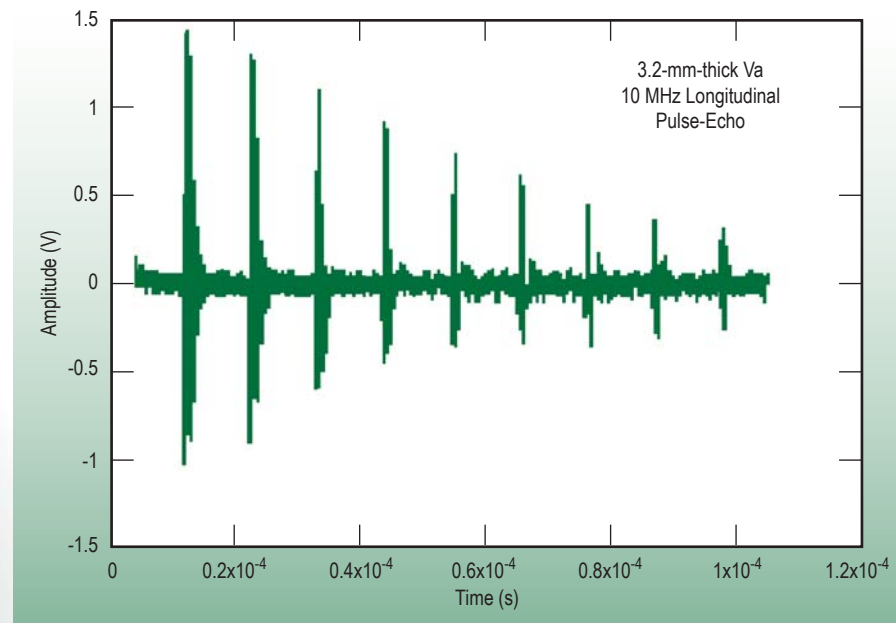


Figure 1. Amplitude vs. time trace in Va using a contact UT.

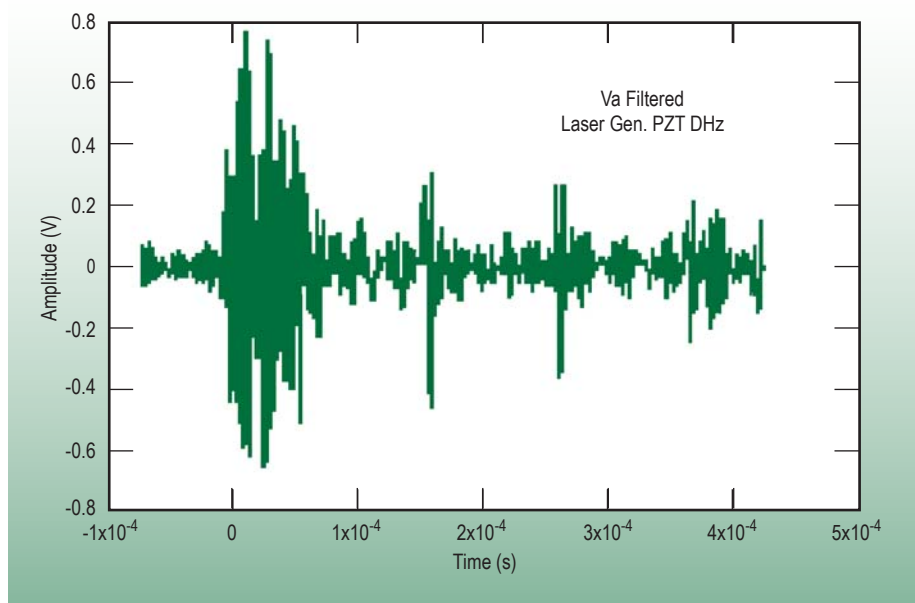


Figure 2. Laser generated ultrasound and contact detected in VA through a glovebox-like window.

laser welding stations. The piezoelectric transducers chosen for these tests had center frequencies of 10 MHz. For both of the materials, 10 MHz has a wavelength of approximately 0.6 mm, and should be sufficient to see voids or cracks on the order of 0.3 mm. The 10-MHz ultrasound propagated very well through the plates with very little attenuation, demonstrating that fairly

high frequency ultrasound could be used for characterization of parts made from the Va and Ti alloys.

Figure 1 shows a typical amplitude vs. time ultrasound trace for the Va sample. Next, a through transmission test was set-up, whereby a pulsed laser was used to generate ultrasound in the plates, and a piezoelectric transducer was used to detect the ultrasound. This

setup allowed a silica window, similar to those used in the welding station, to be placed in front of the sample on the side being hit by the pulsed laser to look for a reduction in signal-to-noise over the case when no window was present. The drop-off in signal level was negligible.

Figure 2 shows a laser generated signal obtained in Va. At this point, it was clear that laser-based ultrasound could indeed be applied to the Va and Ti materials being welded at LLNL.

The final tests involved laser-based detection. Since the materials as welded have smooth but not specularly reflecting surfaces, tests using a low laser power Michelson interferometer had a very low signal-to-noise ratio. Photorefractive interferometers, unlike Michelson interferometers, can work with somewhat diffusely reflecting surfaces and are more suitable for diffuse surfaces.

Figure 3 shows a signal-averaged waveform obtained using the photorefractive interferometer. A contact transducer was used to generate the waveform in Fig. 3. This particular test was not done through a window.

This project shows the potential for the application of laser-based ultrasound to Va and Ti alloys of interest to LLNL in laser welding stations.

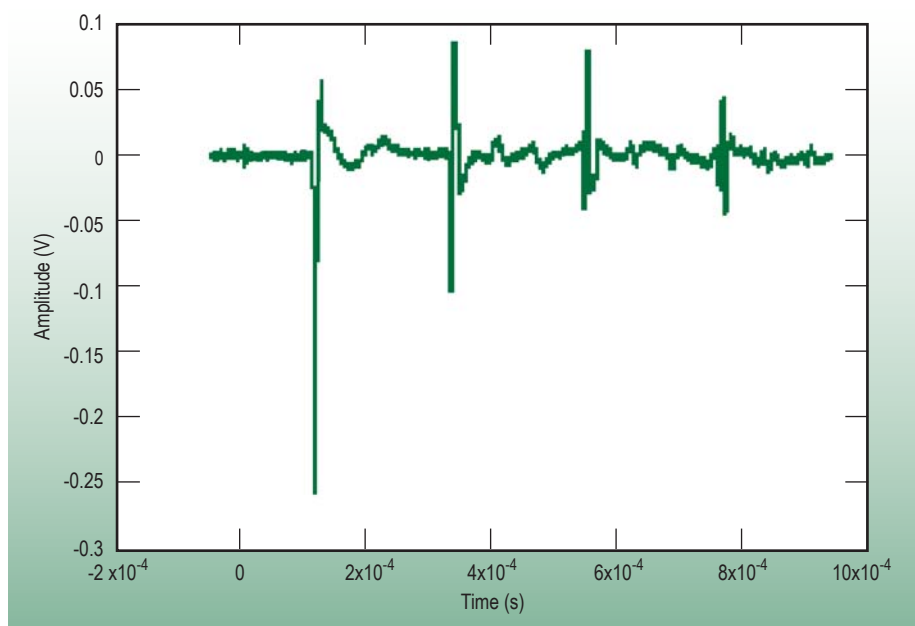


Figure 3. Contact transducer generated UT and detection of ultrasound using photorefractive interferometer.

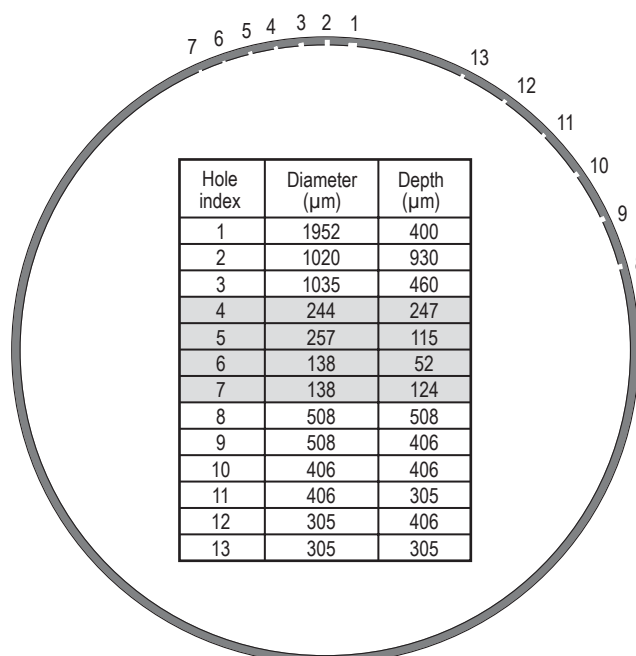
# Defect Detection in Large CT Image Sets



Douglas N. Poland  
(925) 422-4980  
poland1@llnl.gov

This image analysis project has constructed a tool for performing computer-assisted detection of small voids in CT data sets of metal components. We first constructed algorithms using known approaches and measured their performance on a test object, described below. Noise reduction and void detection algorithms based on mathematical morphology demonstrated good performance on the test object and excellent performance on a small but diverse collection of programmatic data sets that had been previously analyzed manually. Implementation issues, such as handling large data sets and automated parameter selection, have been explicitly addressed in the course of working with these data. The result is a standalone C++ application, delivered to the enhanced surveillance program that directs a tomography analyst's attention to candidate void regions in large data sets.

**Figure 1.** Tungsten ring test object, a cylinder with 13 holes drilled into its inner surface. This cutaway sketch shows the hole locations, while the table lists their sizes. Note that in the images used for this work, holes #4 through #7 are very difficult to impossible to detect manually. They are not found by our algorithms.



## Project Goals

The enhanced surveillance program will produce CT data sets that are up to several thousand voxels on a side (*i.e.*, 8000 x 8000 x 8000). The current method of analysis requires a tomographer to view sequences of several thousand images, where each image occupies several computer screens at full resolution. One of the primary objectives is to identify voids of any size. The work of searching for voids at the resolution limit of the system is extremely demanding and tedious in these data sets. The goal of this project is to create a tool that will reduce these data sets to a ranked set of candidate voids that can be quickly validated or rejected by the tomographer; the broader goal is to strengthen the dialog and technical exchange between tomography and image analysis experts so that emerging image analysis issues can be effectively addressed.

The enhanced surveillance program uses a tungsten ring with holes drilled into it (Fig. 1) to study the ability of their systems and analysts to detect small voids

in metal parts. Of the 13 holes in this ring, 9 (ranging from 305 to over 1000 mm in diameter) are well resolved by the CT system and are readily discernible in the processed CT data (the remaining 4 are less than 300 mm in diameter). One key success metric is that our algorithm must place these 9 voids at the top of our ranked list of candidate voids.

## Relevance to LLNL Mission

This project has produced a tool that will increase the efficiency of enhanced surveillance program tomography analysts by focusing their attention on suspect voids in a given data set, thereby allowing them to forego an exhaustive search of many thousands of screens of largely defect-free data. This tool could also make these data sets more accessible to other technical staff, who may not be tomography experts, by performing necessary preprocessing and quickly guiding them to regions with suspect voids. This application should be generally applicable to the detection of small defects (*i.e.*, voids and inclusions) in homogeneous media.

## FY2007 Accomplishments and Results

We accomplished four interrelated tasks in FY2007: 1) algorithm testing and refinement using programmatic data sets; 2) automated parameter selection; 3) implementation in C++; and 4) identification of issues that warrant future work. We have delivered a standalone C++ application that effectively focuses an analyst's attention on localized anomalies in large grayscale 3-D CT data sets.

In the course of testing with these data sets, we have refined the way that we calculate ranking metrics for candidate voids, using, for example, a contrast calculation that handles region boundaries (Fig. 2). Our revised volume-weighted contrast ranking performs well on the tungsten ring defects (9 detected

holes ranked in order of decreasing size, with the most conspicuous false alarm ranked number 10 (Fig. 3).

We have implemented a minimum entropy approach to calculating the void detection threshold parameter, and also a second threshold to yield a more complete void reconstruction (Fig. 4). We have also achieved a 4x speedup, as well as portability and improved data and memory management, with our optimized C++ implementation leveraging published methods.

### Related References

1. Haralick, R., S. Sternberg, and X. Zhuang, "Image Analysis Using Mathematical Morphology," *IEEE Transactions on Pattern Analysis and Machine Intelligence*, **9**, pp. 532-550, 1987.
2. Rosenberg, A., and J. Hirschberg, "V-Measure: A Conditional Entropy-based Cluster Evaluation Measure," *Proceedings of the 2007 Joint Conference of Empirical Methods in Natural Language Processing and Computational Natural Language Learning*, Prague, pp. 410-420, June 2007.
3. van Herk, M., "A Fast Algorithm for Local Minimum and Maximum Filters on Rectangular and Octagonal Kernels," *Patt. Rec. Letters*, **13**, pp. 517-521, 1992.
4. Bloomberg, D., "Implementation Efficiency of Binary Morphology," *International Symp. for Math. Morphology VI*, Sydney, Australia, April 3-5, 2002.
5. van den Boomgard, R., and R. van Balen, "Methods for Fast Morphological Image Transforms Using Bitmapped Images," *Computer Vision, Graphics, and Image Processing: Graphical Models and Image Processing*, **54**, pp. 254-258, May 1992.

### FY2008 Proposed Work

We have identified ideas for future work that may lead to enhanced detection sensitivity and false alarm rejection by performing more sophisticated true and false positive characterization (e.g., classification techniques operating on shape, density, texture, and other features in both the candidate defect and surrounding background regions).

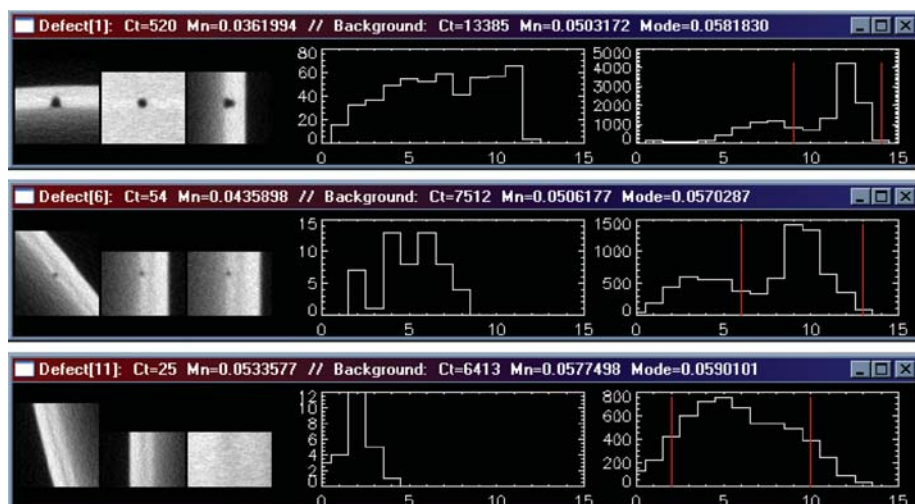


Figure 2. Three candidate defects ranked 1, 6 and 11 by the detection code. For each defect we display (from left to right): x-y, x-z and y-z views; defect voxel intensity histogram; and immediate background voxel intensity histogram. Defects 1 and 6 are true positives, (corresponding to holes #2 and #11 from Fig. 1, respectively) that occur on a region boundary. Their background histograms are bi-modal, with the relevant background intensity captured by the primary mode (defined by the vertical red lines that are generated automatically). Using this primary mode in the contrast calculation improves the ranking metric. The size of the W ring CT data set is 1908 x 1908 x 56. The thumbnails shown are all 64 voxels on a side, displayed at full resolution.

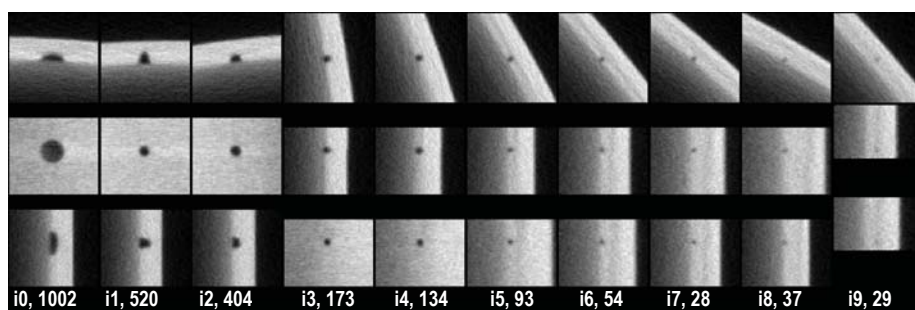


Figure 3. The top 10 ranked tungsten ring candidate defects (in 10 columns above) produced by our application. Rank proceeds from left to right, with x-y, x-z and y-z views (top to bottom) shown for each candidate.

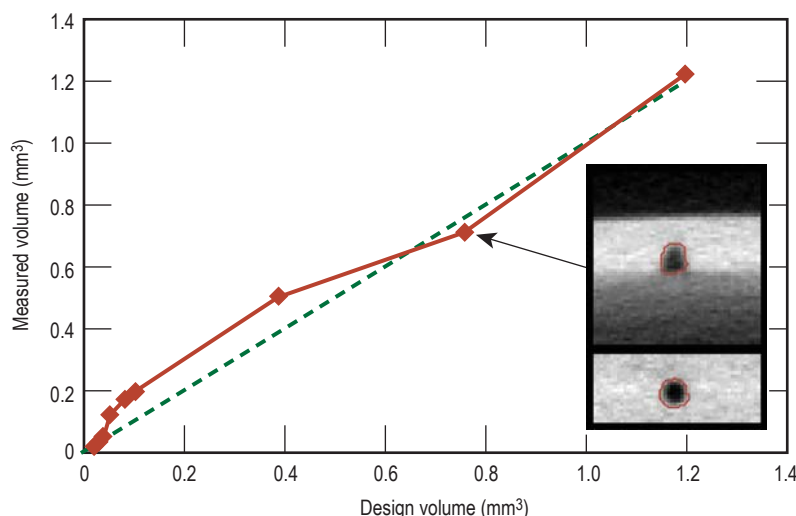


Figure 4. Plot of measured tungsten (brown line) defect volumes vs. design (green dashed line) volumes. Measured volumes were calculated using "double-threshold" morphological reconstruction.

# The Structure and Properties of Nanoporous Materials



Anthony  
Van Buuren  
(925) 423-5639  
vanbuuren1@llnl.gov

**O**ur goal is to quantify the microstructure of highly porous materials, and to determine how processing of the porous material relates to the structure and ultimately to the mechanical behavior. We will quantify structural changes with a combination of small angle x-ray scattering (SAXS) and high-resolution x-ray tomography. Finite element modeling, using the structures determined above, will be used to study how a change in pore structure effects mechanical properties.

## Project Goals

We plan to make SAXS measurements to understand the effect of synthesis conditions on the change in structure. In particular we are interested in how synthesis may affect the amount of mass at the nodal points in the aerogel and then provide feedback for improved processing to control strength (network morphology), uniformity, and density.

We will characterize the pore structure of metal oxide foams immersed in a cryogenic fluid. Knowledge of how the aerogel wets in a cryogenic fluid is unknown but it is needed information if these foams are to be used in laser targets.

We will use finite element modeling to study the effects of mechanical loading on the cell structures, and to map out relationships among processing, density, and strength.

We will determine the extent of any anisotropy in lattice architecture, and improve spatial resolution to examine and characterize graded density structures.

## Relevance to LLNL Mission

This project develops critical experimental technologies for many LLNL applications. A key deliverable will be the ability to predict the mechanical properties of nanoporous materials and characterize gradient density foam microstructures for future laser targets.

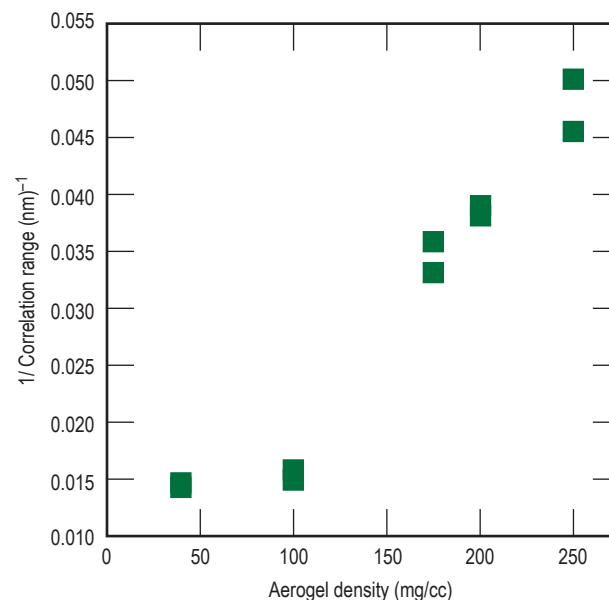


Figure 1. Change in the correlation range (pore diameter) measured by SAXS as a function of  $Ta_2O_5$  aerogel density.

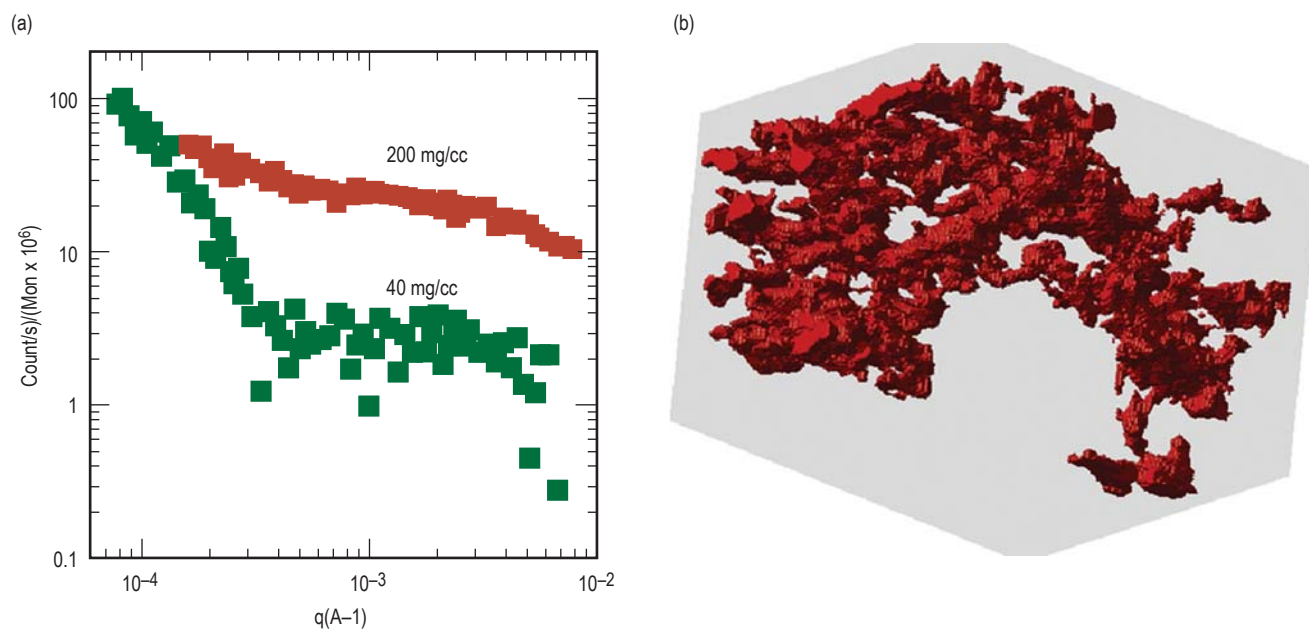


Figure 2. (a) SANS spectra measured on a 40- and 200-mg/cc  $\text{Ta}_2\text{O}_5$  aerogel; (b) high-resolution rendering of 500-nm cube of  $\text{Ta}_2\text{O}_5$  aerogel.

### FY2007 Accomplishments and Results

One of the main objectives of this project was to quantify the pore structure as measured from the SAXS experiments due to changes in the metal oxide foam preparation condition. In Fig. 1, the correlation range or the distance between two ligaments in the aerogel measured in the SAXS experiment is related to the density of the aerogel. We see that the inverse of the correlation range scales linearly with density until a density of 100 mg/cc. Below this, the density decreases with no corresponding change in correlation range.

An explanation of this surprising result was given by measuring the scattering at smaller  $q$  not possible with SAXS, using small angle neutron scattering (SANS). SANS results for 40- and 200-mg/cc are shown in Fig. 2a. The scattering curves show that in the 40- mg/cc sample there is scattering from spherical like objects that are approximately 1  $\mu\text{m}$  in diameter. No such features are observed in the aerogels above 100 mg/cc. The scattering on the  $\mu\text{m}$ -length scale comes from large voids or holes in the aerogel. This result is in agreement with our lensless

image result (Fig. 2b) that shows large voids in the low-density aerogel. As aerogel density is decreased below 100 mg/cc, the nanoporous structure remains constant and the decreased density is obtained by the formation of  $\sim 1000\text{-nm}$  voids. This may be a fundamental limit on the density of the materials.

We have also been successful in our second goal, to measure the pore structure of the metal oxide foam immersed in a cryofluids. We have been able to measure the SAXS of a porous material immersed in liquid nitrogen and measure the deformation of the foam.

X-ray tomography was used to measure density fluctuation in the metal oxide foams at better than 1  $\mu\text{m}$ .

The small angle scattering capability developed in this project has successfully lead to a number of follow up projects in support of various programs at LLNL. A number of examples are the measurement of void structure in highly energetic materials, the study of pore structure and volume in Be capsules, and the *in-situ* SAXS study of carbon aerogels immersed in liquid hydrogen.

# Construction of a Frequency Resolved Optical Gating (FROG) Diagnostic



Corey V. Bennett  
(925) 422-9394  
bennett27@llnl.gov

Many efforts in the area of single-shot, real-time recording of complex ultrafast waveforms (those with 100 fs to 1 ps detail and 100 ps to 1 ns record length) have no way of measuring the true response of the diagnostic systems because of difficulty independently characterizing the true input waveform. When no other measurement technique exists, it is difficult to know if details of the recorded waveform were real or artifacts of the recording instrument.

Frequency Resolved Optical Gating (FROG) is a well known and accepted “gold standard” technique for measuring such complex ultrafast waveforms. While a single-shot FROG system does not exist with the desired sensitivity and time-bandwidth product, a repetitively averaged, slow-scan system, could be constructed to measure these

waveforms. This repetitively averaged measurement system would enable a more accurate characterization of the performance of the real-time recording systems in progress.

## Project Goals

FROG is measurement technique that produces a frequency vs. time map of an optical signal in a manner similar to the way a musical score describes an acoustical signal. It does this by time-gating the optical field with a time-delayed replica of itself and recording the resulting output spectra vs. this delay. It is essentially a spectrally resolved autocorrelation. This analogy is shown in Fig. 1a, with Fig. 1b depicting one typical implementation in which the time gating is done through noncolinear second harmonic generation.

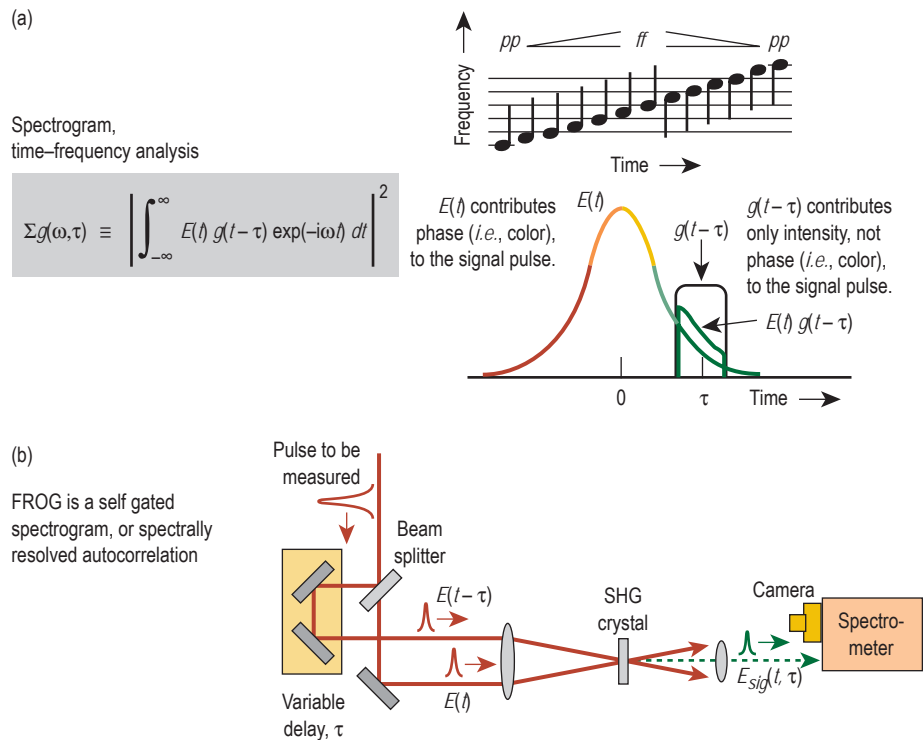
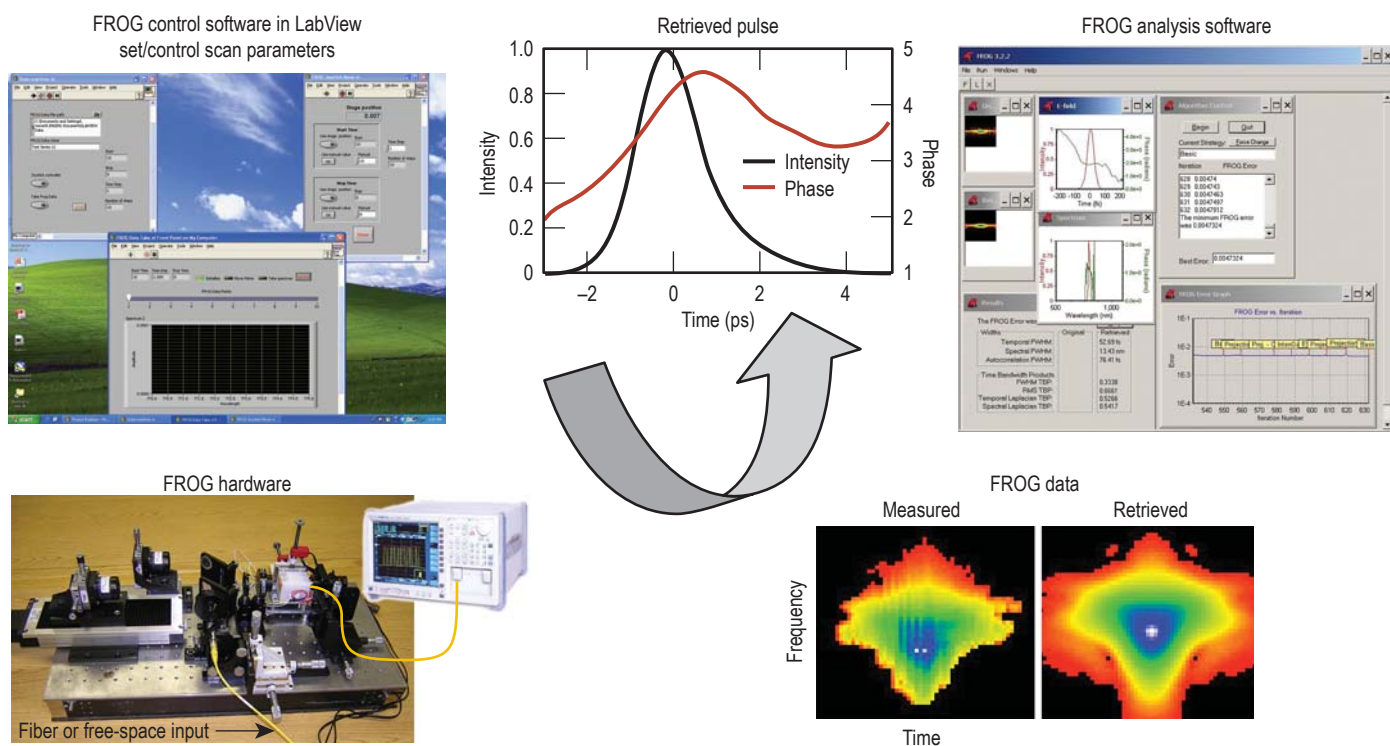


Figure 1. (a) Analogy between FROG and acoustic frequency analysis; (b) typical implementation in which the time gating is done through noncolinear second harmonic generation.



**Figure 2.** The FROG system. The process flow starts with the computer control windows in the upper left and flows in a counter-clockwise direction, resulting in the final pulse shape at the top. The actual hardware we constructed is shown in the lower left. The lower right shows a typical experimentally measured FROG trace along side a retrieved, or best matched, FROG trace obtained using retrieval software shown in the upper right. The desired information, the actual intensity and phase of the pulse vs. time is reported by the software and shown at the middle top of the figure.

The goal of this project was to build and test a FROG system with time-bandwidth product, and sensitivity necessary to measure ultrafast test signals in multiple projects within LLNL, *i.e.*, to add FROG to its measurement tool kit.

Typical signals have energies as low as 5 pJ/pulse, pulse durations from 100 fs to nearly 1 ns, time-bandwidth products up to 4000, and are approximately centered at a 1550-nm optical wavelength.

### Relevance to LLNL Mission

Future high-energy-density science experiments at NIF and other facilities will require ultrafast real-time measurement systems with performance well beyond current technology, *i.e.*, ps and even faster temporal resolution with 10,000:1 dynamic range. There are also externally funded national security applications that require faster real-time diagnostics. What is needed is a 1-THz real-time oscilloscope, 50 times faster than the existing state of the art. Better

tools, even if repetitively averaged, are required to aid in the creation and characterization of these new real-time recording instruments.

### FY2007 Accomplishments and Results

We have successfully built and tested, and are in regular use of the FROG system shown in Fig. 2. One example of the accomplishments of this FROG system was the measurement of pulses matching in duration to within 1 ps, and frequency chirp (slope of the optical frequency vs. time) to within 2% of that reported by our temporal imaging-based diagnostic. The temporal imaging system makes a complete measurement on one pulse at a time and can repeat the measurement at 155 million measurements/s. The FROG system is an average of trillions of assumed to be identical pulses. The good agreement between these two different diagnostics gives us high confidence in the accuracy of the new temporal imaging technology.

### Related References

1. Trebino, R., *et al.*, Georgia Institute of Technology, <http://www.physics.gatech.edu/gcuo/subIndex.html>
2. Trebino, R., Frequency-Resolved Optical Gating: The Measurement of Ultrashort Laser Pulses, Kluwer Academic Publishers, 2000.
3. Kane, D. J., and R. Trebino, "Characterization of Arbitrary Femtosecond Pulses Using Frequency-Resolved Optical Gating," *IEEE J. Quant. Electron.*, **29**, pp. 571-579, 1993.
4. Trebino, R., K. W. DeLong, D. N. Fittinghoff, J. N. Sweetser, M. A. Krumbu, and B. A. Richman, "Measuring Ultrashort Laser Pulses in the Time-Frequency Domain Using Frequency-Resolved Optical Gating," *Rev. Sci. Instrum.*, **68**, 9, pp. 3277-3295, September 1997.

### FY2008 Proposed Work

FROG will continue to be used as a tool in further work on SLIDER, ROPER, and the temporal imaging systems.

# Picosecond Response, Recirculating Optical Probe for Encoding Radiation (ROPER)



Stephen P. Vernon  
(925) 423-7836  
vernon1@llnl.gov

**L**LNL is performing physics experiments on the NIF, OMEGA and Phoenix platforms, including those addressing deuterium-tritium (DT) burn physics, equations of state, and dynamic material properties. The dynamic range, spatial resolution, bandwidth, and noise-robustness required in these experiments are extremely challenging and surpass present capabilities. This project is undertaking engineering reduction to practice of a picosecond response time, radiation to optical down-converting detector that can address these requirements.

The Picosecond Response, Recirculating Optical Probe for Encoding Radiation (ROPER) sensor is a resonant optical cavity consisting of high-reflectance mirrors that surround a direct band-gap semiconductor detection medium (Figs. 1 and 2). Radiation absorption within the detection medium induces a change in its optical refractive index. The index change is detected with an optical probe. The perturbation in the refractive index modulates the phase of the probe beam. Interferometry is used to convert the phase modulation to amplitude modulation, down-converting the radiation signature to the optical domain.

The sensor architecture can be optimized for detection of  $\gamma$  rays, x rays and neutrons. We project that integration of these sensors with advanced optical data recorders offers the possibility of probing the DT burn rate with good detection sensitivity ( $4 \times 10^3$  g/cm<sup>2</sup>) and  $\sim$  ps temporal resolution.

## Project Goals

At the end of the project we hope to successfully demonstrate a fully characterized, optimized, prototype, high-bandwidth, x-ray sensor, and provide a plan for integrating the sensor with a next-generation optical recorder, to address the possibility of creating an  $\sim$  ps response,  $\gamma$  detector for Weapons Complex Integration (WCI) experiments on NIF.

## Relevance to LLNL Mission

This project specifically addresses the instrumentation requirements of WCI. It is well aligned with LLNL engineering focus areas and enhances LLNL's core competency in measurement science at extreme dimensions. We anticipate that, when available, ICF and HEDS experimental programs, and NIF will identify applications for these detectors.

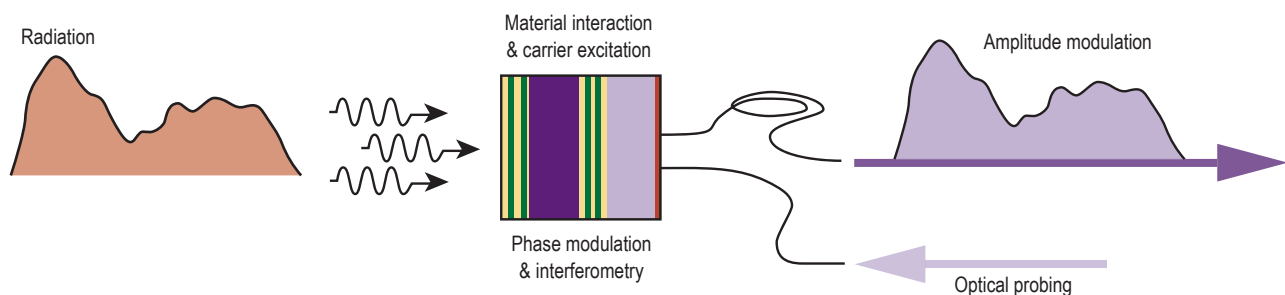


**Figure 1.** The ROPER system. Radiation absorption within the ROPER sensor modifies the sensor optical properties. Interferometric detection of the phase-modulated probe beam converts the radiation signature to an amplitude-modulated optical signal.

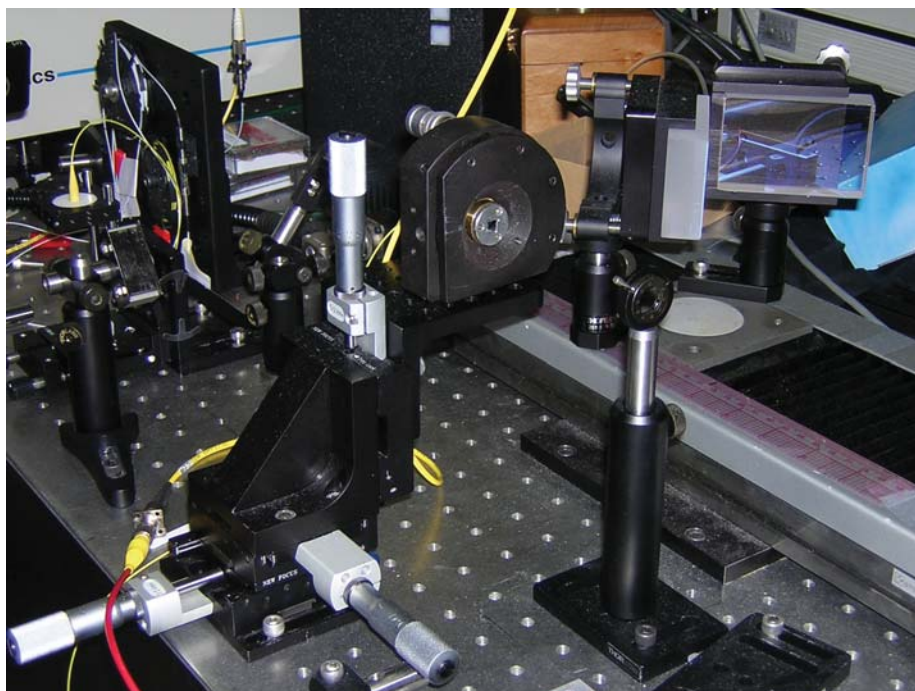


**Figure 2.** Fiber-based ROPER, pump-probe, optical testbed. A Ti:sapphire pump laser (140-fs pulse duration at 800 nm) is used as a surrogate excitation source and 1550-nm CW fiber-coupled probe is used for readout. The sensor is mounted on the translation stage at the top center of the figure.

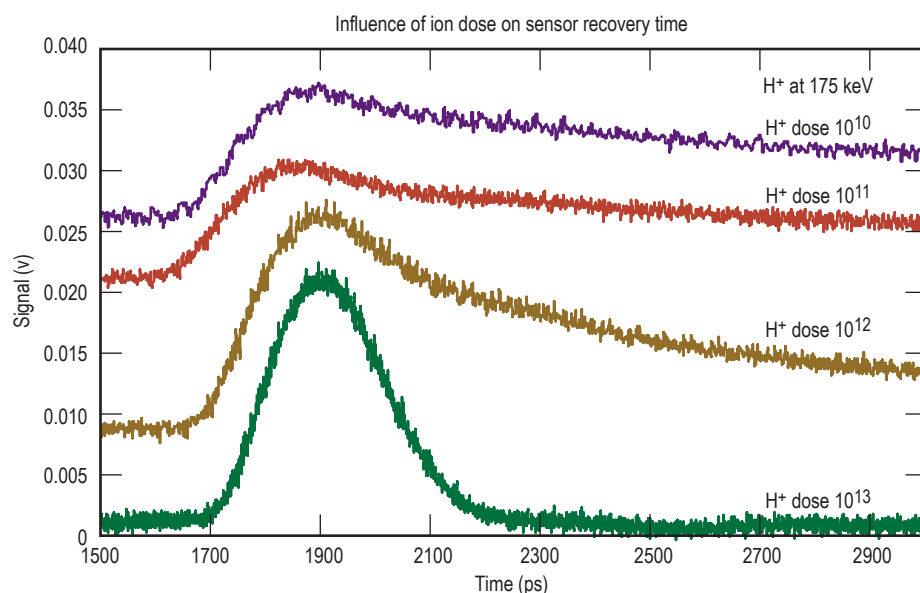


**Figure 3.** Sensor characterization. Radiation damage ( $H^+$  ion implantation) is used to tailor the sensor response time. Note that the sensor recovery time varies from 10 ns to 100 ps as the  $H^+$  dose is increased from  $10^{10}$  (purple curve) to  $10^{13}$  (green curve) ions/cm<sup>2</sup>.

## FY2007 Accomplishments and Results

Pump-probe optical testbeds with both free-space and fiber optical systems were implemented for sensor characterization. High finesse ( $f \sim 20$ ) Fabry-Perot sensors, operating at or near 1550 nm, using radiation damaged  $In_xG_{1-x}As_yP_{1-y}$  sensor material were fabricated and characterized. Proton ion,  $H^+$ , implantation was used to tailor the carrier recombination time in the sensor medium and, therefore the temporal response of the detector (Fig. 3). Measurements made with 140-fs pulse duration, 800-nm Ti:sapphire excitation, and a 1550-nm CW probe show that sensor bandwidth can be tuned with ion dose. For  $H^+$  at 175 keV and  $10^{13}/cm^2$ , an instrument-limited sensor temporal response of  $\sim 100$  ps is observed.

Current engineering efforts are focused on improving the fidelity and S/N in pump-probe characterization of radiation damaged sensors using 800-nm Ti:sapphire excitation and a spectrally filtered slave optical parameter amplifier at 1550 nm.

## Related References

1. Lowry, M. E., C. V. Bennett, S. P. Vernon, R. Stewart, R. J. Welty, J. Heebner, O. L. Landen, and P. M. Bell, *Rev. Sci. Instr.*, **75**, pp. 3995-3997, 2004.
2. Bennett, C. V., and B. H. Kolner, *IEEE J. Quant. Electr.*, **36**, pp. 430-437, 2000.
3. Lambsdorff, M., J. Kuhl, J. Rosenzweig, A. Axmann, and J. Schneider, *Appl. Phys. Lett.*, **58**, 1881, 1991.

## FY2008 Proposed Work

In FY2008 optimized ROPER sensors will be engineered for integration with an advanced optical recorder. Our goal is demonstration of a working "front-end" for a high-bandwidth x-ray detection system. In parallel, we will work on an implementation plan for integrating the ROPER sensor and a recording system to address the possibility of implementing an  $\sim$  ps response  $\gamma$  detector for WCI experiments at NIF.

# Serrated Light Illumination for Deflection Encoded Recording (SLIDER)



John E. Heebner  
(925) 422-5474  
heebner1@llnl.gov

Ultrafast, high dynamic range, single-shot diagnostics are critical to performing experiments in high-energy-density physics (HEDP). In recent years, conventional single-shot recording instrumentation has undergone minor incremental performance improvements. This instrumentation is largely based upon oscilloscopes and streak cameras that are fundamentally limited to trading off dynamic range for temporal resolution and do not scale well into the ps regime. More recently developed ultrafast optical methods can achieve 0.01 ps resolution but only over short record lengths of a few ps. No current technology is aptly suited for high dynamic range measurement in the 1 to 100 ps regime.

In this project, we address this technology gap by demonstrating a novel technique for single-shot recording of optical signals that is extendable to x rays. Using an auxiliary pump beam and a serrated mask, a prism array pattern is optically imprinted onto the guiding channel of a semiconductor waveguide. The transient prism array deflects signals in a stepwise manner linearly encoding time into multiple

angular channels. A slow camera in the back focal plane of a cylindrical lens is used to record the swept signal in parallel with high dynamic range (Fig. 1).

## Project Goals

We aim to demonstrate an all-optical analog of the conventional streak camera that can meet upcoming HEDP end-user requirements. Specifically, our goal is to demonstrate the SLIDER concept for

single-shot, high dynamic range recording (>8 bits) in a temporal regime (1 to 100 ps) that currently does not have any strong technology base. The technique leverages a wide body of research on ultrafast all-optical phenomena in semiconductors and combines it with well-established high dynamic range camera technology.

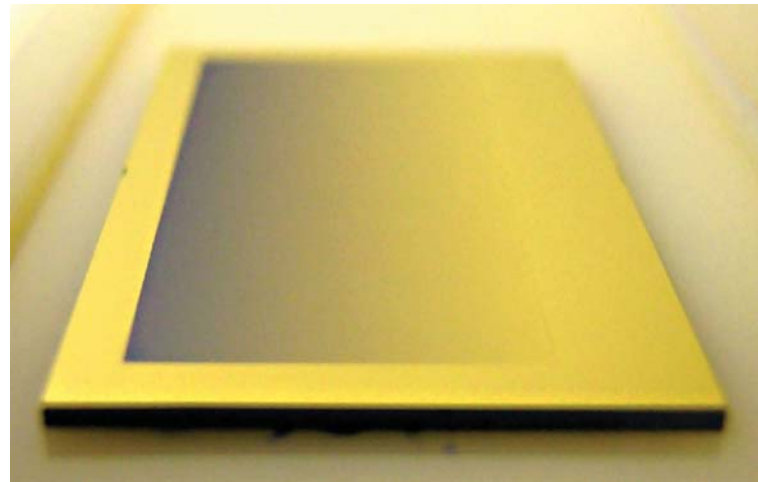


Figure 2. Fabricated 1-cm-x-2-cm SLIDER deflector consisting of a gold patterned coating on a GaAs waveguide. The prism array is manifested as a continuous gradient because the 60- $\mu\text{m}$  pitch is too fine to be resolved.

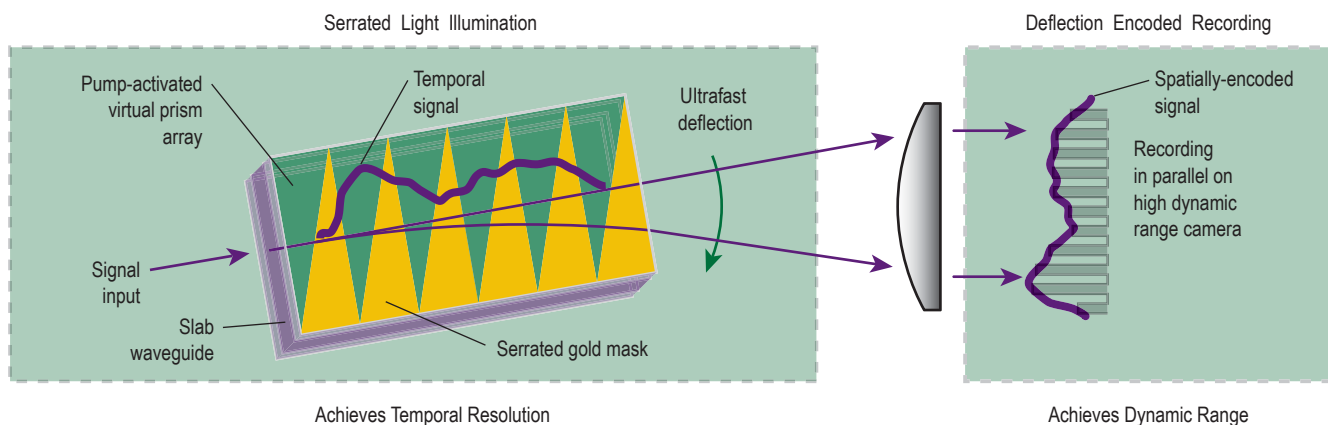


Figure 1. Schematic illustrating the SLIDER concept. The concept is based on the optically-induced deflection of an optical signal propagating in a slab waveguide. The deflection is caused by a sequential array of transient prisms that are created by a pump beam applied perpendicular to the guide through a serrated mask. The tradeoff between temporal resolution and dynamic range in traditional recording instruments is decoupled here by implementing ultrafast nonlinear mechanisms for the sweep followed by recording on a high dynamic range camera.

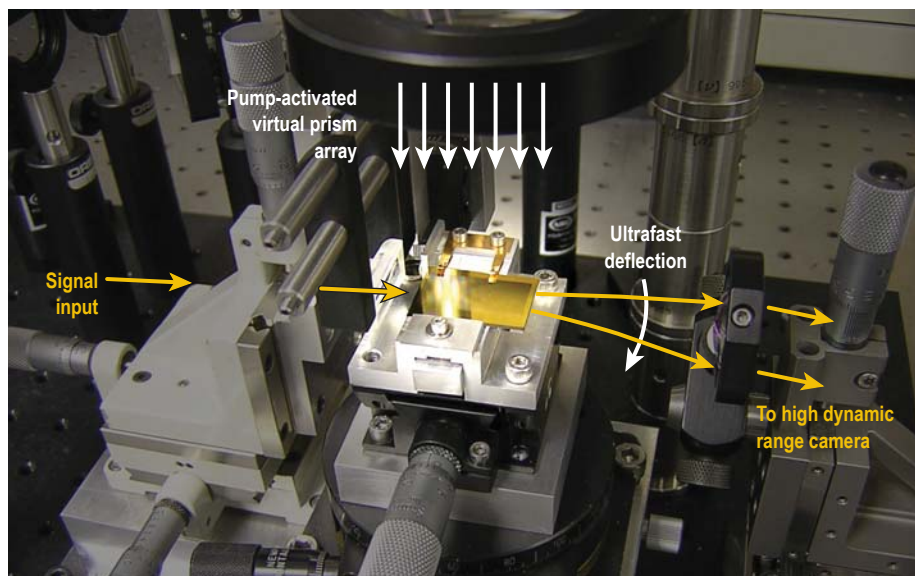


Figure 3. Experimental testbed setup showing the SLIDER deflector mounted in a multi-axis coupling stage. The signal and pump beam pathways are illustrated.

### Relevance to LLNL Mission

The proposed work directly addresses instrumentation performance gaps in engineering at LLNL. Future WCI and NIF experiments will require single-shot, high-dynamic range characterization of fusion burn histories.

### FY2007 Accomplishments and Results

We fabricated and tested a SLIDER device (Fig. 2) constructed from a 0.6- $\mu\text{m}$  core GaAs planar slab waveguide. A gold serrated mask was patterned sufficiently far above (1.2  $\mu\text{m}$ ) the core so as to not perturb the guided signal, yet close enough such that diffraction of the illuminating pump beam

was negligible. A 60- $\mu\text{m}$  prism array pitch ensured sub-ps temporal discretization into deflection encoded channels.

An ultrafast Ti:Sapphire based oscillator and chirped pulse regenerative amplifier provided a 0.15-ps pump pulse at 800 nm. This wavelength is suitably above the bandgap of GaAs to be strongly absorbing in the guiding layer generating electron-hole pairs that subsequently alter the refractive index in a transient manner.

Part of the pulse energy was tapped off to drive an optical parametric amplifier (OPA) that generated an idler beam at 1920 nm that was subsequently frequency-doubled to 960 nm for use as a test signal beam. This wavelength was chosen to

optimize the pump-induced modification of the refractive index of GaAs resulting from the interplay of the plasma effect, charge screening, and the Burstein-Moss effect. A ringdown test pattern consisting of  $\sim 1$  ps pulses separated at 10-ps was used for a proof-of-concept.

Figure 3 shows the experimental testbed setup. A cylindrical lens was used to couple the 1-cm test signal beam into the waveguide. Cylindrical lenses on the output end focused the beam to a nearly diffraction limited spot. The pump beam was expanded and applied perpendicularly to the guiding channel passing first through the serrated mask. The pump and signal pulses were synchronized by use of a motorized delay stage.

A recorded single-shot trace is shown in Fig. 4.

### Related References

1. Walden, R. H., "Analog-to-Digital Converter Survey and Analysis," *IEEE J. Sel. Area. Comm.*, **17**, p. 539, 1999.
2. Heebner, J. E., *et al.*, "Enhanced Linear and Nonlinear Optical Phase Response of AlGaAs Microring Resonators," *Optics Letters*, **29**, p. 769, 2004.
3. Hubner, S., *et al.*, "Ultrafast Deflection of Spatial Solitons in AlGaAs Slab Waveguides," *Optics Letters*, **30**, p. 3168, 2005.
4. Lowry, M. E., *et al.*, "X-ray Detection by Direct Modulation of an Optical Probe Beam-Radsensor: Progress on Development for Imaging Applications," *Rev. Sci. Instrum.*, **75**, p. 3995, 2004.

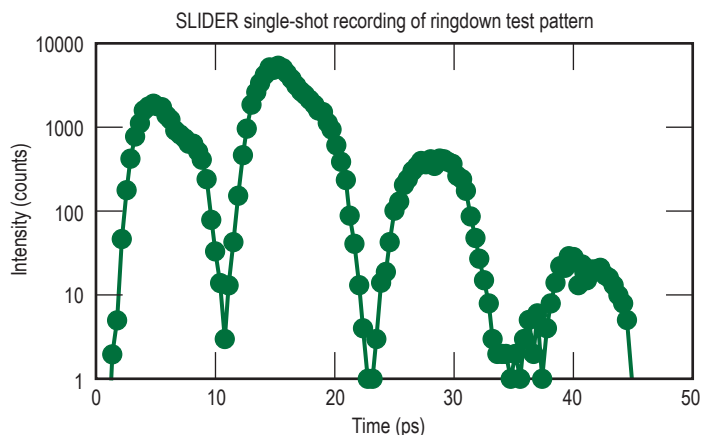
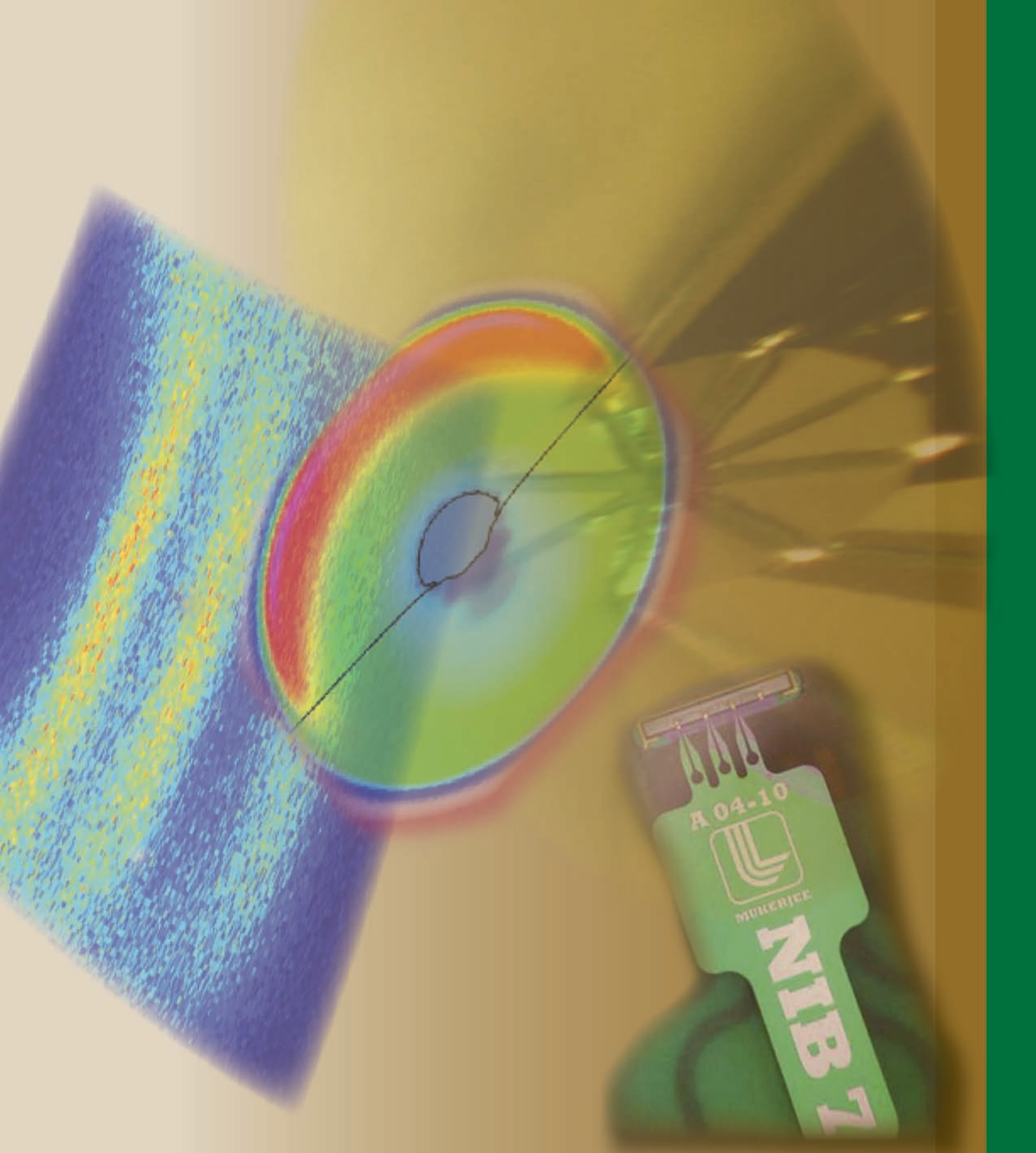


Figure 4. Recorded single-shot trace of a ringdown test pattern of  $\sim 1$ -ps pulses derived from a Gires-Tournois cavity with a 10-ps round trip time. The measured resolution is 3-4 ps FWHM and the dynamic range is in excess of 1000.

### FY2008 Proposed Work

We plan to conduct a detailed characterization of the merits and drawbacks of the SLIDER concept with a refined device. Numerous technical challenges remain before the proof-of-concept can be turned into a working instrument. Primary technical challenges include overcoming dynamic absorption (free-carrier and two-photon) and pump beam nonuniformities. We will further study the feasibility of combining SLIDER with an x-ray-to-optical converter for characterizing fusion burn histories on NIF.





Micro/Nano-Devices and Structures



# Biological Sample Preparation Infrastructure



*N. Reginald Beer*  
(925) 424-2232  
beer2@llnl.gov

**D**roplet-based microfluidic systems allow the ability to manipulate independent microdroplets as individual reactors, enabling reliable and quantitative sample processing and detection. Aqueous droplet formation in an oil crossflow at low Reynolds numbers is highly reproducible using extremely simple microfluidic devices.

We are now using an LLNL-created chip (to generate and stop microdroplets) to perform polymerase chain reaction (PCR) on viral nucleic acid samples. PCR is an enzymatic process that amplifies a specific DNA target sequence in response to temperature cycling that leads to denaturation, annealing, and extension. Each microdroplet contains the necessary biochemical constituents for selectively amplifying and fluorescently

detecting a specified portion of a sample DNA via PCR.

Isolating the PCR reaction in such small volumes provides an order of magnitude reduction in overall detection time by significantly reducing the total number of cycles required. Dilution of the fluorescently generated signal is largely eliminated in such a small volume, allowing much earlier detection, since the brightness of the small droplet, for a fixed quantity of product, is much greater than the brightness of a larger sample with the same quantity of product. This capability will enable the next generation of biothreat detectors to operate faster with lower reagent consumption, and provide the ability to amplify individual viral or bacterial genomes without interference.

**Figure 1.** Integrated and Labview-automated microfluidic workstation used to optimize on-chip PCR devices. Shown are the computer, programmed pumps, imaging electronics, and thermal control system hardware.



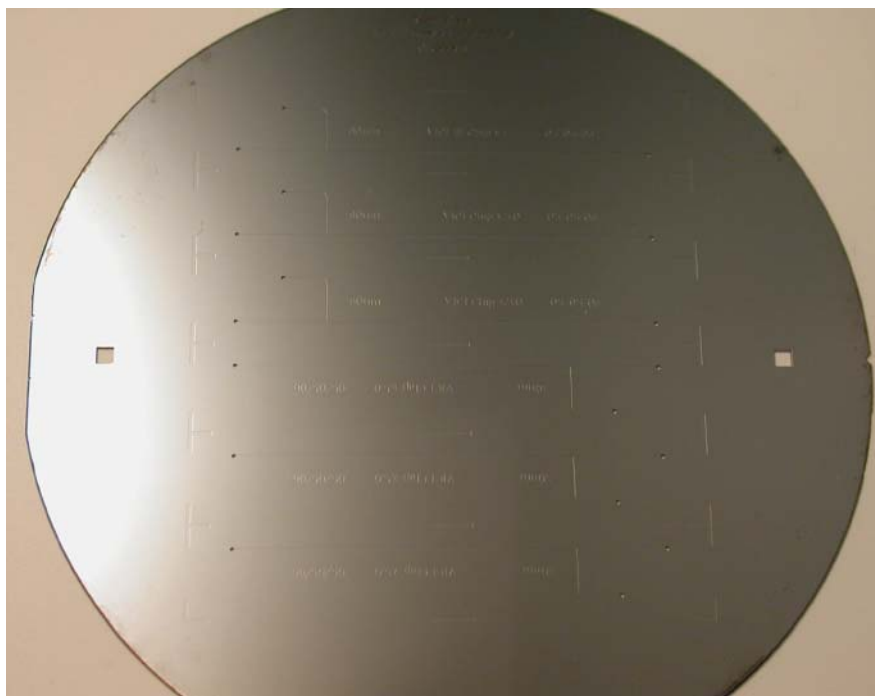


**Figure 2.** Silicon wafer fabrication process after DRIE, performed at LLNL. The wafer shown awaits anodic bonding to Pyrex, dicing into individual devices, and hydrophobic surface coating.

### Project Goals

The result of this work will be the capability to fabricate the microfluidic devices, including an optimized molecular vapor deposition (MVD) coating process for the microfluidic channel surfaces, as well as the implementation of a Labview-automated instrumentation system to operate the microfluidic experiments. Deliverables include:

1. complete benchtop system integration and optimization;
2. automate data acquisition and control system;
3. fabricate microfluidic channels;
4. optimize microfluidic model; and
5. optimize fabrication processes.

### Relevance to LLNL Mission

Optimized microfluidic devices and instrumentation systems enable greatly improved chemical and biological detectors for countering emergent chemical and biological threats. The optimization of these technologies advances the core microfabrication competencies at LLNL, while supporting a vital counterterrorism program.

### FY2007 Accomplishments and Results

As a result of this work, LLNL now has an integrated and automated benchtop system for conducting microfluidic testing, including on-chip PCR amplification and detection (Fig. 1). This sys-

tem integrated Watlow PID controllers and power supplies for Peltier Thermo-electric Cooling (TEC), a Coolsnap HQ2 CCD camera for fluorescence imaging (data acquisition), a Redlake high-speed CMOS camera for droplet production dynamics analysis, two programmable KD Scientific infusion syringe pumps, an Excite metal-halide arc-lamp light source, a Nikon TE-2000U fluorescence microscope, a Uniblitz shutter and controller, a cooling fan, and three Valco Instruments multiport valves. Integration and automation allowed repeatable and efficient experiment processing, resulting in more data and faster iteration cycles.

This work also provided an optimized fabrication and device surface coating process for the silicon substrate (Fig. 2). The optimized device used a Deep Reactive Ion Etched (DRIE) 0.5-mm-thick silicon wafer with topside etching for the microchannels and backside etching for the fluidic vias. The device was then anodically bonded to a 0.5-mm Pyrex wafer and diced into individual devices.

Furthermore, device coating optimization was performed, with the results that liquid treatment with SigmaCote was the most cost-efficient method, but molecular vapor deposition (MVD) with FDTS was the most resilient and effective method.

The results of the device optimization are visible in Fig. 3, where a stream of monodisperse droplets with diameters of only 27  $\mu\text{m}$  are visible after droplet generation and stopping on-chip. The droplets are now ready to undergo the PCR amplification and real-time detection process. Due to the optimized channel surface coating, the droplets do not wet the channel walls.

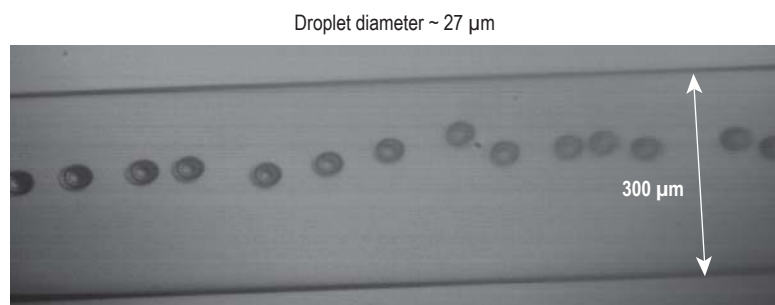


**Figure 3.** Image of the device in operation showing the generation and trapping of a monodisperse stream of 27- $\mu\text{m}$  droplets. After droplet-stopping the device is thermally cycled to power the PCR amplification process.

# Rapid Defense Against the Next-Generation Biothreat



Raymond P.  
Mariella Jr.  
(925) 422-8905  
mariella1@llnl.gov

**B**ioengineered and emerging pathogens represent a significant threat to human health. The best defense against a rapidly expanding pandemic is to isolate the pathogen quickly from biological samples so that it may be identified, characterized, and have treatments developed against it. The one persistent technology gap in the process of identifying and quantifying the presence of pathogenic agents has been sample handling and preparation that must precede any assay. Also, we need higher-performance, multiplex assays for families of rapidly-mutating RNA viruses.

## Project Goals

The objective of this project is to replace burdensome manual techniques for sample handling and preparation with new automated technologies. We will use microfluidics with ultrasonics, and electrokinetics to separate and purify viruses from biological and environmental samples. We will also create less costly, but more general multiplex assays for viruses, using multiplex,

ligation-dependent probe amplification (MLPA).

## Relevance to LLNL Mission

Sample preparation is a critical requirement for biological assays and is a major bottleneck in the process of detecting and identifying biological agents, particularly unknown/engineered/emerging pathogens. Viruses are an important category of pathogens because some of its members, such as influenza and smallpox, are extremely infectious and very virulent forms could result in sudden, massive pandemics. Viruses are often difficult to isolate due to their small size (diameter < 200 nm), compared with the bulk of the particles in a sample. Multiplex assays are also a key part of this work. This project strongly aligns with LLNL's missions in national security.

## FY2007 Accomplishments and Results

We have created new simulation capabilities, along with experimental validation, including full 3-D models

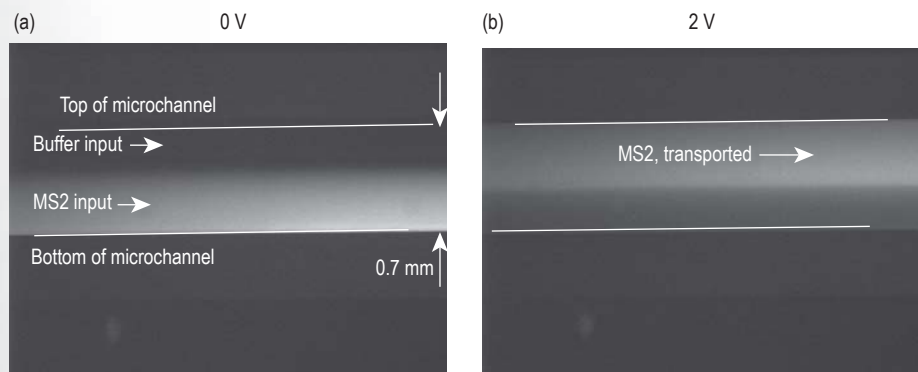


**Figure 1.** Monochrome photographs of a low-conductivity solution of fluorescently-labeled virus MS2, flowing in a microchannel with top and bottom electrodes (not shown). Two solutions are being introduced from the left of the channel: the upper solution is a clean buffer and the lower solution contains the labeled MS2. In (a) there is no voltage applied and the laminar flow and relatively low diffusivity of the MS2 confine the MS2 to the bottom half of the flow. In (b) with 2 V applied perpendicular to the flow, the MS2 has been almost entirely transported up into the buffer solution, as desired.

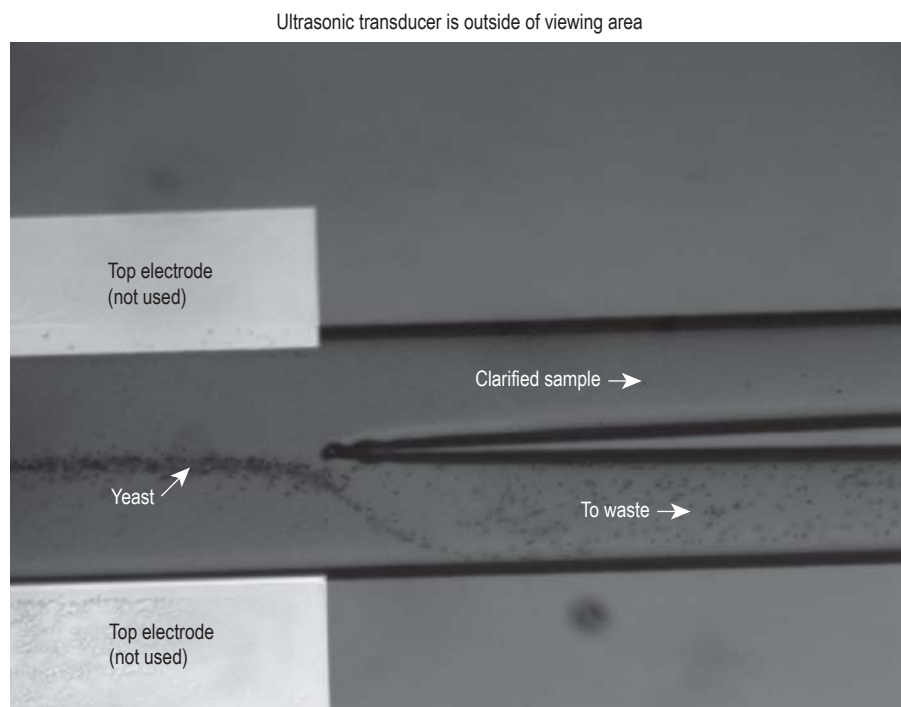


**Figure 2.** Photograph of yeast flowing in a 0.5-mm microchannel that has an ultrasonic standing wave, perpendicular to the image plane and running along the center of the flow channel. Ultrasonic transducer is outside of viewing area.

with Monte Carlo models for transport of biological particles. In our modeling and experimental research, we have investigated acoustics, electrokinetics (including effects of electroosmosis), electrochemistry, including local pH changes due to wall/electrode processes in our microfluidic systems.

We have established quantitative assays for the titers of MS2, *E. coli*, *S. cerevisiae*, murine herpesvirus, torque teno virus (TTV), Epstein-Barr Virus (EBV) and Adeno virus subgroup C (types 1 and 5). Prior to using human nasopharyngeal samples (NPS), we have used prepared mixtures of viruses both RNA and DNA with bacteria and eukaryotic cells in our research on microfluidic separation techniques. Some examples of these mixtures are the bacteriophage MS2, a RNA virus, with its prokaryotic host bacteria, *E. coli*; and BSL-1, Risk-Group-1 virus such as the murine herpes virus, a DNA virus; and eukaryotic *S. cerevisiae* (Baker's yeast). NPS collection from volunteers has commenced and the samples have been analyzed with quantitative assays

for EBV, Adeno C and TTV as well as spikes of EBV, AdenoC and murine herpes virus.

We designed, fabricated, and tested numerous configurations of microfluidics that demonstrated that we could use ultrasonic standing waves with high-Q at 10- $\mu$ /min flow rates to drive yeast (model organism for human cells) to the energy/pressure-wave nodes and that we could use electrophoresis at 1.4 V or slightly less to transport virus-sized (40-nm-diameter) latex beads. We have conceived of new separation configurations that use continuous flow with dielectrophoretic forces (negative dielectrophoresis). We have established a quantitative flow-cytometer-based assay for the yeast and bacteria with diameters ranging from 0.5  $\mu$ m to 10  $\mu$ m. We designed a fluidic system that is capable of excluding the host DNA/RNA from well-characterized biological samples consisting of cells, bacteria, and viruses using Isotachophoresis.

Our general research effort has been coordinated with the Viral Identification and Characterization Initiative.

We have initiated an extensive effort to collect published data on the electrophoretic mobilities of DNA, proteins, viruses, bacteria, and other biological particles that we will need to manipulate. These data, coupled with our modeling of transport versus pH and solution conductivity, have driven our designs of microfluidics-based sample processing systems.

We used cyclic voltammetry to characterize the electrode processes, so that we could avoid the extensive electrolysis of water, with its collateral generation of bubbles. We still are addressing the effects of pH changes, when we operate at or slightly above the overpotential.

Non-specific binding of non-ligated, PCR-amplified probes to bead oligos has been a significant and on-going problem for the MLPA assay. This problem has been addressed by optimization of the probe design and MLPA assay parameters (probe concentration, nucleic acid concentration, ligation and hybridization buffer properties, and ligation parameters). None of these modifications resulted in adequate reduction of background signal and therefore the assay probes were redesigned into a Molecular Inversion Probe (MIP) format to allow digestion of unligated probes that may cause a non-specific signal.

A polymerase step was added to the protocol to adjust for the 5-ft truncation of probes that commonly occurs during probe synthesis. A DNA polymerase has been identified for the PCR amplification step that greatly increases the signal-to-noise ratio. The probe hybridization and ligation protocols have been optimized so that the hybridization-ligation reaction time is decreased from 4 h to 90 min. This modified protocol yields a very high signal-to-noise ratio in a 10-plex assay format and is capable of detecting Adenovirus in a clinical nasopharyngeal sample. This is the first time the MIP technology has been modified for use on a bead-based microarray.

Figures 1 and 2 illustrate our accomplishments.

# Validation of 3-D Acoustic Modeling of Commercial Codes for Microfluidic Systems



Raymond P. Mariella, Jr.  
 (925) 422-8905  
 mariella1@llnl.gov

Nearly-ideal, single-node, planar standing waves can be modeled and established experimentally for waves that are centered in rectangular microfluidic flow channels. However, similar single-node, planar standing waves that are proximate to one wall of such a

microchannel have never been realized experimentally. It is unclear whether the non-ideality arises from intrinsic defects and inhomogeneities in the materials that are used in such microsystems or whether it arises from non-ideality in the assembly/bonding/packaging.

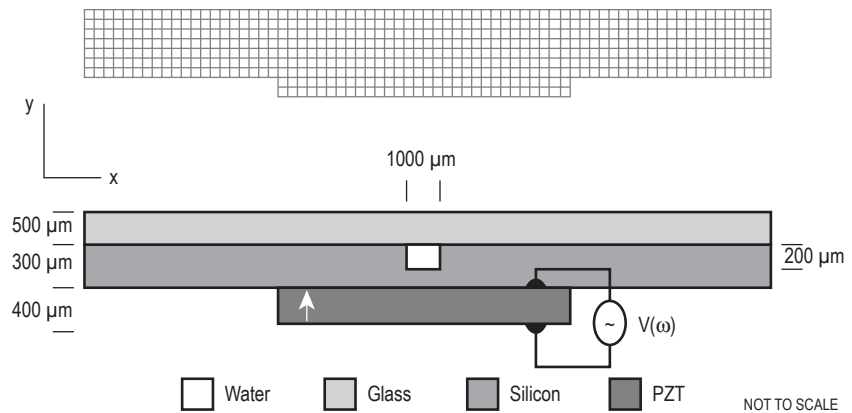
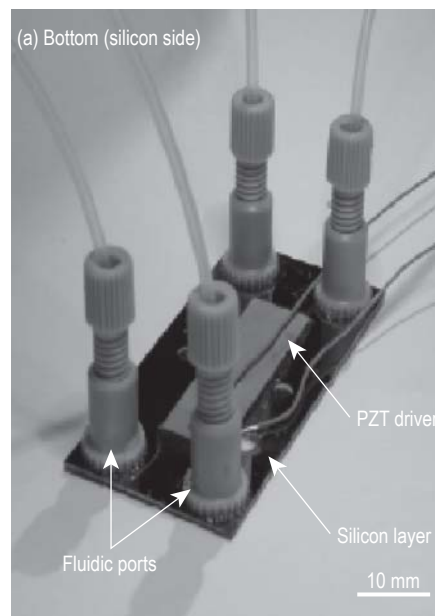
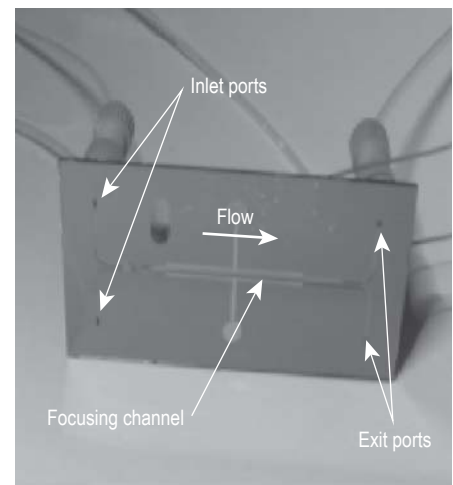


**Figure 1.** Two-dimensional computational region for the ATILA finite element code. The planar structure is comprised of an upper glass layer, and a silicon wafer in the middle with a fluidic channel etched into the upper surface. The structure is acoustically driven into resonance by a thin thickness-poled PZT layer, bonded to the bottom of the silicon wafer. The fluid flow is perpendicular into the modeled plane. Dynamic flow behavior of the fluid is not taken into account in this approximation.

**Figure 2.** The experimental microfluidic chip (H-bridge) test package, owing to similar designs found in the literature. Here, the PZT is bonded to the silicon layer, and plastic surface-mounted fluidic ports are used to couple the fluid and beads from a syringe pump into the focusing channel. The channel splits at the ends resulting in two inlet and two exit ports. A wide variety of separation, mixing, and fractionation schemes can be realized with this design.



(b) Top (glass side)



### Project Goals

Our goal is to use an existing code, ATILA, that can be used to perform 1-D, 2-D, and 3-D modeling of acoustic waves at ultrasonic frequencies within microsystems. We can use this capability to simulate the ultrasonic pressure fields in a variety of structures with microchannels that could be used to manipulate particles of scale 2  $\mu\text{m}$  or larger in water or similar aqueous fluids, including possible generation of nearly-proximate standing waves. We also have fabrication expertise to test and validate the accuracy of these simulations. We compared these simulations with experimental measurements on microchannels in a variety of structures with microchannels passing particle-bearing fluids in order to validate these simulations on relevant microsystems.

### Relevance to LLNL Mission

Acoustic manipulation of  $\mu\text{m}$ -scale particles is important for biosecurity applications and for biological sample handling and processing. Sample processing is still performed in a tedious, manual manner today, requiring large amounts of time from skilled technical personnel. Having a validated simulation capability to model acoustic manipula-

tion of particles will significantly enhance LLNL's engineering capabilities.

### FY2007 Accomplishments and Results

We used a commercial code, ATILA, which is already available, to perform 2-D and 3-D modeling of relevant possible structures with microchannels and bonded piezoelectric transducers. This enabled the fabrication and testing of several generations of microfluidic systems with ultrasonic transducers bonded to enable the manipulation of particles larger than 2- $\mu\text{m}$  diameter via acoustic standing waves. We have experimentally validated 1) the code at

the resonant frequencies of the ultrasound for our configurations, where larger particles are captured at the nodes of standing waves; and 2) the fact that sub-1- $\mu\text{m}$  scale particles are largely unaffected by non-cavitating power levels of standing waves in the microfluidic channels.

The ATILA code and our results are shown in Figs. 1 to 4.

### Related Reference

Coakley *et al.*, "Spore And Micro-Particle Capture on an Immunosensor Surface in an Ultrasound Standing Wave System," *Biosens. Bioelectron.*, **21**, pp. 758-767, 2005.

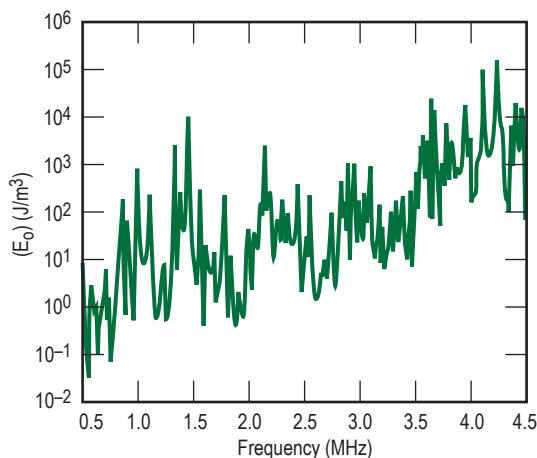


**Figure 3.** Theoretical energy density as a function of frequency for the 2-D channel described in Fig. 1. The amplitude of the drive voltage is 1 V. Several frequencies show energy densities in excess of  $5 \times 10^3 \text{ J/m}^3$ . Large energy densities indicate potentially useful operating conditions for manipulation of particles. Conversely, there are regions where there is very little energy in the fluid, implying that all of the energy is in the elastic structure.

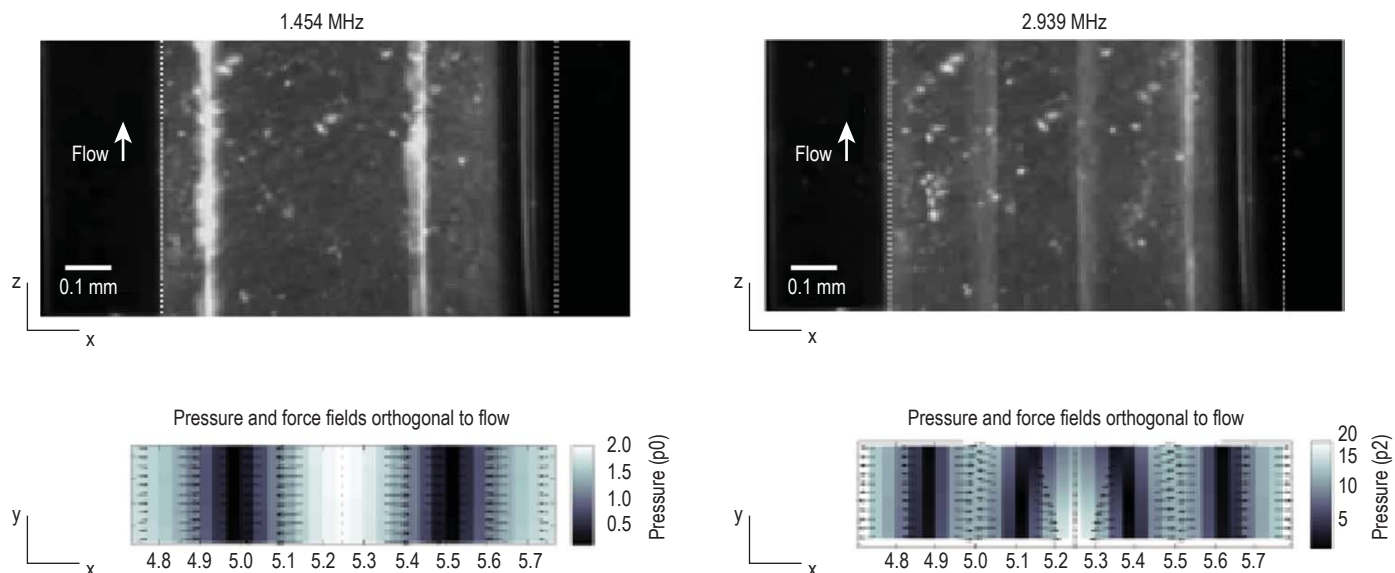


**Figure 4.** Two representative operating conditions of the microfluidic channel  $f = 1.454 \text{ MHz}$  and  $2.939 \text{ MHz}$ . The upper images are microscope views of the channel through the glass substrate as the fluid and latex spheres flow from the inlet to the exit through the standing wave pattern in the channel. The lower images are the 2-D numerical estimate of the pressure field from ATILA and a vector plot corresponding to the direction of the calculated acoustic force fields. Here the dark regions represent nodes in the sound field and the light regions are antinodes.

# Thermal-Fluidic System for the Manipulation of Biomolecules and Viruses

We are developing a reconfigurable fluidic system that demonstrates the ability to *simultaneously* perform separations, concentrations, and purifications of biomolecules and viruses using temperature gradient focusing (TGF). Many projects throughout LLNL, particularly those related to pathogen detection, mitigation, and protection, require the manipulation of biomolecules or viruses to accurately 1) quantify the presence of a particular substance; or 2) synthesize and investigate the function of a molecule.

This novel microfluidic technology is an equilibrium gradient version of capillary electrophoresis (CE) that allows for the stationary fractionation and concentration (up to 10,000 x) of target analytes on the dimension of bulk or free solution electrophoretic mobility. In this technique a delicate balance is achieved in a microchannel between a net fluid flow and an opposing electrophoretic velocity gradient to capture charged

analytes at a specific location (Fig. 1). The analytes are then separated based on their free solution electrophoretic mobility.

## Project Goals

The project goals are to develop an automated TGF instrument to improve the separation resolution and throughput when applied to front-end sample processing of biological samples. Two specific application areas are identified to demonstrate the novel sample manipulation capabilities inherent to TGF: 1) the purification and separation of different virus strains in complex samples; and 2) improving the performance of protein concentration and separation for *in vitro* transcription/translation (IVT) protein expressions.

## Relevance to LLNL Mission

TGF specifically addresses LLNL's interests in the detection of biomolecules, viruses, or cells at low concentra-



Kevin D. Ness  
(925) 423-1856  
ness5@llnl.gov

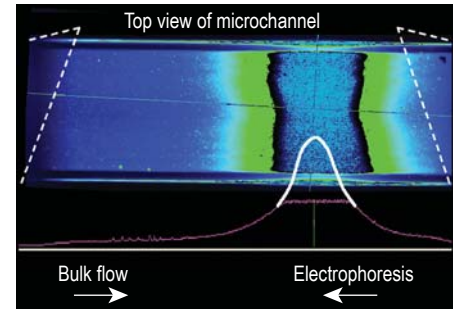


Figure 2. Automated TGF capture and concentration (>2000-fold) of a fluorescent dye.

tions through enhanced collection, separation, and purification strategies. This is facilitated by performing the necessary front-end sample preparation through concentration procedures and removing noisy background signals/contaminants. This project supplies LLNL engineers with a novel capability to perform biomolecular, viral, and cellular control in a flexible format to address a wide range of programmatic assay conditions.

## FY2007 Accomplishments and Results

**Automated TGF capture.** We demonstrated the successful capture and concentration (> 2000-fold) of a small fluorescent dye molecule in an automated sequential injection analysis system (Fig. 2). We improved the overall instrument performance by improving the stability of the applied electric field and flow rate, improving the linearity of the temperature field, and increasing the magnitude of the temperature gradient.

**Stable flow.** We designed a pressure-controlled flow system with integrated flow rate feedback to achieve the desired ~1 nL/min flow rate control. Our flow rate control system enables steps, ramps, and other functions (Fig. 3) necessary for our project goals.

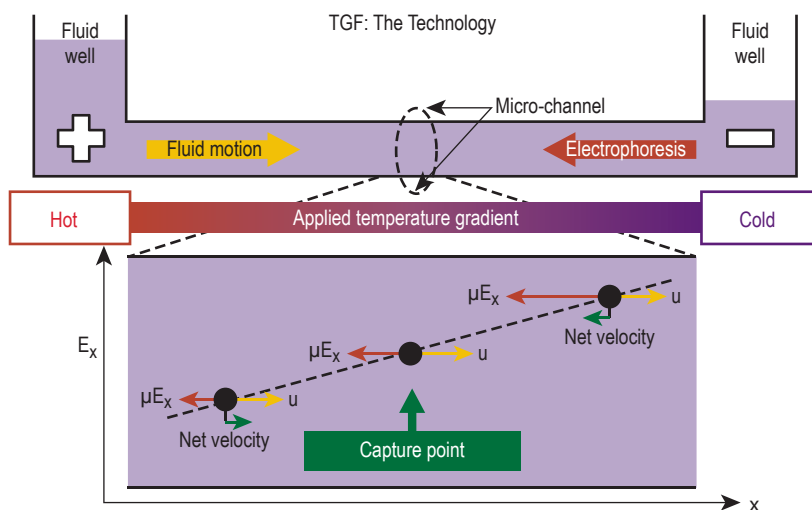


Figure 1. Schematic of temperature gradient focusing (TGF). Bulk fluid motion (yellow arrow) is balanced by an opposing electrophoretic velocity (red arrow) to capture analytes at a unique spatial location within a specific electrophoretic mobility range.

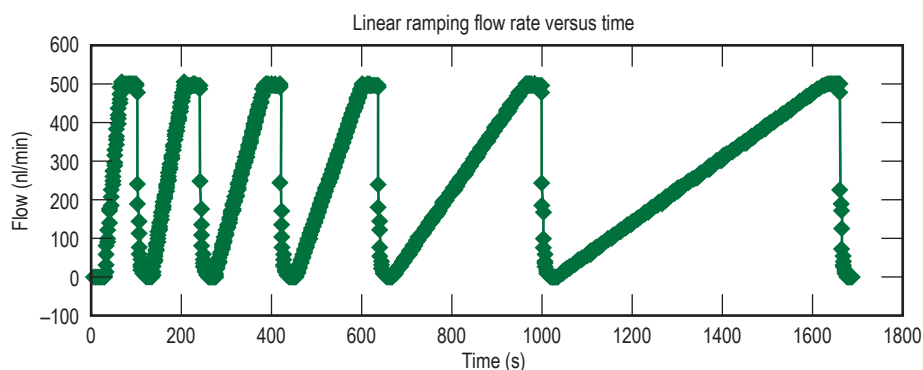


Figure 3. Flow rate stability of LLNL pump control system in a varying flow rate ramping mode.

**Linear temperature gradients.** We used numerical modeling of the governing equations (energy equation and Stokes flow) and multi-physics simulations (COMSOL Multiphysics) to determine optimal device designs for the generation of thermal gradients (50 °C/mm) in a high-throughput microfluidic structure. An example of the temperature gradient as a function of applied electric field is shown in Fig. 4. Our models demonstrate the need for “thick walled” capillaries and robust thermal mounting to the heat source. We achieve these requirements using microfabricated glass chips with etched microchannels in a copper package using compression mounting and a high performance thermal interface material.

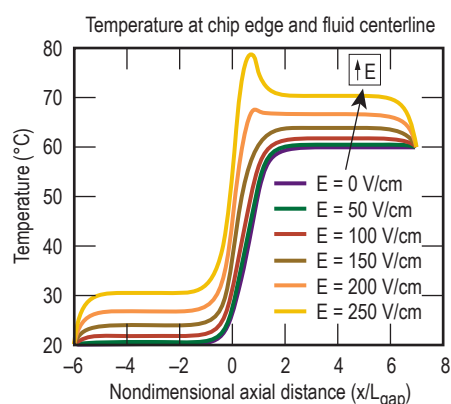


Figure 4. Numerical simulation results showing the varying temperature profile in the focusing region of our microfluidic chip. The model includes externally applied temperature gradients, natural convective losses through the packaging, nonuniform Joule heating, and convective/conductive conjugate heat transfer through the fluid/wall structure.

**Modeling effort.** For the initial modeling of the relevant field variables (temperature, velocity, and voltage) we use the commercially available finite element modeling package, COMSOL Multiphysics. To solve for the analyte concentration profiles in a TGF system, these known field variables feed into a Brownian dynamics simulation. From these specific metrics, such as peak height, peak width, throughput, and limit of detection, are extracted to determine the efficiency and resolving power of a particular TGF run (Fig. 5). Design guidelines and rules (geometric and operating conditions) were constructed for various applications to aid in the design and testing of TGF devices.

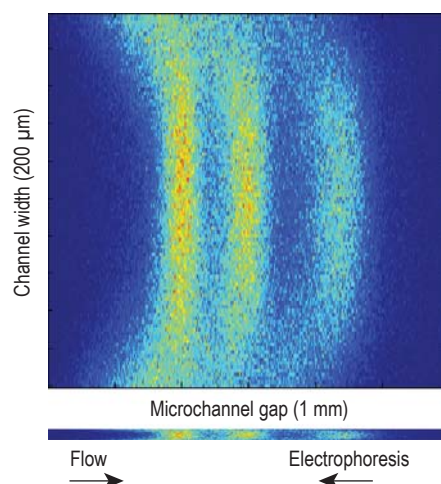


Figure 5. Monte Carlo particle tracking simulations, predicting the steady state shape and band location of three analytes with different electrophoretic mobilities that are captured, concentrated, and separated using TGF. The top image is scaled to aid in visualization.

### FY2008 Proposed Work

In FY2008, we plan to 1) move from fluorescent analytes to biological samples (virus and protein); 2) build up a fluorescently labeled sample library (virus and protein) to characterize system performance with biological samples; 3) organize the library into biologically relevant groupings; 4) determine how biologically relevant groupings of our sample library relate to electrophoretic mobility; 5) demonstrate an ability to separate three spiked viral samples in a “simplified” background (repeat with proteins) and purify spiked virus from a “dirty” background of multiple contaminants (repeat with proteins); and 6) move to more relevant and complex sample matrixes (nasopharyngeal and IVT protein productions).

# Flow-Through Pyrosequencing in a Microfluidic Device



*Klint A. Rose*  
(925) 423-1926  
rose38@llnl.gov

**P**yrosequencing is a recent DNA sequencing technique based on DNA replication. Using special cascading chemistry, a light-emitting reaction is triggered each time a nucleotide, A, C, G or T, is incorporated into the complementary strand of DNA. The sequence of the DNA can be determined by iteratively introducing one type of nucleotide and detecting the emitted signal. This method is primarily used for sequencing short lengths of DNA (up to 100 bases) and detecting single nucleotide polymorphism.

Sequencing provides one option for the final identification step in an ongoing effort to start with a clinical sample and identify all known and unknown viruses within it. Although sequence data is considered the “gold standard” for microbial identification, the implementation of this technique is currently limited by time and cost. Since identification of a virus is improved with longer sequences, the 100-base cutoff is also a limitation. Therefore, other identification approaches, such as fragment length analysis in capillary

gel electrophoresis, are being pursued at LLNL. These processes, however, are less amenable to the rapid sample analysis needed to characterize the viral load within a single clinical sample.

By reducing to practice the microfluidic approach in which beads carrying a DNA template are washed with 200-nl volumes of the sequencing chemicals, we can reduce the sequencing cycle time per nucleotide, reduce the volume of expensive reagents used, and potentially increase the number of bases sequenced. This sequencing method is shown in Fig. 1.

## Project Goals

The four major goals of this project were: 1) create a microfluidic chip for rapid, small-volume pyrosequencing; 2) replicate the biochemistry necessary to bind DNA to a magnetic polystyrene bead; 3) replicate the sequencing biochemistry; and 4) assemble an automated system to control sample loading, sequential nucleotide injection, and signal detection.

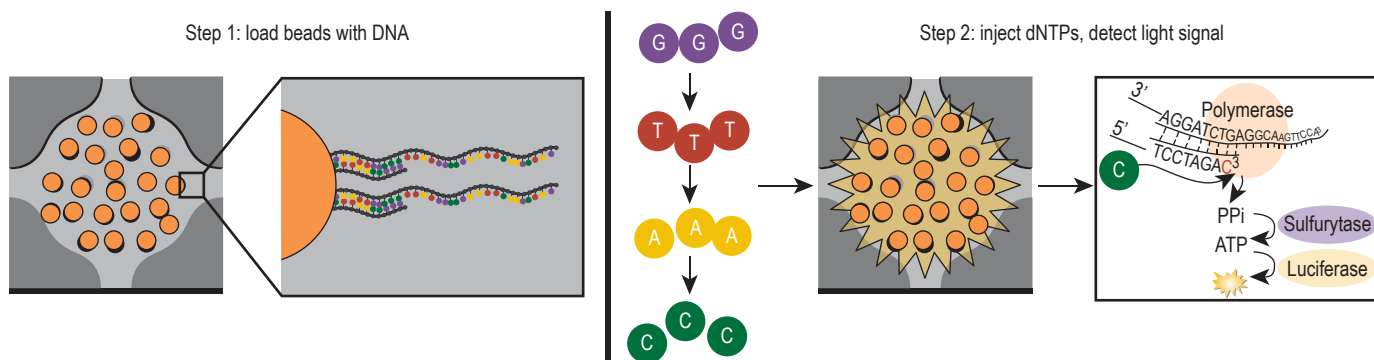


**Figure 1.** Description of microfluidic pyrosequencing technique. Step 1: The DNA template to be sequenced is bound to a magnetic polystyrene bead then loaded into the center sequencing chamber of the microfluidic chip. The particles are held in this region using an external permanent magnet. Step 2: Solutions containing dCTP, dATP, dTTP, and dGTP are sequentially injected into the chamber and washed over the bound DNA. Successful incorporation of a nucleotide initiates a cascade reaction resulting in the release of light.

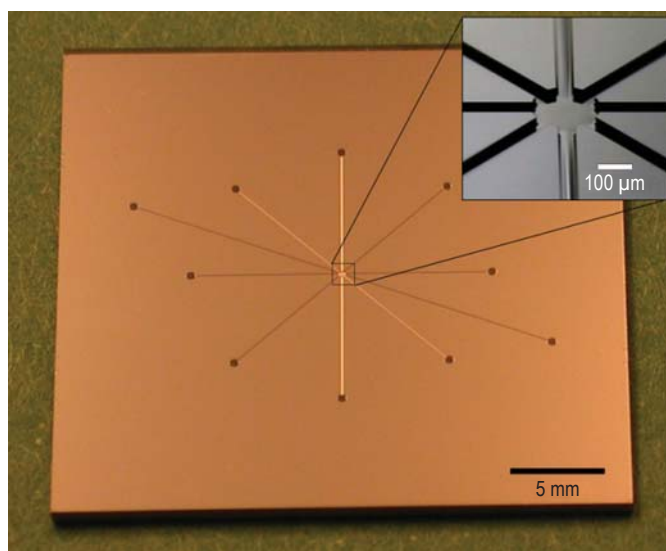


**Figure 2.** Example of the multiport microfluidic sequencing chip. The sequencing chamber has a 200- $\mu\text{m}$  diameter and total volume of approximately 6 nl. The chips are microfabricated in a silicon substrate for high reflectivity and bonded to glass.

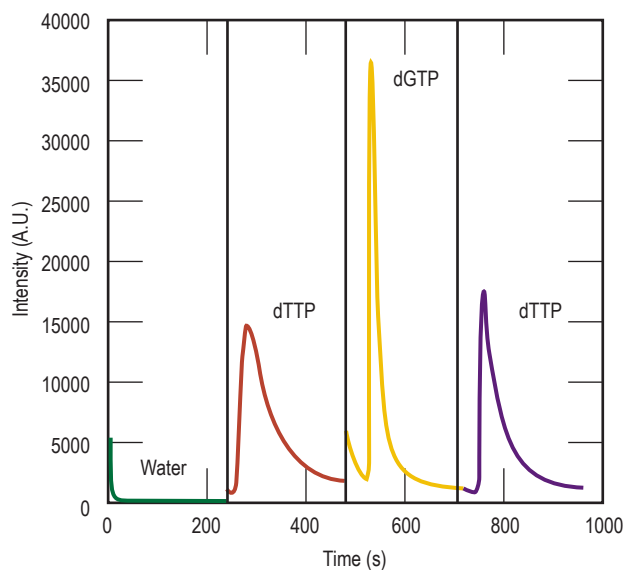


**Figure 3.** Example of the detected intensity signal from a DNA sequencing reaction. The height of each peak corresponds to the number of nucleotides incorporated.

### Relevance to LLNL Mission

This project addresses needs identified by LLNL for the detection of viruses at low concentrations (10 to 1000 copies/ml). Specifically, this project addresses the need for rapid identification of individual viruses based on a low number of DNA sequences. This work has direct impact on LLNL's Viral Identification and Characterization Initiative (VICI).

### FY2007 Accomplishments and Results

We accomplished the overall goals of this project by delivering an automated microfluidic system for sequencing bead-bound DNA. Specific results and accomplishments include the following.

1. Modeled sequencing chamber plans to optimize light capture from sequencing reactions.
2. Implemented two microfluidic sequencing chips. The first has dual input and output ports and a 1- $\mu\text{L}$  volume. The second version has multiple input ports (up to 8) and two output ports with a 6-nl volume (Fig. 2). Figure 3 is an example of

the detected intensity signal from a DNA sequencing reaction.

3. Successfully bound DNA template to magnetic polystyrene beads using a biotin-streptavidin linker.
4. Demonstrated magnetic capture of the template-covered beads in the sequencing chamber.
5. Replicated the bioluminescence reporter system for identifying incorporation of dNTPs onto the existing DNA template.
6. Assembled an automated sequencing system with fine fluidic control, multiple sample injection, and a detection component for low signals.

### Related References

1. Margulies, M., M. Egholm, *et al.*, "Genome Sequencing in Microfabricated High-Density Picolitre Reactors," *Nature*, **437**, 7057, pp. 376-380, 2005.
2. Ronaghi, M., "Pyrosequencing Sheds Light on DNA Sequencing," *Genome Research*, **11**, pp. 3-11, 2001.
3. Zhou, Z., A. C. Poe, *et al.*, "Pyrosequencing, a High-Throughput Method for

- Detecting Single Nucleotide Polymorphisms in the Dihydrofolate Reductase and Dihydropteroate Synthetase Genes of *Plasmodium Falciparum*," *Journal of Clinical Microbiology*, **44**, 11, pp. 3900-3910, 2006.
4. Russom, A., N. Tooke, *et al.*, "Pyrosequencing in a Microfluidic Flow-Through Device," *Analytical Chemistry*, **77**, pp. 7505-7511, 2005.

# Investigation of Hybridization Times for DNA Microarrays



**Robin Miles**  
(925) 422-8872  
miles7@llnl.gov

Large DNA hybridization arrays (microarrays) are used to detect the presence of specific genetic sequences in samples. They are used for many applications including pathogen detection, detection of genetic mutations, and sequencing. Oligos, short strands of single-stranded DNA, are bound to a surface in spots. Complementary DNA strands present in the samples bind (hybridize) to the surface-bound strands and are often optically-labeled to indicate that the binding event has occurred. Detection is determined through correlation of the location of known oligo sequences in the microarray and the indication of a binding event with the DNA in the sample. For a pathogen detection application, for example, the microarray can be populated with oligos with sequences unique to a given pathogen. Positive optical detection of binding implies the presence of the pathogen in the sample.

Microarrays can consist of thousands of different oligos, making microarrays a very powerful tool for multiplexed pathogen detection or sequencing. One drawback of microarrays for pathogen detection is that they can exhibit long hybridization times, up to several hours, making them unattractive for fast detection applications.

## Project Goals

The long hybridization time makes the microarrays less attractive for detection when thousands of samples must be processed. Factors affecting the hybridization time were investigated to assess if the process time could be minimized.

**Table 1.** Typical sample processing steps.

Processing step	Typical processing time
Culture	16 h
Purification	1 h
PCR	1 h
Label	30 min
Hybridize	16 h
Wash	15 min
Read array	15 min

**Table 2.** Factors affecting hybridization times.

Factors affecting hybridization time	Effect	Mitigation steps
Temperature	Activity	Maintain about 40 °C
Concentration of nonbound	Interaction time	Increase concentration, mixing
Number oligos bound	Detection limit	System design
Optics	Detection limit	System design
Background	Detection limit	Wash step
Competitive assay	Interference (2)	Design of assay
Hairpins in oligo	Lower association rate (1)	Design of oligos
Free vs. bound hybridization	Steric effects lowers activity for bound oligos(1)	

## Relevance to LLNL Mission

Microarrays are used in the biodetection program at LLNL to identify known pathogens in field samples and ultimately to help identify emerging pathogens through their RNA sequences.

## FY2007 Accomplishments and Results

Typical assay processing steps include culturing of the sample, purification of the DNA or RNA, converting RNA to cDNA, performing PCR amplification, labeling the DNA, performing hybridization to the microarray, washing the array and reading the results. The processing time can be lengthy. Typical assay processing times for each step are listed in Table 1.

It is clear from Table 1 that culturing and hybridization times are the main obstacles to obtaining timely assay results. Culturing is used for initial amplification and purification and PCR can be used in some circumstances to substitute for these functions. The elimination of the culturing step will reduce the overall assay time. Several of the factors affecting hybridization time are shown in Table 2. Of the factors shown in Table 2, increased concentration and mixing can have a substantial effect on hybridization times without changing the assay or the hardware. That said, assay/oligo models, including the existence of hairpins in the oligos, which reduce activity, can eliminate gains

achieved though increased concentration/mixing.

Microarrays can have tens of thousands of spots per array. The Nimblegen system used by LLNL builds the microarray on a microscope slide over an area measuring approximately 18 mm x 13 mm. The oligo strands arrive at the surface through a combination of convection and diffusion. A typical diffusion coefficient for DNA strands is  $1 \times 10^{-7}$  cm<sup>2</sup>/s. Using this number, one can calculate the time required for strands to migrate via diffusion from the edge of a hemisphere of a radius calculated such that the enclosed volume contains the number of strands for a given concentration of the strands in solution. The results of this calculation assuming a 10<sup>6</sup> oligo detection limit is shown in Fig. 1 as the “diffusion” curve. Similar results are plotted for the “Maui” mixer, which is currently used to enhance the mixing of the solution. The Maui mixer is a laminar flow device that pushes the sample fluid back and forth past the chip. While there is convection in the flow direction, vertical and lateral mixing is likely to be the result of diffusion only.

As the concentration of strands in solution decreases, a greater volume of liquid is required to provide the required strands for detection and the reaction time increases to allow the strands to migrate from the limits of the volume to

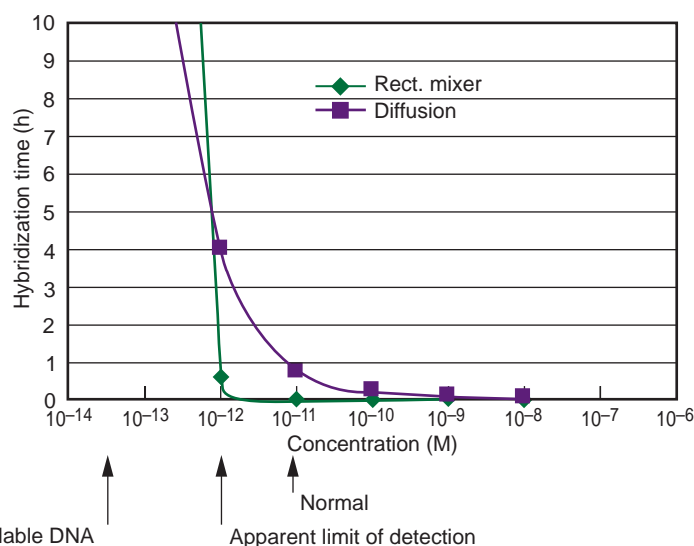


Figure 1. Calculated hybridization times for diffusion (diamonds) and Maui (rectangles) mixer.

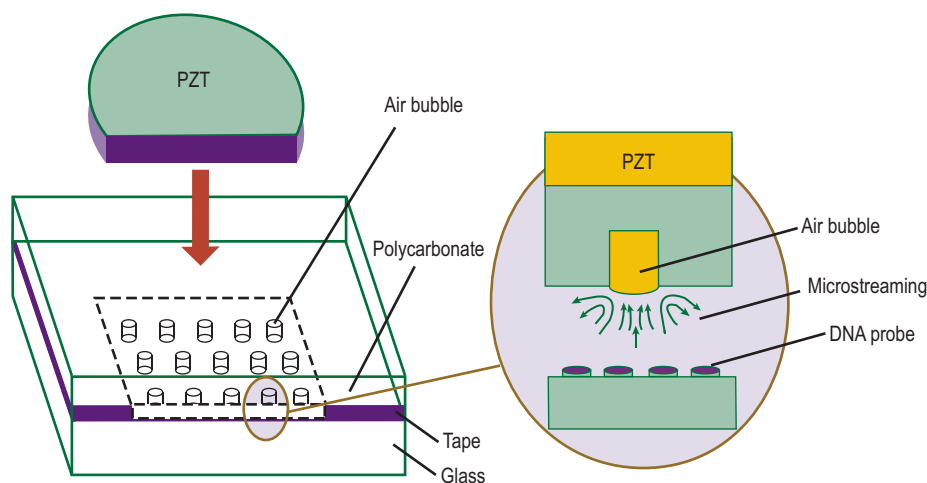


Figure 2. Schematic of acoustic-streaming mixer.

Table 3. Data of hybridization times for various conditions.

DNA Sample Source	Concentration	Mixer Type	Hyb. Time (h)	Detected (Y/N)
E. coli	$4.6 \times 10^{-11}$	Maui	2	Y
E. coli	$4.6 \times 10^{-11}$	Maui	1	Y
E. coli	$4.6 \times 10^{-11}$	Acoustic-streaming	2	Y
E. coli	$4.6 \times 10^{-11}$	Acoustic-streaming	1	Y
E. faecalis	$6.5 \times 10^{-12}$	Maui	2	Y
E. faecalis	$2.2 \times 10^{-12}$	Maui	2	Y – on verge of non-detection

the bound oligos. The knee of the curve is at about  $10^{-12}$  to  $10^{-11}$  M. Above this concentration, reactions happen in less than 1 h. Below this concentration, many hours may be needed to complete the reaction.

Mixing can aid in reducing the hybridization time between the knee and the ultimate limit-of-use, which occurs when the number of oligos in the sample is equal to the detection limit. Improvements over the Maui mixer would consist of a device that provides convective mixing from all parts of the sample volume. On the microscale, acoustic streaming, chaotic advection, and manipulation through electric fields represent methods for effecting mixing in an inherently low-Reynold's number regime. A mixer based on acoustic streaming instigated at the air-water interface of an array of bubbles, as shown in Fig. 2, was built and tested along the Maui mixer. Test data in Table 3 shows that acoustic streaming is at least as effective as the Maui mixer. Future effort will focus on understanding the effects of mixing in both the Maui mixer as well as the acoustic streaming device on the surface hybridization and detection process for various concentrations of the analyte/sample.

### Related References

- Gao, Y., *et al.*, "Secondary Structure Effects on DNA Hybridization Kinetics: A Solution Versus Surface Comparisons," *Nucleic Acid Research*, **34**, pp. 3370-3377, 2006.
- Zhang, Y., *et al.*, "Competitive Hybridization Kinetics Reveals Unexpected Behavior Patterns," *Biophysical Journal*, **89**, pp. 2950-2959, 2005.
- Gadgil, C., *et al.*, "A Diffusion-Reaction Model for DNA Microassay Assays," *Journal of Biotechnology*, **114**, pp. 31-45, 2004.
- Liu, R. H., *et al.*, "Hybridization Enhancement Using Cavitation Microstreaming," *Anal. Chem.*, **75**, pp. 1911-1917, 2003.
- Michel, W., "Optical Study of DNA Surface Hybridization Reveals DNA Surface Density as a Key Parameter for Microarray Hybridization Kinetics," *Biophysical Journal*, **92**, pp. 999-1004, 2007.

# Microfabricated Silicon Nib for Low-Cost, Multiplexed Micro-Coating



Erik V. Mukerjee  
 (925) 423-4841  
 mukerjee2@llnl.gov

Chemical and biological detection systems are key areas of interest at LLNL, directly supporting its mission of nonproliferation and homeland security. Many modalities of sensor platforms are presently being pursued (e.g., BAMS, IMS, GC-MS), including novel microscale detection systems. Current LLNL micro-cantilever-based detection systems have shown promise for both biological and chemical detection and identification. This system couples organic polymer (polyolefin) swelling to mechanical stress causing resistance changes in the sensing element as a function of analyte exposure.

However, the fabrication and integration of these systems involves time-consuming serial processes for coating each micro-cantilever with the chemically sensitive polymer. The current coating set-up consists of a single-machined stainless steel nib (tip of a fountain pen) structure engineered to wick and store fluid into a reservoir until dispensed via contact with a higher surface energy material. Mechanical contact between the nib and cantilevers often causes the cantilevers to break. The fixed

large reservoir capacity is governed by macroscale machining and therefore the dispensing volume is controlled by differences in surface energies and not by total reservoir volume.

The effort of this work was to use a modified coating structure similar to the meso-contact printing mechanism currently in use. Creating an in-plane silicon array of micro-coating structures will enable much faster throughput of polymer film selection and trials. Film thickness uniformity across devices is essential for device functionality. The sheer volume of polymers trials/selection necessary for sensor viability and selectivity almost certainly precludes serial coating methods.

## Project Goals

The goal of this project is to fabricate a multiplexed polymer micro-coating system. Near term application is specific to the GS chemical agent detection project; however, the application space can be expanded to include chemical/biological assays and microscale organic materials deposition processes.

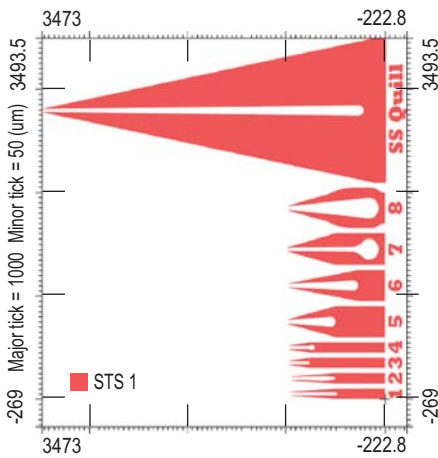


Figure 1. Schematic of nib geometries including the current stainless steel configuration.

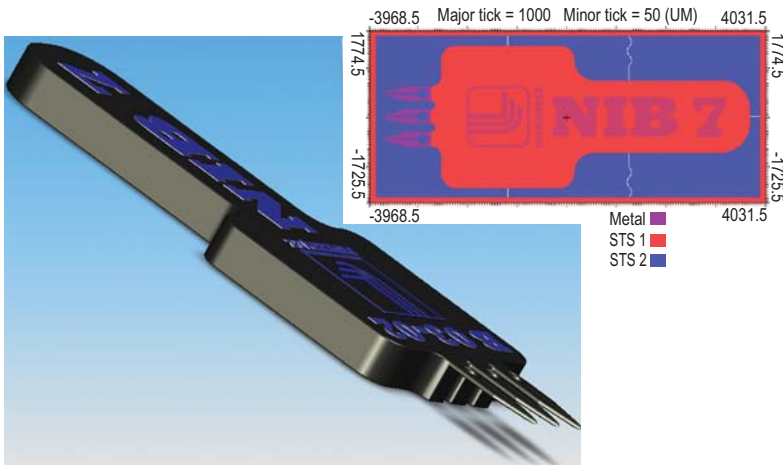


Figure 2. Illustration of final nib structure and mask (insert).

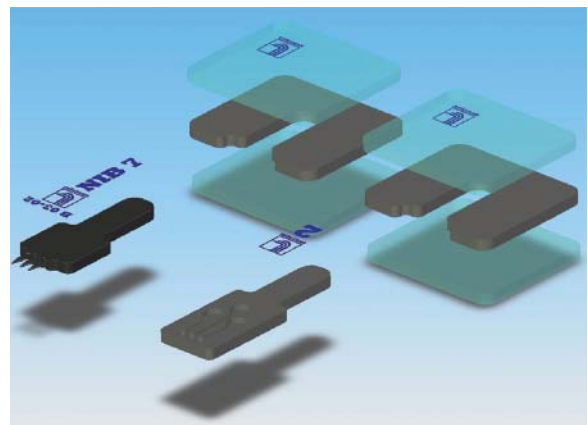


Figure 3. Exploded schematic of nib, reservoir, and universal socket structures.

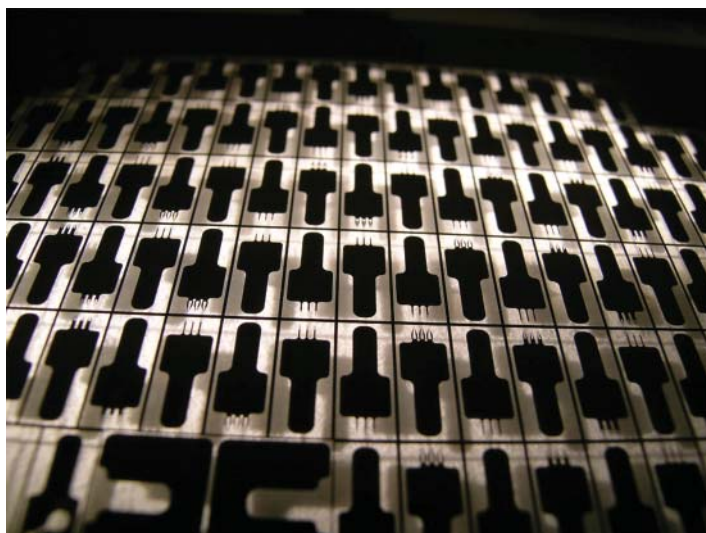


Figure 4. Wafer level view of various nib configurations.

### Relevance to LLNL Mission

Work on this device advances several processing techniques to extend LLNL's capabilities and will produce a significant technological impact on the instrumentation community. The resulting technologies will aid in the fabrication of deployable detection systems that are well aligned with the national security mission of LLNL, *e.g.*, biodetection of pathogens and chemical warfare agent detection.

### FY2007 Accomplishments and Results

In FY2007 the milestones that were achieved include layout, fabrication, characterization, and testing of several silicon micro-nib structures. An

overarching technical challenge was thickness uniformity of the individual final nib elements. Cross-wafer etch rates of the deep reactive ion etcher (DRIE) varied as a function of position on the silicon substrate (1.8  $\mu\text{m}/\text{min}$  to 2.4  $\mu\text{m}/\text{min}$ ,  $\sim 25\%$ ). This resulted in final device thicknesses ranging between 5  $\mu\text{m}$  to 125  $\mu\text{m}$  on a single silicon substrate. Changing localized loading effects (*i.e.*, amount of exposed silicon in a given region) improved etch uniformity to an acceptable level of  $\sim 10\%$ .

Each lithographic mask set produced 1) eight nib geometries; 2) three reservoir geometries; 3) universal sockets;

and 4) a set of larger demonstration structures (4x larger).

The nib geometries varied in length (0.5 mm to 1mm, and 3.5 mm for stainless steel); total reservoir volume (4 nl to 25 nl, and 400 nl for stainless steel); and volume to surface area (15:1 to 50:1, and 35:1 for stainless steel). The universal sockets facilitated rapid switching of nib configuration during characterization runs and fit both the nibs and the reservoir structures. The testing assembly consisted of two micromanipulator stages (X-Y cantilever mounted stage, X-Z nib mounted stage) and a stereoscope for visualization of cantilever coating.

Results are as follows:

1. Maximum fracture load
  - a. Average nib 1 through 4: 1.3 N
  - b. Average nib 5 through 8: 3.8 N
2. Average spot size (0.1% polyolefin/dioxane, nibs 5 through 8 on planar silicon nitride surface): 423  $\mu\text{m}$   $\pm$  5%
3. Nib thicknesses 20  $\mu\text{m}$  to 30  $\mu\text{m}$  most consistent dispensing
4. Cantilever coating
  - a. Dummy cantilevers structures (nibs 6 and 7 most consistent)
  - b. Real cantilever sets (nibs 6 and 7 to be tested and run against various analytes)

From these results, optimal nib geometries (nibs 6 and 7) and thicknesses (25  $\mu\text{m}$   $\pm$  5  $\mu\text{m}$ ) were determined for consistent/uniform polyolefin dispensing. This preliminary data suggest that the microfabricated silicon nib arrays can be used as a cost/time effective alternative to the serial stainless steel system currently in use.

### Related References

1. Baller, M. K., "A Cantilever Array-Based Artificial Nose," *Ultramicroscopy*, **82**, pp. 1-9, 2000.
2. Porter, T. L., "Sensor Based on Piezoresistive Microcantilever Technology," *Sensors and Actuators A-Physical*, **88**, pp. 47-51, 2001.
3. Sepaniak, M. "Microcantilever Transducers: A New Approach to Sensor Technology," *Analytical Chemistry*, **74**, pp. 568A-575A, 2002.
4. Then, D., "A Highly Sensitive Self-Oscillating Cantilever Array for the Quantitative and Qualitative Analysis of Organic Vapor Mixtures," *Sensors and Actuators B-Chemical*, **117**, pp. 1-9, 2006.



Figure 5. Demonstration of 1-to-1 registering of nib elements with micro-cantilevers and size comparison with current stainless steel nib structure.

# Advanced Polymerase Chain Reaction Module



Satinderpall  
Pannu  
(925) 422-5095  
pannu1@llnl.gov

**P**olymerase chain reaction (PCR) is a widely used technique for amplifying DNA signatures. It is used in many biodetection systems such as LLNL's Autonomous Pathogen Detection System (APDS). To create a field deployable system, the current PCR reactors have to be miniaturized in terms of size, weight, reagents, and detection times.

This project describes the implementation of an advanced PCR module with an integrated polyimide heater and an integrated temperature sensor. An older version of this PCR module is currently an integral component of the APDS and ASTEP programs. The current PCR module uses a series of discrete resistors to heat a thermal mass during the PCR cycle. However, these discrete resistors and the temperature sensor are mounted on the outside of the thermal mass. The heater and the temperature sensor can be integrated into a polyimide flex cable and mounted inside the thermal mass near the reagent tubing. This implementation will improve the thermal efficiency and temperature sensor reading. This new PCR module will improve the

performance of the APDS and ASTEP programs by improving the reliability and minimizing the power requirements of the module. These programs are vital to the Laboratory's mission in homeland security.

## Project Goals

This project implemented a fully characterized PCR module with integrated polyimide heaters and temperature sensors. The characterization will focus on measuring the thermal performance of each module and the thermal stability as a function of time.

## Relevance to LLNL Mission

The need for advanced PCR modules that allow for the detection of biological and chemical agents is directly aligned with LLNL focus areas that outline key technology needed for biological security/defense of the nation. This project will enable a robust, reliable PCR module that is field deployable in systems such as the APDS. There is also a significant opportunity to produce intellectual property in novel integration and assembly techniques.

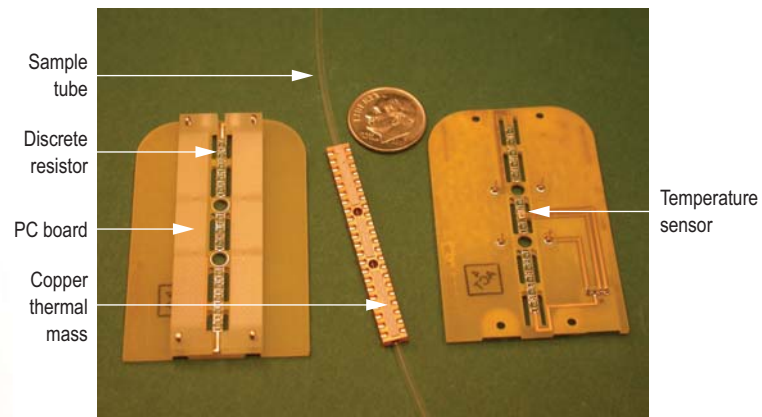


Figure 1. Previous version of the PCR module with discrete resistive heaters and temperature sensor.

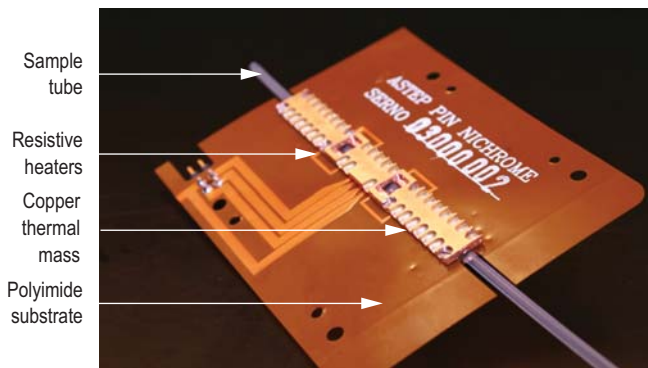


Figure 2. New version of the polyimide substrate for the PCR module with integrated resistive heaters and temperature sensor.



Figure 3. Complete PCR system with control electronics used to test the PCR module.

### FY2007 Accomplishments and Results

The previous version of the PCR module is shown in Fig. 1. It consists of discrete resistors mounted to a printed circuit board. The temperature sensor is also mounted to the printed circuit board. The discrete resistors and the temperature sensor are mounted to the copper thermal mass that has a through hole for the reagent tube. The reactants for PCR are contained in this tubing and reactants are kept in the middle of the thermal mass to provide a uniform temperature to the reactants.

The previous version of the PCR module has several failure modes including delamination of the discrete resistors from the thermal mass and a varying temperature offset from the temperature sensor since it is mounted away from the reagent tubing. In order to correct

these issues, the discrete resistors were replaced with a high-resistance, thin-film nickel alloy laminated on polyimide. Further, the temperature sensor was mounted onto the polyimide substrate as well to place it in contact with the reagent tubing. The polyimide substrate with integrated resistive heating elements and temperature sensor was fabricated (Fig. 2).

The integrated heaters on the polyimide substrate were tested for long-term reliability, and passed successfully. The temperature sensor was also integrated onto the polyimide substrate and tested successfully. This polyimide substrate was then integrated into the PCR system for testing and evaluation. The complete PCR system is shown in Fig. 3.

For the first test, two positive controls and one negative control were pumped into the reagent tubes. Forty-five PCR cycles were run to verify that the PCR was successful. As expected, signals from the positive controls increased with each PCR cycle and the negative control signal remained flat. Next, a target DNA molecule was inserted into the sample and a new test was performed. Again, the test was successful. The signal from the positive control increased with each cycle as well as the target signal. The negative control performed as expected.

Upon the successful completion of these tests, this technology was transferred to the APDS and ASTEP programs, and these programs are currently integrating this technology into their systems.

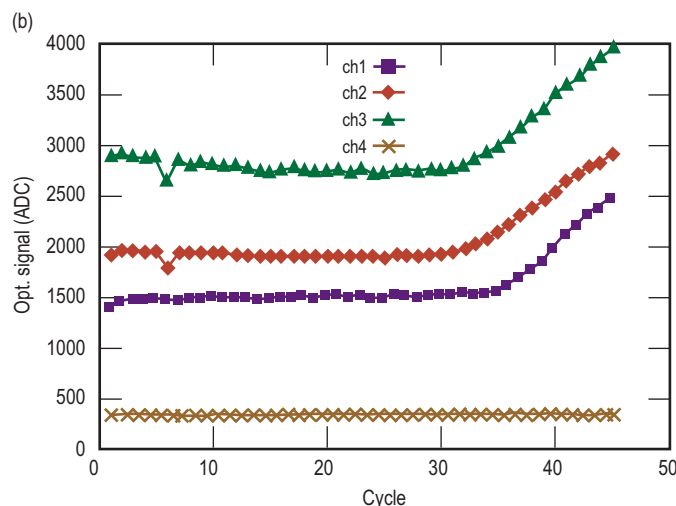
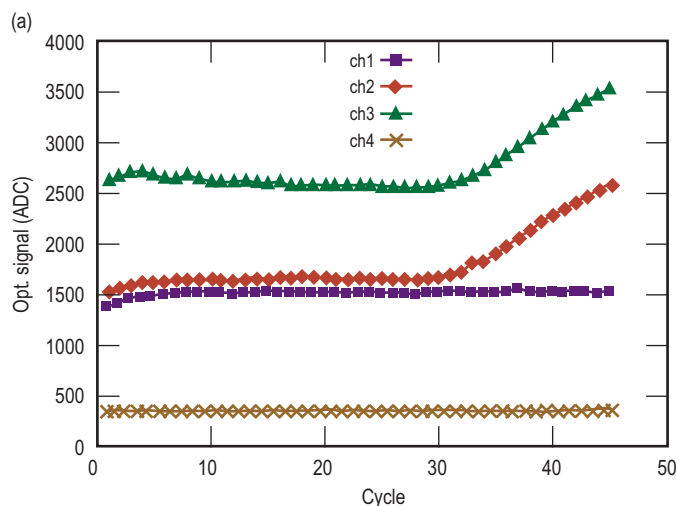


Figure 4. (a) Performance of the PCR module with only control samples and no target; (b) performance of the PCR module with the controls and a target.

# Tunable Optical Cavities for Gas Sensor



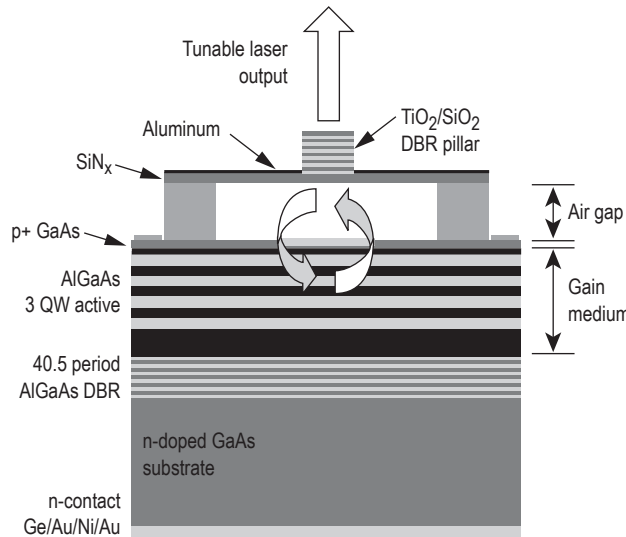
Tijiana Bond  
(925) 423-2205  
bond7@llnl.gov

**T**race-gas analysis is critical for real-time environmental monitoring, weapons surveillance, combustion studies, and space exploration. Tunable diode laser absorption spectroscopy (TDLAS) is a powerful approach for in-field IR chemical detection and identification. Recently, MEMS tunable vertical cavity surface emitting lasers (VCSELs) have been implemented for NIR TDLAS. We are exploiting this technology to bridge a capability gap in sensing low weight

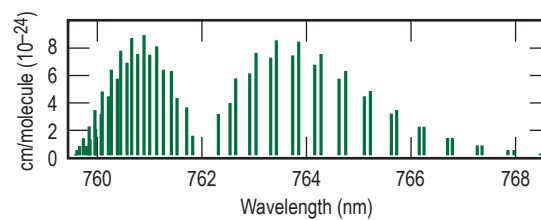
molecules, and to extend it to a miniaturized gas *in-situ* detection platform with built-in multiplexed detection potential. Ground or avionic systems that respectively need unattended, flexible or lightweight, highly sensitive sensors will greatly benefit from this approach.

The technology relies on extended coupled cavity (ECC) MEMS-tunable vertical cavity devices: the epitaxial material is engineered to align the laser emission to a specific absorption wavelength (coarse tuning), and the top suspended mirror causes a continuous scanning across the absorption lines of the gas (fine tuning) when deflected by an applied voltage. The device will be used for standard TDLAS. Ultimately, it can be described as a multipass cell with optical gain (Fig. 1). In operation, the laser is electrically driven above threshold; the gas flowing through the air gap spoils the gain-loss balance necessary for lasing by increasing the absorption losses within the cavity. Absorption is enhanced as the light is reflected several times within the resonant cavity, between the top and bottom distributed Bragg reflectors (DBRs).

**Figure 1.** Cross-sectional schematic of MEMS tunable ECC-VCSEL for O<sub>2</sub> sensing. The presence of gas in the air gap quenches the laser emission when the resonance wavelength is tuned to correspond with an appropriate absorption line.



(a)



(b)

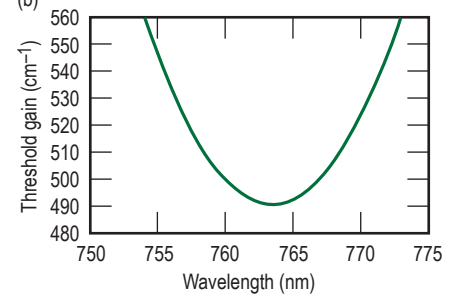


**Figure 2.** (a) Signature of O<sub>2</sub> at ~760- HITRAN source; (b) modeled laser threshold gain displaying continuous emission tuning for O<sub>2</sub> sensing.

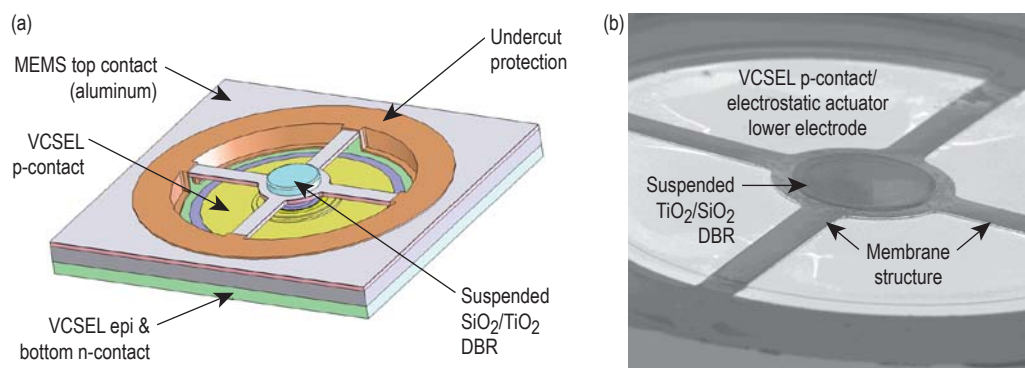


**Figure 3.** (a) 3-D model of the tunable VCSEL. Note that the scale of the air gap has been exaggerated to clarify the free-standing nature of the micromechanical structure. (b) SEM picture of tunable membrane.

## Project Goals

Our goal is to establish complex fabrication procedures to reliably reproduce electrostatically tunable MEMS vertical lasers. The project focuses on reducing them to efficient and miniature gas sensors. Finally, we wish to explore their effectiveness, in selectively detecting the signature absorption lines of the gas of interest, and the limit of detection (LOD) both theoretically and experimentally. We expect to be able to scan with a very narrow linewidth ( $< 1$  pm) the full 10- to 20-nm gas spectrum with actuation voltages  $< 10$  V, and power consumption of a few mWs.

An example of gas spectral signature is given in Fig. 2 (a) for  $O_2$ . Some initial estimates of the sensitivity show that LODs of 100s of ppm (for a system level resolution  $\Delta P/P = 10^{-3}$ ) are achievable for gases with cross-sections  $\sigma_{NIR} \sim 10^{-22}$   $cm^2/molecule$ .

## Relevance to LLNL Mission

Our project supports several applications at the core of LLNL's national security missions, from Stockpile Stewardship to Homeland Security. It will

sustain the generation of a new class of compact, fiber compatible optical gas sensors for real-time detection of chemical agents. This will facilitate minimally invasive trace-gas analysis for next-generation weapons with built-in persistent surveillance; monitoring of in-field explosive detection; nuclear material production activities and environmental pollution; and healthcare. The 2-D nature of the technology enables other interesting applications such as multiplexed smart detection systems, adaptive imaging, beam forming, optical computing, and high power lasers.

## FY2007 Accomplishments and Results

In the first year we started, as planned, with a survey of the state-of-the-art technology reported in literature for low-weight molecules detection and investigation of gas species spectral properties. We down selected  $O_2$  for a proof-of-concept at  $\lambda = 760$  nm, based on membrane and epilayers requirements and constraints. We have assessed and established the required processes on dummy samples (Fig. 3). We have fabricated 760-nm LEDs on the

epistructure (Fig. 4), which performed well, demonstrating the good quality of the material. We have set up optical and mechanical measurement systems for (tunable) MEMS characterization. Fixed and tunable VCSELs have been fabricated, tested and are going through troubleshooting for optimization.

## Related References

1. Welre, P., *et al.*, "Near and Mid-Infrared Laser Optical Sensors for Gas Analysis," *Optics and Lasers Engin.*, **37**, pp. 101-4, 2002.
2. Kogel, B., *et al.*, "Micromechanically Widely Tunable VCSEL for Absorption Spectroscopy at Around 1.55," *IEEE MEMS Conference*, MA2, pp. 7-8, 2006.
3. Cole, G. D., E. S. Björin, Q. Chen, C.-Y. Chan, S. Wu, C. S. Wang, N. C. MacDonald, and J. E. Bowers, "MEMS-Tunable Vertical-Cavity SOAs," *IEEE J. Quantum Elect.*, **41**, pp. 390-407, March 2005.

## FY2008 Proposed Work

We will complete the establishment of the enabling capability by fully characterizing the MEMS membrane and tunable VCSELs in terms of reflectivity, emitted power, spectra, voltage tuning, and power consumption. Preliminary gas testing experiments for  $O_2$  TDLAS at 760 nm will be attempted using existing facilities. The spectral and intensity cross-sensitivity to different gases will also be investigated. We will focus the efforts on gas testing and determination of spectral and amplitude sensitivity of the devices.

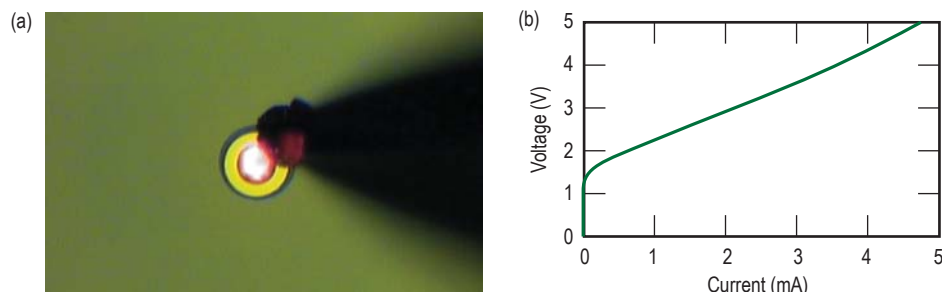


**Figure 4.** (a) Light emission from LED before completing full VCSEL process; (b) IV curve with the turn on  $< 2V$ .

# Extending Lasers to Universal Gates for Photonic FPGAs



Tiziana Bond  
(925) 423-2205  
bond7@llnl.gov

The photonic field programmable gate array (P-FPGA) is an all-optical integrated circuit that has the reprogrammability of software and the algorithm acceleration of application-specific hardware. The P-FPGA is a core enabling technology because of its speed and versatility (Fig. 1). Compared to electronic FPGAs, computational and functional

reprogramming speeds are one to two and three to four orders of magnitude faster, respectively, and so we expect a proportional speedup in signal processing, encryption, graphics rendering, or genetic algorithms. Other advantages are efficient gate usage, EMI insensitivity, and direct compatibility with optical signals used in communications and photonic sensors.

The basic array element of the P-FPGA is the reconfigurable universal logic gate (Fig. 2). With feedback, the gate can act as an optical clock source or as a SET-RESET flip-flop, *i.e.*, a single bit of memory. The gate is a multiple section quantum well laser, with three lateral input optical ports with a gate selection, and two lasing outputs. The specific logic operation performed by the gate is optically selectable. The mirrors are sampled grating distributed Bragg reflectors (SG-DBRs) configured to let the output facet alternate as the laser wavelength is tuned by the optical inputs. The mirrors and phase control sections are blue-shifted by quantum well intermixing (QWI) and thus are non-absorbing at the laser wavelength. The control and slave sections provide optical gain for the circulating power.

In summary, the critical effects in the device operation are: 1) special AR/HR mirrors to create an alternating output facet laser; 2) vernier effect to reduce tuning power, so that small refractive index change causes alignment of phase with round-trip gain to jump to the next wavelength; and 3) gain-index lever to reduce tuning power and generate enhanced wavelength modulation efficiency in multiple section lasers.

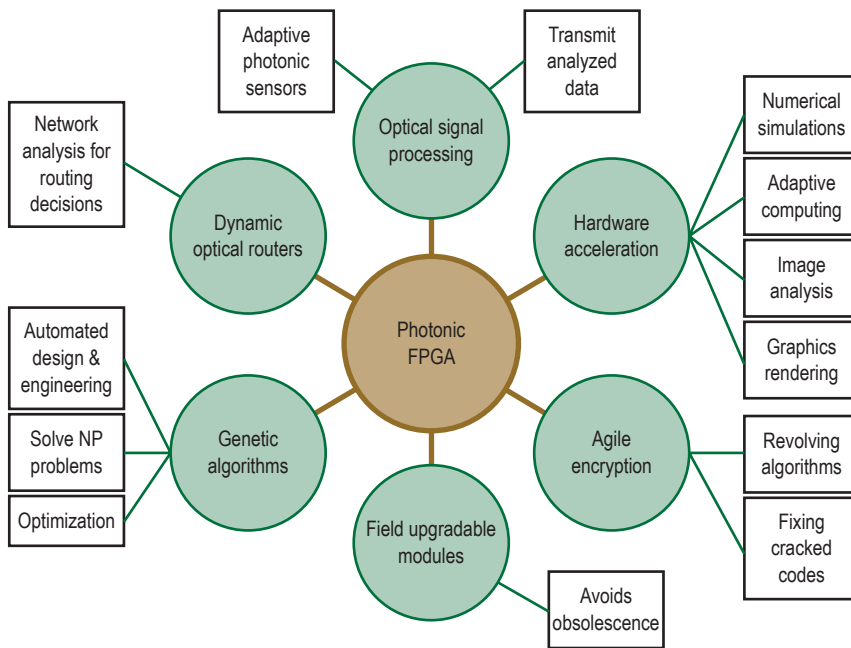


Figure 1. The P-FPGA, a core enabling technology that will enhance system performance.

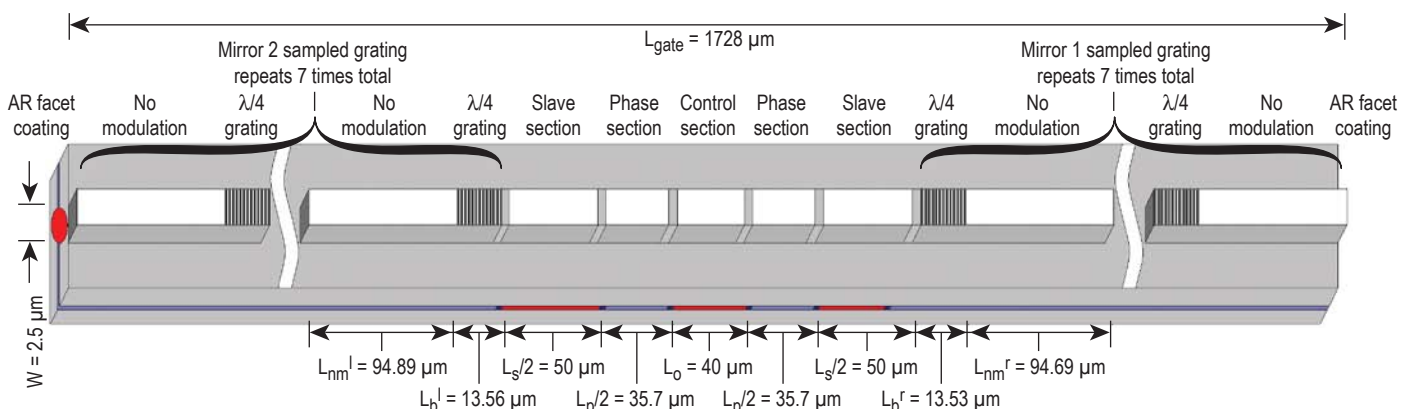


Figure 2. Layout (not to scale) for a universal logic gate. Laser output is the red ellipse. The active layer is shown in red. The active layers for the mirrors and the phase control section have been slightly blue-shifted using quantum well intermixing and are shown in medium blue. Heavily intermixed section boundaries are shown in dark blue.

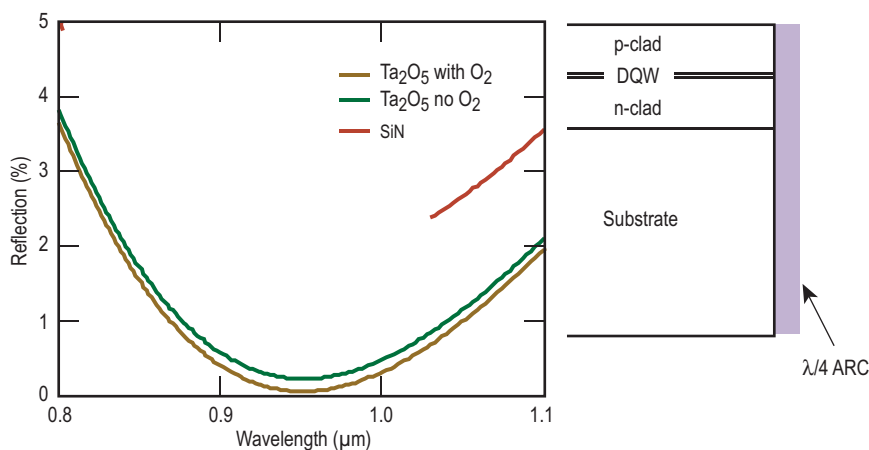


Figure 3. AR coating ellipsometry measurement results. The value  $n = 1.904$  for  $Ta_2O_5$  with the  $O_2$  backfill is the best ( $R_{min} < 0.1\%$  and  $R < 1\%$  over 150 nm allows slight inaccuracies in  $\lambda/4$  film thickness).

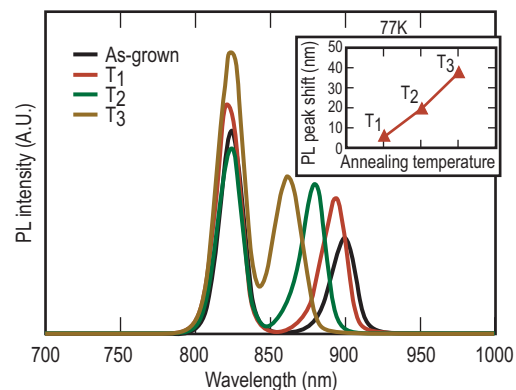


Figure 4. Photoluminescence (PL) of QWI for different annealing temperatures. PL excitation is 532 nm DPSS laser with excitation density  $200 \text{ W/cm}^2$ . Visible are the first peak (left) from GaAs and the second peak from InGaAs DQW. PL peak intensities increase after intermixing; a 38-nm shift is achieved at  $T_3$  (inset).

### Project Goals

This project focuses on establishing and troubleshooting some of the fundamental processing steps in a fairly complex fabrication procedure in order to reduce the universal gate to practice. Several of these processing steps (e.g., etched facet lasers, low-loss passive waveguides, mode-matched laser to waveguide interfaces, and waveguide turning mirrors) are routinely performed on site. The four other necessary capabilities are: deposition of AR  $\lambda/4$  coatings on etched facet lasers; mounting samples on patterned heat sinks; performing QWI; and defining SG-DBRs. The acquired techniques and professional relationships will expand LLNL’s processing capabilities and will be valuable to future projects.

### Relevance to LLNL Mission

The two applications of the P-FPGA of most interest to LLNL are implementing hardware-accelerated algorithms and processing data from photonics-based sensors because of their benefit to many Laboratory core applications. Some sample hardware-accelerated algorithms are 1) self-evolving genetic algorithms for efficiently solving NP problems; 2) adaptive computing for enhanced speed in computationally intensive simulations or graphics rendering; and 3) reconfigurable encryption algorithms for secure communications, e.g., constantly changing encryption algorithms or repairing broken algorithms in field deployed units. On-chip data processing would

expand the capabilities of all photonics-based sensors created at the Laboratory. For example, the sensors can adapt or make decisions based on collected data, or could transmit analyzed data rather than raw images when the downlink bandwidth is limited.

### FY2007 Accomplishments and Results

We have accomplished the following: 1) completed AR coating and gratings configurations; 2) characterized AR coatings and demonstrated a vertical facet deposition procedure (Fig. 3); 3) purchased, patterned, and evaluated heat sinks; 4) specified and procured a five-mask set; 5) established a collaboration to perform QWI and observe induced blue shift (Fig. 4); 6) fabricated multi-section lasers with new engineered epitaxial material and a new chemical etch recipe to handle an InGaP stop layer (Fig. 5); and 7) implemented

and used automatic measurement and post-processing techniques to evaluate the gain-index lever effect.

### Related References

- Vahala, K., *et al.*, “The Optical Gain Lever: A Novel Gain Mechanism in the Direct Modulation of Quantum Well Semiconductor Lasers,” *Appl. Phys. Lett.*, **54**, pp. 2506-2508, June 1989.
- Stohs, J., *et al.*, “Gain, Refractive Index Change, and Linewidth Enhancement Factor in Broad-Area GaAs and InGaAs Quantum-Well Lasers,” *IEEE J. Quantum Electron.*, **37**, pp. 1449-1459, November 2001.
- Todt, R., *et al.*, “Demonstration of Vernier Effect Tuning in Tunable Twin-Guide Laser Diodes,” *IEEE J. Proceed.*, pp. 66-71, April 2005.
- Goddard, L., *et al.*, “Rapidly Reconfigurable All-Optical Universal Logic Gates,” *Proc. SPIE*, **6368**, pp. 6368 OH-1-13, October 2006.

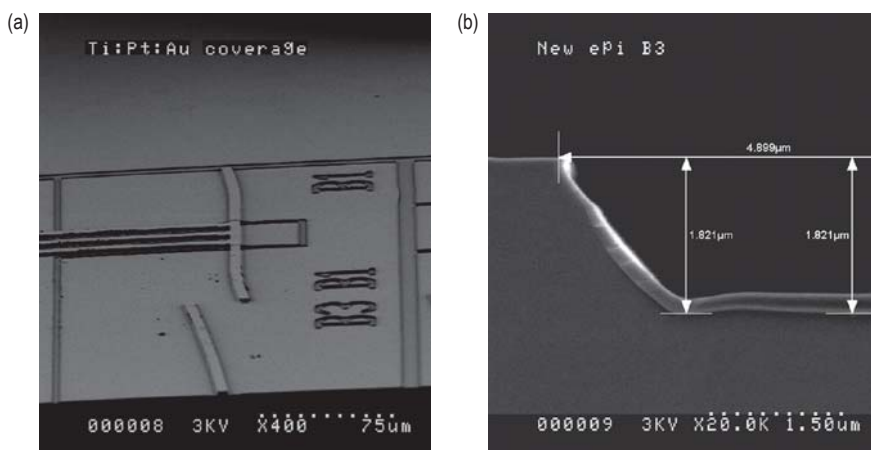


Figure 5. SEM of (a) 3-side input InGaAs QW laser; and (b) lateral ridge etch.

# Compact Tunable Optical Sensors



*Jack Kotovsky*  
(925) 424-3298  
kotovsky1@llnl.gov

This project reduces to practice a scanning Fabry-Perot (FP) cavity-based absolute conditioner, an “optical force probe” (OFP), and an “optical gap gauge” (OGG). Two tasks were attempted to establish the FP conditioner: 1) fabrication of a transimpedance amplifier to reduce detection circuitry noise for observing fringes; and 2) experimental verification of a synthesized broadband light source using two or three different wavelength LEDs. We also demonstrate experimental results for the fiber-based OFP that is capable of sensing compressive loading transverse to the long-axis of an optical fiber. We have achieved experimental results for a fiber-based OGG capable of measuring displacements transverse to the long axis of a fiber. These devices constitute a class of compact optical sensors realized through the integration of microfabricated and machined components and strain sensitive fiber Bragg grating (FBG) elements.

## Project Goals

For the conditioner, a new amplifier is needed primarily when using an incandescent bulb or broadband

light source for illumination, since the optical intensity in the fiber is very low with these sources. Furthermore, this amplifier will help make more accurate measurements when using the brighter LED light sources.

The goals of the OFP and OGG are to demonstrate tunable sensors appropriate for weapons and other load and displacement measurements. The sensors must be inherently safe and able to accurately perform measurements over long periods of time without access to the sensor.

## Relevance to LLNL Mission

LLNL’s stockpile stewardship mission demands microsensors and signal conditioning that are able to survive harsh environments of temperature, vibration, and radiation while maintaining very small form factors, inherent safety, and long-term accuracy. These constraints pose significant challenges and require low-power methods, microscale features and carefully configured devices and material choices. These technologies address these performance goals.

## FY2007 Accomplishments and Results

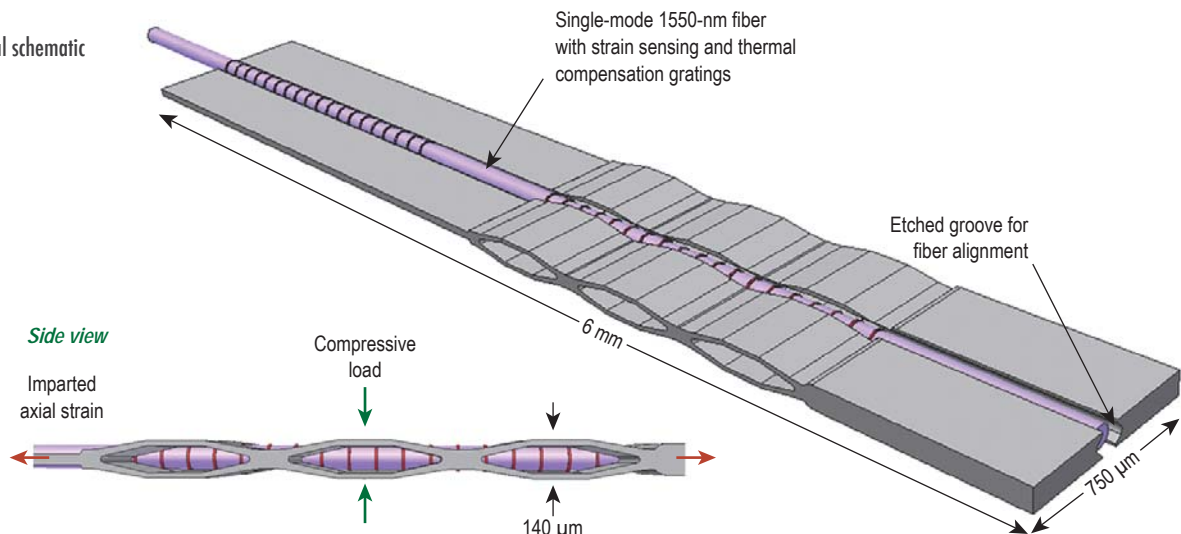
For the optical conditioner, a new amplifier was built that gave a 10-dB improvement in signal/noise ratio.

A multi-LED package was obtained to experiment with the synthesized light source. It consisted of LEDs ranging in wavelengths from 570 nm to 850 nm, covering most of the bandwidth of interest. Two problems with this new light source were a significant difference in intensity between the shortest wavelength LED and the longest wavelength LEDs, and a spacing of the LEDs that would not allow simple coupling of multiple LEDs into one fiber. Several experimental setups were tried to solve these problems.

Uniform intensity can be achieved at the cost of some loss of intensity by simply attenuating the light from the brighter LEDs; however, coupling multiple LEDs into a fiber proved to be a more difficult problem. It will require the implementation of a special coupling structure, which will be addressed in a future effort.

Figure 1 shows a 3-D schematic of the OFP. The device is a hybrid optical

Figure 1. Three-dimensional schematic of the OFP.



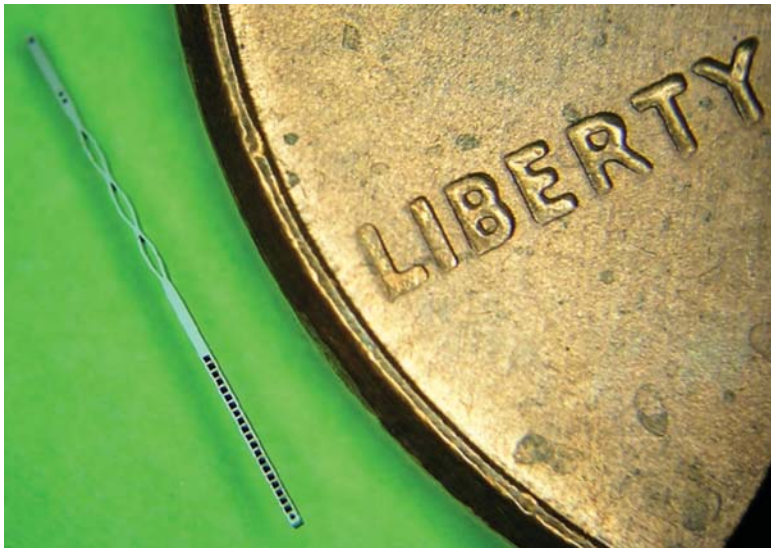


Figure 2. A microfabricated silicon component of the OFP, pictured next to a US penny for scale.

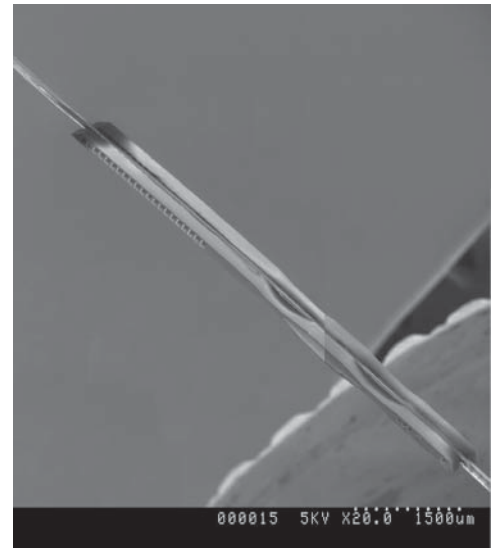


Figure 4. SEM of a completed OFP. This view was generated by stitching together two separate images.

fiber sensor consisting of a fiber-based strain-sensing element integrated with micromachined transducers. The strain-sensing element consists of a single-mode 1550-nm optical fiber containing two FBGs (one for load sensing, one for thermal compensation). The transducer elements, an example of which can be seen in Fig. 2, consist of single-crystal silicon (SCS) structures that are micro-machined to define geometry for fiber alignment as well as mechanical transduction, converting an applied compres-

sive load to a tensile strain in the fiber. Finite element simulations are used to properly dimension the flexure elements.

A typical axial strain response is included in Fig. 3. Under an applied compressive load, the transducers generate a tensile strain along the fiber, increasing the periodicity of the FBG and resulting in a red shift in the peak reflectance that can be recorded via standard FBG interrogation hardware.

An SEM of a completed OFP is presented in Fig. 4. Data from a

single-transducer sensor is presented in Fig. 5. In this experiment, the sensor was subjected to a compressive load resulting in an applied pressure varying from 40 to 180 psi. The sensor exhibits a repeatable linear response in the range of 60 to 180 psi with a sensitivity of 6.52 pm/psi. Assuming a strain-induced peak shift of 1.21 pm/ $\mu\epsilon$  at 1550 nm, this converts to an axial strain transduction of 5.38  $\mu\epsilon$ /psi for this geometry.

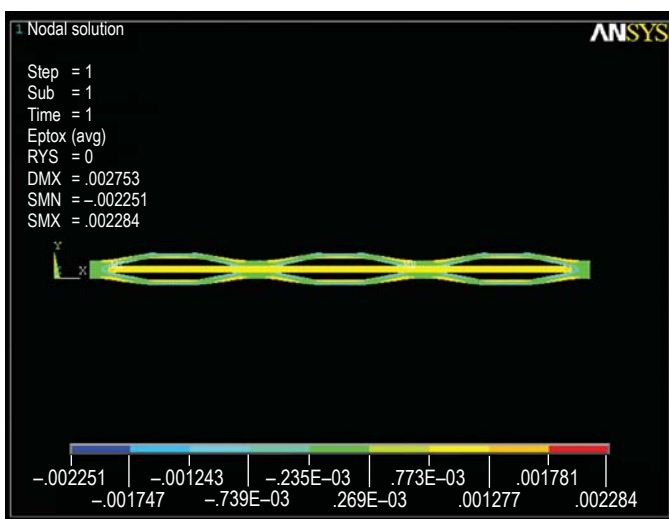


Figure 3. Finite element simulation of the OFP strain response. The device modeled here has three sets of 40- $\mu\text{m}$  flexures. At 200 psi, 773  $\mu\epsilon$  is imparted to the optical fiber sensor.

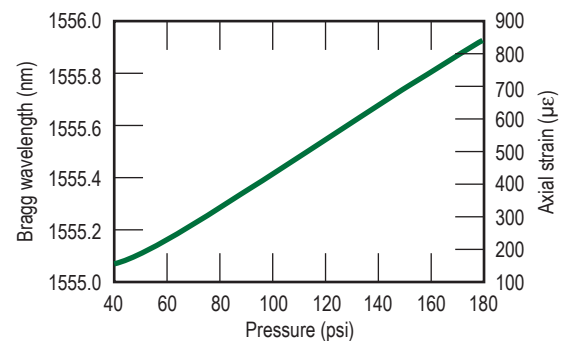


Figure 5. Typical response of the single-transducer OFP to a loading cycle up to 180 psi.

# Transport Behavior and Conversion Efficiency in Pillar Structured Neutron Detectors



Rebecca J. Nikolic'  
(925) 423-7389  
nikolic1@llnl.gov

**R**oom temperature, high efficiency and scalable radiation detectors can be realized by manipulating materials at the microscale. With micro-semiconductor-pillars, a thermal neutron detector with an efficiency of over 70% is possible. New material science, new transport behavior, neutron-to-alpha conversion dynamics and their relationship with neutron detection will be discovered with the proposed structures.

## Project Goals

Our goals for FY2007 include:

- 1) neutron-to-alpha conversion efficiency in high resistivity CVD  $^{10}\text{B}$  films and understanding of impurities;
- 2) thermal neutron detector demonstration with 20+  $\mu\text{m}$  pillar height;
- 3) electron and hole transport in vertical high-aspect-ratio structures; and
- 4) model of pillar detector that includes both nuclear physics and semiconductor device physics.

## Relevance to LLNL Mission

Radiation detection requires both neutron and gamma detectors that are inexpensive, operable at ambient temperature, high efficiency and robust. Currently available detectors typically fall short in at least one of these areas.

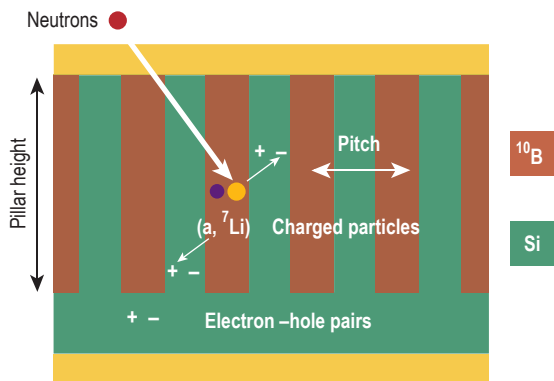


Figure 1. Schematic diagram of pillar detector design.

$^3\text{He}$  neutron detectors are currently used for typical neutron detection. However, they have major fieldability issues, such as microphotonic interference, high voltage, and large device footprint. Also, the  $^3\text{He}$  gas makes air transport difficult. New materials and device structures are needed for revolutionary improvement in radiation detectors. By applying microtechnology methods to the area of neutron detection, we will be able to make revolutionary improvements in the device efficiency and fieldability.

The proposed solution has a large potential payoff in the area of national security. If all of the requirements in our proposed device can be met, these detectors would be manufactured by partnering with an industrial collaborator and readily deployed to many agencies.

## FY2007 Accomplishments and Results

A schematic diagram of the detector is shown in Fig. 1. The platform consists of a P-I-N layer structure grown epitaxially on an n+ silicon (Si) substrate. The epitaxial Si is dry-etched utilizing high-density plasma to form the pillars

structure. The converter material ( $^{10}\text{B}$ ) is deposited on the sample in the space between the pillars by chemical vapor deposition (CVD) (Fig. 2).

In FY2007 we have achieved a fill factor of 95+ % for pillar diameter of 2  $\mu\text{m}$ , pitch of 4  $\mu\text{m}$ , and height of 12  $\mu\text{m}$  with  $^{10}\text{B}$ . By using this inter-digitated device structure, charged particles (alpha and  $^7\text{Li}$ ) from the thermal neutron -  $^{10}\text{B}$  reaction have a higher probability of impinging on the Si P-I-N structures, where electrons and holes are created, which results in high efficiency.

The pillar detector roadmap was further developed in FY2007 using Monte Carlo N Particle (MCNP) transport code to simulate a near-by neutron point source interaction with the structure, after which the range of the charged particles was calculated using Ion-Range-In-Matter (IRMA) code (Fig. 3).

Further refinement of the pillar detector model was carried out by determining the energy loss within the semiconductor pillar. Silvaco's Atlas was then used to calculate the transport of the electrons and holes generated by the alpha and  $^7\text{Li}$

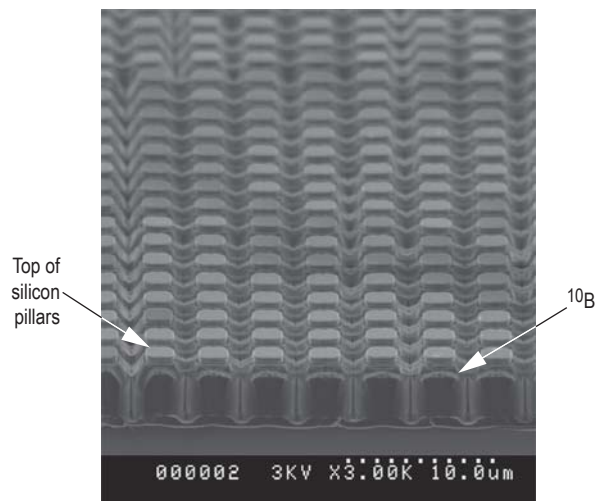


Figure 2. SEM of pillar platform filled with CVD  $^{10}\text{B}$ .

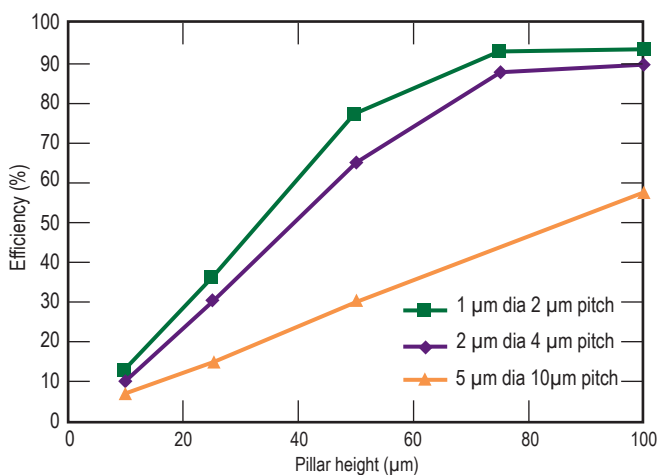


Figure 3. MCNP and IRMA simulations of thermal neutron capture efficiency versus pillar height for several pillar diameters and pitches.

particles in the Si diode portion of the detector at sampled particle energies and heights within the pillar. The collected charge was then calculated by scaling the energy deposited by the ionized particles in the Si pillars by the percentage of carriers that recombine before reaching the contacts, as determined from Atlas charge transport simulations. The pillar geometry simulated in this work had a height of 20 μm, diameter of 2 μm and a pitch of 4 μm. The resulting energy spectrum for the pillar detector is shown in Fig. 4, for 4 million neutron histories and a minimum energy threshold for detection of 100 keV. For the geometry used the efficiency simulated is 18%. This is compared to the 24 % efficiency simulated for the same structure

without including the energy loss within the silicon pillars.

Neutron measurements were performed using a 12-μm pillar detector filled with the <sup>10</sup>B converter material, as shown in Fig. 5. A <sup>252</sup>Cf neutron source with neutron flux of 2.3 x 10<sup>6</sup> n/s was embedded in 15-cm-thick polyethylene blocks for the measurement. The measurement time was 20 h. To obtain the thermal neutron efficiency, the observed events were compared with results from a Monte Carlo simulation. The thermal neutron detection efficiency is estimated to be 7.3 % with an error of 1.4 %.

**Related References**

1. Deo, N., J. Brewer, C. L. Cheung, R. J. Nikolic, C. E. Reinhardt, and T. F. Wang,

- “Chemical Vapor Deposition of Boron for Neutron Detector Application,” Materials Research Society (MRS) Spring Meeting, San Francisco, California, 2007.
2. Deo, N., J. Brewer, C. L. Cheung, R. J. Nikolic, C. E. Reinhardt, and T. F. Wang “Growth of Boron Thin Films by LPCVD from Decaborane,” American Chemical Society, Quincy, Illinois, October 2006.
3. Welty, R. J., C. L. Cheung, C. E. Reinhardt, T. F. Wang, “Roadmap for High Efficiency Solid-State Neutron Detectors,” SPIE Optics East, Boston, Massachusetts, October 2005.
4. Welty, R. J., C. L. Cheung, C. E. Reinhardt, and T. F. Wang, “Solid-State Pillar Structured Thermal Neutron Detector,” IEEE Nuclear Science Symposium, Puerto Rico, October 2005.
5. Nikolic, R. J., C. L. Cheung, T. F. Wang, and C. E. Reinhardt, “Semi-Conductor Materials Matrix for Neutron Detection,” patent filed April 27, 2005.

**FY2008 Proposed Work**

- In FY2008 we will pursue:
- 1) fabrication of *Pillar Detector* (20 μm pillar);
  - 2) <sup>10</sup>B coatings of high-aspect-ratio structures and understanding of stress origin and mechanics;
  - 3) electrical, alpha, and neutron measurements of *Pillar Detector*;
  - 4) the addition of recombination to *Pillar Detector* model.

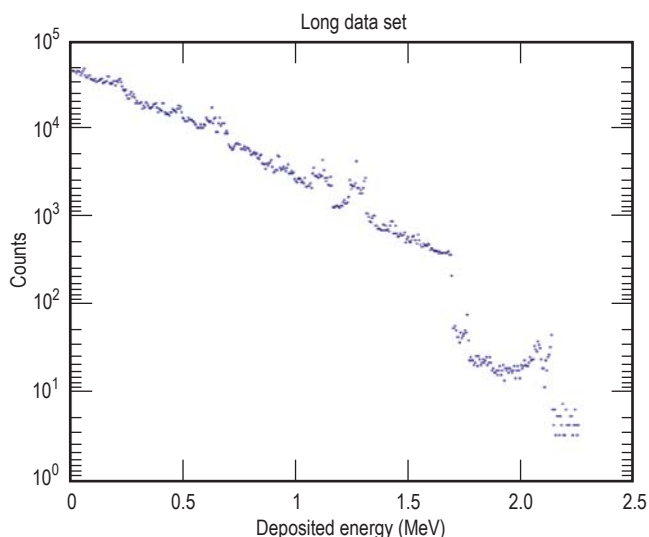


Figure 4. Simulated total energy spectrum (alpha + <sup>7</sup>Li) for neutron interaction with 20-μm-tall pillars with 2-μm diameter and 4-μm pitch.

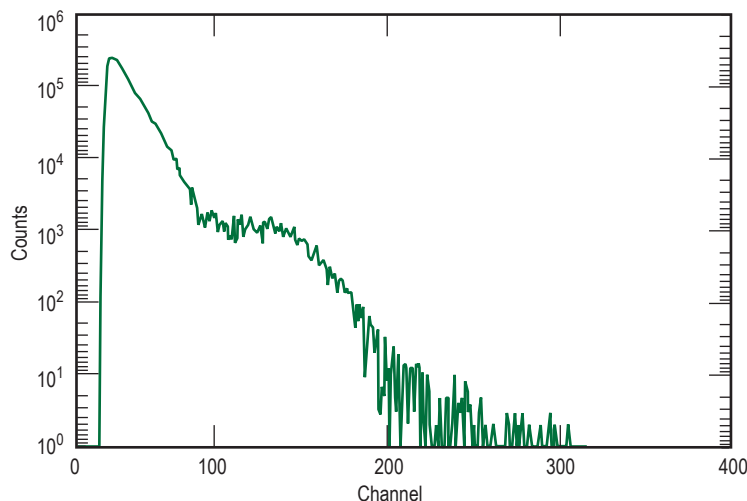


Figure 5. Energy response of a <sup>10</sup>B filled 12-μm-tall pillar detector from neutron interaction with <sup>10</sup>B.

# Compact High-Intensity Crystal-Driven Neutron Source

Active neutron interrogation is a promising technique for identification of threats such as explosives or shielded nuclear material. Neutrons are generated from fusion reactions when ions of appropriate species and energy impinge upon a target of a specific material having adequate cross-section to yield a neutron. For example the  $d(D,n)$ , or  $d(T,n)$  reactions can be facilitated by deuteron beams hitting a deuterated or tritiated target, respectively. Accelerator-based technologies are rather large, and include large

high-voltage power supplies. A crystal-driven neutron source offers a means to compact the high-voltage power supply, ion source, and accelerator structure in an integrated design one to two orders of magnitude smaller than alternative sources having similar neutron yields.

Pyrofusion has been demonstrated in recent years using pyroelectric crystals that generate large surface charge and voltages when subjected to thermal ramping. This effect is illustrated in Fig. 1. In this case, a tungsten needle of sufficient



Jeffrey D. Morse  
(925) 423-4864  
morse3@llnl.gov

length and tip diameter is positioned on the positively charged surface of the crystal. As the charge and voltage build up during thermal ramping, the electric field intensifies at the radius of curvature of the needle tip until it becomes sufficient to cause field ionization of background deuterium molecules (3 mTorr) in proximity to the crystal surface. Once ionized, the deuterons are accelerated away from the positively charged high-voltage surface of the crystal.

## Project Goals

The objective of this project is to provide a comprehensive understanding of the operation and limitations of pyrofusion as a means of generating neutrons in applications for identifying potential threats. As such, a compact (<1 liter), high-intensity ( $>10^7$  n/s) source is desired for rapid detection of hidden or shielded materials of concern. The goal of this effort is to demonstrate neutron yields in excess of  $10^6$  n/s using the  $d(T,n)$  fusion reactions. The targeted problems include effective generation and control of deuteron ion beams, stable generation of acceleration voltages in the 100 to 200 kV range, and system integration and scaling.

## Relevance to LLNL Mission

Active neutron interrogation is becoming a key approach for the detection and screening of hidden threats including explosives and shielded nuclear materials. This results from the penetrating nature of fast neutrons and subsequent specificity of the resulting gammas produced through inelastic scattering and capture of the neutrons from materials exposed to the neutrons. As such, this technology will make a significant impact for applications in homeland security, the military, and intelligence gathering needs. Furthermore, it has the potential

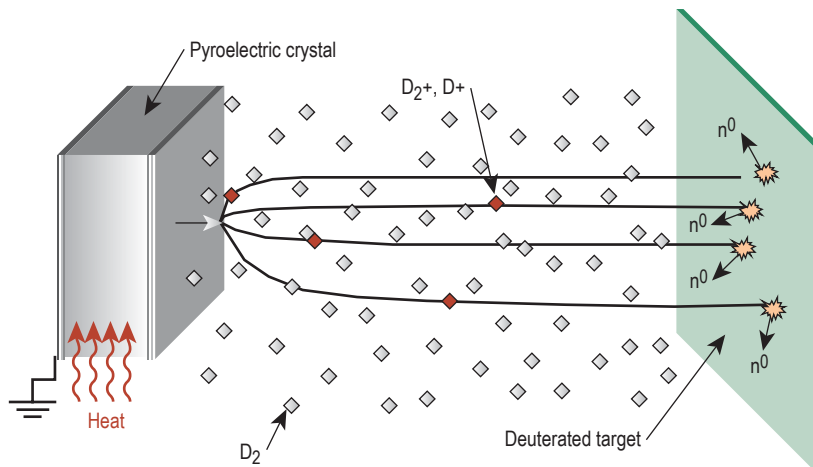


Figure 1. Illustration of pyrofusion effect.

Figure 2. Pyroelectric crystal mounting assembly including thermal control element.

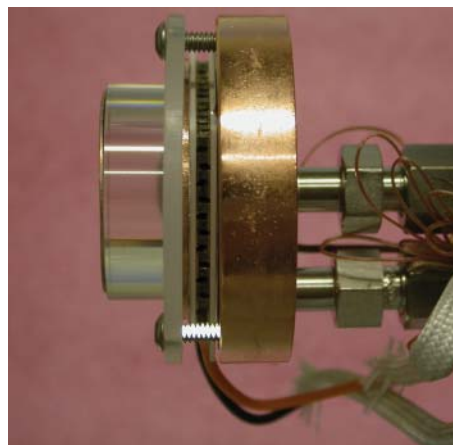




Figure 3. Pyroelectric crystal mounted with arc suppression dielectric guard ring at base of assembly.

to provide new methods of interrogation that are not presently possible due to the nature of existing neutron sources. In this sense, a crystal-driven neutron source represents a new paradigm for active interrogation of threats..

### FY2007 Accomplishments and Results

We have made significant progress on experimental efforts to understand the limits of pyrofusion for specified configurations, and further extend these limits to useful operational regimes. The key contributions to the field have been the design and assembly of a precision thermal control assembly for crystal actuation and thermal cycling; high-voltage engineering designs implemented to suppress high electric fields that result in electron cascading and subsequent breakdown events; and demonstration of record neutron yields using ungated, crystal-driven field ionization sources.

Figure 2 illustrates the crystal mounting assembly, which incorporates

a thermal electric element for rapid heating and cooling of the crystal. Figure 3 shows a  $\text{LiTaO}_3$  crystal (1 cm thick by 3 cm diameter) with a dielectric guard ring formed around the base to suppress flashover at the base electrode and crystal interface where high electric fields build up during thermal ramping. This has resulted in significant improvement in reproducing the ion beams for each thermal cycle. Figure 4 illustrates the ion beam current, and subsequent neutrons generated during a single thermal cycle. In this experiment, a deuterated target ( $\text{ErD}_2$ ) was placed in series with a Faraday cup to simultaneously measure the ion beam while generating neutrons. A  $\text{He}^3$  scintillator detector was used to measure the neutron yield. Figure 5 shows the x-ray spectra measured during the crystal thermal cycle, which provides a measure of the voltage that the crystal is charged to, in this case  $>80$  kV. Incorporating active thermal control, these results have demonstrated  $>2$  times the neutron

yields produced by other groups using this technique. This is mainly due to the precision thermal control, along with the arc suppression approaches that enable long, persistent ion beams generated from a single thermal cycle.

### Related References

1. Naranjo, Gimzewski, and Putterman, *Nature*, **434**, 28, pp. 1115-1117, April 2005.
2. Geuther and Danon, *J. Appl. Phys.*, **97**, 074109, 2005.
3. Geuther, Danon, and Saglime, *Phys. Rev. Lett.*, **96**, 5, pp. 054803-1-4, February 10, 2006.

### FY2008 Proposed Work

During FY2008 efforts will focus on the inverse configuration in which the target is mounted on the high-voltage surface of the crystal. This configuration has the advantage that the ion beam will be better focused on target without the need for focusing optics due to the electric field distribution. Additional efforts will continue the development of a gated ion source that will decouple field ionization from the crystal charge state, providing a separate, low voltage ( $<500$  V) power supply for either pulsed or DC ion beam operation.

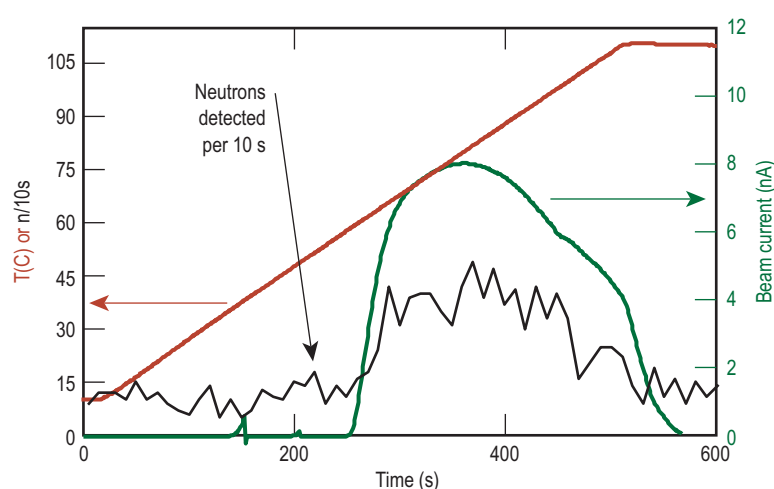


Figure 4. Crystal-generated ion beam and resulting neutron yield during thermal ramping cycle.

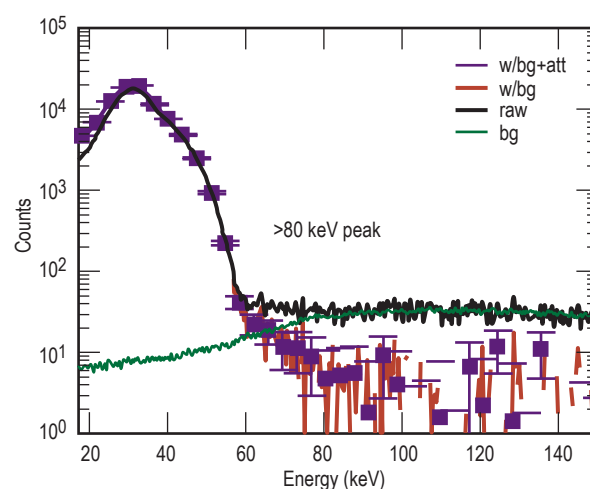


Figure 5. Resulting x-ray spectra generated during ion beam measurements indicating a crystal voltage on the order of  $>80$  kV achieved during thermal ramping.

# Pillar Neutron Detector Fabrication



Rebecca J. Nikolic'  
(925) 423-7389  
nikolic1@llnl.gov

The goal of this project is to implement a set of process recipes for the fabrication of the “pillar detector” device that identifies special nuclear materials by detection of thermal neutrons. This new device can meet the demands of high efficiency and fieldability while maintaining a small device footprint, enabling covert applications.

## Relevance to LLNL Mission

Thermal neutron detectors are used to determine the presence of special nuclear materials. This falls under the Laboratory’s mission area of global security.

## FY2007 Accomplishments and Results

The work carried out in FY2007 was focused on the processing of the pillar detector device. The process flow is shown in Fig. 1. We are using contact photolithography to define 2- $\mu\text{m}$ -diameter pillars with 2- $\mu\text{m}$  separation. Next, plasma etching is used to etch the pillars with varying etch depth. The pillars are then filled with boron-10. This boron-10 material is responsible for converting the neutrons to alpha and lithium particles.

The next step in this process is the planarization of the boron. This is a major task of this project. We have evaluated

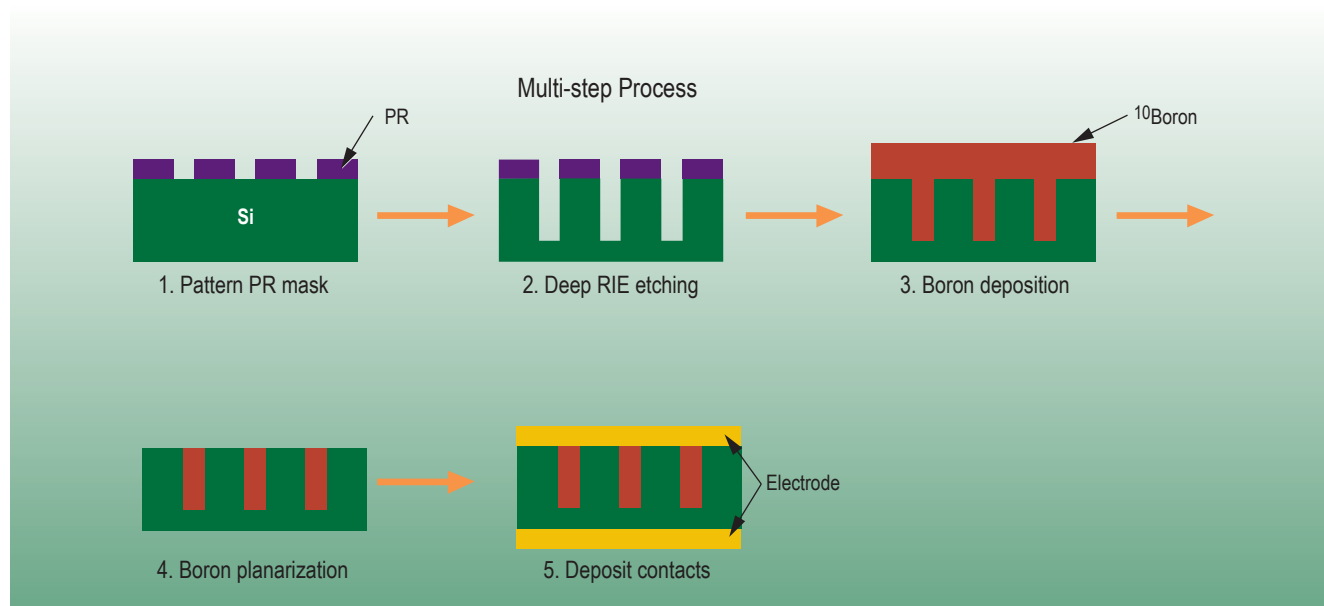


Figure 1. Multi-step fabrication process for pillar detector.

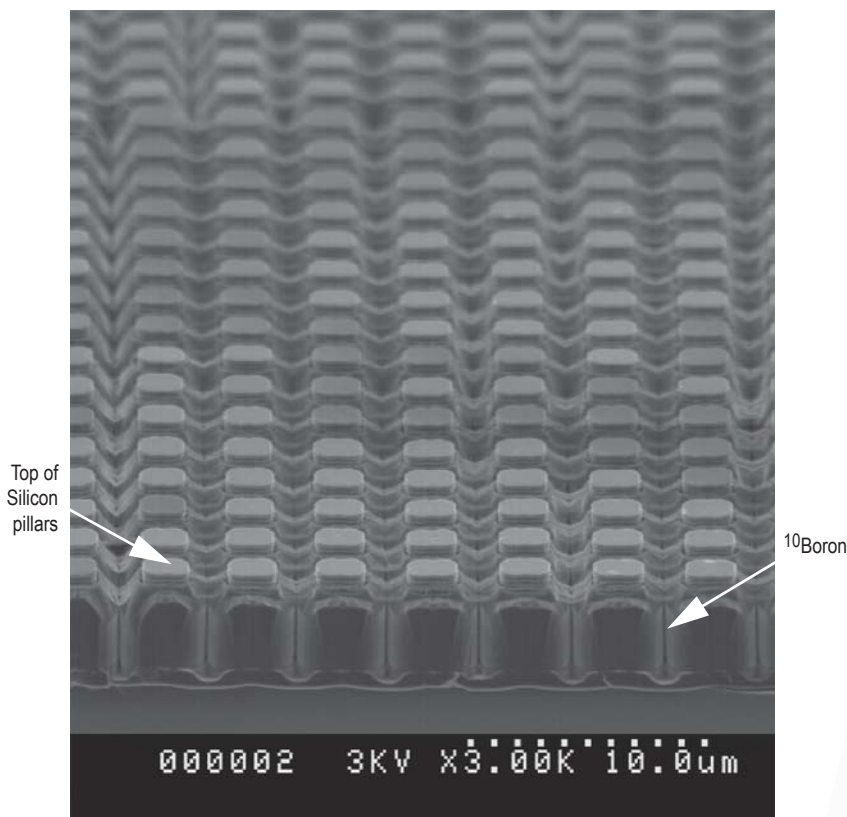


Figure 2. Pillar array after  $\text{CF}_4/\text{H}_2/\text{O}_2$  plasma etch-back process.

chemical mechanical polishing, wet etching and plasma processing to determine an appropriate recipe for this planarization. Plasma etching using a mixed gas composition of  $\text{CF}_4/\text{O}_2/\text{H}_2$  gave the best results in terms of a fast etch rate of  $0.2 \mu\text{m}/\text{min}$  while maintaining a smooth and planar surface.

Each component of the reaction gas mixture is required for the fast etch rate. The  $\text{O}_2$  removes the carbon layer that forms on the surface. If the carbon layer is not removed the etch process will terminate. The  $\text{CF}_4$  and  $\text{H}_2$  are both responsible for the chemical etching of the boron by reacting with the fluoride and hydrogen.

Figure 2 shows a representative pillar chip after the boron etch step. Once the device is planarized, electrical contacts can be placed on the top and bottom of the device. Aluminum is used for both the top and bottom electrode. For the top electrode, a higher pressure (25 mT vs. 6 mT) sputter deposition is required to coat the uneven topography. In packaging the devices, we used conductive silver epoxy to attach the pillar chip to the package and simultaneously make electrical connection to the bottom contact of the pillar chip. Wire bonding was then used to connect the top electrode to the package leads.

# Flow Programmed Mesoscale Assembly of Nanoengineered Materials and Net Shape Components

We have reduced to practice a bottom-up mesoscale assembly tool capable of integrating highly dissimilar materials and producing features with critical dimensions in the submicron range. This system enables nanometer-scale precision synthesis of millimeter-scale materials and parts in a simple, low-cost system.

We perform this synthesis by computer-controlled electrophoretic deposition in a miniature aqueous deposition cell interfaced to computer-controlled automated fluidics. Nanoparticle solutions are available in a wide and ever-growing variety of material compositions, morphologies, and surface chemistry states. We introduce mixtures of various precursor solutions into the deposition cell, and deposit nm- to  $\mu\text{m}$ -scale layers by the pulsed-field electrophoretic deposition of particles onto substrates. We use post-deposition sintering to achieve densification of these films.

The high degree of control and wide range of heterogeneous materials made accessible by this approach brings

powerful, low-cost capabilities to the fabrication of density- and composition-varying layers. The highly conformal nature of the deposition allows the fabrication of near-net shape high precision parts. The lack of need for vacuum conditions allows high-speed and low-cost nanomaterial synthesis in a simple benchtop system.

The system is available for follow-on work to capitalize on the broader capabilities it makes accessible, including the programmed synthesis of parts incorporating dissimilar and custom materials, the *in-situ* fabrication of hemispherical and other net-shape parts, and ultimately the electronically-controlled biochemically templated nanoscale self-assembly of nanostructured composite and functional materials.

## Project Goals

The goals of this project were to: 1) produce a powerful and flexible prototype system for mesoscale assembly, ready to be leveraged for future work;



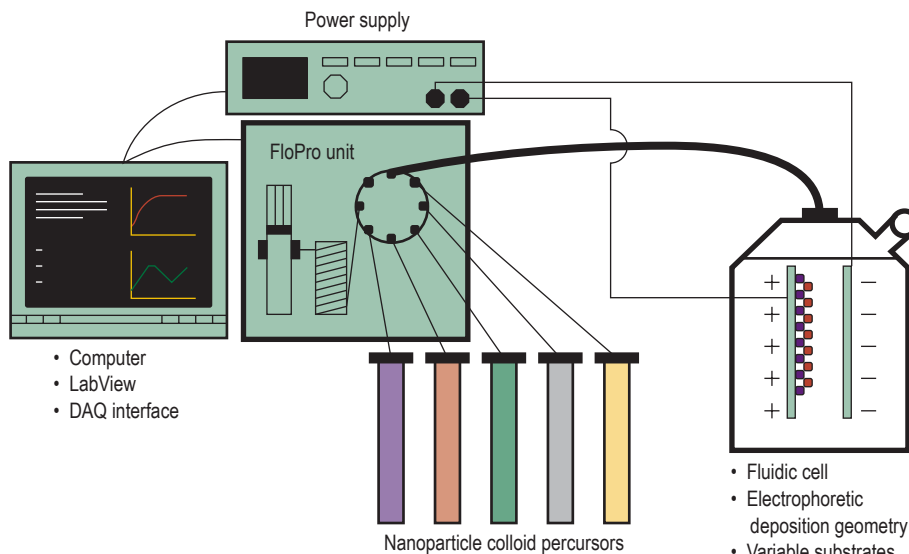
Klint A. Rose  
(925) 423-1926  
rose38@llnl.gov

2) demonstrate the synthesis of porous polymer layers with defined, varying density profiles, via the computer-controlled electrophoretic deposition of submicron polystyrene spheres; and 3) convert an existing Brownian dynamics simulation code for this application.

## Relevance to LLNL Mission

The proposed project is a seed effort for a new, integrated, mutually supporting, and dynamic multi-project portfolio in novel nanomaterial synthesis capabilities for mesoscale manufacturing. This portfolio is directed to LLNL application areas in target materials and structures, sensor materials, and biodection devices. The short-term payoff is the creation of new nanoscale target structures. The proposed technology is ideal for combining novel nanomaterial components such as engineered nanoparticles, carbon nanotubes, and others into complex materials and structures.

**Figure 1.** Schematic of the mesoscale assembly system. A FloPro unit provides automated valving and pumping to move particle solutions through the deposition cell. The power supply provides either constant voltage or constant current across the particle-laden fluid. The fluidics and the power supply are controlled via Labview software for full automation.



**FY2007 Accomplishments and Results**

We have accomplished the overall goal of this project by delivering the automated mesoscale assembly system. Specific results and accomplishments include the following.

1. Instrumentation (Figs. 1 and 2): Built a prototype system by combining a mini FloPro system (Global FIA) for automated control of the sample solutions, LabView-based control architecture, and a

2. Process testing and reduction to practice: Carried out a series of parametric tests to quantify and optimize the aqueous electrophoretic deposition process to allow predictive control; tested multiple electrode materials, particle materials, solution properties, and applied electric field.

3. Film synthesis: Demonstrated the deposition of thick ( $> 50 \mu\text{m}$ ) films of polystyrene particles using particles of a single diameter; also demonstrated stacked film layers as shown in Fig. 3.
4. Density-gradient materials. Produced a two-layer film with a base layer of 200- $\mu\text{m}$  polystyrene particles and 80-nm gold particles (Figs. 4 and 5).

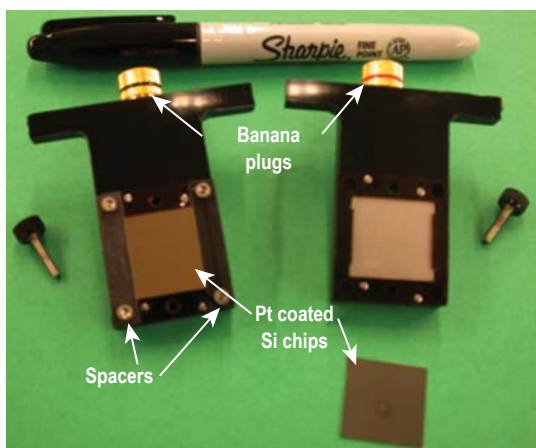


**Figure 2.** Exploded view of the electrophoretic deposition cell. The cell holds the platinum coated electrodes at a fixed distance to maintain a uniform and constant electric field. Depending on their charge, the particles are deposited onto either the cathode or the anode.

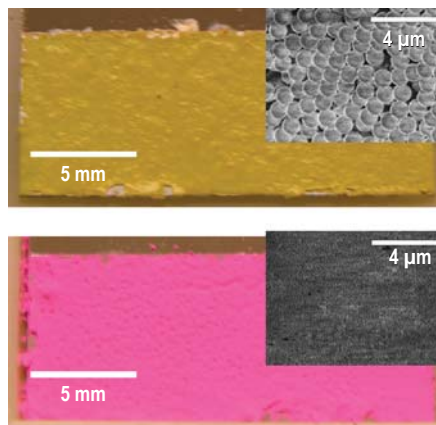


**Figure 3.** Examples of particle films of single particle types. Top: 1- $\mu\text{m}$ -diameter yellow-green polystyrene particles deposited approximately 150  $\mu\text{m}$  thick. Bottom: 200-nm-diameter red polystyrene particles deposited approximately 60  $\mu\text{m}$  thick. Insets show SEM images of the top surface of the respective films.

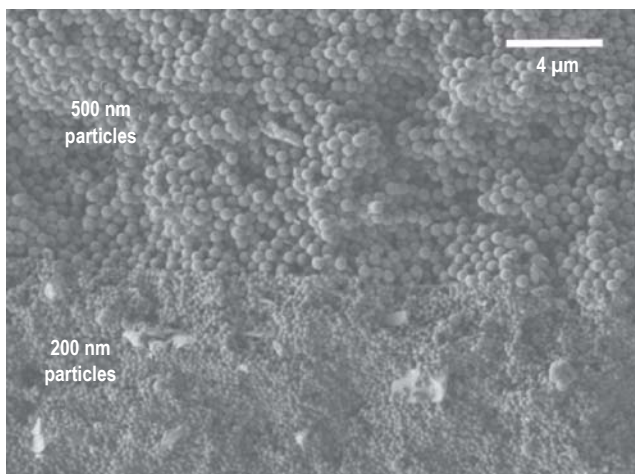


**Figure 4.** SEM cross-section of a two-layer particle film. The bottom layer is approximately 60  $\mu\text{m}$  thick and comprised of 200-nm-diameter polystyrene particles. The top layer is approximately 15  $\mu\text{m}$  thick and comprised of 500-nm-diameter polystyrene particles.

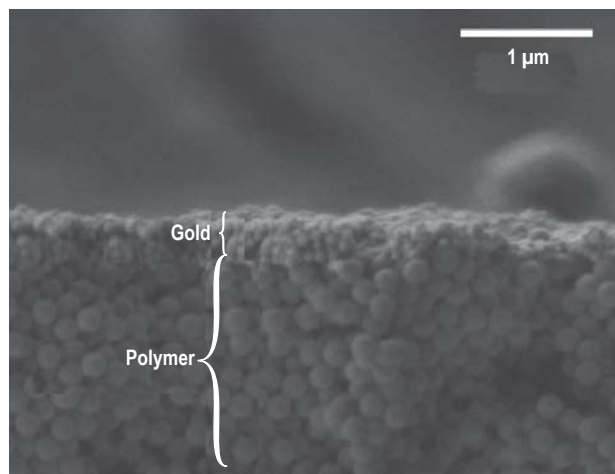


**Figure 5.** SEM cross-section of a two-layer particle film. The bottom layer is approximately 17  $\mu\text{m}$  thick and comprised of 200-nm-diameter polystyrene particles. The top layer is approximately 300 nm thick and comprised of 80-nm-diameter gold particles.

# Laser Pantography



*Christopher M.  
Spadaccini*  
(925) 423-3185  
spadaccini2@llnl.gov

**L**aser Pantography (LP) is a unique lithographic technology created at LLNL in support of a number of projects and programs. LP is the only technology that can routinely draw patterns on 3-D objects such as cylinders, spheres, flats, and diamonds. These patterns are usually metal, and are typically used as circuits for sensors and actuators.

In one example, LP is being used to pattern coils on the tips of microcatheters intended for use in the brains of stroke patients (Fig. 1). These coils can be energized with a continuous current, creating a magnetic moment that will attempt to align with an exterior field, such as the magnetic field of an MRI. This magnetic interaction will cause the catheter to deflect, in effect steering it. By having three orthogonal coils on the catheter, the tip can be deflected in any direction, providing a mechanism for guiding the catheter into a desired blood vessel. Other uses of LP include the fabrication of microreceiver coils for

a portable NMR spectrometer (Fig. 2), and the patterning of tungsten sensors on the tips of diamond anvils for the study of material properties at high pressure (Fig. 3).

For over two decades the various LP systems have been physically separate from most of the micro- and nanofabrication facilities and personnel. This project endeavors to collocate the systems with other capabilities and integrate with existing programs and projects in the micro- and nanotechnology area.

## Project Goals

The purpose of this project is to ensure the future vitality of this unique capability. Specific goals include:

1. moving the two LP systems and all associated support hardware to the micro- and nanofabrication center at LLNL in order to better integrate with and leverage other capabilities;
2. training new technical staff in the technique; and

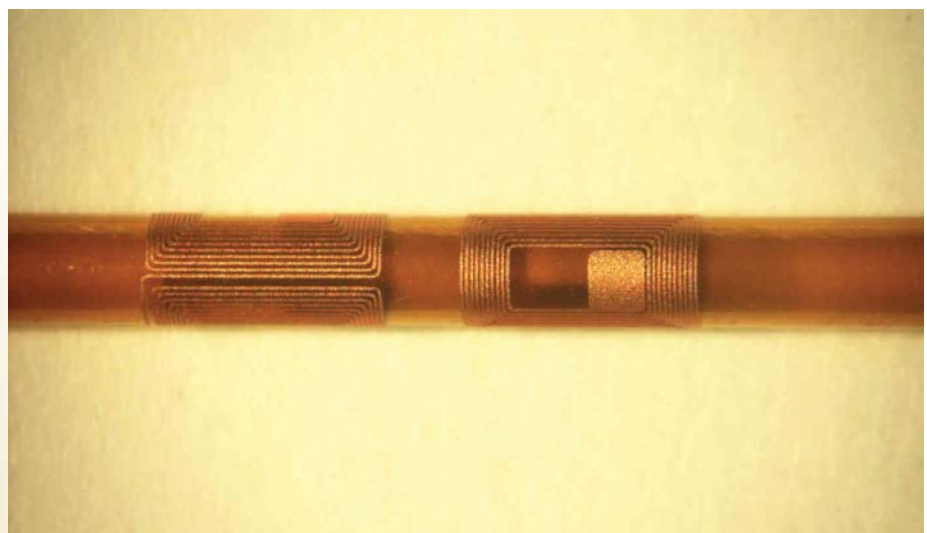


**Figure 1.** Orthogonal saddle coils on polyimide cylinders for MRI guided catheters.

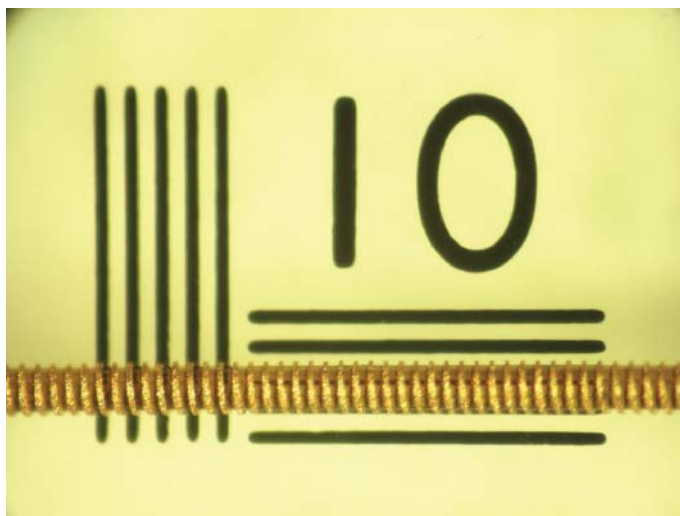


Figure 2. 150-mm OD helical coil for a portable NMR spectrometer.

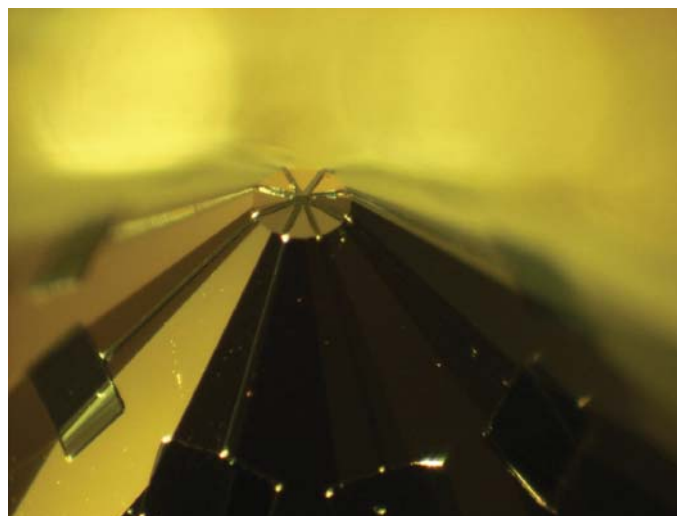


Figure 3. Designer diamond anvil with LP-generated electrodes and contact pads.

- educating the LLNL micro- and nanofabrication community so that LP can be integrated with existing and future projects and programmatic work.

#### Relevance to LLNL Mission

The ability to fabricate microscale patterns on arbitrary 3-D surfaces (slopes, spheres, cylinders, and compound curvatures) is a unique capability available only via the LLNL LP process. These systems and processes have serviced critical program needs in the past and the vitality of the technique needs to be maintained in order to do so in the future. The availability and advancement of LP will contribute to the core microfabrication competencies at LLNL that provide vital support to both internal and external customers.

#### FY2007 Accomplishments and Results

Two LP systems have been moved to the LLNL microfabrication facility. These systems include a full five-axis tool with a diode laser and three-axis system with an Ar-ion laser. Also included were laser system enclosures, floating optical tables, and associated computer controls and electronics. Figure 4 shows the five-axis LP system in its enclosure with computer controls at its new location.

In addition to the lasers and associated equipment, an entire set of other support equipment, including a wet processing bench and sputter tool, was moved.

Training of new personnel and education of the micro- and nanofabrication community at LLNL has been ongoing throughout this project. New engineers and technicians have been involved with patterning 3-D components for the projects that LP currently supports: portable NMR, MRI guided catheters, and diamond anvils. These personnel have also participated in planning and strategy meetings with customers to better understand individual project needs. LP experts have actively marketed the technology to potential new

customers and other microfabrication personnel via a series of seminars and individual meetings and tours to give the community at large a better understanding of the capability.

As a result of this work, the LP capabilities have been both physically and intellectually integrated with the micro- and nanofabrication community at LLNL. This is critical to maintaining and advancing this important and unique technology that is capable of patterning features on any 3-D surface.



Figure 4. An LP system in its new location.

# Bridging the Length and Time Scales from Atomistics to the Microscale



Todd Weisgraber  
(925) 423-6349  
weisgraber2@llnl.gov

**P**olymer networks of interest to LLNL's mission undergo structural and mechanical changes over time. These changes occur due to radiation damage, contaminant transport and reaction, and prolonged deformation due to physical loads. To date, useful molecular dynamics (MD) and finite element analysis (FEA) efforts have been performed. These efforts, however, focus on the nano and continuum scales, respectively. The missing link in this effort is a "meso" or micron-to-centimeter scale that uses interaction potentials generated by MD simulations and supplies time-dependent material properties to continuum models. This last year has resulted in a capability to generate 3-D foam networks with the ability to track Brownian walkers with steric effects and local interaction potentials derived from MD simulations.

## Project Goals

The goal of this project is to bridge the length and time scales from atomistics to microscale.

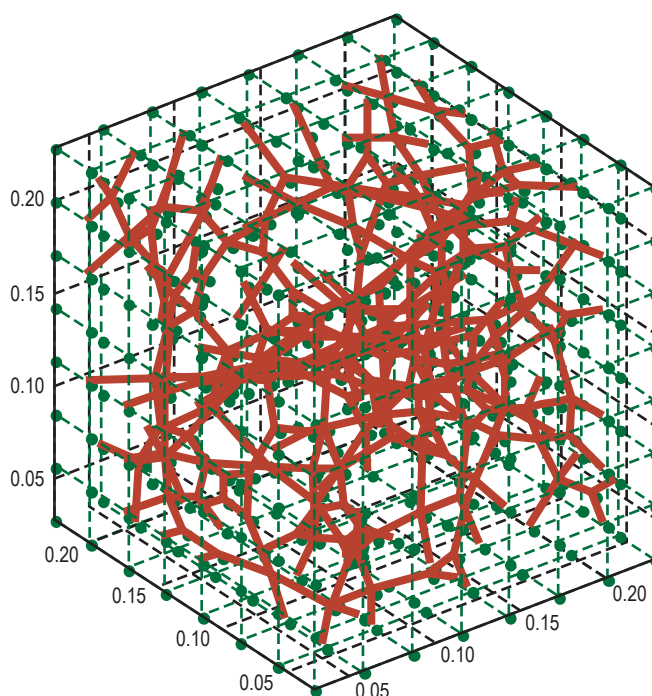
## Relevance to LLNL Mission

LLNL has an interest in polymer networks and their structural changes. A fundamental numerical approach to understand and characterize what happens to the micro and nanostructures of polymeric materials is a central need of LLNL's commitment to DOE's Enhanced Surveillance Campaign.

## FY2007 Accomplishments and Results

The mechanical properties of polymeric materials are a function of the bonds between crosslinks and the crosslink density of the material. Given that the bulk material length scales are typically on the order of centimeters and

Figure 1. 3-D vertex model of a polymer foam. The final structure (shown in red) is evolved from an initial cubic lattice (shown in green).



the polymer structure is on the order of nanometers, modeling of polymeric materials is inherently a multiscale problem. In the work being performed on this project, a 3-D representation of the microstructure with a quantifiable crosslink density was adapted from a vertex model. This model allows the user to prescribe mechanical properties to the bonds between crosslinks, such as Hookean springs, and allows automatic tracking of crosslink density. Additionally, the numeric polymeric media can be mechanically assayed, using tension, compression and shear, to yield continuum property information. In parallel with this adaptation of the vertex model, a Brownian dynamics simulation was adapted to track random walkers through the 3-D medium.

These random walkers “react” with the medium at crosslinks in accord with the interaction potentials generated by MD simulation. It has been shown that the modulus of polymeric material is directly dependent on the crosslink density of the material. As the random walkers traverse the medium as a function of time, they sever crosslinks, modifying the modulus of the material and yielding a time-dependent change in mechanical properties.

This approach can also be modified to track the interaction of radiation with the polymeric medium while accounting for the degradation in bonds, crosslinks, and resulting mechanical properties. Furthermore, the vertex model provides a starting point to get a glimpse of polymeric microstructure of real systems. With some calibration to experimental data, this model can be used to postulate microstructural properties.

To date, we have implemented a 3-D vertex polymer foam model that enables a new way to assess bulk material properties (Fig. 1). The model also includes a capability to characterize contaminant diffusion in the foam (Fig. 2). Our programmatic customers see promise in this mesoscale approach since it is less costly than MD simulations and they would like to further enhance the current model.

#### Related References

1. Grimson, M. J., “Structure and Elasticity of Model Gel Networks,” *Mol. Phys.*, **74**, pp. 1097-1114, 1991.
2. Flory, P. J., Principles of Polymer Chemistry, Cornell University Press, Ithaca, New York, 1953.

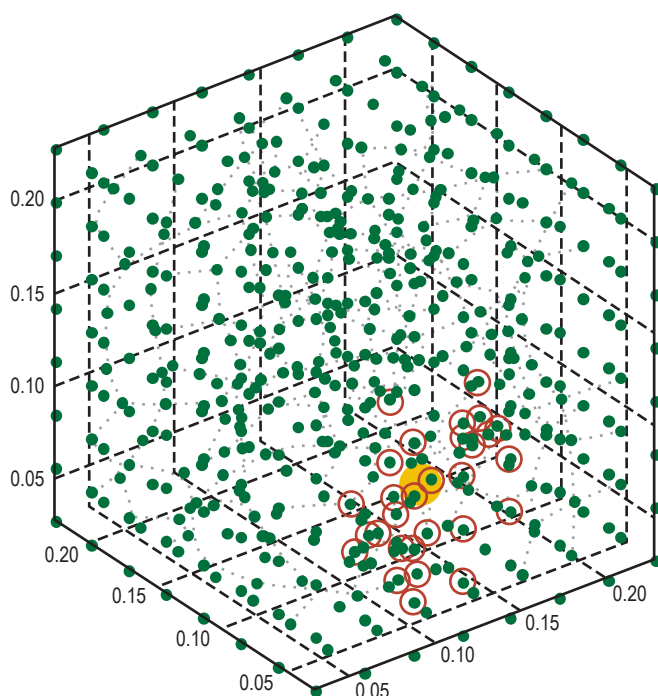


Figure 2. Contaminant particle (gold) represented by a random walker in the vertex model. Crosslinks within the containment's range of influence are highlighted in red.

#### FY2008 Proposed Work

We have submitted a proposal to incorporate these enhancements and validate with experiments. Continuing the work would have high impact to the program since it aligns with their goals and would also strengthen the relationship between Engineering and the Enhanced Surveillance Campaign.

# “HE-Less” Detonator Modeling



James F. McCarrick  
(925) 423-8182  
mccarrick1@llnl.gov

**A** combined modeling and experimental effort was undertaken to see if existing simulation tools at LLNL contain a combination of physics models suitable to study the initiation of high explosives (HE) by an electrical arc.

## Project Goals

Our goals were to 1) determine if the shock initiation model implemented in a particular ALE hydrocode is capable of reproducing previously measured arc initiation data; and 2) if so, to map out the space for an arc-based detonator that would not require its own internal HE (an “HE-less” detonator). The experimental effort provides a map from fireset parameters to shock pressures, and the modeling effort gives a map from shock pressures to initiation.

## Relevance to LLNL Mission

Arc initiation phenomena are directly relevant to LLNL stockpile safety studies and to improved initiation system plans.

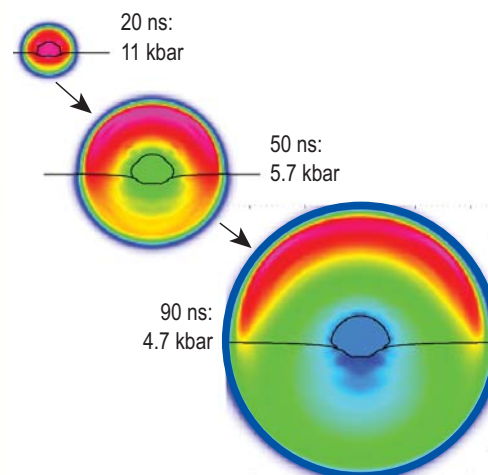


Figure 1. Air bridge model of arc-initiated PETN.

## FY2007 Accomplishments and Results

In the modeling portion of the project, an existing 2-D ALE hydrocode model of pentaerythritol tetranitrate (PETN)-based exploding bridge wire (EBW) detonators was modified to simulate an arc-driven “air bridge” in place of the metal bridge wire. To avoid attempting a first-principles model of the arc itself, the electrical behavior of the air bridge was matched to experimental measurements. An extensive matrix of studies was performed in a parameter space containing the initial arc radius, the source capacitance, source inductance, and source voltage. Figure 1 shows a typical result of the simulated pressure field in PETN that was successfully ignited by the air bridge.

The intent was to see if the simulated “go vs. no-go” results resembled data taken from a set of measurements of detonator sensitivity to electrostatic discharge (ESD). In particular, we looked to reproducing the observed trend of lowered threshold with decreased circuit inductance, which we chose as our indicator that the shock-based initiation model was sufficient. Further simulations would then map out the arc-driven shock pressures useful in a detonator intentionally engineered to use arc initiation.

However, as shown in Fig. 2, while the simulations do show arc initiation of PETN, they do not reproduce the observed dependence of threshold energy on inductance. It has not yet been determined if this is due to the assumption that only shock pressure participates in the initiation mechanism, or to the lack of a significant energy transport mechanism in this particular mode of operation of the hydrocode, or to a purely numerical effect not discernible in simple baseline tests.

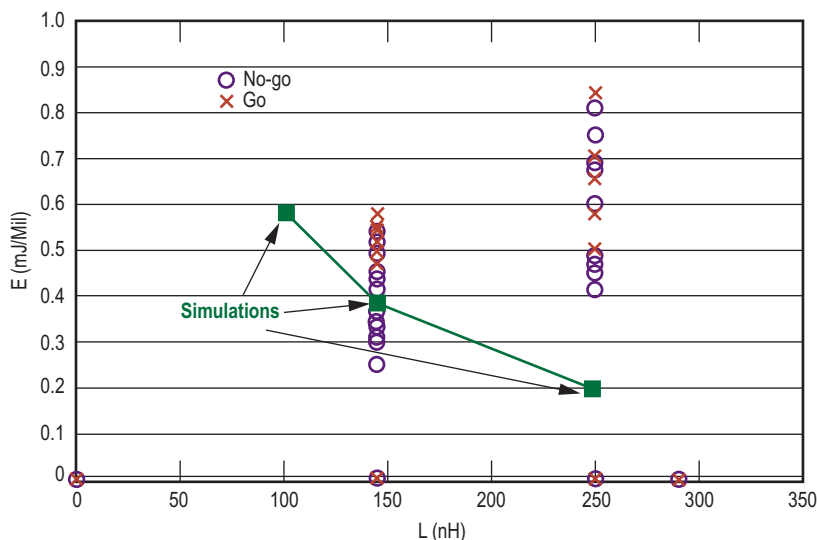


**Figure 2.** Simulated and measured energy thresholds. The agreement at 150 nH is forced by fixing the energy and finding the threshold in initial arc radius. The resulting radius (0.9 mil) is then used to find the energy thresholds at 100 and 250 nH.

In the complementary experiments, photonic Doppler velocimetry (PDV) was used to measure the velocity front of an arc in air, using fireset parameters scaled to match the detonator ESD safety study. The setup is shown in Fig. 3. The purpose was to determine if the shock pressure required to drive the expansion of the air was of the right order for shock initiation of HE; and, if so, to

build a map between electrical parameters and the pressures produced in the resulting arcs. This map could then be combined with the modeling study to find fireset parameters that would produce initiation in a variety of useful HEs (since the model itself lacks a first-principles coupling between the fireset and the resulting arc). However, as shown by the typical results in Fig. 4,

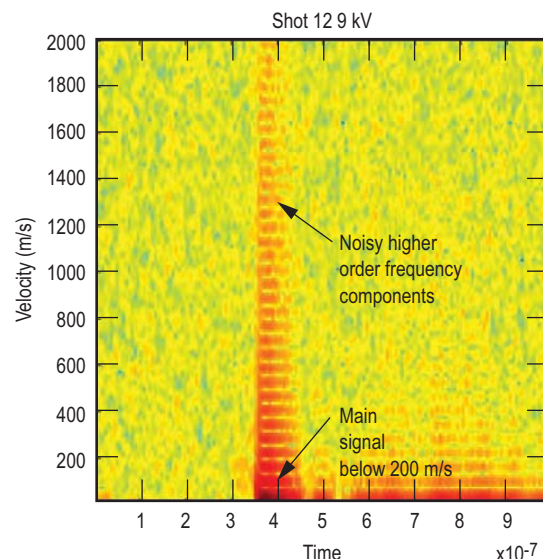


**Figure 4.** Sample PDV results, showing noisy return signal and low expansion speed.

signal-to-noise is not strong and the error bars in the expansion speed are fairly large.

Furthermore, even at the high end of  $v \sim 1000$  m/s, an order-of-magnitude estimate of the pressure yields  $P \sim \rho v^2 \sim 12$  atm for a mass corresponding to molecular nitrogen and ambient density. This is several orders of magnitude below typical shock initiation thresholds. Tests were done for 20-, 40-, and 150-mil arc lengths with source voltages in the 8 to 10 kV range, a 1-nF source capacitance, and a circuit inductance of about 250 nH. If the peak pressure in the arc volume resulted from all of the energy initially stored in the fireset, it would be of the order 600 atm at the 40-mil spacing, assuming an initial arc diameter even as large as 1 mm.

Thus, these results again point to the importance of understanding the correct energy transport, since a considerable amount of energy is not accounted for.

**Related References**

1. Lee, E. L., and C. M. Tarver, "Phenomenological Model of Shock Initiation in Heterogeneous Explosives," *Physics of Fluids*, **12**, pp. 2362-72, 1980.
2. Strand, O. T., et al., "Compact System for High-Speed Velocimetry Using Heterodyne Techniques," *Review of Scientific Instruments*, **8**, pp. 83108-1-8, 2006.

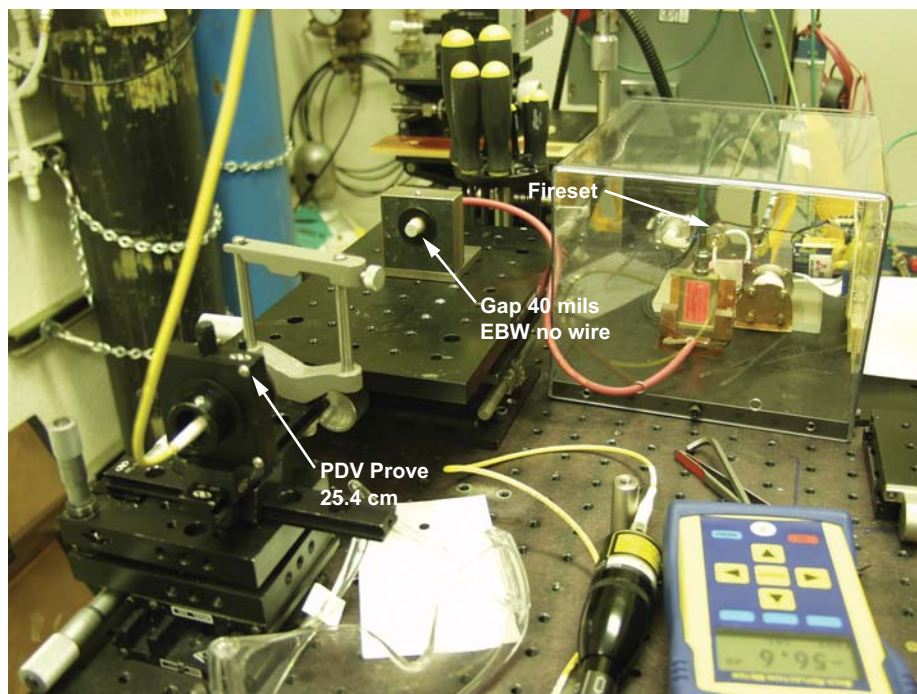


**Figure 3.** Experimental setup for PDV measurement of arc-driven air expansion speeds.

# Chip Slapper Detonator Processing for Rapid Prototyping and Hydrodynamic Properties

Next generation weapons require reliable, compact, energy-efficient initiation systems that will perform for the lifetime of the stockpile. Chip slapper detonators are now being evaluated for future use. There are limitations in the present technology and high costs associated with tooling for each configuration as we strive to produce reliable, low-energy slappers. The present manufacturing process uses thick-film, hybrid-circuit, photolithographic processing with solvent-based polymers. Two main problem areas exist:

1. for the multilayer metallization process—poor alignment tolerances and high tooling costs; and
2. for the flyer polymer process—solvent-based aging issues and inadequate hydrodynamic properties.

## Project Goals

This three-year project has two goals: reduce the costs associated with creating chip slapper patterns by applying rapid prototyping techniques; and evaluate alternative detonator flyer materials by using LLNL's SolventLess

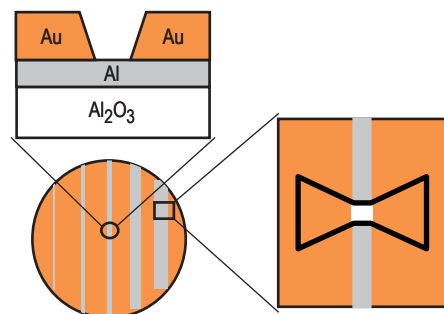


Figure 1. Schematic of thick-film deposition and patterning of Au over Al using femtosecond laser machining to define final geometries.

vapor deposition followed by an *In-situ* Polymerization (SLIP) process.

## Relevance to LLNL Mission

Efficient chip slapper fabrication can enable future initiation systems with improved safety and performance that would be relevant to both DOE and DoD missions at the Laboratory.

## FY2007 Accomplishments and Results

Fabrication of the initial rapid prototyping plan included thick film PVD coatings, gold electroplating combined with photolithography, and femtosecond laser machining to define final geometries (Fig. 1). All coatings and laser definition were within manufacturing tolerances for a slapper device.

Software was written to “direct write” slapper arrays on a processed substrate (Figs. 2-3) with the femtosecond laser (Fig. 4) and is in its preliminary stage of implementation. Once the software for rapid prototyping is complete, it will include a feature that allows the user to arbitrarily change the slapper dimensions quickly (seconds)



Figure 2. Processed substrate with various bridge widths defined.



Mark A. Schmidt  
(925) 422-9118  
schmidt15@llnl.gov

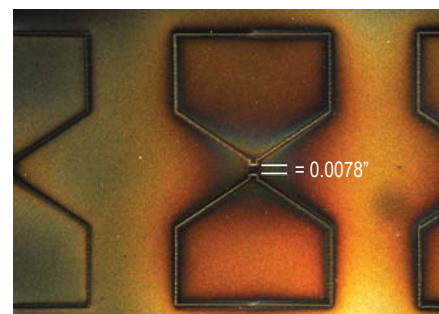


Figure 3. Prototype slappers laser-machined into Au on an alumina substrate.

between runs. Full-scale slapper models are initially laser machined from paper to check dimensions, and repeatability is well within requirements.

The processed substrates must be coated with a protective film before laser-machining operations to avoid re-coating and contamination of deposited films. It takes approximately 20 s to cut a simple slapper pattern on a substrate. A substrate full of finished slapper patterns can be machined in approximately 6 min.

The SLIP process consists of monomers in the vapor phase being mixed in a nozzle system and deposited onto a substrate (Fig. 5). Deposited films range in thickness from 6  $\mu\text{m}$  to 100  $\mu\text{m}$ . Substrates remain at room temperature or can be heated. Stoichiometric polyimide has been confirmed with a PMDA/ODA molar ratio of 0.83 for flat substrates. This is quite different from the molar ratio of 1.17 that produced stoichiometric films for ICF targets (Fig. 6). The process parameters for flat substrates are not the same as those for spherical substrates, which made it challenging to find the proper operating conditions since we started with the ratios for ICF applications.

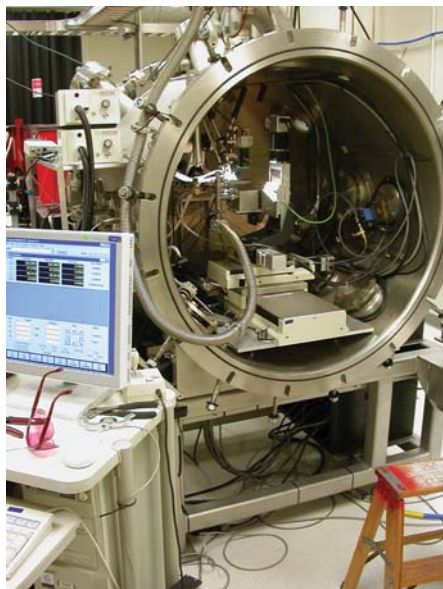


Figure 4. Femtosecond laser micromachining laboratory, which includes a 4-axis motion control system that enables rapid prototyping of slappers and slapper arrays.

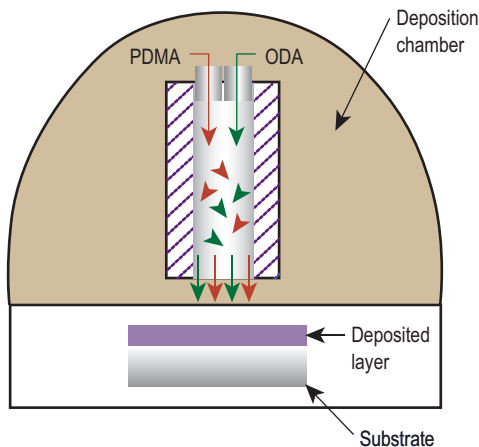


Figure 5. Solvent-less process for deposition of polyimide films.



Significant progress was made extending past work on exploding bridewire models into a small slapper detonator initiation model. Early attempts looked at fairly sophisticated 2-D representations, but have been reduced to simple 1-D models for the sake of model robustness, and for verification with other modeling attempts and validation against experiments. The present

model accepts an electrical stimulus (in the form of a charged external capacitor – a fireset) and predicts burst time, burst current, and flyer speed as functions of chip slapper materials, geometry, and excitation. Recent work focuses on the proper initiation response from the acceptor HE, building toward comparison with experiments planned for the first quarter of FY2008.

### FY2008 Proposed Work

Next year we will test the rapid prototyping pattern and compare it to a standard part made by present manufacturing methods. The experimental data will be evaluated alongside the model. Efforts will also include implementing a robust 2-D slapper detonator initiation model and comparing it to the 1-D model for consistency. For the polyimide flyer material, we need to determine the temperature(s) that will produce the desired mechanical film properties, establish adhesion characteristics on multiple materials, and investigate adhesion promoters, if required.

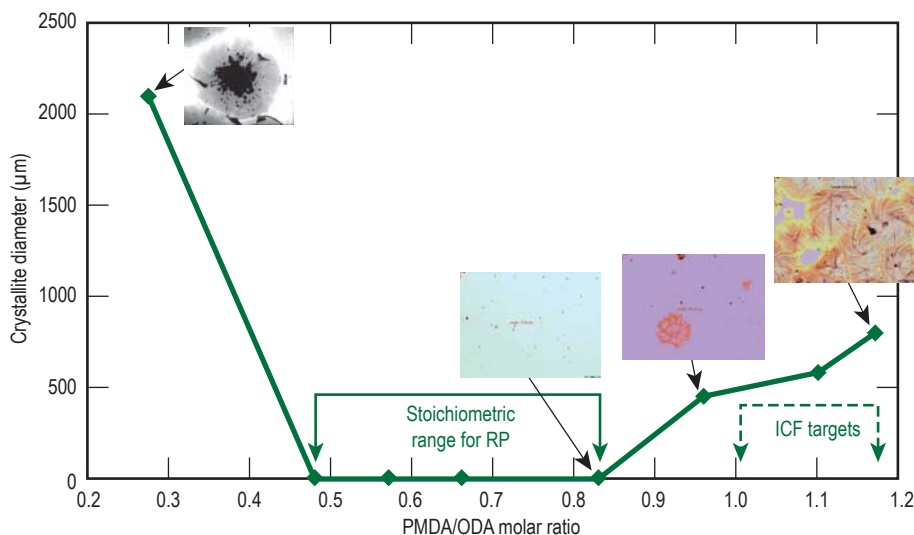
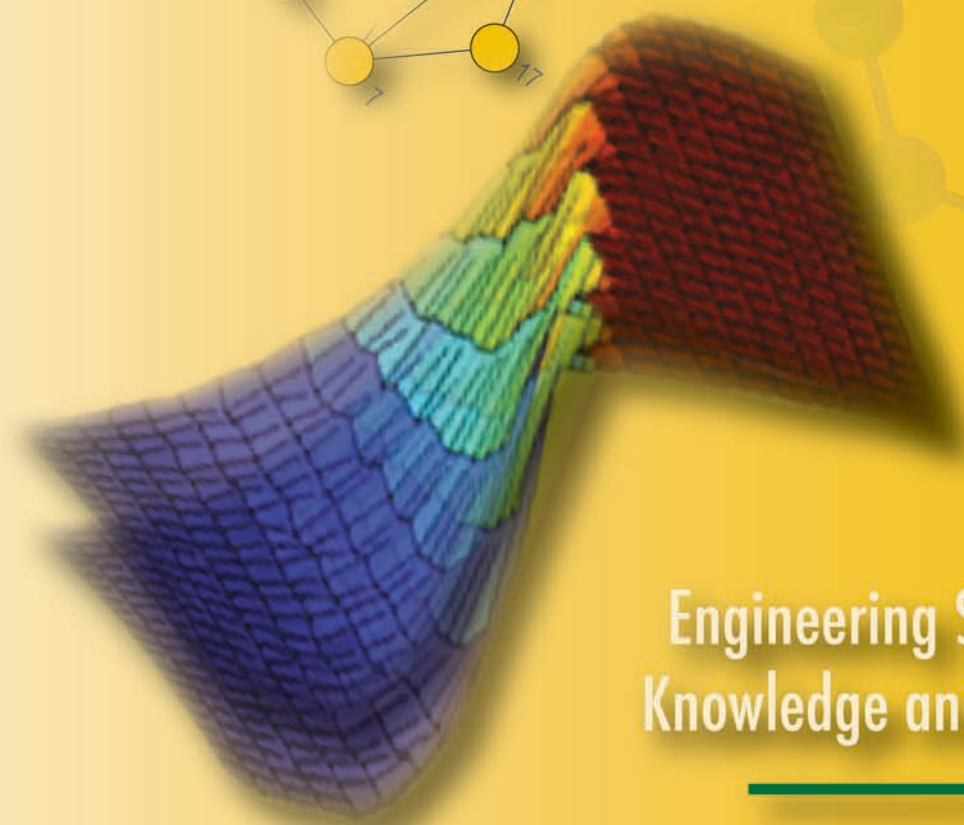


Figure 6. Stoichiometry per molar ratio as determined by crystallite formation.





Engineering Systems for  
Knowledge and Inference



# Semantic Graph Hierarchical Clustering and Analysis Testbed



Tracy D. Lemmond  
(925) 422-0219  
lemmond1@llnl.gov

**L**LNL has invested more than a decade in inference methodologies for semantic graph analysis to facilitate knowledge discovery. However, knowledge discovery systems based on semantic graphs are rarely optimal for enabling the construction and testing of these algorithms.

We have addressed this deficiency by building a testbed to serve as a companion to analysts for the rapid prototyping of graph-based algorithms in an environment equipped to evaluate and compare their efficiency and performance. Due to the unique needs of LLNL to process massive graphs, we have constructed this environment to emphasize hierarchical clustering methodologies as the foundation of the analysis process.

## Project Goals

The testbed provides a suite of modular algorithm components, categorized according to their typical function in graph analysis algorithms, which may be combined as desired to create distinct algorithms. Algorithm evaluation takes place within a testing framework suitable for the evaluation of numerical algorithm results as well as for the visualization of

non-numerical algorithm output, such as the dendrogram shown in Fig. 1.

For hierarchical clustering techniques, performance evaluation frequently requires highly subjective assessment and, therefore, extensive analyst interaction. We have provided tools to help guide analysts in evaluating many aspects of algorithm performance.

## Relevance to LLNL Mission

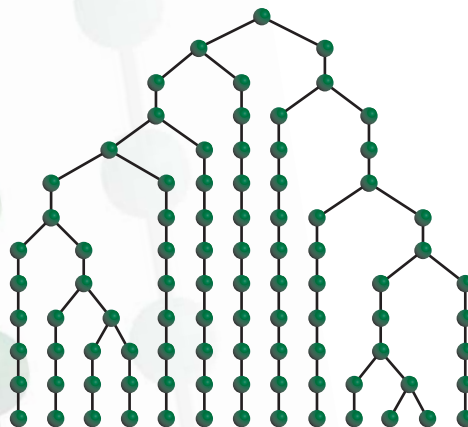
New large knowledge discovery systems may revolutionize our ability to perform real-time inference activities, since massive graphs are capable of fusing terabytes of multisource data that conceal complex relationships. Effective graph analysis techniques can expose these relationships, leading to more competent decisions through a more thorough understanding of vital, and frequently obscured, signature behaviors. This testbed makes the creation of these analysis techniques more efficient and cost-effective, leading to more productive use of semantic graphs and the knowledge discovery systems that leverage them in support of LLNL's intelligence/security mission.

## FY2007 Accomplishments and Results

Our testbed has been built as a plugin to Everest, a relatively mature graph visualization environment at LLNL. During FY2007, we completed the algorithm interface, called the Algorithm Builder, accompanied by a library of "tasks" comprising metrics and operations commonly used by graph analysis algorithms. In addition, we have completed an interactive environment for exploring algorithm results.

The Algorithm Builder has been constructed on the premise that most graph analysis algorithms are composed of multipurpose metrics and

Figure 1. A dendrogram representation of the hierarchical decomposition of a semantic graph. Each node in the dendrogram represents a cluster.



graph operations. These algorithms can be modularly represented in a fashion consistent with a plug-and-play paradigm, such that individual algorithm components can be easily modified. In the spirit of the flow diagram concept, a classical approach to algorithm representation, we found it convenient to model our algorithms using semantic graphs.

Figure 2 shows a screenshot of the Algorithm Builder, in which the task library is depicted to the left (categorized by function, e.g., metrics, flow, or diagnostics), and the Girvan-Newman community decomposition algorithm has been constructed to the right.

After executing an algorithm, an analyst must assess both its computational efficiency and the quality of the results produced. Many decomposition algorithms are hierarchical, i.e., they proceed through a series of operations that incrementally break the graph into clusters. We refer to each stage of such an algorithm as a *partition*. We have built an interactive result analysis system that attempts to facilitate quality assessment by providing

the capability to visualize/drill down into the partitions produced by the algorithm process and track intermediate results.

Figure 3 shows the primary results window, depicting pertinent information relating to a cluster at the 20<sup>th</sup> partition of Newman’s agglomerative decomposition algorithm. The information shown includes the cluster size; its node type distribution; high degree nodes of its child, parent, and sibling clusters; the point in the algorithm at which it was created; the point at which it formed two new clusters; and the high degree nodes of every other cluster within the partition. Other information that is available includes a breakdown of runtime for individual algorithm tasks, a graph of modularity (partition quality) as it evolves throughout the algorithm, and the ability to track nodes of interest from one partition to the next.

All of these analysis capabilities combine with others to provide a comprehensive view of algorithm output by which an analyst may efficiently make performance assessments of multiple

algorithms. The accompanying extensible task library will form a solid foundation for future enhancement, with the expectation that it will prove beneficial for the next generation of semantic graph inference algorithms at LLNL.

**Related References**

1. Duch, J., and A. Arenas, “Community Detection in Complex Networks Using Extremal Optimization,” *Phys. Rev. E*, **72**, 027104, 2005.
2. Fortunato, S., V. Latora, and M. Marchiori, “Method to Find Community Structures Based on Information Centrality,” *Proc. Natl. Acad. Sci.*, **70**, 056104, 2004.
3. Guimerà, R., and L. A. N. Amaral, “Cartography of Complex Networks: Modules and Universal Roles,” *J. Stat. Mech.*, P02001, 2005.
4. Newman, M. E. J., “Fast algorithm for Detecting Community Structure in Networks,” *Phys. Rev. E* **69**, 066133, 2004.
5. Newman, M. E. J., and M. Girvan, “Finding and Evaluating Community Structure in Networks,” *Phys. Rev. E* **69**, 026113, 2004.

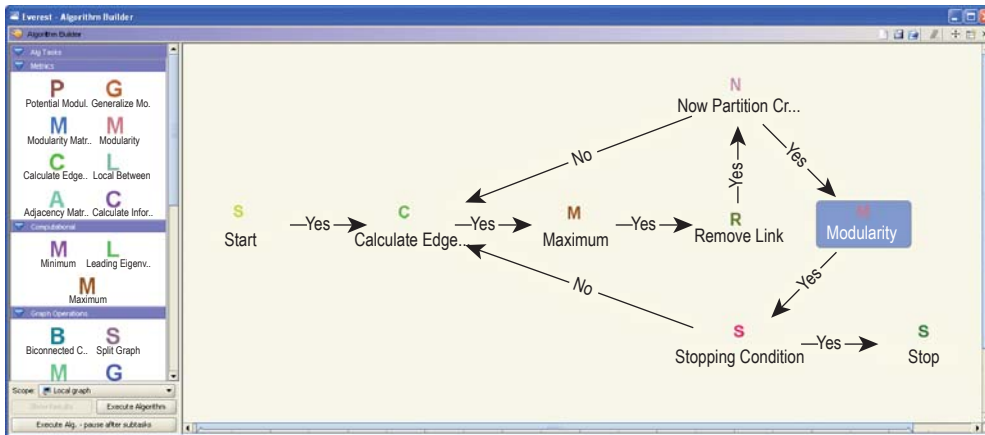


Figure 2. Screenshot of the Algorithm Builder. Girvan-Newman decomposition is shown on the right.

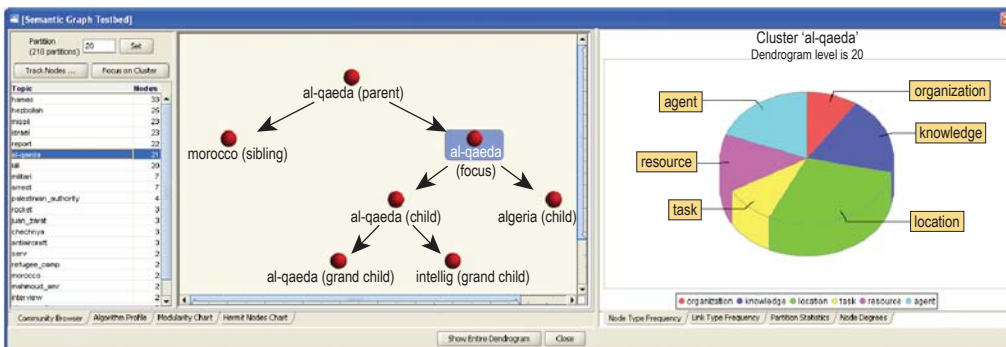


Figure 3. Primary results window. Left to right: cluster list by partition; local dendrogram; and node type frequency, given a selected cluster.

# Decomposition of Large-Scale Semantic Graphs via an Efficient Communities Algorithm



Yiming Yao  
(925) 422-1922  
yao3@llnl.gov

Semantic graphs have become key components in analyzing complex systems such as the Internet or biological and social networks. These types of graphs generally consist of sparsely connected clusters or “communities” whose nodes are more densely connected to each other than to other nodes in the graph. The identification of these communities is invaluable in facilitating the visualization, understanding, and analysis of large graphs by producing subgraphs of related data whose interrelationships can be readily characterized. Unfortunately, the ability of LLNL to effectively analyze the terabytes of multi-source data at its disposal has remained elusive, since existing decomposition algorithms become computationally prohibitive for graphs of this size. We have addressed this limitation by developing more efficient algorithms for discerning community structure that can effectively process massive graphs.

## Project Goals

Current algorithms for detecting community structure are capable of processing only relatively small graphs. The cubic complexity of Girvan and

Newman makes it impractical for graphs with more than approximately  $10^4$  nodes. Our goal for this project was to develop methodologies and corresponding algorithms capable of effectively processing graphs with up to  $10^9$  nodes. From a practical standpoint, we expect the developed scalable algorithms to help resolve a variety of operational issues associated with the productive use of semantic graphs at LLNL.

## Relevance to LLNL Mission

In recent years, LLNL has developed semantic graph technologies capable of fusing disparate facts from diverse sources into massive semantic graphs to facilitate inference of complex and anomalous behaviors embedded within the data. A critical challenge in effectively applying this technology to the Laboratory’s mission is to decompose massive graphs into meaningful subgraphs that an analyst can efficiently interrogate to identify these behaviors. This research represents a significant contribution to LLNL’s counterterrorism, biodefense, and nonproliferation missions, because efficient decomposition methodologies will provide the foundation for information analysis environments enabling large-scale data mining, and information discovery and visualization.

## FY2007 Accomplishments and Results

During FY2007, we completed a graph clustering implementation that leverages a dynamic graph transformation to more efficiently decompose large graphs. In essence, our approach dynamically transforms the graph (or

Table 1. Computation time reduction over Girvan & Newman’s method.

Graph	Nodes	Links	$T_{gn}$	T	R(%)
Erdos972	5488	8972	1180.1	129.6	89.0
Hep-Th	7610	15751	1524.5	670.0	56.1
Kohonen	4470	12720	22.8	8.7	62.0
Power	4941	6594	723.0	550.4	23.9

$T_{gn}$ : Girvan & Newman’s time (min); T: our time (min);  $R = 100(T - T_{gn}) / T_{gn}$

Table 2. Computation time for parallel graph clustering.

Graph	Nodes	Links	CPUs	T	Q
G10m	10000000	43749984	4	28.9	0.40
G100m	100000000	298437392	32	706.0	0.72
G1000m	1000000000	2624753446	512	710.0	0.78

T: computation time (min); Q: modularity

subgraphs) into a tree structure consisting of bi-connected components interconnected by bridge links. This isomorphism allows us to compute edge betweenness, the chief source of inefficiency in Girvan and Newman's decomposition algorithm, much more efficiently, leading to significantly reduced computation time. Test runs on a desktop computer have shown reductions of up to 89% (Table 1).

Our focus this year has been on the implementation of parallel graph clustering on one of LLNL's supercomputers. To achieve efficiency in parallel

computing, we have exploited the fact that large semantic graphs tend to be sparse, comprising loosely connected dense node clusters. When implemented on distributed memory computers, our approach performed well on several large graphs with up to one billion nodes, as shown in Table 2. The rightmost column of Table 2 contains the associated Newman's modularity, a metric that is widely used to assess the quality of community structure.

Existing algorithms produce results that merely approximate the optimal solution, *i.e.*, maximum modularity.

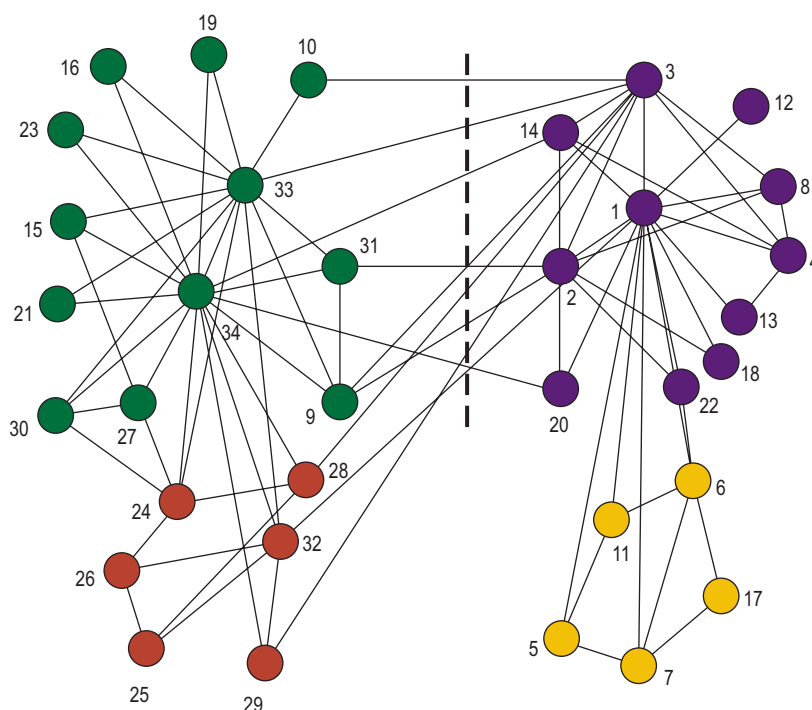
We have developed a verification tool for decomposition algorithms, based on a novel integer linear programming (ILP) approach, that computes an exact solution. We have used ILP methodology to find the maximum modularity and corresponding optimal community structure for several well-studied graphs in the literature (see figure).

The above approaches assume that modularity is the best measure of quality for community structure. In an effort to enhance this quality metric, we have also generalized Newman's modularity based upon an insightful random walk interpretation that allows us to vary the scope of the metric. Generalized modularity has enabled us to develop new, more flexible versions of our algorithms.

In developing these methodologies, we have made several contributions to both theoretical graph algorithms and software engineering.

### Related References

1. Newman, M. E. J., and M. Girvan, "Finding and Evaluating Community Structure in Networks," *Phys. Rev. E* **69**, 026113, 2004.
2. Zachary, W., "An Information Flow Model for Conflict and Fission in Small Groups," *Journal of Anthropological Research*, **33**, pp. 452-473, 1977.
3. Yao, Y., T. L. Hickling, W. G. Hanley, and J. S. Lenderman, "Graph Clustering Evaluation via Integer Linear Programming," *Proceedings of the 2007 International Conference on Data Mining*, pp. 369-375, 2007.



Optimal community structure for Zachary's karate club.

# Statistical Approach to Complex Systems in the Presence of Uncertainty



Lee G. Glascoe  
(925) 423-2922  
glascoe1@llnl.gov

The optimization of engineering systems often inappropriately assumes deterministic input parameters. The effect of such assumptions is generally unknown particularly for complex systems. We address this problem using a probabilistic framework accounting for parametric uncertainties and allowing for quantification in system response or performance. In this framework the performance functions of interest are random, and their optimization is performed with respect to the design variables. We adapted and implemented an advanced statistical learning technique, sequential importance sampling (SIS), to make predictions about the response of complex uncertain systems, including an HE-detonation model and an energy policy model, and their sensitivity to variations of the variables.

## Project Goals

The purpose of the project is to establish a stochastic framework that enables the efficient calculation of response statistics over the entire variable space. The framework consists of two components.

First, directly parallelizable advanced sampling techniques are used to evaluate the system response as a function of design and random variables using the least number of deterministic simulations. Second, the output of this sampling process is statistically classified using robust probit regression and boosting schemes to derive the dependence of the performance statistics as functions of the variables.

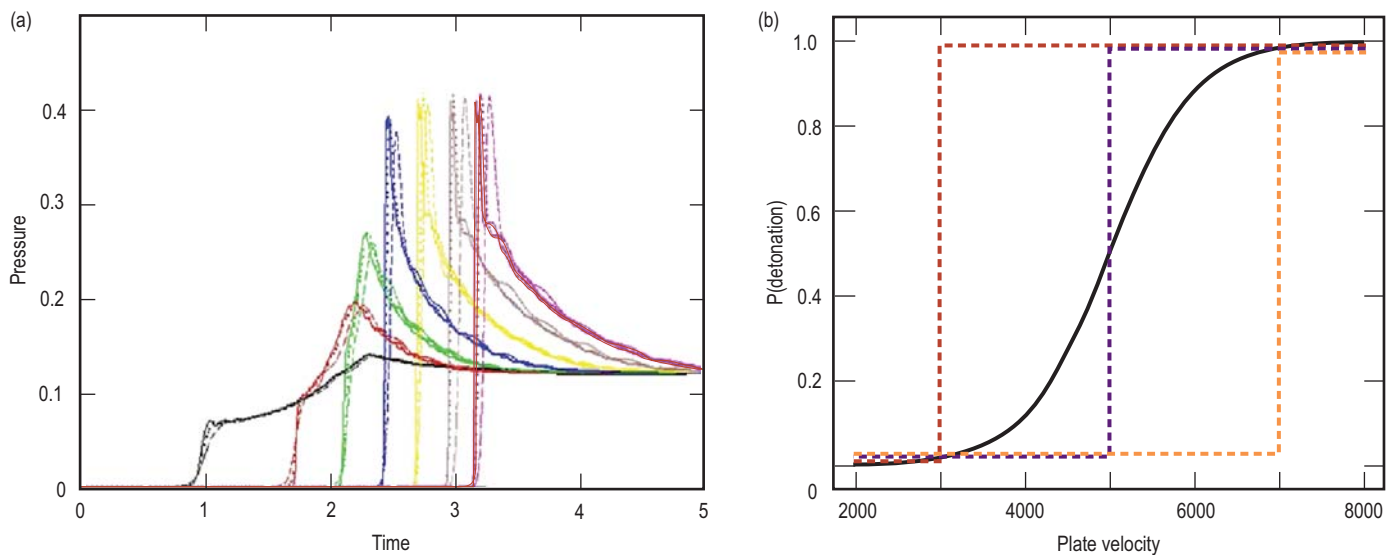


Figure 1. (a) Pressure vs. time at different gages for a deterministic ALE3D detonation simulation. (b) Probability of detonation as a function of plate velocity for three spatially fixed HE mass-fraction values (dotted lines) and accounting for zonal HE mass-fraction uncertainty using SIS (solid line).

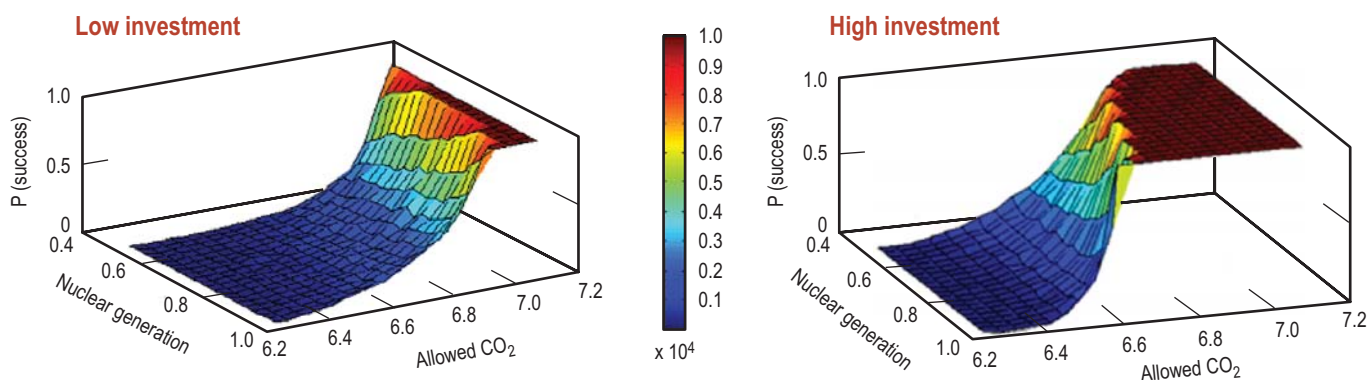


Figure 2. Probability of policy success as a function of three variables.

### Relevance to LLNL Mission

Our project addresses the need for uncertainty quantification and sensitivity analysis of complex systems and enhances LLNL's ability to apply advanced stochastic techniques to existing deterministic codes. The advocated techniques increase efficiency and predictive ability of existing computational codes and are applicable to problems in infrastructure protection, energy security, and national security.

### FY2007 Accomplishments and Results

Our accomplishments have been in the area of detonation modeling and energy policy.

Modeling HE detonation is potentially a multivariate nonlinear problem with uncertainty in several parameters. The ALE3D hydrodynamics code deterministically predicts detonation based on peak overpressure, assuming a spatially fixed HE mass-fraction ratio as a function of flyer plate velocity (Fig. 1a). Using SIS we efficiently compute and optimize the likelihood of detonation accounting for uncertainty in

the zonal HE mass fraction. Illustrated in Fig. 1b is one possible response space using SIS along with three deterministic, *i.e.*, spatially fixed HE mass-fraction, ALE3D simulations.

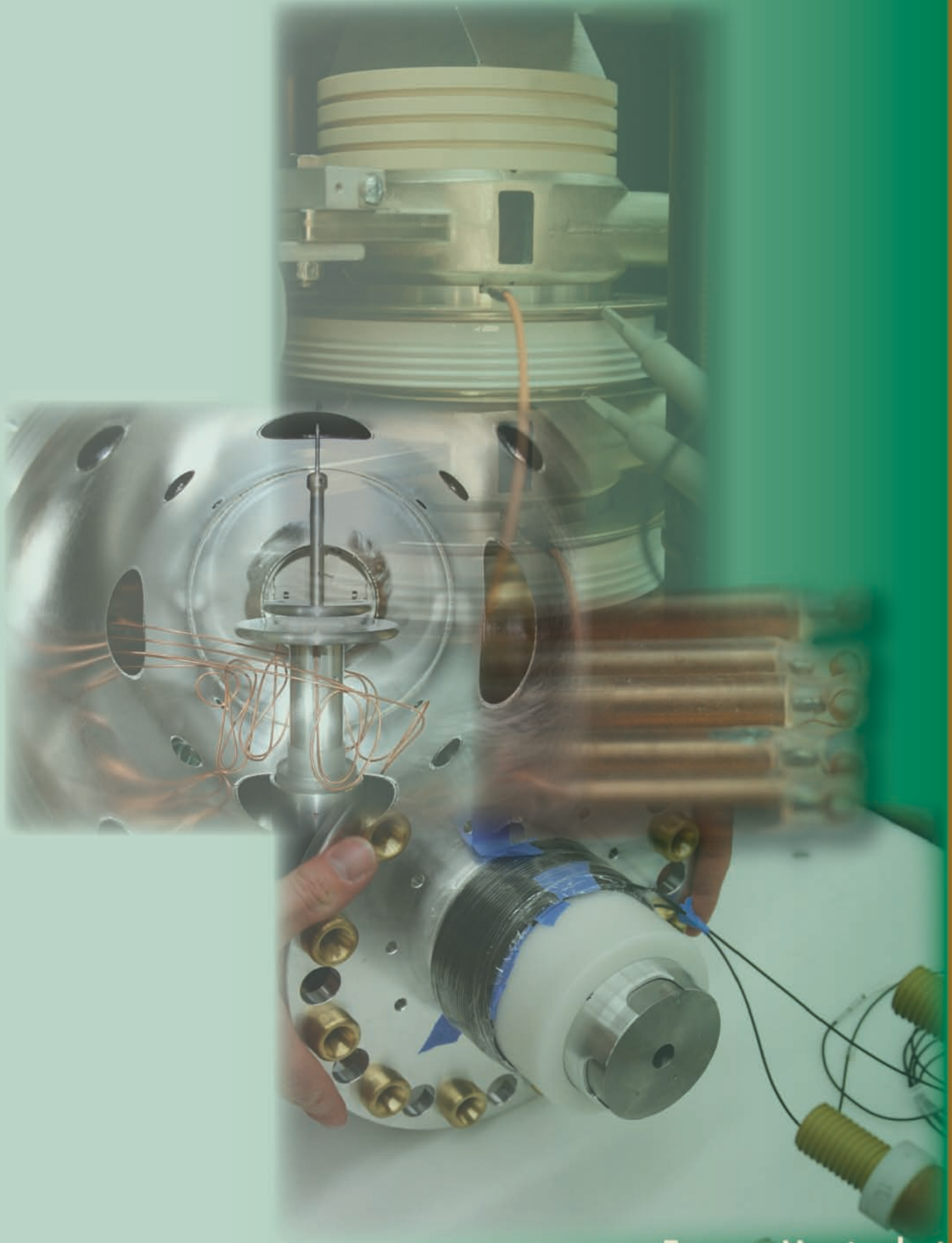
The mathematical modeling of energy systems is used to optimize policy strategies but is hampered by large uncertainties associated with several key parameters. Policy decisions made in the presence of uncertainty work best with a probabilistic objective function, *e.g.*, the probability that the cost will not exceed a certain threshold.

In this example we use MARKAL, a deterministic model for energy systems that accounts for a very large number of uncertain parameters. We consider two random variables (gas and oil prices) as well as three design variables (national R&D investment, nuclear generation, and CO<sub>2</sub> allowance) and predict the probability of successfully attaining a cost-effective CO<sub>2</sub> emission reduction. Figure 2 depicts the probability of success as a function of the three design variables.

### Related References

1. Doucet, A. J., F. G. de Freitas, and N. J. Gordon, Eds., *Sequential Monte Carlo Methods in Practice*, Springer, New York, 2001.
2. Griffiths, W. E., R. C. Hill, and P. J. Pope, "Small Samples Properties of Probit Model Estimators," *Journal of the American Statistical Association*, **82**, pp. 929-937, 1987.
3. Neal, R. M., "Annealed Importance Sampling," *Statistics and Computing*, **1**, 1, pp. 125-139, 2001.
4. Urtiew, P., K. Vandersall, C. Tarver, F. Garcia, and J. Forbes, "Shock Initiation Experiments and Modeling of COMPB and C-4", *13th International Detonation Symposium*, July 2006.





Energy Manipulation



# Ultrahigh-Velocity Railgun

A railgun is a very simple device, essentially a single-turn coil (Fig. 1). Electric current is sent down one rail, through the moveable armature, and returns down the other rail. The magnetic “pressure” developed in the railgun bore behind the armature creates a driving force to accelerate it down the rails. For speeds less than about 2.5 km/s, designs typically use a solid armature made of aluminum. At speeds higher than that plasma forms, and therefore either a hybrid armature (solid armature with plasma brushes) is used, or the solid portion of the armature is eliminated *a priori* and a plasma armature is allowed to form.

During the late 1980’s, Lawrence Livermore National Laboratory took a leading role in the development of railguns as a means of launching projectiles at ultrahigh velocities, *i.e.*, > 8 km/s. A practical ultrahigh-velocity (UHV)

railgun would have contemporary applications in equation-of-state research, space launch, and kinetic energy weapons.

Our UHV railgun project aims to understand the physics that currently limits railgun performance, by leveraging the history of railgun development with our world-class leadership in modeling and simulation.

## Project Goals

Today’s railgun technology is limited by poorly understood mechanisms at velocities between 5 and 6 km/s. The most commonly accepted mechanism for this poor performance is “restrike,” defined as the short-circuiting of the main current path at a distance significantly behind the armature. The ultimate cause of restrike has been variously attributed to viscous/ablative drag, thermally-driven avalanche, or 3-D MHD effects (Fig. 2). Progress toward isolating the mechanisms had been impeded by the limited simulation and diagnostic capabilities available in the 1980’s when most railgun tests were conducted.

This project aims to overcome these twin hurdles, by 1) developing ALE3D as a useful tool for the simulation of UHV railguns; and 2) performing experiments adequate to verify the capability of ALE3D in railgun-relevant regimes.

Ultimately, an understanding of the limiting physics of railguns could lead to candidate railgun designs capable of



Jerome M. Solberg  
(925) 422-5971  
solberg2@llnl.gov

generating projectile velocities above 8 km/s.

## Relevance to LLNL Mission

The development of a 3-D modeling capability tool for materials in the warm-dense-matter regime characteristic of railgun plasmas, including the physics of melt and transition to the ionized state, has a wide range of application within the Laboratory’s mission. Related applications include the modeling of exploding detonator bridge wires, explosive pulsed power applications, and arc welding/cutting. Diagnostic techniques developed and used in the validation experiments have similar applications.

A UHV railgun that exceeds current velocity limits would be well-suited to high-velocity impact-driven equation-of-state experiments, for which the present technology (two-stage gas guns) has limitations above 8 km/s.

## FY2007 Accomplishments and Results

We augmented ALE3D with plasma conductivity models, primarily from the Laboratory’s Purgatorio code, and SESAME conductivity models from Sandia National Laboratories. Validation studies comparing ALE3D to the legacy 2-D code CALE began. Both CALE and ALE3D were used to design the Fixed Hybrid Armature experimental facility (Figs. 3 and 4).

The Fixed Hybrid Armature test facility was constructed leveraging legacy hardware from the early 1990’s. In this experiment, a railgun with the hybrid armature held in place is coupled to a long-pulse power source. Two plasma brushes are initiated from exploding aluminum foils. Since no gross motion of the armature occurs, this experiment allows detailed analysis of the plasma behavior,

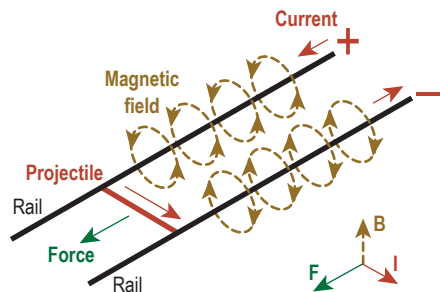


Figure 1. Basic railgun physics. *I* is the current; *B* is the magnetic field; and *F* is the resultant Lorentz force. Maximum efficiency occurs when the current is concentrated at the rear of the projectile.

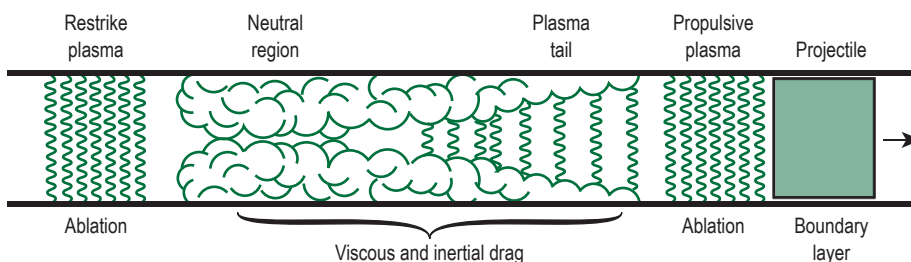


Figure 2. Restrike Hypothesis. The restrike plasma short-circuits the propulsive plasma, resulting in a reduction in the Lorentz force.

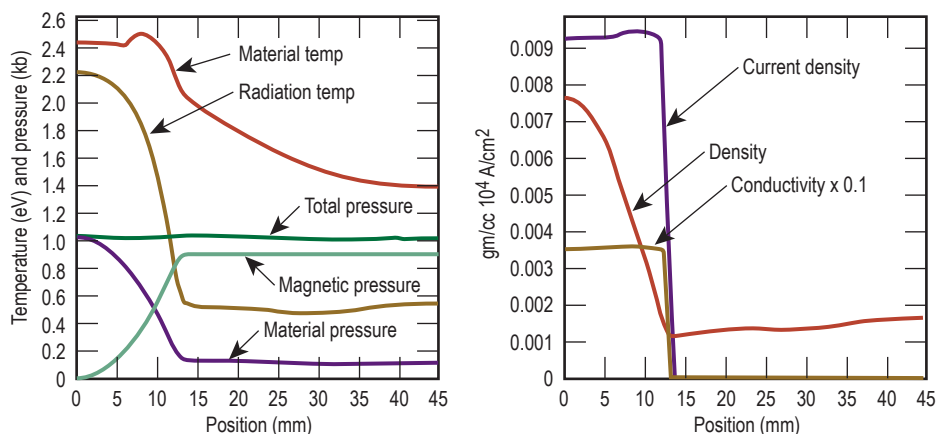


Figure 3. 2D CALE Fixed Armature Simulations, used both as a reference for ALE3D development and to help design the Fixed Armature Experiment.

including measurements of currents and magnetic fields, plasma pressure, and various optical diagnostics.

The experiment (Fig. 5) permits investigation of armature plasma dynamics due to both ablation and high plasma ejection speeds, as well as investigating near steady-state conditions. Diagnostics includes a fine array of B-dots for the magnetic field, Rogowski coils for currents, and piezo-electric pressure sensors. Fiber optics captured the light emission data in preparation both for future use of fiber-optic-based pressure sensors and for optical techniques to measure the plasma emission characteristics as a function of time and position.

We initiated a project with the U.S. Navy for modeling and simulation efforts that focus on a different portion of the mass/velocity space. This effort aims to replace conventional ship-based artillery with electrically launched kinetic energy weapons.

### Related References

1. Hawke, R. S., *et al.*, "Measurements of Experimental Plasma Brush Behavior in Hybrid Armatures," *IEEE Transactions on Magnetics* **29**, 1, pp. 814-818, 1993.
2. Crawford, R., D. Keefer, and R. Tipton, "Velocity Limiting Magnetohydrodynamic Effects in Railgun Plasma Armatures," *IEEE Transactions on Magnetics*, **29**, 1, pp. 781-786, 1993.
3. Boyton, G. C., *et al.*, "Secondary Arcs in 2-D MHD Numerical Simulations of EML Plasma Armatures," *IEEE Transactions on Magnetics* **31**, 1, pp. 564-569, 1995.
4. Parker, J. V., "Why Plasma Armatures Don't Work (and What Can Be Done About It)," *IEEE Transactions on Magnetics* **25**, 1, pp. 418-424, 1999.



Figure 4. ALE3D Fixed Armature Simulations. The aluminum in light blue has exploded and is being contained by magnetic pressure against the insulator wall (pink). The red bars are the rails; the dark blue is the air.

### FY2008 Proposed Work

Simulation efforts will focus largely on improving and understanding ALE3D as it applies to railgun physics. This will include further comparisons with CALE and application to railguns with moving armatures. Ultimately, the goal is to model legacy LLNL railgun experiments with a view toward understanding the observed velocity limitations.

The Fixed Hybrid Armature experiments will continue. A number of diagnostics will be fully vetted within the context of the experiment. Ultimately, the results of these experiments will be used to increase confidence in the simulation results.

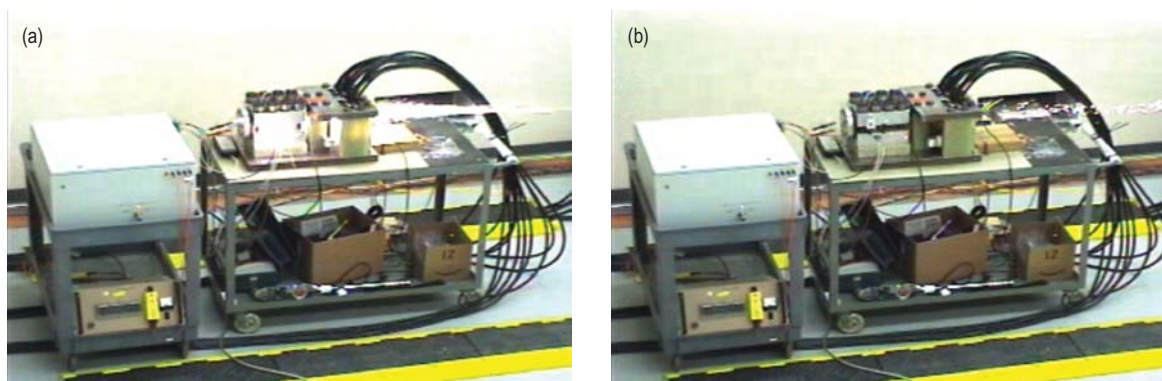


Figure 5. Fixed Armature Experiment Shot 1, 290 kA. (a) As the aluminum foils explode, part of the plasma is lost out the back of the experiment. (b) The remainder is contained by the magnetic forces, and forms plasma brushes that conduct current through the fixed armature.

# Pulse Power Systems and Diagnostics for the Fixed Hybrid Armature Railgun



Todd J. Clancy  
(925) 422-8571  
clancy5@llnl.gov

Plasma physics within the confines of railgun science is not well understood. Since plasmas and “restrike” are primarily responsible for preventing ultrahigh velocities (UHV) in such guns, there is a great need to predict and control that behavior.

Given the potential role of UHV railguns in equation of state (EOS) studies, we must regain our expertise in all aspects of railgun science. Working toward this goal we rebuilt the Fixed Hybrid Armature Railgun (pictured in the previous report in this volume), implemented advanced diagnostics, and began to recreate past experiments. Experimental data will be provided to the UHV railgun project and applied to the validation of a new plasma model in ALE3D, a 3-D multi-physics computational platform.

## Project Goals

The primary goal of this project is to provide diagnostic data with sufficient resolution and relevance to validate a plasma model in ALE3D that is applicable in the railgun regime. To achieve this, we assembled the railgun and configured a testbed for the application of high-energy pulsed power and sensitive diagnostics. We intend to perform multiple experiments, with multiple parameter modifications similar to those performed a decade ago, along with new configurations.

## Relevance to LLNL Mission

This project directly addresses diagnostic systems for a railgun testbed and also addresses the feasibility of UHV railguns, which would be well suited to shock physics and EOS studies. Both of these goals are expressed as immediate needs for LLNL, and impact all pulsed power programs at LLNL.

## FY2007 Accomplishments and Results

By leveraging legacy hardware from the early 1990’s, we assembled the Fixed Hybrid Armature test facility and performed the first experiment in late FY2007. In this experiment, plasma brushes were formed from exploding aluminum foils, which then provided a current path through the armature. Peak current was 290 kA and a post-shot inspection of the armature exhibited evidence of plasma brush creation (Fig. 1).

Since the armature was fixed in place, a pseudo-steady state was achieved and diagnostic investigation was simplified. This shot included

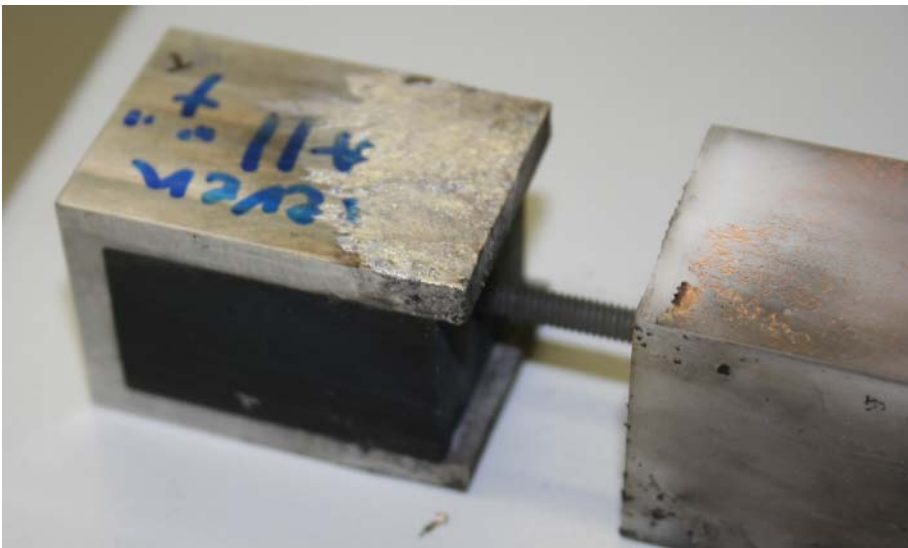
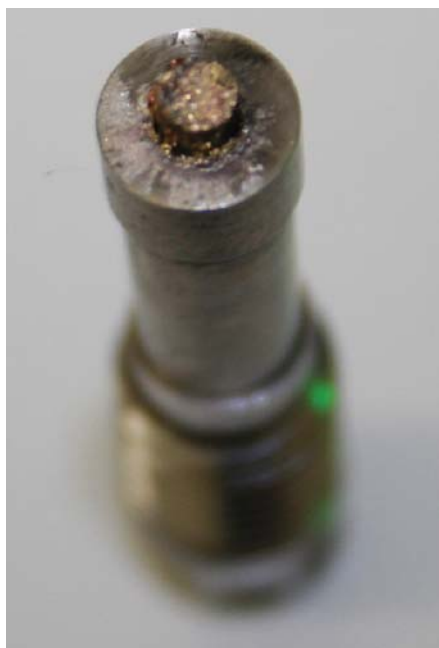


Figure 1. Post-shot picture of a small hybrid armature that had been held stationary between rails by the rod and stop block. The plasma brush creation caused material ablation, evident on the armature.

many diagnostic sensors. Two arrays of five B-dots each were used to measure magnetic fields produced by the plasma. These small loop antennas were oriented with their loop normals orthogonal to the rail magnetic fields, and were thus unaffected by rail current (Fig. 2). The array was used to diagnose plasma currents as a function of position.

Two counter-wound Rogowski coils were positioned around the upper rail for measurement of the total input current, and plasma pressure was obtained with a piezoelectric quartz sensor (Fig. 3). The rail voltage was measured with a differential probe, and the pulsed power system included additional current and voltage diagnostics.

Fiber optic pressure and optical emission sensors were used as a proof of concept in determining plasma characteristics, and will be implemented fully in future experiments. The experiment produced a total of 45 files of data that we are currently analyzing. A sample of B-dot data is shown in Fig. 4.



**Figure 3.** Piezoelectric quartz pressure sensor with integrated electronics that has a form factor capable of pressure measurements up to 30 kpsi. This post-shot photograph shows evidence of hardened copper and aluminum debris on the sensing diaphragm which is just 0.1 in. in diameter.

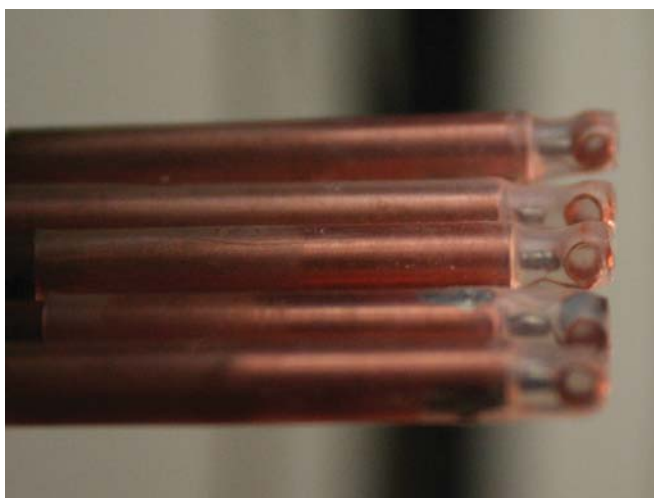


**Figure 2.** One of two B-dot arrays positioned to sense plasma magnetic field generation. These are 15-turn loop antennas with an ID of 0.063 in. and a measured effective area of 33mm.<sup>2</sup> They are soldered to semi-rigid coax and encased in transparent shrink-wrap.

### Related References

1. Drobyshvski, E. M., *et al.*, "Physics of Solid Armature Launch Transition into Arc Mode," *IEEE Transactions on Magnetics*, **37**, 1, pp. 62-66, 2001.
2. Hawke, R. S., *et al.*, "Summary of EM Launcher Experiments Performed at LLNL," *IEEE Transactions on Magnetics*, **22**, 6, pp. 1510-1515, 1986.
3. Hawke, R. S., *et al.*, "Plasma Armature Formation in High Pressure, High-Velocity Hydrogen, Starfire: Hypervelocity Rail Gun Development of High Pressure Research," *IEEE Transactions on Magnetics*, **25**, 1, p. 219, 1989.

### FY2008 Proposed Work

We intend to continue experiments on the Fixed Hybrid Armature Railgun. Data from FY2007 will be processed and analyzed, providing guidance for additional shots. Fiber optic diagnostics will be implemented, allowing faster response times and less physical intrusion, thus providing additional precision to ALE3D validation.

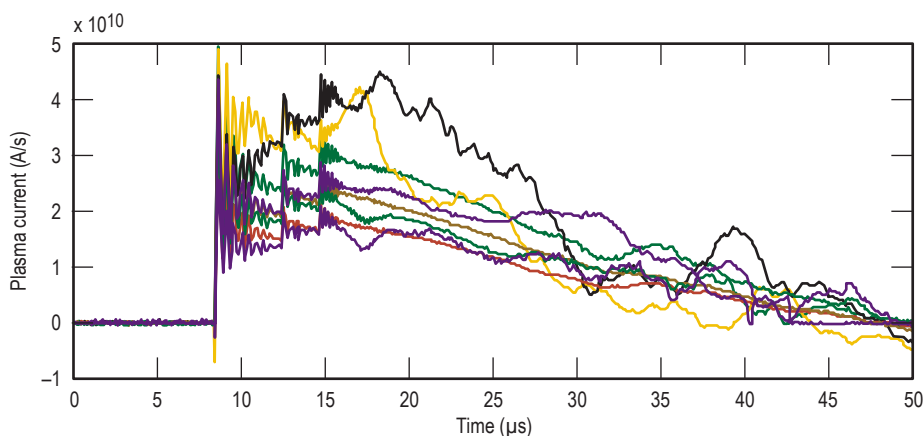


**Figure 4.** Eight traces of scaled B-dot data from an early experiment shot. The initiation of each of the three capacitor banks is evident at 8.5, 12.5, and 14.7  $\mu$ s, followed by cable ringing.

# Fast Diagnostic for Electrical Breakdowns in Vacuum



Timothy L. Houck  
(925) 423-7905  
houck1@llnl.gov

An important area of pulsed-power R&D is high-voltage vacuum insulator breakdown, often referred to as flashover due to the sudden avalanche of electrons across the insulator surface. This phenomenon is often the limiting factor in attaining the highest possible performance in pulsed-power devices. While several hypotheses attempt to explain the initiating mechanism(s), flashover is not well understood. Computational modeling is limited to establishing the electromagnetic field and radiation imposed on the insulator. The designer then makes adjustments to the configuration and/or materials until the modeling results are within safety margins based on empirical data. This design approach is believed to be overly conservative since the bulk dielectric strength of the insulating material can be an order of magnitude greater than the flashover limitation. However, without a quantitative understanding of the phenomenon this is the only approach to ensure reliability.

A major obstacle to gaining a quantitative understanding of insulator flashover is the time scale for the

phenomenon. Typical vacuum electrode spacing is dependent on voltage standoff expectations with spacings on the order of a centimeter experiencing flashover in a fraction of a nanosecond. To record such flashover we require diagnostics with response times on the order of a few hundred picoseconds or faster. Equally important, the diagnostic must be compatible with the geometry of the experiment. In most applications and test stands, the insulator is located between parallel electrodes a few centimeters to tens of centimeters in transverse dimension and separated by distances of a few millimeters to a few centimeters. Diagnostics that are located away from the electrode gap, *e.g.*, on the power feeds, record a signal delayed and distorted by the intervening inductance and capacitance. These inductances and capacitances are normally very small, but for the extremely fast signals associated with flashover they act as filters that remove critical spectral components of the signal.

The goal of this project is to provide an appropriate diagnostic.

## Project Goals

The deliverable for this project is a compact, high-bandwidth diagnostic that can measure the electric field in the immediate vicinity of an insulator flashover with a temporal resolution capable of capturing the initiating mechanism. In addition, the design methodology for the diagnostic is to be evaluated and documented so that similar diagnostics can be fabricated for other projects. There are presently multiple experiments and proposals directed toward the understanding of vacuum insulator breakdown/flashover. All of these studies require a fast diagnostic to record the initial buildup of the electron avalanche.

## Relevance to LLNL Mission

This project provides LLNL with a more capable diagnostic for pulsed power R&D, specifically vacuum insulator studies. Our diagnostic can be included in the suite of diagnostics used for monitoring the performance of new hardware under extreme conditions, *e.g.*, explosively driven flux generators.

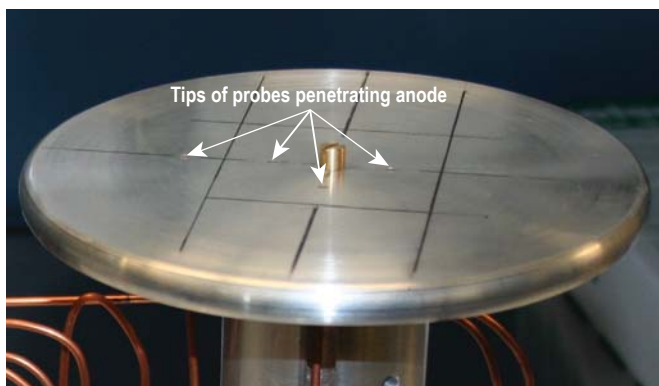


Figure 1. Anode plate with capacitively coupled diagnostic probes installed. Lines on the anode indicate the footprint of the test insulator. All but one probe are positioned under the insulator during testing.

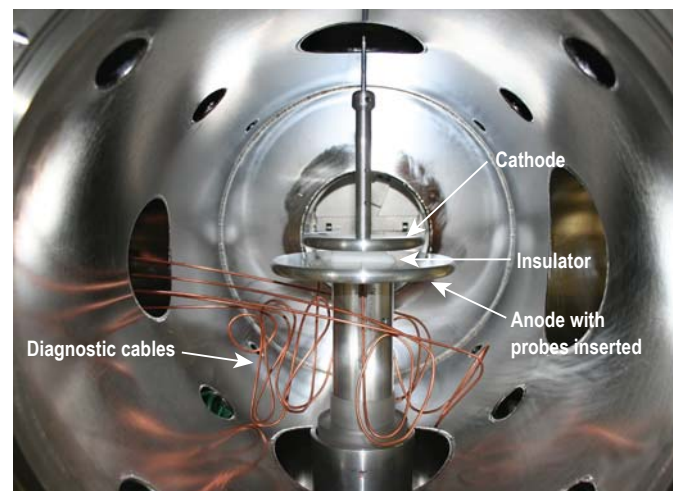


Figure 2. Electrodes positioned in vacuum test chamber.

At a more basic level, this fast diagnostic is a tool for understanding flashover and benefits projects studying flashover in general. If the information acquired by this diagnostic leads to a fundamental understanding of flashover, all high power, pulsed power systems would be impacted. These systems include high-current particle-beam accelerators, high-power radio frequency and microwave sources, high-power laser sources, pulsed neutron sources, nuclear weapons effects simulators, lightning and electromagnetic pulse effects simulators, x-ray and proton radiography machines, inertial fusion drivers, directed energy weapons, and electromagnetic launchers.

### FY2007 Accomplishments and Results

Diagnostic probes were fabricated and demonstrated involving insulator flashover testing. Several steps were involved in the successful fielding of the probes:

1. A general design based on a D-dot probe for measuring the time rate of change of the electric field was chosen, based on measurement quantity and physical size constraints.
2. A survey of commercially available components was undertaken.
3. Electrostatic simulations were performed to calculate the probe's response and estimate its sensitivity and potential bandwidth.

4. A prototype was fabricated and tested/calibrated.
5. Five probes were installed in the anode of an insulator test chamber (Figs. 1 and 2).

The frequency response of the probe was computationally estimated to be in excess of 100 GHz. Figure 3 is a sample probe signal. The response of the probes exceeds commercially available digitizing capability. The two traces correspond to a flashover on the insulator surface immediately above the probe and a breakdown event distant from the probe. The changing electric field due to the electron avalanche is noted and partially resolved. The raw probe signal has been converted to diode voltage in Fig. 4. The conversion parameters used were calculated from simulations and agreed well with the known charge voltage.

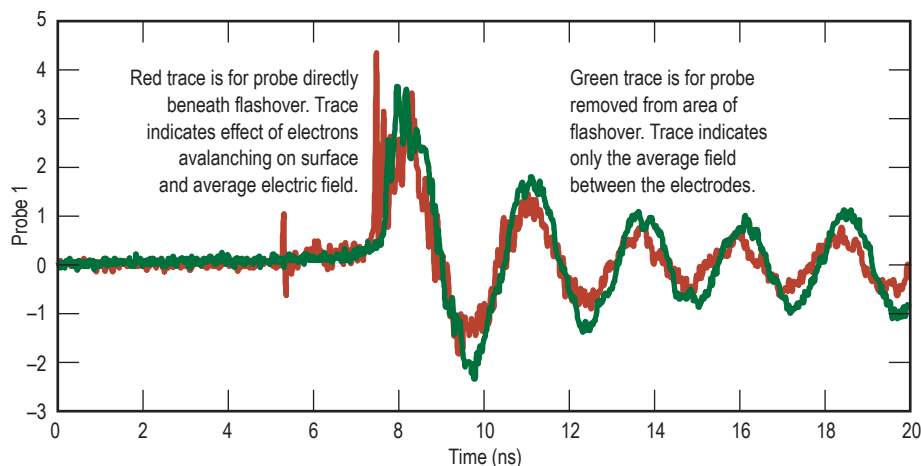


Figure 3. Raw signal from fast diagnostic probe. The signal is proportional to the electric field on the surface of the inner conductor of the probe.

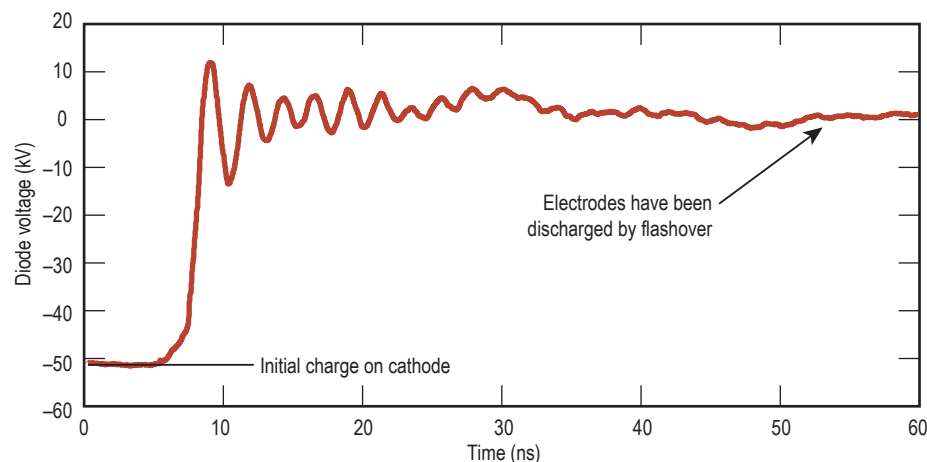


Figure 4. The raw probe signal, converted to show the potential difference between the electrodes with the cathode at -52.5 kV prior to discharge.

### Related References

1. Humphries, S. Jr., *Principles of Charged Particle Acceleration*, John Wiley and Sons, New York, 1999, Chapter 9.14.
2. Wetzer, J. M., "Vacuum Insulator Flashover: Mechanisms, Diagnostics and Design Implications," *Proc. XVIIth International Symposium on Discharges and Electrical Insulation in Vacuum*, Berkeley, California, pp. 449-458, 1996.
3. Enloe, C. L., and R. M. Gilgenbach, "Microscopic and Macroscopic Material Property Effects on Ultraviolet-Laser-Induced Flashover of Angled Insulators in Vacuum," *IEEE Trans. Plasma Sci.*, **16**, 3, pp. 379-389, June 1988.

### FY2008 Proposed Work

With our confidence in the success of this project, we will explore placing probes in Flux Compression Generators. Further R&D related to the application of the probes is expected to be associated with techniques for processing/analyzing the output signals to take advantage of the large bandwidth.

# UV-Induced Insulator Flashover



Jay Javedani  
(925) 422-8569  
javedani1@llnl.gov

Insulators are critical components in high-energy, pulsed power systems. The insulator's main function in these devices is to provide an interface between regions of insulating fluid/gas and vacuum that separate electrodes at different high-voltage potentials. It is known that the vacuum surface of the insulator will flashover when illuminated by ultraviolet (UV) radiation at voltages depending on the insulator material, insulator cone angle, applied voltage, and insulator shot-history. Surface flashover refers to a cascade of electrons along the insulator's surface leading to the collapse of the voltage between the conductors.

The UV radiation may be generated by ohmic heating of metal surfaces, coronas in high electrical field regions, or plasmas from explosive emission. As the power of the pulsed power system is increased, so is the UV fluence. An accurate knowledge of the UV fluence (energy per unit area) required for flashover is critical for the next generation of high power flow systems.

## Project Goals

The objective of this project is to measure the UV fluence required for flashover of insulator as a function of material and cone angles. The data gathered would validate the measurements reported in the 1980's and extend the knowledge base to present parameters. These results will be useful to electrically stressed, UV-radiated systems in many pulsed power applications.

## Relevance to LLNL Mission

For many systems the delivery of pulsed power into a vacuum region is the most critical factor impacting performance and reliability. The applicability of our investigation in UV flashover performance addresses issues related to power flow channels for flux compression generators. As such, the results have a significant impact on the LLNL national security mission.



Figure 1. Photograph of the experimental apparatus with an opened cylindrical vacuum test chamber.



**Figure 2.** Photograph of insulators (clear HDPE, milky Rexolite ©). The HDPE insulator on its edge displays a rectangular damaged area from the UV laser beam.

### FY2007 Accomplishments and Results

A testbed comprised of an excimer laser (KrF, 248 nm), a vacuum chamber ( $<1.0 \times 10^{-6}$  Torr), and a dc high-voltage power supply ( $<60$  kV) was established. Fast capacitive probes (D-dot) were embedded in the anode electrode underneath the insulator to give the time of arrival of UV pulse and flashover. A photograph of the test equipment is provided in Fig. 1.

Testing included two types of insulator materials: high-density polyethylene (HDPE), and a crossed linked polystyrene (Rexolite®). Insulator angles of  $0^\circ$ ,  $\pm 30^\circ$ , and  $\pm 45^\circ$  were extensively tested with a maximum UV fluence of  $70 \text{ mJ/cm}^2$  at varying static charge on the insulator. Figure 2 is a photograph of tested insulators.

Over 700 data records were obtained. This information clarified/

corrected earlier published studies and provided design guidance for ongoing pulsed power programs. A sample of the data is shown in Fig. 3.

A new effect was observed related to the UV intensity on flashover that had not been previously reported. It appears that UV pulses with intensity greater than the minimum UV fluence need more than the established minimum energy/fluence to induce surface flashover. In other words, the fluence required for flashover is also a function of the intensity of the UV pulse. This effect would bias the data toward higher minimum flashover fluence and lead to an incorrect interpretation of the previously reported data. We have proposed doing further studies to understand and quantify this effect.

### Related References

1. Enloe, C., *et al.*, "Vacuum Ultra-Violet Effects on Power Transport Across a Vacuum/Solid Dielectric Interface," *Proc. Xth International Symposium on Discharges and Electrical Insulation in Vacuum*, Columbia, South Carolina, I, pp. 308-314, October 1982.
2. Enloe, C. L., and R. E. Reinovsky, "Ultra-Violet Induced Insulator Flashover as a Function of Material Properties," *Proc. 4th IEEE Pulsed Power Conf.*, Albuquerque, New Mexico, I, pp. 679-682, June 1983.
3. Enloe, C. L., and R. M. Gilgenbach, "Microscopic and Macroscopic Material Property Effects on Ultraviolet-Laser-Induced Flashover of Angled Insulators in Vacuum," *IEEE Trans. Plasma Sci.*, **16**, 3, pp. 379-389, June 1988.

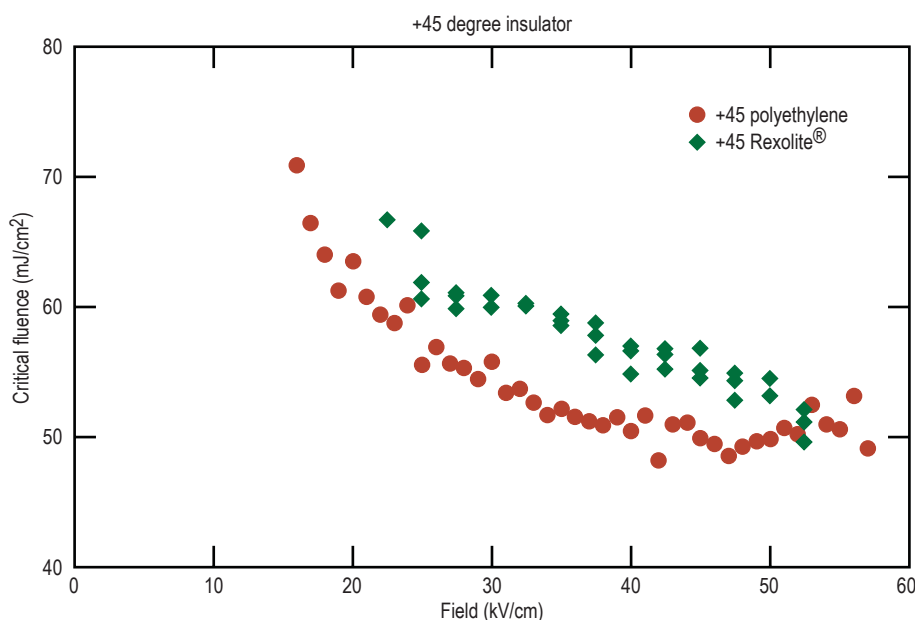


**Figure 3.** Critical fluence at which surface flashover occurs versus the electric field strength for two materials. The relatively complex relationship between the two variables is evident.

### FY2008 Proposed Work

We propose to extend our studies to include other typically used insulator materials such as Macor and Micalex (machinable ceramics), polyurethane and Mica-filled epoxies. These materials have desirable mechanical properties for proposed applications, but their electrical properties in a UV radiation environment are not quantitatively known. We also propose to study the effect of the UV intensity on flashover.

# Evaluation of Light Activated Thyristors for Pulsed Power Applications



Laura Tully  
(925) 424-2235  
tully2@llnl.gov

In pulsed power system design, the switch is arguably the most critical fundamental element. By definition, pulsed power is the compression of energy in space and time. Reliable switching of stored energy is essential to the performance of a pulsed power system. Solid-state switch technology offers the demonstrated advantage of reliability under a variety of conditions. Light-triggered switches operate with a reduced susceptibility to electromagnetic interference commonly found within pulsed power environments. Despite the advantages, commercially available solid-state switches are typically not designed for extreme pulsed power requirements.

High current switching poses a unique set of challenges. This effort focused on two key switch characteristics: high peak current and high di/dt.

A high peak current handling capability in a switch decreases the number of parallel switches required in a high peak current system, thus reducing system cost and complexity. High di/dt capability increases the range of possible loads to the system. Both criteria are important for pulsed power switch selection.

## Project Goals

The goal of this project was to determine the suitability of light-triggered thyristors for pulsed power applications beyond manufacturers' ratings. To test the applicability of the most recent commercial light-triggered solid-state designs, an adjustable high current switch test stand was assembled in the LLNL Pulsed Power Lab. A typical switch stack is shown in Fig. 1. The selected devices (Eupec T2563NH) were stressed beyond the di/dt rating of 5 kA/ $\mu$ s while maintaining low peak currents and, conversely, stressed beyond the peak current rating of 93 kA while maintaining a low current rate of rise.

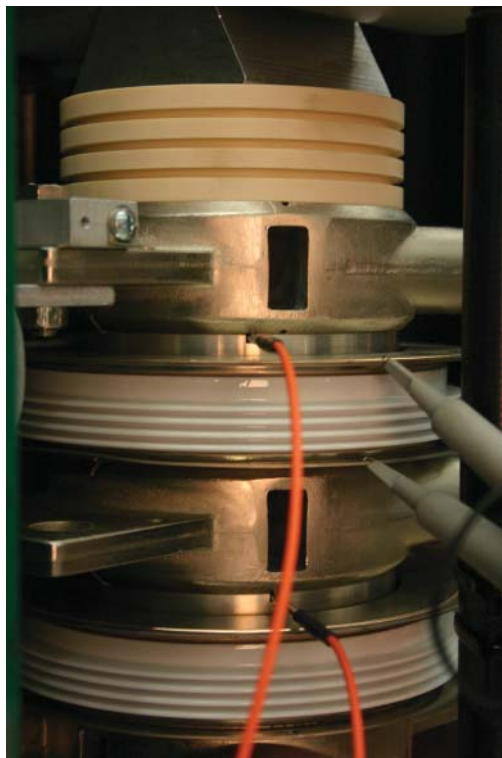
## Relevance to LLNL Mission

Solid-state switching is the future direction for many pulsed power applications with high-current, high-energy capacitor discharge units. LLNL has many switching needs including magnetic flux compression generators, flash-lamp banks, pulsed high-field magnets, compact electric power conversion, and electromagnetic launchers.

## FY2007 Accomplishments and Results

Switch testing was conducted in two customizable testbeds. A resistive load (Fig. 2) was implemented for high di/dt testing while maintaining low peak current. An inductive load (Fig. 3) was constructed for high peak current testing while maintaining low di/dt. Each load

Figure 1. Switch stack with optical trigger fibers inside orange jackets.



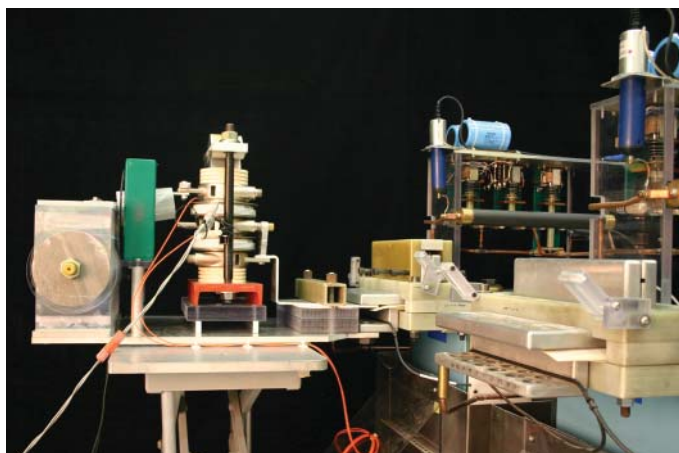


Figure 2. High di/dt test stand with resistive load.

consisted of a variable number of resistors and inductors, respectively, to target the bounds of operation for the device. Full pulsewidth was minimized to less than 10% of nominal 10 ms rating. Switch action was kept orders of magnitude below specified rating. Switch performance diagnostics included Rogowski coils to measure current into the switch and a differential voltage probe to measure the voltage drop across the switch.

During high di/dt testing (5.6 to 7.2 kA/ $\mu$ s), the device failed after four shots operating above rated di/dt despite minimal current injection (28 to 36 kA). High peak current testing indicated failure imminent at currents slightly

over rated values (95 kA) despite low di/dt (1.6 kA/ $\mu$ s). The optical trigger pulsewidth was optimized such that no observable decrease in turn-on time could be achieved. The trigger pulse amplitude was maximized until it was driver-board limited. The decrease in power dissipated by the switch due to the slight reduction in device turn-on time appeared to reduce the magnitude of destruction evident during dissection post-mortem. No increased peak current-carrying ability was demonstrated as a result of modification of the trigger pulse. Detailed investigation of the failed devices was undertaken to determine the failure mechanisms (Fig. 4).

For high reliability, we have concluded that the tested devices should

not be operated outside of the specified ratings. With the current state of the technology, light-triggered solid-state switches may be self-limiting for demanding high current pulsed power applications. The increased cost and complexities introduced with series/parallel combinations to achieve operation within ratings may prove too cumbersome for high current applications in the near future.

### Related References

1. General Electric Corporation, *SCR Manual: Including Triacs and Other Thyristors*, Sixth Edition, Prentice-Hall, Inc., Englewood Cliffs, New Jersey, 1979.
2. Ruff, M., H. Schulze, and U. Kellner, "Progress in the Development of an 8-kV Light-Triggered Thyristor with Integrated Protection Functions," *IEEE Trans. on Electron Devices*, **46**, 8, August 1999.
3. Podelsak, T. F., S. Schneider, and F. M. Simon, "Single Shot and Burst Repetitive Operation of Involute Gate 125 mm Symmetric Thyristors up to 221 kA with a di/dt of 2.0 kA/ $\mu$ s," *IEEE Trans. on Plasma Science*, **28**, 5, October 2000.
4. Wisken, H. G., F. Podyen, T. H. Weise, J. Dorn, and D. Westerholt, "Light Activated Semiconductors for ETC Pulsed Power Applications," *IEEE Trans. on Magnetics*, **37**, 1, January 2001.
5. Podelsak, T. F., F. M. Simon, and S. Schneider, "Single Shot and Burst Repetitive Operation of Thyristors for Electric Launch Applications," *IEEE Trans. on Magnetics*, **37**, 1, January 2001.

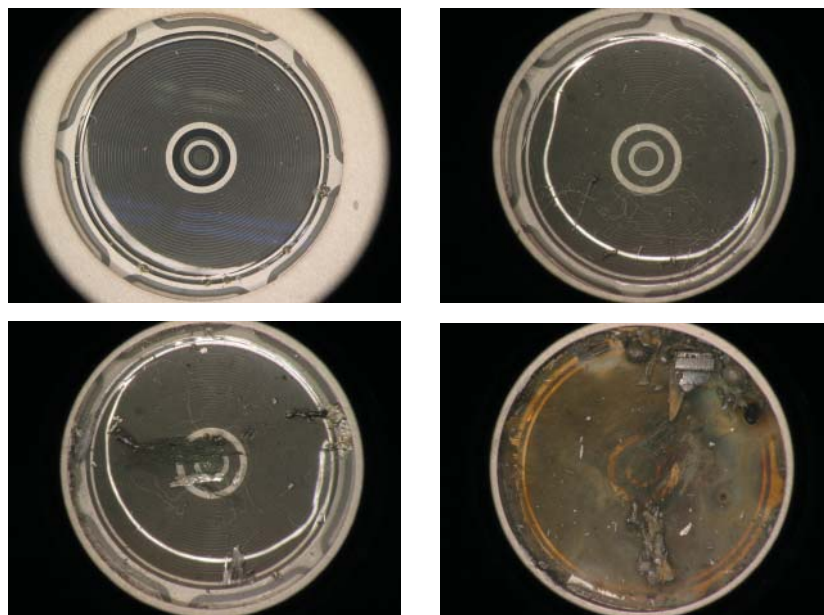


Figure 4. Microscopic views of the gate structures. These images assist in determining exact mode of failure in the switching device.



Figure 3. High peak current test stand with inductive load.

# Fiber Optic Current Measurements Using Faraday Rotation Diagnostics



*Brent McHale*  
(925) 422-8730  
mchale3@llnl.gov

It is often necessary to measure extremely large pulsed electric currents when conducting pulsed power, explosively driven pulsed power, or controlled fusion experiments. There are a limited number of diagnostics that can be used to accurately measure currents at these levels. The most common are calibrated inductive field sensors which are very susceptible to undesirable field coupling and EMI.

Faraday Rotation Diagnostics (FRDs) rely on magneto-optical rather than inductive phenomena and are largely immune to EMI. The polarization of the light in a magneto-optical material is rotated due to a circular birefringence. This rotation is directly proportional to the magnetic field strength and the length over which the magnetic field and optical field interact in the material. FRDs have been used as a method of measuring large pulsed currents for more than 40 years and are presently used at other institutions in a range of high-value pulsed power experiments. A FRD of proven configuration was successfully installed in LLNL's Pulsed Power Lab (PPL) and used to measure current on the ALE3D coaxial load experiment.

## Project Goals

Our goal for FY2007 was to install and operate a FRD in the PPL high-current test cell, and to acquire the capabilities and knowledge base to support all aspects of FRD implementation, including sensor fabrication, experimental installation and operation, and data analysis.

## Relevance to LLNL Mission

FRD sensors have excellent linearity and bandwidth characteristics, and are optically isolated. These qualities make FRDs particularly well suited for application in experiments that involve large quantities of guided or radiated electromagnetic energy. Since failure modes of FRDs differ from those of conventional inductive field sensors, FRDs offer a level of data redundancy for high-value single-shot experiments that is not easily achievable otherwise. Numerous programs at LLNL stand to benefit from this expertise, including explosive pulsed power for high energy density physics research, EM launcher/shaker experiments for military applications, and operations at the NIF.

## FY2007 Accomplishments and Results

FRD hardware was acquired and installed in the PPL high-current test cell on the ALE3D coaxial load testbed. A graphical depiction of this system is shown in Fig. 1. A diode laser launches a few mW of linearly polarized light at 850 nm into a FRD sensor fiber, which is a single-mode fiber that is wrapped 50 to 100 times around the coaxial load input (Fig. 2). The magnetic field in the vicinity of the sensor fiber induces Faraday rotation of the linearly polarized

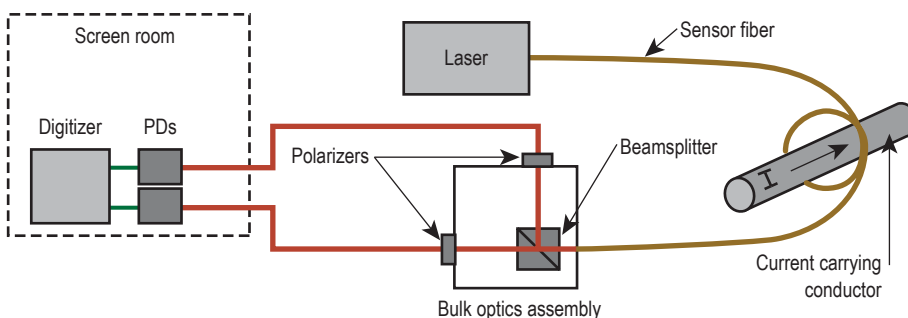


Figure 1. Block diagram of the FRD system.

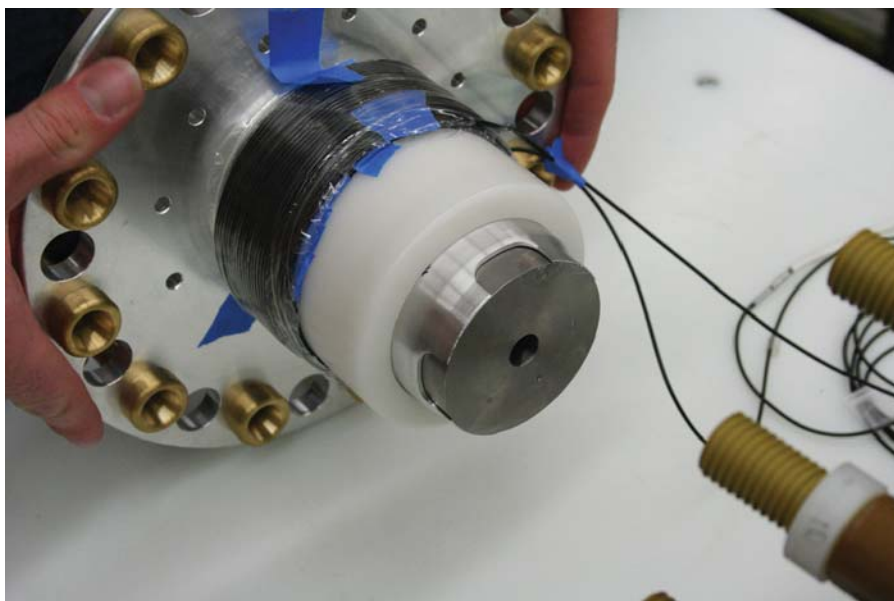


Figure 2. FRD sensor fiber installed on the ALE3D coaxial load testbed.

light. The polarization-rotated signal is coupled into a bulk optics assembly that splits the beam via a non-polarizing beam splitter and passes each beam through polarizers that are at a known relative angle. Both signals are then coupled through multimode fiber onto photodetectors and a digitizer in the screen room.

We have implemented the FRD on four shots of the ALE3D coaxial load validation test. An example of raw data representing the two components of the polarized signal is shown in Fig. 3.

The total Faraday rotation is extracted from the digitized data and is scaled by material constants and geometric factors to yield current. We have created an algorithm that automates this process. A time history of current obtained using this process is shown in Fig. 4, where it is compared to integrated Rogowski coil data. These data demonstrate excellent agreement, within 1% at peak current.

#### Related References

1. Rose, A. H., S. M. Etzel, and C. M. Wang, "Verdet Constant Dispersion in Annealed

- Optical Fiber Current Sensors," *J. Lightwave Technology*, **15**, pp. 803-807, May 1997.
2. Day, G. W., and A. H. Rose, "Faraday Effect Sensors: The State of the Art," *Proc. SPIE*, **985**, pp. 138-150, September 1988.
3. Bland, S. N., D. J. Ampleford, S. C. Bott, A. Guite, G. N. Hall, S. M. Hardy, S. V. Lebedev, P. Shardlow, A. Harvey-Thompson, F. Suzuki, and K. H. Kwek, "Use of Faraday Probing to Estimate Current Distribution in Wire Array Z Pinches," *Rev. Sci. Instrum.*, **77**, 10E, p. 315, 2006.

#### FY2008 Proposed Work

We will continue working on a FRD at 635 nm that will provide improved sensitivity and noise characteristics over the present implementation. Motivating this wavelength change is the fact that the sensitivity of the device varies with the inverse of wavelength squared. The system will be deployable in support of pulsed power experiments at LLNL, NTS, LANL and Site 300. We will continue to work on ancillary aspects of FRD implementation such as sensor fabrication, modeling, and data analysis that permit improvement of the precision and accuracy of the diagnostic.

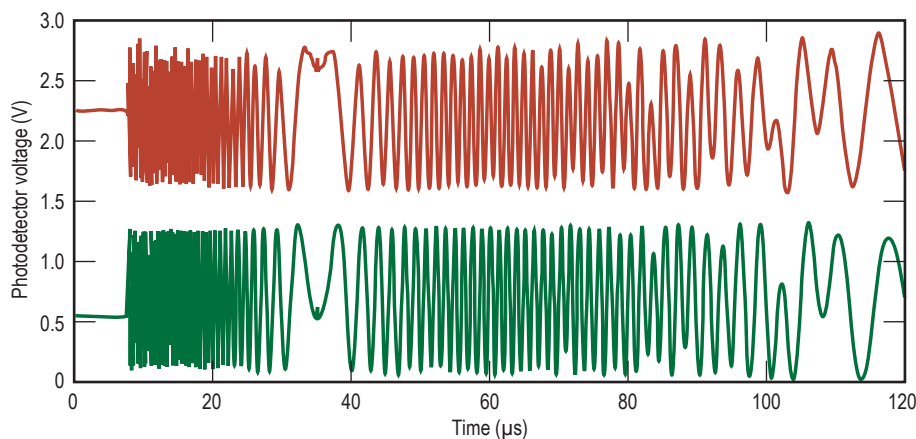


Figure 3. Raw FRD data representing two components of the Faraday-rotated polarized light.

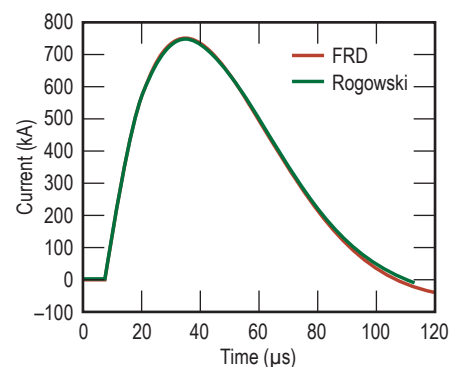


Figure 4. FRD and Rogowski measurements of a large amplitude, time varying current.



# Author Index

Alves, Steven W. ....	22	Miles, Robin .....	74
Anderson, Andrew .....	26	Morse, Jeffrey D. ....	88
Barton, Nathan R. ....	2	Mukerjee, Erik V. ....	76
Beer, N. Reginald .....	64	Nederbragt, Walter W. ....	42
Bennett, Corey V. ....	56	Ness, Kevin D. ....	70
Bond, Tiziana .....	80, 82	Nikolić, Rebecca J. ....	86, 90
Brown, Charles G., Jr. ....	28	Noble, Charles R. ....	24
Brown, William D. ....	44	Pannu, Satinderpall .....	78
Burke, Michael W. ....	48	Poland, Douglas N. ....	52
Candy, James V. ....	46	Puso, Michael A. ....	6, 20
Clancy, Todd J. ....	114	Rose, Klint A. ....	72, 92
Corey, Bob .....	16	Schmidt, Mark A. ....	100
Florando, Jeffrey N. ....	4	Seugling, Richard M. ....	38
Glascocoe, Lee G. ....	108	Solberg, Jerome M. ....	112
Heebner, John E. ....	60	Spadaccini, Christopher M. ....	94
Houck, Timothy L. ....	116	Stölken, James S. ....	8
Huber, Robert .....	50	Tully, Laura .....	120
Javedani, Jay .....	118	Van Buuren, Anthony .....	54
Kotovsky, Jack .....	84	Vernon, Stephen P. ....	58
Kroll, Jeremy J. ....	40	Walton, Christopher .....	30
Lemmond, Tracy D. ....	104	Weisgraber, Todd .....	96
Lin, Jerry I. ....	18	Wemhoff, Aaron P. ....	32
Mariella, Raymond P., Jr. ....	66, 68	White, Adam .....	34
May, John M. ....	12	White, Daniel .....	10, 14
McCarrick, James F. ....	98	Yao, Yiming .....	106
McHale, Brent .....	122		



*Manuscript Date April 2008*

*Distribution Category UC-42*

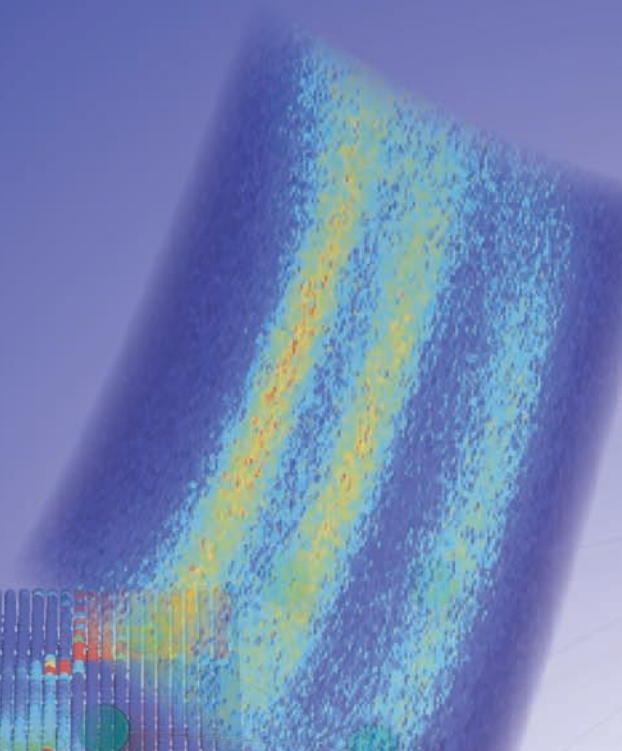
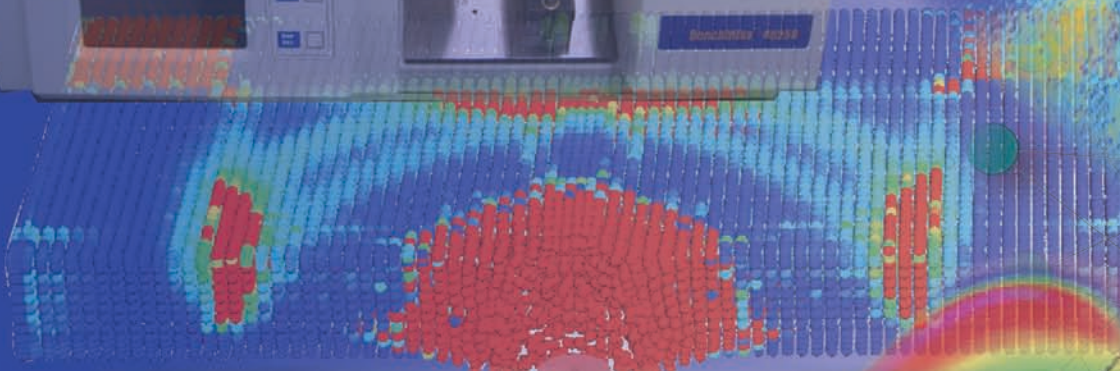
This report has been reproduced directly from the best copy available.

Available from  
National Technical Information Service  
5285 Port Royal Road  
Springfield, VA 22161

Or online at [www-eng.llnl.gov/pubs.html](http://www-eng.llnl.gov/pubs.html)

This document was prepared as an account of work sponsored by an agency of the United States Government. Neither the United States Government nor Lawrence Livermore National Security, LLC, nor any of their employees, makes any warranty, express or implied, or assumes any legal liability or responsibility for the accuracy, completeness, or usefulness of any information, apparatus, product, or process disclosed, or represents that its use would not infringe privately owned rights. Reference herein to any specific commercial product, process, or service by trade name, trademark, manufacturer, or otherwise, does not necessarily constitute or imply its endorsement, recommendation, or favoring by the United States Government or Lawrence Livermore National Security, LLC. The views and opinions of authors expressed herein do not necessarily state or reflect those of the United States Government or Lawrence Livermore National Security, LLC, and shall not be used for advertising or product endorsement purposes.

This work was performed under the auspices of the U.S. Department of Energy by Lawrence Livermore National Laboratory under Contract DE-AC52-07NA27344. ENG-07-0052



# ENGINEERING

Lawrence Livermore National Laboratory  
PO Box 808, L-151  
Livermore, CA 94551-0808  
<http://www-eng.llnl.gov/>